Democratic and Popular Republic of Algeria
Ministry of High Education and Scientific Research

University of Ferhat Abbas Setif 1

THESIS

Presented at Faculty of Sciences
Department of Physics
To obtain the degree of

Doctor of Science

Option: Solid State Physics

By

BEDJAOUI Abdelhak

Title

Ab initio Study of Some Physical Properties of the Cu_2MgSiS_4 and Cu_2MgGeS_4 diamond-like semiconductors and Sr_2GeN_2 Polymorphs

---

Discussed publicly at 08/ 07/ 2017 with the board of examiners:

Mr. K. KASSALI	Professor	Univ. F. Abbas Setif 1	Chairman
Mr. A. BOUHEMADOU	Professor	Univ. F. Abbas Setif 1	Thesis Advisor
Mr. R. KHENATA	Professor	Univ. M. Stambouli Mascara	Examiner
Mr. T. CHIHI	M.C.A	Univ. F. Abbas Setif 1	Examiner
Mr. M. SALMI	M.C.A	Univ. M. Boudiaf M'sila	Examiner
Mrs. S. FETAH	M.C.A	Univ. M. Boudiaf M'sila	Examiner
Mr. A. MOSBAH	M.C.A	Univ. F. Abbas Setif 1	Invited
Mr. N. GUECHI	M.C.B	Univ. Y. Fares Medea	Invited


بسم الله الرحمن الرحيم

ملخص

في هذا العمل، قمنا بدراسة بعض الخواص الفيزيائية لمجموعتين من المركبات. المجموعة الأولى تضم مركبين رباعيين حديثي التوليف، هما نصفا النواقل مثيلا الماس Cu_2MgSiS_4 و Cu_2MgGeS_4 . المجموعة الثانية تتمثل في متعددي الأشكال ثلاثيي النتريدات $\alpha-Sr_2GeN_2$ و $\beta-Sr_2GeN_2$. وذلك باستخدام حسابات المبدأ الأول في إطار نظرية دالية الكثافة (DFT). وقد تم اعتماد النسخة الجديدة لتقريب التدرج المعمم من أجل معالجة كمون التبادل والارتباط (GGA-PBEsol) .

تمت دراسة الخواص البنيوية، المرونة، الالكترونية والضوئية لنصفي النواقل Cu_2MgSiS_4 و Cu_2MgGeS_4 بالتفصيل مستخدمين طريقتين متكاملتين من طرق المبدأ الأول، هما طريقة الأمواج المستوية مع الكمونات الكاذبة (PP-PW)، و طريقة الأمواج المستوية المزادة خطيا مع الكمون الكامل (FP-LAPW). تتوافق معاملات البنية البلورية (ثابت الشبكة البلورية، الإحداثيات الذرية وأطوال الروابط بين الذرات) المحسوبة للحالة الأساسية توافقا جيدا مع المعطيات التجريبية والنظرية المتوفرة. تم التنبؤ بمعاملات المرونة (ثوابت المرونة، معامل الانضغاط، معامل القص، معامل يونغ، نسبة بواسون) لكل الطورين أحادي البلورة ومتعدد البلورات والخواص المرتبطة بها (مؤشرات التباين المرن، معيار بوغ، سرعات الموجات المرنة ودرجة حرارة ديباي). فيما يخص الخواص الإلكترونية، وجدنا أن إدراج تقريب دالية TB-mBJ لمعالجة كمون التبادل والارتباط يحسن وصف البنية الإلكترونية. وجدنا أن هذه المواد من انصاف النواقل ذات فاصل طاقوي أساسي مباشر (Γ-Γ)، قيمته 2.64 eV لـ Cu_2MgSiS_4 و 1.54 eV لـ Cu_2MgGeS_4. تم كذلك حساب أطياف دالة العازلية الكهربائية، معامل الانكسار، معامل الإخماد، معامل الامتصاص، الانعكاسية، معامل فقدان الطاقة والناقلية البصرية، وتم تعيين أصول الانتقالات الإلكترونية المشاركة في البنيات المشاهدة في هذه الأطياف. يمتاز كل من المركبين Cu_2MgSiS_4 و Cu_2MgGeS_4 بامتصاص معتبر للأشعة فوق البنفسجية.

تمت دراسة الخواص البنيوية، المرونة والديناميكية الحرارية لمتعددي الأشكال α (رباعي قائم) و β (معيني قائم) للمركب Sr_2GeN_2 بالتفصيل، باستخدام طريقة الأمواج المستوية مع الكمونات الكاذبة (PP-PW). باستثناء الخواص البنيوية في الظروف العادية، فإن بقية النتائج تم الحصول عليها لأول مرة. تتوافق القيم المحسوبة لثوابت الشبكة البلورية وأطوال الروابط بين الذرات للمركبين توافقا جيدا مع المعطيات التجريبية المتوفرة. لقد وجد أن الطور $\alpha-Sr_2GeN_2$ أكثر استقرارا من الطور $\beta-Sr_2GeN_2$. يتشابه المركبان المدروسان بشكل كبير فيما يخص بنيتيهما البلورية. تم التنبؤ أيضا بمعاملات المرونة (ثوابت المرونة، معامل الانضغاط، معامل القص، معامل يونغ، نسبة بواسون) للطورين أحادي البلورة ومتعدد البلورات وبالخصائص ذات الصلة بها (مؤشرات التباين المرن، معيار بوغ، سرعات الموجات المرنة ودرجة حرارة ديباي). تمت دراسة تأثير الحرارة والضغط الهيدروستاتيكي على العديد من المعاملات الفيزيائية الماكروسكوبية، مثل معامل الانضغاط، معامل التمدد الحراري الحجمي، السعة الحرارية ودرجة حرارة ديباي، مستعملين النموذج شبه التوافقي لديباي.

الكلمات الدالة: مركب مثيل الماس؛ متعددا الأشكال Sr_2GeN_2؛ حسابات المبادئ الأولى؛ الثوابت البنيوية؛ معاملات المرونة؛ البنية الإلكترونية؛ الخواص البصرية؛ الخواص الديناميكية الحرارية.

Abstract

In the present work, we have explored some physical properties of the two newly synthetized quaternary diamond-like semiconductors Cu_2MgSiS_4 and Cu_2MgGeS_4, and two polymorphs of the ternary nitrides α-Sr_2GeN_2 and β-Sr_2GeN_2, using first-principle calculations based on the density functional theory (DFT). The exchange-correlation effects were treated within the new version of the generalized gradient approximation (GGA-PBEsol).

The structural, elastic, electronic and optical properties of the two considered diamond-like semiconductors were studied in detail using two complementary first-principles approaches: the pseudopotential plane wave (PP-PW) and the full potential augmented plane wane (FP-LAPW). The calculated equilibrium structural parameters are in good agreement with the available experimental data. Single-crystal and polycrystalline elastic moduli and their related properties, including elastic constants, bulk modulus, shear modulus, Young's modulus, Poisson's ratio, elastic anisotropy indexes, Pugh's criterion, elastic wave velocities and Debye temperature, were predicted. We find that the inclusion of the electronic exchange-correlation through the newly developed TB-mBJ improves the description of the electronic structure. The TB-mBJ yields a direct band gap (Γ-Γ) of 2.64 and 1.54 eV for Cu_2MgSiS_4 and Cu_2MgGeS_4, respectively. Frequency-dependence of the dielectric function, refractive index, extinction coefficient, absorption coefficient, reflectivity, energy loss function and optical conductivity were predicted, and the origins of the observed electronic transitions were assigned. Both Cu_2MgSiS_4 and Cu_2MgGeS_4 exhibit noticeable absorption in the ultraviolet range.

The structural, elastic and thermodynamic properties of the α (tetragonal) and β (orthorhombic) polymorphs of the Sr_2GeN_2 compound have been examined in detail using *ab initio* pseudopotential plane-wave calculations. Apart the structural properties at ambient conditions, all present reported results are predicted for the first time. The calculated equilibrium lattice parameters and inter-atomic bond-lengths of the considered polymorphs are in good agreement with the available experimental data. It is found that α-Sr_2GeN_2 is energetically more stable than β-Sr_2GeN_2. The two examined polymorphs are very similar in their crystal structures and have almost identical local environments. The single-crystal and polycrystalline elastic parameters and related properties, including elastic constants, bulk, shear and Young's moduli, Poisson's ratio, anisotropy indexes, Pugh's criterion, elastic wave velocities and Debye temperature, have been predicted. Temperature and pressure dependence of some macroscopic properties - including the bulk modulus, volume thermal expansion coefficient, heat capacity and Debye temperature - have been evaluated using *ab initio* calculations combined with the quasi-harmonic Debye model.

Key words: Diamond-like compound; Sr_2GeN_2 polymorphs; First-principles calculations; structural parameters; Elastic moduli; Electronic structure; Optical properties; thermodynamic properties.

تشكرات

نحمد الله تعالى أولا و نشكره على إنعامه و منه و كرمه علي بأن يسر لي طريقا من طرق العلم، و على توفيقه لي في إنجاز هذا العمل المتواضع. فنسأله سبحانه أن يجعل هذا العمل خالصا لوجهه الكريم، و أن يجعله ذخرا لي و نافعا لكل طالب علم يبتغي خدمة الإنسانية، و نسأله أن يسهل لي به طريقا إلى الجنة. آمين.

ثم أتوجه بالشكر الجزيل إلى أستاذي **عبد المجيد بوحمادو**، أستاذ و باحث بجامعة فرحات عباس- سطيف، على تفضله بالإشراف على تأطيري و متابعته المستمرة لهذا العمل طيلة مدة إنجازه، و على المجهودات التي بذلها و صبره معي على حساب راحته، إيمانا منه بالعمل الدؤوب من أجل إرساء قواعد متينة و قوية في بناء صرح العلم و المعرفة.

كما أتوجه بتشكراتي للأستاذ **كمال كسالي**، أستاذ و باحث بجامعة فرحات عباس- سطيف على تشريفه لي و تفضله برئاسة لجنة المناقشة.

و أتوجه كذلك بتشكراتي إلى أعضاء اللجنة الممتحنين على تفضلهم بقبول الدعوة لمناقشة هذه الرسالة رغم انشغالاتهم الكثيرة، و هم: الأستاذ **رابح خناتة** من جامعة مصطفى سطمبولي بمعسكر، الأستاذ **الطيب شيحي** من جامعة فرحات عباس- سطيف، الأستاذان **سالمي محمد** و **فتاح صباح** من جامعة محمد بوضياف بالمسيلة، و كذا الأستاذان المدعوان **عمار مصباح** من جامعة فرحات عباس- سطيف و **نصير قشي** من جامعة يحيى فارس بالمدية.

ولا يفوتني أن أتقدم بالشكر لكل من ساعدني أو ساهم في إنجاز هذا العمل من قريب أو من بعيد، و أخص بالذكر كلا من **فارس زرارقة**، **خليفة حدادي**، **جمال علالي**، **منير رفاس**، **كريم بلجودي** و **صلاح الدين بن سالم**.

Published Papers

1. *Structural, elastic and thermodynamic propertiesof tetragonal and orthorhombic polymorphs of Sr_2GeN_2: an ab initio investigation*, A. Bedjaoui, A. Bouhemadou & S. Bin-Omran, High Pessure Research, Vol. 36, No. 2, 198-219 (2016).
2. *Structural, elastic, electronic and optical properties of the novel quaternary diamond-like semiconductors Cu_2MgSiS_4 and Cu_2MgGeS_4*, A. Bedjaoui , A. Bouhemadou, S. Aloumi, R. Khenata, S. Bin-Omran, Y. Al-Douri, F. Saad Saoud and S. Bensalem, Solid State Sciences 70, 21-53 (2017).

Nomenclature

Frequently used abbreviations:

DFT	Density Functional Theory.
H	Hartree.
HF	Hartree-Fock.
xc	Exchange Correlation.
KS	Kohn-Sham.
LDA	Local Density Approximation.
LSDA	Local Spin Density Approximation.
GGA	Generalized Gradient Approximation.
PBEsol	Perdew-Burke-Ernzerhof functional for Solids.
TB-mBJ	Tran-Blaha modified Becke-Johnson potential.
PP-PW	Pseudopotential-Plane Wave.
ZB	Brillouin Zone.
AE	All Electrons.
NC	Norm-Conserving.
BHS	Bachelet, Hamann, Schluter procedure for constructing norm-conserving PP.
KB	Kleinman and Bylander.
US-PP	Ultrasoft pseudopotential.
APW	Augmented Plane Wave.
LAPW	Linearized Augmented Plane Wave.
FP	Full Potential.
MT	Muffin-Tin region.
I	Interstitial region.
LO	Local Orbitals.
EOS	Equation Of State.
BM	Birch Murnaghan.
V-R-H	Voigt-Reuss-Hill.
$\mathbf{E_g}$	Energy band gap.
VB	Valence Band.
CB	Conduction Band.
TDOS	Total Density Of States.
PDOS	Partial Density Of States.

Contents

Part II: Results and discussions

List of Figures

List of Tables

CHAPTER 1

General introduction

Chapter 1

General introduction

1.1. Preamble

Solids are the physical objects with which we come into contact continuously in our everyday life. They exhibit a wide range of properties, which what makes them so useful and indispensable to humankind. The use and understanding of matter in its condensed (liquid or solid) state have gone hand in hand with the advances of civilization and technology since the first use of primitive tools. So important has the control of condensed matter been to man that historical ages -the Stone Age, the Bronze Age, the Iron Age- have often been named after the material dominating the technology of the time [1]. Today, the search for new materials with specific physical or chemical properties is a major challenge of the current industry, which makes the number of synthesized materials very considerable and constantly increasing. Indeed, the modern scientific and technological development makes it possible to design new materials adapted to each new application, depending on the physical properties required. One of the best examples that can be given is the search of semiconducting materials, which constitute today the basic building blocks of emitters and receivers in cellular, satellite, and fiberglass communication.

Solid-state physics constitutes one of the largest subfields of modern physics. It is the most important branch of condensed matter physics[1] that occupies something like 50% of physicists working in fundamental research, and the industrial opportunities in the engineering sciences [2,3]. One definition of solid-state physics is that it is the study of the physical properties of solids in terms of basic physical laws. Solid-state physics branch began in the early years of twentieth century, following the discovery of X-ray diffraction by

[1] Condensed matter physics is the field of physics that deals with the macroscopic physical properties of matter. In particular, it is concerned with the "condensed" phase matter; phases that appear whenever the number of constituents in a system is extremely large and the interactions between the constituents are strong. The most familiar examples of condensed phases are solids and liquids.

crystals and the publication of a series of simple calculations and successful predictions of crystal properties [4]. However, a separate field going by the name of solid-state physics did not emerge until the 1940, with the publication of Fredrick Seitz's book, *Modern Theory of Solids* in 1940 [5], and had its most extensive expansion with the development of the transistor, integrated circuits, and microelectronics [2].

The term "solid-state" is often restricted to mean only crystalline (periodic) materials that exhibit translational symmetry [2,4]. The existence of crystals has facilitated considerably the study of solids, since a crystalline solid can be analyzed by considering what happens in a single unit of the crystal (referred to as the unit-cell), which is then repeated periodically in all three dimensions to form the idealized perfect and infinite solid. This regularity has made it possible to develop powerful analytical tools and to use clever experimental techniques to study the properties of solids [6]. It is the most important property for developing the theory of the energy spectrum of electrons, lattice vibrations or the matter-radiation interaction, in which, from these theories, one can calculate the thermal, electrical, optical, elastic or magnetic magnitudes. There is a wide variety of crystal structures, which are formed by different elements or by different combinations of elements. Physics tends also to investigate new materials under artificial conditions in order to characterize certain properties. Near perfect macroscopic crystals can be formed by simply melting and then slowly cooling a substance in the laboratory, produced more and more artificial materials.

Interaction between electrons in the outer shells of atoms, the so-called *valence* electrons, determines the atomic structure and all other properties of solids, including mechanical, electrical, optical, thermal, magnetic and so on properties [6,7]. The basic concepts of modern physics in the form of statistical physics and quantum mechanics are thus essential to understand the macroscopic behavior of electrons in solids [3]. The characteristic properties of free atoms do, of course, determine the nature of the solid they make up, but, when embedded in a crystal lattice, these properties are greatly influenced by the surroundings. Electrical conductivity, ferromagnetism, specific heat, and phase transitions are, moreover, examples of concepts which can be defined for the solid but not for an individual atom. A theoretical description of the properties of solids must therefore use methods appropriate to many-body systems [8]. Thus, two properties of the solid state are of special importance: the solid as a many-body system and the symmetries of the crystal lattice.

Today, with the advanced technology it has become possible to analyze experimentally the structural properties of crystals, even under conditions of high temperature

and high pressure. However, the pressure and temperature domain is limited by the experimental device. Parallel to these experimental advances, the emergence of computer simulations based on the development of computational power of recent computers and the rapid advances in calculation methods, it has become possible to determine the properties of materials with high precision without any empirical parameters by means of *ab initio* (*first-principles*) electronic structure methods. In this way, it is possible not only to explain the already known properties of a given material, but also to predict suitable properties for new materials. This made it possible to replace very expensive experiments or even impractical in the laboratory [9,10]. For these reasons, ab initio computational methods become more and more important in materials science, and constitute today an essential complement to experimental research techniques in multiple fields.

Description of physical properties of solids from *first-principles* theory implies solving the Schrödinger equations for a huge number of interacting electrons and nuclei [11], i.e., a complex many-body problem. The *Density Functional Theory* (DFT) [12,13] offers a good reformulation of this problem. In its formulation given by Kohn, Hohenberg, and Sham in the 1960's, the real system of interacting many-electrons and nuclei is replaced by an effective non-interacting, fictitious particles moving in an effective potential of fixed nuclei, and the complex many-body wave function is abandoned in favor of the electronic density which only depends on the three spatial coordinates [14]. Solving the single-electron equations self-consistently, one obtains the equilibrium electron density and the total energy of the system, where from the latter, all physical properties that are related to it can be calculated [15]. This approach has proved to be highly successful in describing structural and electronic properties in a vast class of materials, ranging from atoms and molecules to simple crystals to complex extended systems (including glasses and liquids). Furthermore, DFT is computationally very simple. All this make DFT today as the most widely used approach that gives a quantum-mechanical basis for most of the *ab initio* methods used in computational materials science; its application is rapidly becoming a standard tool for diverse materials modeling problems in physics, chemistry, materials science, and even nuclear physics[2] [9,16]. DFT *ab initio* methods to solve Schrödinger equations are classified according to the representations that are used for the density, potential and, most importantly, the so-called Kohn-Sham orbitals. The

[2] Traditionally, chemists prefer using the Hartree-Fock wave function as their starting point. Since, the 1970s, physicists, on the other hand, have preferred density functional methods wherein the electron density is used as the primary starting point for describing the system.

choice of representation is made to minimize the computational and human costs of calculations, while maintaining sufficient accuracy [10]. Among various approaches used within the framework of density functional theory, the Pseudo-Potential Plane-Wave (PP-PW) [17-19] and the Full-Potential Linearize Augmented Plane Wave (FP-LAPW) [20,21] methods, which we will be used in the present work. The PP-PW method is one of the dominant methods for calculating ground state properties of extended systems. The simplicity of plane waves leads to very efficient numerical schemes for solving the Kohn–Sham equations, and the employment of pseudopotentials guarantees that the wave functions can be expanded in a relatively small set of plane waves. The FP-LAPW method has emerged as a widely used very robust and precise with reasonable computational efficiency to simulate the electronic properties of materials [10].

1.1. Statement of the problem and research objectives

1.2.1. Quaternary diamond-like semiconductors Cu_2MgSiS_4 and Cu_2MgGeS_4

Binary, ternary and quaternary diamond-like semiconductors (DLSs) have a crystalline structure that resembles either cubic or hexagonal diamond. The diamond-like semiconductor structure is derived from either the cubic or the hexagonal diamond by replacing the carbon in the lattice of the latters with cations and anions of the DLS compound [22-24]. Diamond-like semiconductors adhere to a set of guidelines [25]. First, each atom must have an average number of valence electrons of 4. Second, the average number of valence electrons for each anion must be 8. Third, each atom must have four nearest neighbor atoms located approximately at the corners of the surrounding tetrahedron. Lastly, the octet of each anion must be satisfied by its nearest neighbors. These guidelines can be used not only to classify the known DLS compounds but also to predict new compounds and their properties. Binary diamond-like semiconductors II-VI and III-V (e.g. ZnS and GaAs) and ternary I-III-VI_2 compounds (e.g. $CuGaS_2$) have been studied extensively [26-29], however, for the quaternary DLMs, which were first discovered in the1960s [22,23], relatively less studies have been reported. But recently, quaternary DLSs have seen an increase in attention [28,30-46] because their stable structure and compositional flexibility. The compositional flexibility of the DLSs allows the adjustments of their physical and chemical properties by changing their compositions; the DLSs are ideal tunable semiconductors [44,47,48]. This makes the quaternary DLSs more functional and gives them useful properties.

Quaternary diamond-like semiconductors with chemical formula $A^{I}_{2}B^{II}C^{IV}X^{VI}_{4}$ (A^{I} = Cu, Ag, B^{II} = Mg, Zn, Cd, Hg, X^{IV} = Si, Ge, Sn and X^{VI} =S, Se, Te) have received an increasing attention for their promising tunable physical properties and wide applications in photovoltaics [30,31], non-linear optics [32-34], solar cells [35-37], magnetics [38,39] and thermoelectrics [40-42]. It is worth to note that this kind of compounds possess high degree of electron-phonon interaction including anharmonic effects [49]. The latter factor has effects on some physical properties, such as superconductivity and nonlinear optical features [49,50]. The wide application of these quaternary compounds comes from their increased chemical and structural freedom, which makes their physical properties more flexible relative to binary and ternary compounds. Therefore, it is extremely important from the fundamental point of view to see how the fundamental parameters vary when moving from binary to ternary and further to quaternary compounds. The quaternary DLS $A^{I}_{2}B^{II}C^{IV}X^{VI}_{4}$ compounds (e.g. Cu_2ZnSnS_4) result from the II-VI binaries (e.g. ZnS) by substituting the cation (e.g. Zn) by three types of cations (e.g. Cu, Zn, Sn) [35,51]. Most of the quaternary DLS compounds crystallize in the stannite (tetragonal superstructure of sphalerite) with space group $I\bar{4}2m$ or the wurtzite-stannite structure (orthorhombic superstructure of wurtzite) with space group $Pmn2_1$ [43,52].

Recently, Liu et al [48] have synthetized two novel quaternary diamond-like semiconductors Cu_2MgSiS_4 and Cu_2MgGeS_4 via traditional high-temperature solid-state reactions. Single crystal X-ray diffraction analysis revealed that these compounds crystallize in the wurtzite-stannite structure with the orthorhombic space group $Pmn2_1$, derived from the hexagonal diamond [29]. These two compounds belong to the copper-containing quaternary chalcogenide compounds $Cu_2B^{II}C^{IV}X^{VI}_4$ that are very interesting with respect to their wide applications in optoelectronics and non-linear optics [29,32,53], as well as in thermoelectric applications [40,47,54]. Furthermore, all component elements of these compounds are abundant on the earth's crust and are not toxic. The optical absorption spectra transformed from diffuse reflectance data have been used to determine their band gaps, which are 3.20 and 2.36 eV for Cu_2MgSiS_4 and Cu_2MgGeS_4, respectively [48]. It is worth to note that the substitution of the Zn/Cd atom in the quaternary DLSs Cu_2ZnSiS_4 (E_g = 3.04 eV), Cu_2ZnGeS_4 (E_g = 2.04 eV) and Cu_2CdGeS_4 (E_g = 1.9-2.0 eV) by the Mg atom has increased their band gaps [48], indicating that the element mutation provides an efficient method for manipulating the band edge positions. Theoretically, as far as we know, only the electronic band structures

of the title compounds have been calculated [48] using first-principles pseudopotential plane-wave method. From these aforementioned experimental and theoretical studies [48], it turns out that data on some fundamental physical properties of these compounds, such as the elastic and optical properties, are lacking. Therefore, in order to provide a systematic report about the structural properties, elastic moduli and their related properties, electronic band structure, charge-carrier masses, density of states spectra and optical properties, we have carried out detailed first-principles calculations using two complementary first-principles methods, namely the pseudopotential plane-wave (PP-PW) and full-potential linearized augmented plane wave (FP-LAPW). Our aim is to identify the systematic variation of some physical properties when the Cd/Zn element (atom II) in the Cu_2-II-IV-VI_4 diamond-like compounds is substituted by the Mg element.

1.2.2. Tetragonal and orthorhombic polymorphs of Sr_2GeN_2

Because of their set of excellent useful properties, such as low compressibility, good thermal stability, chemical and radiation inertness and semiconducting, which allow important new technological applications, such as high-performance light-emitting devices, ultraviolet photodetectors, light-emitting diodes, lasers [55,56], converting solar light into electricity, photocatalysis, hydrogen production [57], lithium-ion batteries [58], magnetic and electronic devices [59,60], automotive engine wear parts, cutting tools and so on, the nitride materials have gained increasing interest since the mid-1980s.

In the quest of other nitride materials having the interesting properties of the binary nitrides and at the same time having other new properties that allow other new applications that are limited by the properties of the binary nitrides, such as an optimal band gap for higher effectiveness of possible devices, high-performance chemical and radiation inertness…etc., the attention has been drawn to ternary and quaternary nitrides [61-77]. Consequently, the number of synthesized ternary and quaternary nitrides has progressed rapidly over the last two decades. These new multinary nitrides provide a wider range of interesting mechanical, electrical, electronic, optical and chemical properties that make them potential candidates for probable new technological applications.

Some of the recently synthesized ternary nitrides are based on the germanium nitrides (GeN), such as the orthorhombic and tetragonal polymorphs of the strontium germanium nitrides, labeled α-Sr_2GeN_2 and β-Sr_2GeN_2 polymorphs, respectively [76,77]. The α-Sr_2GeN_2 and β-Sr_2GeN_2 phases were synthesized as single-crystals by DiSalvo *et al*. [76,77] from the

constituent elements in sealed Nb tubes at about 750 °C, using liquid Na as a growth medium. These two Sr2GeN2 polymorphs have several quite similar properties, such as the unit-cell volume and bond-lengths.

Apart the synthesis optimal conditions and structure features [76,77], experimental data on α-Sr_2GeN_2 and β-Sr_2GeN_2 crystals are not available in the scientific literature. Theoretical investigations of these systems are also scarce; as far as we know, there is only one theoretical work [78], which explored the electronic and optical properties of these compounds using full potential linearized augmented plane wave (FP-LAPW) calculations in the framework of the density functional theory. The reported theoretical results [78] reveal that α-Sr_2GeN_2 and β-Sr_2GeN_2 are very narrow band gap semiconductors. The ternary nitrides α-Sr_2GeN_2 and β-Sr_2GeN_2 can be used as substrates for GeN-based devices. Other eventual applications of these considered nitrides can be revealed from exploring and understanding their physical properties.

For optoelectronic device applications, semiconductor layers are commonly grown as thin epitaxial layers and superlattices on substrates. The lattice mismatch and difference in thermal expansion coefficients between epitaxial layers and substrates can cause large stresses in the epitaxial layers, which could affects their physical properties [79-81]. Hence, it is interesting and necessary for practical use to know: (i) the elastic constants, which describe the response of the material to the externally applied strains, and (ii) the evolution of the physical properties of these materials with pressure and temperature. The electronic and optical properties of the title nitrides have been already investigated by Zeyad and Reshak [78], whereas, to the best of authors' knowledge, no theoretical or experimental studies of the elastic and thermodynamic properties for these two nitrides are available in the scientific literature. On other hand, it is worth noting that the former reported theoretical calculations [78] investigated α-Sr_2GeN_2 and β-Sr_2GeN_2 phases at zero temperature only without any thermal effects included. Commonly, measurements of the elastic constants and effects of pressure and temperature on physical proprieties of materials are very difficult. Therefore, the lack of experimental data on these properties can be fulfilled via theoretical simulation based on accurate ab initio calculations. Thus, the first main objective of the present work is accurate calculations of the elastic constants and related properties at ambient as well as elevated pressures up to 15GPa using ab initio pseudopotential plane-wave method (PP-PW) based on density functional theory. The second main objective is the exploration of the pressure and temperature effects on the unit-cell volume, bulk modulus, volume thermal

expansion, isochoric heat capacity, Debye temperature and Grüneisen parameter of the title compounds using the PP-PW method in combination with the quasi-harmonic Debye model. We hope that the reported data can provide theoretical support to the existing experimental and theoretical data and provide a basis for future experimental and theoretical studies in order to have insight about eventual technological applications of the considered ternary nitrides α-Sr_2GeN_2 and β-Sr_2GeN_2.

1.3 Thesis outline

The present thesis is divided into 7 chapters:

In *chapter* 1, we introduce the important of the present study.

In *chapter* 2, we outline some of the founding principles of the density functional theory.

In *chapter* 3, we describe the Pseudopotential Plane-Waves method.

In *chapter* 4, we describe the Full Potential Linearized Augmented Plane Wave method.

In *chapter* 5, we present and discuss the predicted physical properties of the Quaternary diamond-like semiconductors Cu_2MgSiS_4 and Cu_2MgGeS_4.

In *chapter* 6, we present and discuss the predicted physical properties of the Tetragonal and orthorhombic polymorphs of Sr_2GeN_2.

Finally, in chapter 7, we summarize the main results obtained so far.

We hope that the reported data can provide theoretical support to the existing experimental and theoretical data and provide a basis for future experimental and theoretical studies in order to have insight about eventual technological applications of the considered two groups of materials concerned in our study.

References

[1] P. M. Chaikin and T. C. Lubensky, *Principles of condensed matter physics*, Cambridge University Press, Cambridge, 1995.

[2] J. D. Patterson, B.C. Bailey, *Solid-State Physics*, Springer, Berlin, 2007.

[3] H. Alloul, *Introduction to the Physics of Electrons in Solids*, Translated by Stephen Lyle, Springer-Verlag, Berlin, 2011.

[4] C. Kittel, *Introduction to Solid State* Physics, 8th Ed., John Wiley and Sons, Inc., New York, 2005.

[5] Seitz F, *The Modern Theory of Solids*, McGraw-Hill Book Company, New York, 1940.

[6] E. Kaxiras, *Atomic and Electronic Structure of Solids*, Cambridge University Press, New York, 2003.

[7] R. M. Martin, *Electronic Structure: Basic theory and practical methods*, Cambridge University Press, UK, 2004.

[8] O. Madelung, *Introduction to Solid-State Theory*, Springer-Verlag, Berlin, 1978.

[9] L. Vitos, *Computational Quantum Mechanics for Materials Engineers: The EMTO Method and Applications*, Springer-Verlag, London, 2007.

[10] D. J. Singh, L. Nordström, *Planewaves, Pseudopotentials, and the LAPW Method*, 2nd Ed, Springer Science+Business Media, Inc., USA, 2006.

[11] J. T. Devreese, P. Van Camp, *Electronic Structure, Dynamics, and Quantum Structural Properties of Condensed Matter*, Springer Science+Business Media, New York, 1985.

[12] P. Hohenberg and W. Kohn, *Inhomogeneous Electron Gas*, Phys. Rev. **136**, B864-B871 (1964).

[13] W. Kohn and L. J. Sham, *Self-Consistent Equations Including Exchange and Correlation Effects*, Phys. Rev. **140**, A1133-A1138 (1965).

[14] C. Fiolhais F. Nogueira M. Marques, *A Primer in Density Functional Theory*, Springer-Verlag, Berlin, 2003.

[15] M. C. Payne, M. P. Teter, D. C. Allan, T. A. Arias, and J. D. Joannopoulos, *Iterative minimization techniques for ab initio total-energy calculations: molecular dynamics and conjugate gradients*, Rev. Mod. Phys. **64**, 1045-1097 (1992).

[16] D. Sholl and J. S. Wiley, *Density functional theory: a practical introduction*, John Wiley & Sons, Inc., Hoboken, New Jersey, 2009.

[17] J. C. Phillips and L. Kleinman, *New Method for Calculating Wave Functions in Crystals and Molecules*, Phys. Rev. **116**, 287-294 (1959).

[18] D. H. Hamalm, M. Schluter, and C. Chiang, *Norm-Conserving Pseudopotentials*, Phys. Rev. Lett. **43**, 1494-1497 (1979).

[29] G. B. Bachelet, D. R. Hamann, and M. Schlüter, *Pseudopotentials that work: From H to Pu*, Phys. Rev. **B 26**, 4199-4228 (1982).

[20] O. K. Andersen, *Linear methods in band theory*, Phys. Rev. **B 12**, 3060-3083 (1975).

[21] D. D. Koelling and G. O. Arbman, *Use of energy derivative of the radial solution in an augmented plane wave method: application to copper*, J. Phys. F **5**, 2041-2054 (1975).

[22] E. Parthé, *Crystal Chemistry of Tetrahedral Structures*, Gordon and Breach Science Publishers, New York, 1964.

[23] N. A. Goryunova, in: J. C. Anderson (Ed.), *The Chemistry of Diamond-like Semiconductors*, The M.I.T. Press, Cambridge, 1965.

[24] F. P. Bundy, J. S. Kasper, *Hexagonal Diamond-A New Form of Carbon*, J. Chem. Phys. 46 3437-3446 (1967).

[25] C. D. Brunetta, B. Karuppannan, K. A. Rosmus, J. A. Aitken, *The crystal and electronic band structure of the diamond-like semiconductor* Ag_2ZnSiS_4, J. Alloys Compd. 516, 65-72 (2012).

[26] J.L. Shay, J.H. Wernick, *Ternary Chalcopyrite Semiconductors: Growth, Electronic Properties and Applications*, Pergamon Press. Elmsford, NY, 1975.

[27] E. Honig, H. Shen, G. Yao, K. Doverspike, R. Kershaw, K. Dwight, A. Wold, *Preparation and characterization of* $Cu_2Zn_{1-x}Mn_xGeS_4$, Mat. Res. Bull. 23, 307-312 (1988).

[28] M. Quintero, A. Barreto, P. Grima, R. Tovar, E. Quintero, G.S. Porras, J. Ruiz, J. C. Woolley, G. Lamarche, A. M. Lamarche, *Crystallographic properties of* I_2*–Fe–IV–*VI_4 *magnetic semiconductor compounds*, Mat. Res. Bull. 34 (1999) 2263-2270.

[29] D. M. Schleich, A. Wold, *Optical and electrical properties of quaternary chalcogenides*, Mat. Res. Bull. 12, 111-114 (1977).

[30] C. Steinhagen, M. G. Panthani, V. Akhavan, B. Goodfellow, B. Koo, B. A. Korgel, *Synthesis of* Cu_2ZnSnS_4 *Nanocrystals for Use in Low-Cost Photovoltaics*, J. Am. Chem. Soc. 131, 12554-12555 (2009).

[31] Q. Guo, G. M. Ford, W. C. Yang, B. C. Walker, E. A. Stach, H. W. Hillhouse, R. Agrawal, *Fabrication of 7.2% Efficient CZTSSe Solar Cells Using CZTS Nanocrystals*, J. Am. Chem. Soc. 132, 17384-17386 (2010).

[32] S. Levcenco, D. Dumcenco, Y. S. Huang, E. Arushanov, V. Tezlevan, *Polarization-dependent electrolyte electroreflectance study of $Cu_2ZnSiS4$ and $Cu_2ZnSiSe_4$ single crystals*, J. Alloys Comp. 509, 7105-7108 (2011).

[33] Y. Li, W. Fan, H. Sun, X. Cheng, P. Li, X. Zhao, *Electronic, optical and lattice dynamic properties of the novel diamond-like semiconductors Li_2CdGeS_4 and Li_2CdSnS_4*, J. Phys.: Condens. Matter 23, 225401-225411 (2011).

[34] J. W. Lekse, M. A. Moreau, K. L. McNerny, J. Yeon, P. S. Halasyamani, *Second-Harmonic Generation and Crystal Structure of the Diamond-like Semiconductors Li_2CdGeS_4 and Li_2CdSnS_4*, J.A. Aitken, Inorg. Chem. 48, 7516-7518 (2009).

[35] S. Chen, X. G. Gong, A. Walsh, S. H. Wei, *Electronic structure and stability of quaternary chalcogenide semiconductors derived from cation cross-substitution of II-VI and I-III-VI_2 compounds*, Phys. Rev. B. 79, 165211-165218 (2009).

[36] T. Schnabel, M. Löw, E. Ahlswede, *Vacuum-free preparation of 7.5% efficient $Cu_2ZnSn(S/Se)_4$ solar cells based on metal salt precursors*, Solar Energy Materials & Solar Cells117, 324-328 (2013).

[37] C. M. Fella, Y. E. Romanyuk, A. N. Tiwari, *Technological status of $Cu_2ZnSn(S,Se)_4$ thin film solar cells*, Solar Energy Materials & Solar Cells 119, 276-277 (2013).

[38] G. H. McCabe, T. Fries, M. T. Liu, Y. Shapira, L. R. Ram-Mohan, R. Kershaw, A. Wold, C. Fau, M. Averous, E. J. McNiff, *Bound magnetic polarons in p-type $Cu_2Mn_{0.9}Zn_{0.1}SnS_4$*, Phys. Rev. B. 56, 6673-7 (1997).

[39] X. Y. Shi, F. Q. Huang, M. L. Liu, L. D. Chen, *Thermoelectric properties of tetrahedrally bonded wide-gap stannite compounds $Cu_2ZnSn_{1-x}In_xSe_4$*, Appl. Phys. Lett. 94, 122103-122105 (2009).

[40] M. L. Liu, I. W. Chen, F. Q. Huang, L. D. Chen, *Improved Thermoelectric Properties of Cu-Doped Quaternary Chalcogenides of $Cu_2CdSnSe_4$*, Adv. Mater. 21, 3808-3812 (2009).

[41] C. Sevik, T. Cağin, *Ab initio study of thermoelectric transport properties of pure and doped quaternary compounds*, Phys. Rev. B 82, 045202-6 (2010).

[42] E. Parthé, K. Yvon, R. H. Deitch, *The Crystal Structure of Cu_2CdGeS_4 and Other Quaternary Normal Tetrahedral Structure Compounds*, Acta Cryst. B 25, 1164-1174 (1969).

[43] G. E. Davidyuk, O. V. Parasyuk, S. A. Semenyuk, Y. E. Romanyuk, *Electrical and Optical Properties of Cu_2CdGeS_4 Single Crystals*, Inorg. Mater. 39, 919-923 (2003).

[44] C. D. Brunetta, W. C. Minsterman, C. H. Lake, J. A. Aitken. *Cation ordering and physic chemical characterization of the quaternary diamond-like semiconductor* Ag_2CdGeS_4, J. Solid State Chem. 187, 177-185 (2012).

[45] C. D. Brunetta, J. A. Brant, K. A. Rosmus, K. M. Henline, E. Karey, J. H. MacNeil, J. A. Aitken, *The impact of three new quaternary sulfides on the current predictive tools for structure and composition of diamond-like materials*, J. Alloys and Compd. 574, 495-503 (2013).

[46] S. Y. Chen, A. Walsh, Y. Luo, J. H. Yang, X. G. Gong, S. H. Wei, *Wurtzite-derived polytypes of kesterite and stannite quaternary chalcogenide semiconductors*, Phys. Rev. B. 82, 195203-8 (2010).

[47] O. Y. Khyzhun, V. L. Bekenev, V. A. Ocheretova, A. O. Fedorchuk, O. V. Parasyuk, *Electronic structure of* $Cu_2ZnGeSe_4$ *single crystal: Ab initio FP-LAPW calculations and X-ray spectroscopy measurements*, Physica B 461, 75-84 (2015).

[48] B. W. Liu, M. J. Zhang, Z. Y. Zhao, H. Y. Zeng, F. K. Zheng, G. C. Guo, J. S. Huang, *Synthesis, Structure, and Optical Properties of the Quaternary Diamond-Like Compounds* I_2-*II-IV-*VI_4 (*I = Cu; II = Mg; IV = Si, Ge; VI = S, Se*), J. Solid State Chem. 204, 251-256 (2013).

[49] M. G. Brik , I. V. Kityk , O. V. Parasyuk, G. L. Myronchuk, *Photoinduced features of energy bandgap in quaternary* $Cu_2CdGeS4$ *crystals*, J. Phys.: Condens. Matter 25, 505802-11 (2013).

[50] J. K. Freericks, Mark Jarrell, and G. D. Mahan, *The Anharmonic Electron-Phonon Problem*, Physical Review Letters 77, 4588-4591 (1996).

[51] E. Roque Infante, J. M. Delgado, S. A. López Rivera, *Synthesis and crystal structure of* $Cu_2FeSnSe_4$*, a* I_2-*II-IV-*VI_4 *semiconductor*, Mat. Lett. 33, 67-70 (1997).

[52] W. Schäfer, R. Nitsche, *Tetrahedral quaternary chalcogenides of the type* Cu_2-*II-IV-*S_4(Se_4) Mater. Res. Bull. 9, 645-654 (1974).

[53] O. V. Parasyuk, L. D. Gulay, Y. E. Romanyuk, L. V. Piskach, *Phase diagram of the* Cu_2GeSe_3*-ZnSe system and crystal structure of the* $Cu_2ZnGeSe_4$ *compound*, J. Alloys and Comp. 329 202-207 (2001).

[54] G. Y. Davydyuk, O. V. Parasyuk, Y.E., S. A. Semenyuk, V. I. Zaremba, L. V. Piskach, J. J. Kozioł, V. O. Halka, *Single crystal growth and physical properties of the* Cu_2CdGeS_4 *compound*, J. Alloys and Compd. 339, 40-45 (2002).

[55] T. Matsuoka, *Progress in nitride semiconductors from GaN to InN-MOVPE growth and characteristics*, Superlattice Microstruct. 37, 19-32 (2005).

[56] K. T. Lam, P. C. Chang, S.J. Chang, C.L. Yu, Y.C. Lin, Y.X. Sun, C.H. Chen, *Nitride-based photodetectors with unactivated Mg-doped GaN cap layer*, Sens Actuators A. 143, 191-195 (2008).

[57] H. Yan, Y. Chen, S. Xu, *Synthesis of graphitic carbon nitride by directly heating sulfuric acid treated melamine for enhanced photocatalytic H_2 production from water under visible light*, Int. J. Hydrogen Energy 37, 125-133 (2012).

[58] Z. Wen, K. Wang, L. Chen, J. Xie, *A new ternary composite lithium silicon nitride as anode material for lithium ion batteries*, Electrochem. Commun. 8, 1349-1352 (2006).

[59] X. Z. Chen, H. A. Eick, *A new quaternary nitride, $Li_3Ba_2NbN_4$*, Solid State Chem. 113, 362-366 (1994).

[60] P. S. Herle, N. Y. Vasanthacharya, M.S. Hegde, J. Gopalakrishnan, *Synthesis of new transition metal nitrides, MWN_2 (M = Mn, Co, Ni)*, J. Alloys Compd. 217, 22-24 (1995).

[61] F. Cheviré, F. J. DiSalvo, *A new ternary nitride La_2GaN_3: synthesis and crystal structure*, J. Alloys Compd. 457, 372-375 (2008).

[62] D. G. Park, Y. Dong, F.J. DiSalvo, *$Sr(Mg_3Ge)N_4$ and $Sr(Mg_2Ga_2)N_4$: New isostructural Mg-containing quaternary nitrides with nitride-metallate anions of View the Math ML source* $[(Mg_3Ge)N_4]2\text{-}\infty3$ *and View the Math ML source* $[(Mg_2Ga_2)N_4]2\text{-}\infty3$ *in a 3D-network structure*, Solid State Sci. 10, 1846-1852 (2008).

[63] H. Yamane, H. Morito, *$Ba_4Mg[Si_2N_6]$, $Ba_3Ca_2[Si_2N_6]$ and $Ba_{1.6}Sr_{3.4}[Si_2N_6]$ – quaternary barium alkaline-earth silicon nitrides containing isolated nitridosilicate anions of* $[Si_2N_6]10\text{-}$, J. Alloys Compd. 555, 320-324 (2013).

[64] D. G. Park, Z. A. Gál, F. J. DiSalvo, *Synthesis and structure of $Li_4Sr_3Ge_2N_6$: a new quaternary nitride containing* $[Ge_2N_6]10\text{-}$ *anions*, J. Solid State Chem. 172, 166-170 (2003).

[65] S. Pagano, S. Lupart, S. Schmiechen, W. Schnick, *$Li_4Ca_3Si_2N_6$ and $Li_4Sr_3Si_2N_6$-quaternary lithium nitride-silicates with isolated* $[Si_2N_6]10\text{-}$ *Ions*, Zeitschrift fur Anorganische und Allgemeine Chemie. 636, 1907-1909 (2010).

[66] A. J. Ghazai, W. J. Aziz, H. Abu Hassan, Z. Hassan, *Quaternary n-$Al_{0.08}In_{0.08}Ga_{0.84}N$/p-Si-based solar cell*, Superlattices and Microstructures 51, 480-485 (2012).

[67] M. Jetter, C. Wächter, A. Meyer, M. Feneberg, K. Thonke, P. Michler, *Quaternary $Al_xIn_yGa_{1-x-y}N$ layers deposited by pulsed metal-organic vapor-phase epitaxy for high efficiency light emission*, J. Cryst. Growth. 315, 254-257 (2011).

[68] T. Kyono, H. Hirayama, K. Akita, T. Nakamura, *Effects of in composition on ultraviolet emission efficiency in quaternary InAlGaN light-emitting diodes on freestanding GaN substrates and sapphire substrates*, J. Appl. Phys. 98, 113514: 1-8 (2005).

[69] M. S. Bailey, F. J. DiSalvo, *Synthesis and crystal structure of* $LiCaGaN_2$, J. Alloys Compd. 417, 50-54 (2006).

[70] X. Z. Chen, H. A. *Eick, Synthesis and structure of two new quaternary nitrides:* $Li_3Sr_2MN_4$ (*M=Nb, Ta*), J. Solid State Chem. 130, 1-8 (1997).

[71] D. G. Park, Z. A. Gál, F. J. DiSalvo, *Synthesis and structure of* $LiSrGaN_2$*: a new quaternary nitride with interpenetrating two-dimensional networks*, J. Alloys Compd. 353, 107-113 (2003).

[72] X. Z. Chen, D. L. Ward, H.A. Eick, *Synthesis and structure of* $Li_3Ba_2TaN_4$, J Alloys Compd. 206, 129-132 (1994).

[73] A. Bowman, R.I. Smith, D.H. Gregory, *Synthesis and structure of the ternary and quaternary strontium nitride halides,* $Sr_2N(X, X')$ *(X, X'=Cl, Br, I)*, J Solid State Chem. 179, 130-139 (2006).

[74] P. Pust, S. Pagano, W. Schnick, *Organic chemistry*, Eur. J. Inorg. Chem. 7, 1157-1160 (2013).

[75] D. G. Park, F. J. Di Salvo, *Synthesis and crystal structure of a new quaternary nitride,* $Li_4Ca_{13}Ge_6N_{18}$, Bull. Korean Chem. Soc. 33, 1759-1761 (2012).

[76] S. J. Clarke, G.R. Kowach, F.J. DiSalvo, *Synthesis and Structure of Two New Strontium Germanium Nitrides:* $Sr_3Ge_2N_2$ *and* Sr_2GeN_2, Inorg. Chem. 35, 7009-7012 (1996).

[77] D. G. Park, Z. Gál, F. J. DiSalvo, *Synthesis and structure of a second polymorph of strontium germanium nitride:* β-Sr_2GeN_2, Bull. Korean Chem. Soc. 26, 786-790 (2005).

[78] Z. A. Alahmed, A. H. Reshak, *DFT calculation of the electronic structure and optical properties of two strontium germanium nitrides:* α-Sr_2GeN_2 *and* β-Sr_2GeN_2, J. Alloys Compd. 559, 181-187 (2013).

[79] H. Gleize, F. Demangeot, J. Frandon, M.A. Renucci, F. Widmann, B. Daudin, *Phonons in a strained hexagonal GaN–AlN superlattice*, Appl. Phys. Lett. 74, 703:1-3 (1999).

[80] A. Bouhemadou, G. Uğur, Ş. Uğur, S. Al-Essa, M. A. Ghebouli, R. Khenata, S. Bin-Omran, Y. Al-Douri, *Elastic and thermodynamic properties of* $ZnSc_2S_4$ *and* $CdSc2S_4$ *compounds under pressure and temperature effects*, Comp. Mat. Sci. 70, 107-113 (2013).

[81] A. Bouhemadou, R. Khenata, M. Kharoubi, T. Seddik, A. H. Reshak, Y. Al-Douri, *FP-APW + lo calculations of the elastic properties in zinc-blende III-P compounds under pressure effects*, Comp. Mat. Sci. 45, 474-479 (2009).

PART I

Theoretical framework

CHAPTER 2

Fundamentals of the Density Functional Theory

Chapter 2

Fundamentals of Density Functional Theory

Contents

2.1. Introduction

Since the discovery of the electron and the rise of quantum mechanics and particle physics, it has been shown that many natural phenomena of interest can be well explained by how electrons behave in the vast environment of other electrons and nuclei. In this century, the description of many-particle systems has been an important goal of physics. Analytic solutions of the Schrodinger equation are possible for a few very simple systems, and numerically exact solutions can be found for a small number of atoms and molecules [1]. However, many-particle system (e.g. electron-electron interactions in solids) is too complex to actually carry out. The solution to the problem can only be approximated. Such theoretical methods called *first principles* or *ab initio*[1] methods have been appeared before the formalism of *Density Functional Theory* (DFT) which is our subject in this chapter. Quantum mechanics and statistical mechanics are such theories, which should in principle suffice to determine the properties of solids from first principles [2]. A historically very important one is the Hartree-Fock method, described in many condensed matter textbooks [3]. These methods which are based on the many-body wave function as basic variable, present serious limitations: (1) the problem is highly nontrivial, even for very small numbers N and the resulting wave functions are complicated objects and (2) the computational effort grows very rapidly with increasing N, so the description of larger systems becomes prohibitive [4].

A different approach is taken in density-functional theory where, instead of the many-body wave function, the one-body density is used as the fundamental variable. Since the density ρ is a function of only three spatial coordinates (rather than the $3N$ coordinates of the wave function), density functional theory is computationally feasible even for large systems. It is an exact theory in its principle which makes it possible to calculate all the properties of the ground state. Despite the necessary approximations that implies its practical implementation, it offers good accuracy with relatively low computational cost, which allows it to tackle systems beyond the reach of other methods based on the wave function. It has proved to be highly successful in describing structural and electronic properties in a vast class of materials, ranging from atoms and molecules to simple crystals to complex extended systems, and attempts have been made to extend it to obtain excited-states [5]. For these reasons DFT has

[1] The term *ab initio* is Latin for "from the beginning" This name is given to computations that are derived directly from theoretical principles with no inclusion of experimental data. This is an approximate quantum mechanical calculation. The approximations made are usually mathematical approximations, such as using a simpler functional form for a function or finding an approximate solution to a deferential equation.

become a common tool in first-principles calculations aimed at describing - or even predicting - properties.

The theory originates from the pioneering work due to Thomas and Fermi in the early thirties of the twentieth century and further refinements by Hartree, Dirac, Fock and Slater. It was given a firm foundation by Hohenberg, Kohn and Sham almost forty years after the work of Thomas and Fermi. The original scheme as proposed by Hohenberg and Kohn and Kohn and Sham is a ground-state theory which provides a reliable and inexpensive method for the calculation of ground-state energy of an interacting many fermionic system. Today, the Density Functional theory gives a quantum-mechanical basis for most of the *ab initio* methods used in computational materials science [6].

In this chapter, we have returned to the foundations of this theory, in which we have detailed the different levels of approximation that intervene in its practical implementation, beginning with the problem of several bodies, followed by the approximation of Oppenheimer up to Hartree and Hartree Fock approximations. Then, we have presented the DFT and its implementations for solving the Kohn Sham equations.

2.2. The DFT foundations

2.2.1. Many-body problem

A solid is a collection of large number of particles in interactions: heavy, positively charged particles (nuclei) and lighter, negatively charged particles (electrons). In crystalline solids the nuclei of atoms are arranged at the nodes of the crystal lattice that has a spatial periodicity. The properties of these systems are governed by those electrons which are immersed in a periodic potential created by the ions. This is a many-body problem. An exact theory for a system like this is inherently quantum mechanical, and is based on solving a many-body time independent Schrödinger equation of the form [7]:

$$\hat{H}\Psi_{tot} = E\Psi_{tot} \tag{2.1}$$

where E and Ψ are respectively the total energy and the total wave function of the system. $\hat{H}$ is the Hamiltonian operator of the system that takes into account all forms of energies involved in the system [8]:

$$\hat{H} = \hat{T}_e + \hat{T}_n + \hat{V}_{ee} + \hat{V}_{en} + \hat{V}_{nn} \tag{2.2}$$

with:

$\hat{T}_e = -\frac{\hbar^2}{2m_e}\sum_i \vec{\nabla}_i^2$: is the kinetic energy operator of electrons.

$\hat{T}_n = -\frac{\hbar^2}{2}\sum_K \frac{\vec{\nabla}_K^2}{M_K}$: is the kinetic energy operator of nuclei.

$\hat{V}_{ee} = \frac{ke^2}{2}\sum_{i,j\neq i}\frac{1}{\left|\vec{r}_i - \vec{r}_j\right|}$: is the potential of electron-electron Coulomb interactions.

$\hat{V}_{en} = -ke^2\sum_{i,K}\frac{Z_K}{\left|\vec{R}_K - \vec{r}_i\right|}$: is the potential of electron-nucleus Coulomb interactions.

$\hat{V}_{nn} = \frac{ke^2}{2}\sum_{K,L\neq K}\frac{Z_K Z_L}{\left|\vec{R}_K - \vec{R}_L\right|}$: is the potential of nucleus -nucleus Coulomb interactions.

where the summation over i and j correspond to electrons, and summations over K and L correspond to nuclei; M_K and Z_K represent respectively the mass and charge of the K^{th} nucleus; m_e the mass of an electron and k the Coulomb's constant ($k = 1/4\pi\varepsilon_0$).

The wave function Ψ depends on the coordinates of all the particles, that is to say: $\Psi_{tot} = \Psi_{tot}(\vec{r}_1, \vec{r}_2, ..., \vec{r}_N; \vec{R}_1, \vec{R}_2, ..., \vec{R}_P) = \Psi_{tot}(\vec{r}, \vec{R})$ by convention, where N is the number of electrons, and P is the number of nuclei. If we have P nuclei, we are dealing with a problem of P+ZP (in the case where the atoms are identical). Thus, the number of variables is $3(Z+1)P$, and as there are of the order of 10^{23} atoms/cm^3, the number of variables for a macroscopic crystal is very large (~10^{24}-10^{25} variables) [9]. Today, it is out of question to solve this problem of many-body exactly, and we can not obtain exactly analytical solutions except for single-electronic systems, otherwise known as "hydrogen-like atoms" (H, He^+, Li^{2+}, …). So the solution can only be approximate, and use a number of approximations is essential, as stated by Dirac in 1929 [10]: "*progress depends mostly on the elaboration of sufficiently accurate and approximate techniques*". The first step to overcome this objection is given by the Born-Oppenheimer approximation.

2.2.2. Born Oppenheimer approximation

The Born-Oppenheimer approximation [11, 12] or adiabatic is based on the fact that the nuclei are much heavier than electrons (the mass of a proton is approximately 1800 times larger than the mass of an electron), thus, their inertia is greater. The movement of the nuclei is therefore much slower than electrons. We can hence consider them frozen at fixed positions, (i.e. they are at rest) and assume the electrons to be in instantaneous equilibrium with them. The nuclei can therefore be treated adiabatically. This means that the electronic

and nuclear coordinates in the many-body wave function can be separated. Thus, if the nuclei are to rest, their kinetic energy is neglected ($\hat{T}_n = 0$), and the potential energy of the nuclear interaction $\hat{V}_{nn}$ becomes a certain constant (in this case the coordinates of the nuclei $\vec{R}$ appear as parameters noted $\vec{R}_0$). For a suitable choice of the origin of potential energy can cancel $\hat{V}_{nn}$. The Hamiltonian of the system reduced then to his only electronic components: the kinetic energy of the electron gas, the potential energy due to electron-electron interactions and the potential energy of the electrons in the (now external) potential of the nuclei:

$$\hat{H}_e = -\frac{\hbar^2}{2m}\sum_i \vec{\nabla}_i^2 + \frac{ke^2}{2}\sum_{i,j\neq i}\frac{1}{\left|\vec{r}_i - \vec{r}_j\right|} - ke^2\sum_{i,K}\frac{Z_K}{\left|\vec{R}_K - \vec{r}_i\right|} = \hat{T}_e + \hat{V}_{ee} + \hat{V}_{en} \tag{2.3}$$

The new term $\hat{H}_e$ is known as the electronic Hamiltonian, as it describes the movement of *N*Z electrons in the potential of nuclei. The total wave function with separate variables has the form:

$$\Psi_{tot}(\vec{r}, \vec{R}_0) = \phi_N(\vec{R}_0)\Psi_e(\vec{r}, \vec{R}_0) \tag{2.4}$$

where $\Psi_e(\vec{r}, \vec{R}_0)$ is the electronic wave function, and $\phi_N(\vec{R}_0)$ is the wave function of the nuclei. The Schrödinger equation to be solved is now much simpler than equation (1.1):

$$H_e\Psi_e = E_e\Psi_e \tag{2.5}$$

where $E_e = E_e(\vec{R}_0)$ is the electronic energy. Ψ_e and E_e depend only parametrically on nuclei positions. The total energy of the system will be the sum of E_e and energy and the constant nuclear repulsion term E_{nuc}:

$$E_{tot} = E_e + E_{nuc} \tag{2.6}$$

Despite the considerable implications of this approximation, which allows separating the movement of electrons from those nuclei, and therefore the problem of solving the Schrödinger equation reduces to that of the electron behavior, it is still far too difficult to solve the equation (2.5). This is due to the presence of the term $\hat{V}_{ee}$ of electron-electron interactions, which is the most difficult to determine. Therefore the use of other complementary approximations is essential.

2.2.3. Reduction to single-particle Problem

Under the adiabatic approximation, the complexity of solving the equation (2.5) is due to electron-electron interactions that prevents the separation of this equation in *N* electronic equations, and therefore the wave function of the many-electron system remains dependent on

the coordinates of the electrons. Such an approximation which reduces the problem of N electrons in interaction to that of a single-electron is qualified as the *independent particles approximation*.

In order to find a suitable strategy to approximate the analytically not accessible solutions of many-body problems, a very useful tool is the Rayleigh-Ritz variational calculation [13-16], in which the ground state wave function, which corresponds to the lowest energy of the system E_0, can be approached. This technique will be used to derive both the Hartree and Hartree-Fock equations. A variational procedure will also be used with the density functional method to develop the Kohn-Sham equations.

2.2.3.1. Hartree approximation

One of the earliest and most widely used of all approximations for Ψ_e is due to Hartree (1928) [17], who approximated the many-electron wave function as a product of single-particle functions:

$$\Psi_e(\vec{r}_1,\vec{r}_2,...,\vec{r}_N) = \phi_1(\vec{r}_1)\,\phi_2(\vec{r}_2)\ldots\phi_N(\vec{r}_N) = \prod_{i=1}^{N}\phi_i(\vec{r}_i) \tag{2.7}$$

Each of the functions $\phi_i(\vec{r}_i)$ satisfies a one-electron Schrodinger equation, where every electron is assumed to move in an effective potential composed of the external potential due to the nuclei and a contribution which describes the average electrostatic interaction between the electrons. In this approximation, the idea is to replace in equation (2.5) the potential energy of electron-electron interactions $\hat{V}_{ee}$ by the potential energy of the form $\sum_i \hat{V}_H(\vec{r}_i)$, where $\hat{V}_H(\vec{r}_i)$ is the interaction energy of i^{th} electron, which moves independently in the field, created by all other electrons. If we set $\hat{V}_{ext}(\vec{r}_i)$ the external potential of the i^{th} electron in the nuclei field, the potential energy of electron-nuclei interactions will be written:

$$\hat{V}_{en} = \sum_i \left\{ \sum_K -ke^2 \frac{Z_K}{\left|\vec{R}_K - \vec{r}_i\right|} \right\} = \sum_i \hat{V}_{ext}(\vec{r}_i) \tag{2.8}$$

The approximated Hamiltonian is then the sum of the effective one particle Hamiltonians:

$$\hat{H}_e = \sum_i \left(-\frac{\hbar^2}{2m}\vec{\nabla}_i^2 + \hat{V}_H(\vec{r}_i) + \hat{V}_{ext}(\vec{r}_i) \right) = \sum_i \hat{H}_i \tag{2.9}$$

With this approximation, the total energy of the system $E_e^H = \left\langle \Psi_e \middle| H_e \middle| \Psi_e \right\rangle$ becomes:

$$E_e^H = \underbrace{\sum_i \langle \phi_i(\vec{r}) | \frac{-\hbar^2}{2m} \vec{\nabla}_r^2 | \phi_i(\vec{r}) \rangle}_{T_e} + \underbrace{\frac{ke^2}{2} \sum_{i,j \neq i} \langle \phi_i(\vec{r}) \phi_j(\vec{r}') | \frac{1}{|\vec{r} - \vec{r}'|} | \phi_i(\vec{r}) \phi_j(\vec{r}') \rangle}_{E_H}$$

$$+ \underbrace{\sum_i \langle \phi_i(\vec{r}) | V_{ext}(\vec{r}) | \phi_i(\vec{r}) \rangle}_{E_{ext}} \tag{1.10}$$

with $T_e = \langle \Psi_e | \hat{T}_e | \Psi_e \rangle$ is the kinetic energy of the electrons.

$E_H = \langle \Psi_e | \hat{V}_{ee} | \Psi_e \rangle$ is the Hartree energy of electron-electron interactions.

$E_{ext} = \langle \Psi_e | \hat{V}_{en} | \Psi_e \rangle$ is the electron-nuclei energy interactions.

Using a variational argument, we obtain from this the single-particle Hartree equations:

$$\left\{ -\frac{\hbar^2}{2m} \vec{\nabla}_i^2 + \hat{V}_H(\vec{r}_i) + \hat{V}_{ext}(\vec{r}_i) \right\} \phi_i(\vec{r}_i) = \varepsilon_i \phi_i(\vec{r}_i) \tag{2.11}$$

$\hat{V}_H(\vec{r}_i)$ called: *Hartree potential*. It is given by:

$$\hat{V}_H(\vec{r}_i) = ke^2 \sum_{j \neq i} \langle \phi_j(\vec{r}_j) | \frac{1}{|\vec{r}_i - \vec{r}_j|} | \phi_j(\vec{r}_j) \rangle \tag{2.12}$$

The constants ε_i are the Lagrange multipliers introduced to take into account the normalization of the single-particle states ϕ_i. Each orbital ϕ_i can then be determined by solving the corresponding single-particle Schrödinger equation, if all the other orbitals ϕ_j ($j \neq i$), were known. In principle, this problem of self-consistency, i.e. the fact that the equation for one ϕ_i depends on all the other ϕ_j's, can be solved iteratively [18].

Unfortunately, the Hartree approximation does not satisfy all the important criteria for wave functions. Because electrons are fermions, the wave function must change sign if two electrons change places with each other. This is known as the antisymmetry principle. Exchanging two electrons does not change the sign of the Hartree product, which is a serious drawback.

Despite these deficiencies, the Hartree approximation can be very useful, e.g. when applied to many-electron atoms. It is also useful for gaining a crude understanding of why the quasi free-electron picture of metals has some validity. Finally, it is easier to understand the Hartree–Fock method as well as the density functional method by slowly building up the requisite ideas. The Hartree approximation is a first step [19].

2.2.3.2. Hartree-Fock approximation

In 1930, Fock [20] showed that the Hartree wave function (Eqn 2.7) violates the Pauli exclusion principle, because it is not antisymmetric with respect to the exchange of two electrons. The alternative way is based on the minimization of energy using a Slater determinant [21], in which the *N*-electron wave function is formed by combining single-electron wave functions in a way that satisfies the antisymmetry principle. This is known as the Hartree-Fock approximation. The Hartree-Fock many-electron wave function is then:

$$\Psi_e(q_1,q_2,...,q_N)=\frac{1}{\sqrt{N!}}\cdot\begin{vmatrix}\phi_1(q_1) & \phi_2(q_1) & \cdots & \phi_N(q_1)\\ \phi_1(q_2) & \phi_2(q_2) & \cdots & \phi_N(q_2)\\ \vdots & \vdots & & \vdots\\ \phi_1(q_N) & \phi_2(q_N) & \cdots & \phi_N(q_N)\end{vmatrix} \tag{2.13}$$

where N is the number of electrons; q_i refers to the collection of $3N$ spatial coordinates and N spin projections ($q_i=(\vec{r}_i,\sigma_i)$); $\frac{1}{\sqrt{N!}}$ is the normalization factor of this wave function. Note that the antisymmetry principle implies:

$$\Psi_e(q_1,...,q_j,...,q_i,...)=-\Psi_e(q_1,...,q_i,...,q_j,...) \tag{2.14}$$

Using this determinant, the total energy is:

$$E_e^{HF}=\underbrace{\sum_i\left\langle\phi_i(\vec{r})\left|\frac{-\hbar^2}{2m}\vec{\nabla}_r^2\right|\phi_i(\vec{r})\right\rangle}_{T_e}+\underbrace{\frac{ke^2}{2}\sum_{i,j\neq i}\left\langle\phi_i(\vec{r})\phi_j(\vec{r}')\left|\frac{1}{|\vec{r}-\vec{r}'|}\right|\phi_i(\vec{r})\phi_j(\vec{r}')\right\rangle}_{E_H}$$
$$+\underbrace{\sum_i\left\langle\phi_i(\vec{r})|V_{ext}(\vec{r})|\phi_i(\vec{r})\right\rangle}_{E_{ext}}\underbrace{-\frac{ke^2}{2}\sum_{i,j\neq i}\left\langle\phi_i(\vec{r})\phi_j(\vec{r}')\left|\frac{1}{|\vec{r}-\vec{r}'|}\right|\phi_j(\vec{r})\phi_i(\vec{r}')\right\rangle}_{E_x} \tag{2.15}$$

The electron-electron interaction for a single Slater determinant yields, due to the anti-symmetric nature of the determinant, two contributions: $\left\langle\Psi_e\left|\hat{V}_{ee}\right|\Psi_e\right\rangle=E_H+E_x$. The first of these is simply the classical electrostatic interaction between electrons or Hartree energy given in equation (2.10). The second is called the *Fock* or *exchange* energy, which a une origine purement quantique. It reflects the fact that two electrons of the same spin can not occupy the same position, because of the Pauli-exclusion principle effect. This, therefore has the effect of decreasing the total energy since the electrostatic repulsion decreases.

The expressions of energies T_e, E_{ext}, E_H et E_x are:

$$T_e = \frac{\hbar^2}{2m}\sum_i \int \left|\nabla \phi_i(\vec{r})\right|^2 d^3r \tag{2.16}$$

$$E_{ext} = \sum_i \int \left|\phi_i(\vec{r})\right|^2 V_{ext}(\vec{r}) d^3r \tag{2.17}$$

$$E_H = \frac{ke^2}{2}\sum_{i,j\neq i} \iint \left|\phi_i(\vec{r})\right|^2 \left|\phi_j(\vec{r}')\right|^2 \frac{1}{\left|\vec{r}-\vec{r}'\right|} d^3r d^3r' \tag{2.18}$$

$$E_x = -\frac{ke^2}{4}\sum_{i,j\neq i} \iint \phi_i^*(\vec{r})\phi_j^*(\vec{r}')\frac{1}{\left|\vec{r}-\vec{r}'\right|}\phi_i(\vec{r}')\phi_j(\vec{r}) d^3r d^3r' \tag{2.19}$$

The single-particle Hartree-Fock equations, obtained using a variational calculation, are:

$$\left\{-\frac{\hbar^2}{2m}\nabla_r^2 + \hat{V}_H(\vec{r}) + \hat{V}_x(\vec{r}) + \hat{V}_{ext}(\vec{r})\right\}\phi_i(\vec{r}) = \varepsilon_i\phi_i(\vec{r}) \tag{2.20}$$

This equation has one extra term compared with the Hartree equation, the last one, which is the *non-local exchange potential*, which describes the effects of exchange between electrons. It corrects the defect of the Hartree approximation, but it considerably complicates the calculations. Its expression is given by:

$$V_x(\vec{r})\phi_i(\vec{r}) = -ke^2\sum_j \left\langle \phi_j(\vec{r}')\right| \frac{1}{\left|\vec{r}-\vec{r}'\right|} \left|\phi_i(\vec{r}')\right\rangle \phi_j(\vec{r}) \tag{2.21}$$

Because the exchange potential is non local and it depends on the spin orbitals, the Hartree-Fock equations must be solved self-consistently.

The orbitals $\phi_i(\vec{r})$ and the respective energies ε_i, have any physical significance. Koopmans' theorem [22] states that, neglecting the electronic relaxation effects, ε_i is the negative of the energy required to remove an electron in the state $\phi_i(\vec{r})$ from the solid, i.e. $\varepsilon_i \approx E^{(N)} - E^{(N-1)}$, where $E^{(N)}$ and $E^{(N-1)}$ are respectively, the total energy of the N and (N-1) electron system, with $N \gg 1$. The single-particle wave functions $\phi_i(\vec{r})$ describe also the mathematical quasi-particles, without a direct physical meaning.

This approximation leads to good results. It remains an indispensable benchmark in molecular physics, although extended systems such as solids remain a challenge. But it still provides an upper bound to the energy, because It ignores the effects of electron correlations. Such an approach, where effects beyond the Hartree-Fock approximation (correlation effects) are included by improving the many-particle wave function, is known as "configuration interaction" (CI), which involves minimization over a sum of different N-particle Slater

determinants. It leads, in principle, to the exact wave function, but it is extremely expensive since the number of configurations increases very rapidly with the number of electrons. This means that only systems with relatively few electrons can be calculated with high accuracy [23]. This is a major motivation for the development and use of density functional theory, where it is from the electron density, not the wave functions, the Schrödinger equation is solved. The Hartree-Fock method despite everything remains an indispensable landmark.

2.3. Density Functional Theory

2.3.1. The electron density and the Thomas-Fermi model

The electron density is the basic variable in DFT. It determines the probability of finding any of the *N* electrons within volume element d^3r. For an *N*-particle system, the density operator is defined in terms of *N* occupied single-particle orbitals, as:

$$\hat{\rho} = \sum_{i=1}^{N} |\phi_i\rangle\langle\phi_i| \tag{2.22}$$

It can be expressed as measurable observable only dependent on spatial coordinates:

$$\rho(\vec{r}) = \sum_{i=1}^{N} |\phi_i(\vec{r})|^2 \tag{2.23}$$

which can e.g. be measured by X-ray diffraction. The electron density contains all necessary informations about the system. In detail that means it has to contain information about the electron number *N* as well as the external potential [24]. The total number of electrons can be obtained by integration the electron density over the spatial variables:

$$\int \rho(\vec{r}) d^3r = N \tag{2.24}$$

In addition, $\rho(\vec{r})$ is a non-negative function and vanishes at infinity, i.e. $\rho(\vec{r}) \geq 0$ and $\rho(r \to \infty) = 0$.

Depending on the electronic density, the Hartree-Fock total energy will be:

$$E = \underbrace{\int \tau(\vec{r}) d^3r}_{T} + \underbrace{\int V_{ext}(\vec{r})\rho(\vec{r}) d^3r}_{E_{ext}[\rho(r)]} + \underbrace{\frac{ke^2}{2}\iint \frac{\rho(\vec{r})\rho(\vec{r}')}{|\vec{r}-\vec{r}'|} d^3r d^3r'}_{E_H[\rho(r)]} \underbrace{- \frac{ke^2}{4}\iint \frac{|\rho(\vec{r},\vec{r}')|^2}{|\vec{r}-\vec{r}'|} d^3r d^3r'}_{E_x[\rho(r,r')]} \tag{2.25}$$

where $\rho(\vec{r},\vec{r}') = \sum_{i=1}^{N} \phi_i(\vec{r})\phi_i^*(\vec{r}')$ is the mixed electronic density; $\tau(\vec{r}) = \frac{\hbar^2}{2m_e}\sum_i |\nabla\phi_i(\vec{r})|^2$ is the kinetic energy density.

Shortly after the formulation of the quantum mechanic laws, Thomas and Fermi (1927, 1928) [25, 26] had already tried to express the total energy as a function of the electron density. The weakness of this approach, however, lay in the expression of the kinetic energy, and did not allow him to reach a satisfactory accuracy. The Thomas and Fermi model is to treat the kinetic energy based on a homogeneous gas system of free electrons (the wave functions used are plane wave functions). The expression of this energy will be:

$$T[\rho] = \frac{3}{5}\frac{\hbar^2}{2m}\left(3\pi^2\right)^{2/3}\int \rho^{5/3}(\vec{r})d^3r \tag{2.26}$$

The Thomas and Fermi model is a local approximation of the density which does not take into account the correlation of electrons, since it considers an inhomogeneous gas as being locally homogeneous. Ameliorations have been made to this model by adding other effects such as:

- The exchange effect introduced by Dirac [27] which results in the addition of a supplementary term in the Thomas-Fermi energy (Thomas-Fermi-Dirac model):

$$E_{TFD}[\rho] = E_{TF}[\rho] - C_x\int \rho^{4/3}(\vec{r})d^3r \tag{2.27}$$

- The correlation effect proposed by Wigner:

$$E_c[\rho] = -a\int \frac{\rho^{4/3}(\vec{r})}{b+\rho^{1/3}(\vec{r})}d^3r \tag{2.28}$$

Despite these improvements, this model which is the ancestor of the DFT is insufficient.

2.3.2. Density Functional Theory

Although its history goes back to the early thirties of the 20th century, density functional theory (DFT) has been formally established with the publication of two articles of Hohenberg-Kohn in 1964 [28], and Kohn-Sham in 1965 [29], who founded the bases of this theory. Its goal is to determining, with the only knowledge of the electron density, the ground-state properties of a system composed of a fixed number of interacting electrons in an external potential due to the nuclei. The theory of DFT is an accurate theory of the effects of electron correlations.

2.3.2.1. Hohenberg-Kohn theorems

The traditional formulation of the two theorems of Hohenberg and Kohn [28] is as follows:

First theorem (Uniqueness): « *the external potential* $V_{ext}(\vec{r})$ *is* (*to within a constant*) *a unique functional of* $\rho(\vec{r})$».

An immediate consequence is that the ground-state expectation value of any observable $\hat{O}$ is a unique functional of the exact ground-state electron density: $\langle\Psi|\hat{O}|\Psi\rangle = O[\rho]$.

Demonstration: Suppose the opposite, where the density $\rho(\vec{r})$ corresponds two different external potentials $\hat{V}_{en}$ and $\hat{V}'_{en}$, Which lead two different Hamiltonians $\hat{H}$ and $\hat{H}'$, where, $\hat{H} = \hat{T} + \hat{V}_{ee} + \hat{V}_{ext}$ and $\hat{H}' = \hat{T} + \hat{V}_{ee} + \hat{V}'_{ext}$. Let Ψ and E be the fundamental state and its energy relative to $\hat{H}$; Ψ′ and E' those of $\hat{H}'$. Let us calculate the energy of the system with the Hamiltonian H in the state P which is not its ground state:

$$\begin{aligned}\langle\Psi'|H|\Psi'\rangle &= \langle\Psi'|H - H' + H'|\Psi'\rangle \\ &= \langle\Psi'|H - H'|\Psi'\rangle + \langle\Psi'|H'|\Psi'\rangle \\ &= \langle\Psi'|V_{en} - V'_{en}|\Psi'\rangle + E' \\ &= \int \rho(\vec{r})[V_{ext}(\vec{r}) - V'_{ext}(\vec{r})]d^3r + E'\end{aligned}$$

Since Ψ′ is not the ground state of $\hat{H}$, then: $E < \langle\Psi'|H|\Psi'\rangle$, which means:

$$E < \int \rho(\vec{r})[V_{ext}(\vec{r}) - V'_{ext}(\vec{r})]d^3r + E' \quad \text{.....(a)}$$

We do the same thing with the Hamiltonian $\hat{H}'$ in the state Ψ, we obtain:

$$E' < \int \rho(\vec{r})[V'_{ext}(\vec{r}) - V_{ext}(\vec{r})]d^3r + E \quad \text{.....(b)}$$

Addition of the two equations (a) and (b) leads to following contradiction: $E + E' < E + E'$! This proves that there is one-to-one correspondence between an external potential $V_{ext}(\vec{r})$ and the density $\rho(\vec{r})$.

According to this theorem, the total energy of interacting electrons in an external potential is given exactly as a functional of the ground state electronic density ρ:

$$E = E[\rho] \tag{1.29}$$

Separating the interaction with the external potential from the rest (kinetic energy and electron -electron interaction) we can write the total energy as:

$$E[\rho] = F_{HK}[\rho] + \int V_{ext}(\vec{r})\rho(\vec{r})d^3r \tag{2.30}$$

which defines the Hohenberg-Kohn functional as:

$$F_{HK}[\rho] = \langle\Psi_e|\hat{T}_e + \hat{V}_{ee}|\Psi_e\rangle \tag{2.31}$$

$F_{HK}[\rho]$ is *universal* functional of the charge density ρ for any many-electron system, because it does not depend on external potential $\hat{V}_{ext}$. The exchange and correlation effects are contained in this functional.

The problem is now only how to find this density. The second theorem is helpful in this matter:

Theorem 2 (Variational principle): «*For a given external potential, the true density* $\rho_0(\vec{r})$ *minimizes the total energy functional*». Therefore, the ground state density can be obtained from the variational principle. Thus, for any trial electronic density $\rho(\vec{r})$:

$$E[\rho] \geq E[\rho_0] = \min_{\rho} E(\rho) \tag{2.32}$$

Demonstration:

Let $\rho_0(\vec{r})$ the exact density of the system in its ground state Ψ, we have then:

$\rho_0(\vec{r}) \rightarrow V_{ext}(\vec{r}) \rightarrow \hat{H} \rightarrow \Psi$.

Let us $\rho'(\vec{r})$ another different density of $\rho_0(\vec{r})$, with $\int \rho'(\vec{r}) d^3 r = N$, we also have:

$\rho'(\vec{r}) \rightarrow \hat{V}'_{ext}(\vec{r}) \rightarrow \hat{H}' \rightarrow \Psi'$.

Let us now calculate the energy associated with $\hat{H}$ in the state Ψ′ which is not its ground state: $\langle \Psi' | H | \Psi' \rangle = E(\rho') > \langle \Psi | H | \Psi \rangle \Rightarrow E(\rho') > E(\rho_0)$, with $E(\rho_0) = E_0 = \langle \Psi | \hat{H} | \Psi \rangle$ is the energy of the ground state.

This second theorem lends us an approach in order to determine the desired ground state density. The theorem proves that for any external potential we know that a functional $F_{HK}[\rho]$ exists whose global minimum is the exact ground state energy. Furthermore, the actual density that minimizes $F_{HK}[\rho]$ will be the ground state density $\rho_0(\vec{r})$.

However, the explicit density dependence of $F_{HK}[\rho]$ remains unknown. Approximations have been suggested, the oldest one being the well-known Thomas-Fermi approximation. However, its performance is really bad due to the poor approximation of the kinetic energy.

Instead, the Hohenberg-Kohn theorem provides the basic theoretical foundation for the construction of an effective single-particle scheme which allows for the calculation of the ground-state density and energy of systems of interacting electrons. The resulting equations, the so-called Kohn–Sham equations, are at the heart of modern density-functional theory.

2.3.2.23. The Kohn-Sham equations

The task of finding good approximations to the energy functional is greatly simplified by using a different separation introduced by Kohn and Sham (1965) [29], which turn DFT into a practical tool. The central idea of the Kohn-Sham scheme is to calculate the exact kinetic energy of a fictive system of non-interacting electrons with the same density as the real interacting one (see Figure 2.1), i.e. $\rho_s(\vec{r}) = \rho(\vec{r})$.

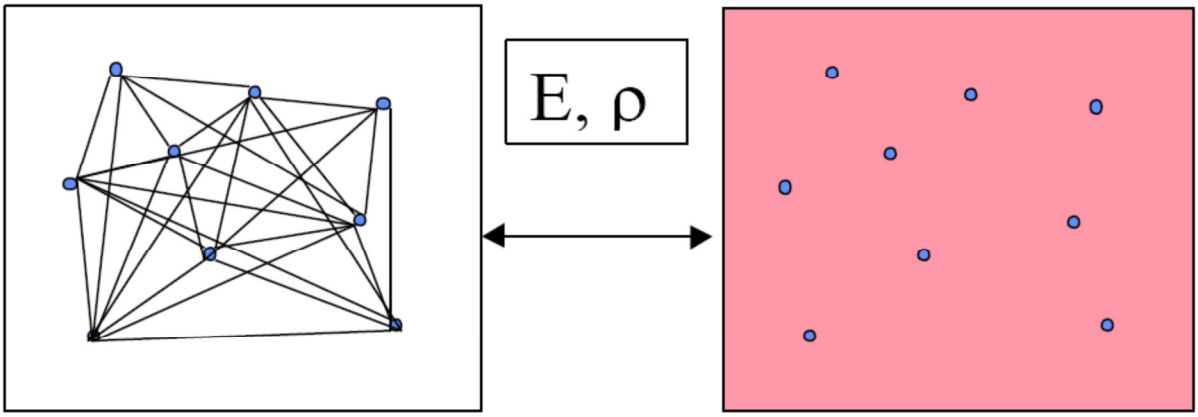

Fig. 2.1: representation of relationship between the real many body system (left hand side) and the non interacting system of Kohn-Sham density functional theory (right hand side).

Formally, the total energy functionals $E[\rho]$ and $E_{HF}[\rho]$ corresponding to the exact and Hartree-Fock Hamiltonians respectively, are:

$$E[\rho] = \underbrace{T[\rho] + E_H[\rho] + E_x[\rho]}_{F_{HK}[\rho]} + E_{ext}[\rho] \tag{2.33}$$

$$E_{HF}[\rho] = T_s[\rho] + E_H[\rho] + E_x[\rho] + E_{ext}[\rho] \tag{2.34}$$

Here T is the exact kinetic and T_s is the kinetic energy of a non-interacting electron gas, E_H stands for the Hartree contribution and E_x for the exchange contribution. Traditionally, one defines the correlation energy E_c as the difference between the Hartree-Fock and the exact energy, i.e:

$$E_c = E - E_{HF} \tag{2.35}$$

By subtracting (2.34) from (2.33), the functional for the correlation contribution appears to be:

$$E_c[\rho] = T[\rho] - T_s[\rho] \tag{2.36}$$

With this knowledge, we can rewrite the Hohenberg-Kohn functional in the following way:

$$F_{HK}[\rho] = T_s[\rho] + E_H[\rho] + \underbrace{E_x[\rho] + E_c[\rho]}_{E_{xc}[\rho]}$$

$$= T_s[\rho] + E_H[\rho] + E_{xc}[\rho] \tag{2.37}$$

Here $E_{xc}[\rho]$ is the exchange-correlation energy functional. It is simply the sum of the error made in using a non-interacting kinetic energy and the error made in treating the electron-electron interaction classically. Thus the total energy of the system will be written:

$$E[\rho] = T_s[\rho] + \frac{ke^2}{2}\iint \frac{\rho(\vec{r})\rho(\vec{r}')}{|\vec{r}-\vec{r}'|} d^3r d^3r' + \int V_{ext}(\vec{r})\rho(\vec{r}) d^3r + E_{xc}[\rho] \tag{2.38}$$

We can interpret the above expression as the energy functional of a *non-interacting* classical electron gas, subject to two external potentials: one due to the nuclei, and one due to exchange and correlation effects. The only term that remains unknown is the $E_{xc}[\rho]$, which is not easy to calculate, but as we verify the advantage of being much smaller in front of the other terms.

Using the variational principle, we finally obtain the single-particle Kohn-Sham equation:

$$\underbrace{\left\{-\frac{\hbar^2}{2m}\nabla_i^2 + V_{eff}^{KS}(\vec{r})\right\}}_{\hat{H}^{KS}} \phi_i(\vec{r}) = \varepsilon_i \phi_i(\vec{r}) \tag{2.39}$$

Here

$$\hat{V}_{eff}^{KS}(\vec{r}) = \hat{V}_H(\vec{r}) + \hat{V}_{ext}(\vec{r}) + \hat{V}_{xc}(\vec{r}) \tag{2.40}$$

where

$\hat{V}_{eff}^{KS}(\vec{r})$ is the Kohn-Sham effective potential.

$\hat{V}_H(\vec{r}) = \dfrac{\delta E_H[\rho(\vec{r})]}{\delta\rho(\vec{r})} = ke^2 \int \dfrac{\rho(\vec{r}')}{|\vec{r}-\vec{r}'|} d^3r'$ is the Hartree potential.

$\hat{V}_{ext}(\vec{r}) = \dfrac{\delta E_{ext}[\rho(\vec{r})]}{\delta\rho(\vec{r})} = -ke^2 \sum_K \dfrac{Z_K}{|\vec{r}-\vec{R}_K|}$ is the external potential.

$\hat{V}_{xc}(\vec{r}) = \dfrac{\delta E_{xc}[\rho(\vec{r})]}{\delta\rho(\vec{r})}$ is the exchange-correlation potential.

ϕ_i and ε_i are called, respectively, orbitals and energies of Kohn-Sham. We note that, except the highest occupied orbital, and ε_{max}, which equals the negative of the exact ionization energy, the Kohn-Sham orbitals ϕ_i and the Kohn-Sham energies ε_i have no physical

significance [3], and it is not defined by Koopmans' theorem [19]. Since $\hat{V}_{eff}^{KS}$ depends on the density, equations (2.23) and (2.39) have to be solved self-consistently. This is known as the Kohn-Sham scheme of density functional theory.

2.3.2.3. Exchange-correlation energy approximations

The beautiful results of Kohn, Hohenberg, and Sham showed us that the ground state we seek can be found by minimizing the energy of an energy functional, and that this can be achieved by finding a self-consistent solution to a set of single-particle equations. But as stated above, the true form of the exchange-correlation functional $E_{xc}[\rho]$ is simply not known, and it is very difficult to be identified. Only the functional system of a uniform electron gas was well known (electron density is constant). It is therefore, necessary to approximate this functional of exchange-correlation, in which, E_{xc} should have all of the following features: (1) *a non-empirical derivation*, since the principles of quantum mechanics are well-known and sufficient; (2) *universality*, since in principle one functional should work for diverse systems (atoms, molecules, solids) with different bonding characters (covalent, ionic, metallic, hydrogen, and van der Waals); (3) *simplicity*, since this is our only hope for intuitive understanding and our best hope for practical calculation; and (4) *accuracy* enough to be useful in calculations for real systems [30].

1.3.2.3.1. Local density approximation (LDA)

The local density approximation (LDA) is the base of all exchange-correlation functional approximations, and it is the simplest of them. It is based on the uniform (homogeneous) electron gas of Tomas-Fermi model [25, 26]. This approximation was originally introduced by Kohn and Sham [29] and holds for a slowly varying density. It states that the exchange-correlation energy due to a particular density $\rho(\vec{r})$ could be found by dividing the material in infinitesimally small volumes with a constant density. Each such volume contributes to the total exchange correlation energy by an amount equal to the exchange correlation energy of an identical volume filled with a homogeneous electron gas, that has the same overall density as the original material has in this volume [3]. The exchange-correlation functional has the following form:

$$E_{xc}^{LDA}[\rho] = \int \varepsilon_{xc}[\rho]\rho(\vec{r})d^3r \tag{2.41}$$

where the function $\varepsilon_{xc}[\rho]$ is the exchange-correlation energy per particle of a homogeneous electron gas with density $\rho(\vec{r})$. Traditionally, the exchange-correlation energy can be decomposed into exchange and correlation terms linearly:

$$\varepsilon_{xc}[\rho]=\varepsilon_x[\rho]+\varepsilon_c[\rho] \tag{2.42}$$

The exchange contribution was originally derived by Dirac [27]:

$$\varepsilon_x[\rho]=-\frac{3}{4}\left(\frac{3}{\pi}\right)^{1/3}\rho^{1/3}=-\frac{3}{4}\left(\frac{9}{4\pi^2}\right)^{1/3}\frac{1}{r_s} \tag{2.43}$$

where $r_s=\left(\frac{4\pi\rho}{3}\right)^{-1/3}$ is the Wigner-Seitz radius [31] (radius sphere that contains one electron).

The correlation part can be fitted on the total energy of the homogeneous electron gas. The current reference calculation of the energy of a homogeneous electron gas is the Quantum Monte-Carlo result of Ceperley and Alder [32]. Parametrisations of the LDA correlation energy using Padé approximates based on these results are those of Vosko, Wilk and Nussair [33], Perdew-Wang [34] and Perdew-Zunger [35].

By its very construction, the LDA is expected to be a good approximation for systems with the density that varies slowly. Although this condition is hardly ever met for real electronic systems, LDA has proved to be remarkably accurate for a wide variety of systems. It is remarkably reliable for the structure, elastic moduli, relative phase stability of many materials, and it is often considered satisfactory in condensed-matter systems.

However, this approximation reached to its limits for systems where the electron density varies greatly, and where long-range bonds (hydrogen bonding and Vander Waals interactions) are presented. The main failures of the LDA approximation are: (1) it is much less accurate in atomic and molecular physics, for which highly accurate experimental data are available; (2) it badly overestimates (~20% and more) cohesive energies and bond strengths in molecules and solids, and as a consequence bond lengths are often underestimated; (3) the underestimation of the band gap of crystalline systems.

The inclusion of the spin dependence by using the local spin-density approximation (LSDA), however, was found to improve the description of the unpaired electron in alkali metals [36], thereby improving the cohesive energy of the solid [37]. This approximation was proposed in the original work of Kohn and Sham [29], and has proved to be remarkably

accurate, useful, and hard to improve upon. It is used most widely in in solid state physic calculations. It has the following form:

$$E_{xc}^{LSDA}[\rho] = \int \varepsilon_{xc}[\rho\uparrow, \rho\downarrow]\rho(\vec{r})d^3r \tag{2.44}$$

where $\varepsilon_{xc}[\rho\uparrow, \rho\downarrow]$ is the exchange and correlation energy per particle of' a homogeneous, spin-polarized electron gas with spin-up and spin-down densities $\rho\uparrow$ and $\rho\downarrow$, respectively. parametrizations of $\varepsilon_{xc}[\rho\uparrow, \rho\downarrow]$ have been given by von Barth and Hedin (1972) [38], Gunnarsson and Lundqvist (1976) [39], Vosko et al. (1980) [33], and Perdew and Zunger (1981) [35], among others.

2.3.2.3.2. Generalized Gradient Approximations (GGA)

The Generalized Gradient Approximations (GGAs) are an extension and an amelioration of LDA to inhomogeneous systems: the local exchange-correlation energy depends not only on the local charge density but also on the local charge density gradient. They have been developed in order to take into account the fact that almost all real systems are inhomogeneous, and therefore, the electron density has a spatial variation. Within GGA, the exchange-correlation energy is written as:

$$E_{xc}^{GGA}[\rho, \nabla\rho] = \int \varepsilon_{xc}[\rho(\vec{r}), \nabla\rho(\vec{r})]\rho(\vec{r})d^3r \tag{2.45}$$

In practice, the exchange and correlation parts are treated independently. Their formulation is purely mathematical. Because there are many ways in which information from the gradient of the electron density can be included in a GGA functional, many different forms of GGA functionals have been suggested [40-45]. Two of the most popular functionals which are widely used in calculations involving solids are the Perdew-Wang functional (PW91) [34] and the Perdew-Burke-Ernzerhof functional (PBE) [45]. The latter has been widely applied in solid-state physics [46]. It almost always overestimates the lattice constants of solids, with the typical errors amount to 1%-2%. A series of alternative GGA functionals have recently been proposed to overcome this problem [47-51]. One such functional is the PBEsol [49] which can be seen as revised version of PBE specifically adapted for solids. It yields indeed lattice constants that are in excellent agreement with experiments [52]. For these reason, we have used this functional in this thesis.

Although hybrid functionals [53-56] which include Hartree-Fock exchange and meta-GGAs [56-60] which include spin kinetic energy density have also been developed and have been popularly and successfully applied in molecular quantum chemistry during the past

decade, they are not widely used in solid-state physics, and very few solid-state codes have the capability of performing calculations with meta-GGAs or hybrid functionals [50].

It is tempting to think that because the GGA includes more physical information than the LDA it must be more accurate, in particular for molecular systems and often work very well for atoms and solids [61]. The following advantages are noteworthy: (1) GGAs significantly improve the ground state properties of light atoms and molecules, clusters and solids composed of them; (2) many properties of 3*d* transition metals are greatly improved; for example, unlike the LSDA (Local Spin-Density Approximation) the correct *bcc* ground state of Fe is obtained [62]; (3) GGAs give better geometry for the weak bonds, and larger band gaps than the LDA, but at a modest additional computational cost; (4) they yield in particular, a good description of the Hydrogen bonds, thus opening the way to calculations for systems, such as water, in which Hydrogen bonds play a crucial role [63].

All this, makes GGA method of choice for many first principles studies of materials. Unfortunately, this is not always correct. The committed error in GGA is often under-estimating the cohesive energies. In some systems, GGA leads to higher errors than those resulting with LDA.

2.4. Solving the Kohn–Sham equations

2.4.1. Basis Sets

DFT based electronic structure methods are classified according to the representations that are used for the density, potential and, most importantly, the Kohn-Sham orbitals. The choice of representation is made to minimize the computational and human (*e.g.* programming) costs of calculations, while maintaining sufficient accuracy. In spite of their differences, all codes try to solve the Kohn-Sham equations:

$$\hat{H}^{KS}\phi_i = \varepsilon_i\phi_i \tag{2.46}$$

There are many possible ways to solve the Kohn-Sham equations. Frequently, a variational method is chosen by which a wave-function $\phi_m(\vec{r})$ is sought as a linear combination of adequate basis functions $\{\varphi_p(\vec{r})\}$:

$$\phi_m(\vec{r}) = \sum_{p=1}^{P} c_p^m \varphi_p(\vec{r}) \tag{2.47}$$

where c_p^m are expansion coefficients. In principle, $\phi_m(\vec{r})$ has an infinite dimension, i.e. P is infinite, but in practice one works with a limited set of basis functions that can generate a function that is 'close' to $\phi_m(\vec{r})$. Since, given a choice of basis, the coefficients c_p^m are the only variables in the problem, and since the total energy in DFT is variational, solution of the self-consistent KS equations amounts to determining the c_p^m for the occupied orbitals that minimize the total energy. By this expansion, solving the Schrödinger equation in the basis set $\{\varphi_p(\vec{r})\}$ then amounts to diagonalizing the Hamiltonian matrix, i.e (**H**-ε**S**)c = 0:

$$\begin{bmatrix} \cdots & \cdots & \cdots \\ \vdots & \langle\varphi_i|\hat{H}^{KS}|\varphi_j\rangle - \varepsilon_m\langle\varphi_i|\varphi_j\rangle & \vdots \\ \cdots & \cdots & \cdots \end{bmatrix}\begin{bmatrix} c_1^m \\ \vdots \\ c_P^m \end{bmatrix} = \begin{bmatrix} 0 \\ \vdots \\ 0 \end{bmatrix} \tag{2.48}$$

where $\langle\varphi_i|\hat{H}^{KS}|\varphi_j\rangle = \hat{H}_{ij}$ is the matrix elements of the Kohn-Sham Hamiltonian in the basis states, and $\langle\varphi_i|\varphi_j\rangle = S_{ij}$ is the overlap matrix elements. This equation will be solved at each k-point in the irreducible wedge of the Brillouin zone. We can see that if the chosen basis set $\{\varphi_p(\vec{r})\}$ is orthogonal (i.e. $S_{ij} = \delta_{ij}$, as for example in case of simple plane-waves), the overlap matrix **S** reduces to the identity matrix **I**, and Eqn. (2.48) reduces to the regular eigenvalue. The larger P, leads to the better approximation of the eigenfunction, but the more time consuming the diagonalization of the matrix in Eqn. (2.48) is required.

The quality of a basis set can, be measured by the extent to which the total energy evaluated using the orbitals of Eqn. (2.47) differs from the true Kohn-Sham energy. To makes both theory development and programming work easier, a good basis set should be [3,62]:

- *Efficient*: if the functions of the basis set are very similar to ϕ_m, one needs only a few of them to accurately describe the wave function, and hence P and the matrix size are small. Such a basis set is called *efficient*.
- *Unbiased* : the basis must not favors certain regions of space over others (*e.g.* by not being more flexible near atomic nuclei than elsewhere).
- *Simple*: it would be nice if the basis functions are mathematically simple.
- *Completeness*: the basis can be improved arbitrarily by adding additional functions of the same type.

The most common bases are divided into two categories:

- *Plane wave* sets, which are particularly effective for describing periodic systems such as crystals. They are certainly unbiased and simple, but they are known to be inefficient in the above sense for a large part of solids. Accuracy can be reached by increasing the number of plane-waves in the basis. Furthermore, due to the simplicity of this basis the implementation of the plane-wave codes is relatively easy, and the matrix elements of many operators can be rapidly estimated.
- *Localized orbitals* (atomic-like and muffin-tin wave-functions) in real space, centered on atoms. This choice is most prevalent in quantum chemistry, where many bases have been developed to ensure rapid convergence at lower costs: the most common are for example linear combinations of atomic orbitals (LCAO), Gaussian type orbitals (GTO) and Slater-type Orbitals (STO). These atomic-like functions are tailored for fast convergence, so that only a few (some tens at most) functions per atom are needed. This approach is well suited to the study of finite systems such as molecules. This type of localized orbitals is however particularly relatively difficult to control the convergence of the results vis-a-vis the base, since there is no systematic process to improve the accuracy of the calculation.

2.4.2. Self-Consistency in DFT calculations

The theorem of Hohenberg-Kohn shows that the total energy is variational and this means that the true ground state density is that which minimizes the energy. Since Hartree potential $\hat{V}_H$ and the exchange-correlation potential $\hat{V}_{xc}$ in the Kohn-Sham Hamiltonian, has a functional dependence on the electronic density ρ, the standard approach to solve the Kohn-Sham equations is the self-consistent procedure, in which the density refined iteratively by solving Eqns. (2.23), (2.39) and (2.40) alternately [64,65], as illustrated in Figure 2.2. The procedure begins with an initial guess of the density ρ^{in} which can be constructed by a superposition of atomic densities:

$$\rho^{in} = \rho^{système} = \sum_{atome} \rho^{atome} \tag{2.49}$$

This initial guess electron density will be used to calculate $\hat{V}_H$ and $\hat{V}_{xc}$. There are several different techniques to evaluate the Hartree potential $\hat{V}_H$ (Coulomb potential), either by direct integration (as it is done when solving the atomic Kohn-Sham equations), or by solving the equivalent differential Poisson's equation (which is most commonly used in solids case):

$\nabla^2 \hat{V}_H(\vec{r}) = -4\pi\rho(\vec{r})$. Calculating the exchange-correlation potential $\hat{V}_{xc}$ which accounts for all other effects is typically carried out on the choice of an appropriate approximation[2].

Once we have solved the non-interacting electron problem in the external potential V_{ext} to obtain one electron orbitals $\phi_m^{out}(\vec{r})$ (expanded on the basis set $\{\varphi_p(\vec{r})\}$) we construct the ground state density of the non-interacting electron system simply as $\rho^{out}(\vec{r}) = \sum_{i=1}^{N} \left|\phi_i^{out}(\vec{r})\right|^2$. Self consistency is reached if $\rho^{out}(\vec{r}) = \rho^{in}(\vec{r})$. If this is not the case, the procedure is iterated with a new guess density constructed from $\rho^{out}(\vec{r})$. In the most simple scheme for example, the new guess is $\rho^{out}(\vec{r})$ itself [66].

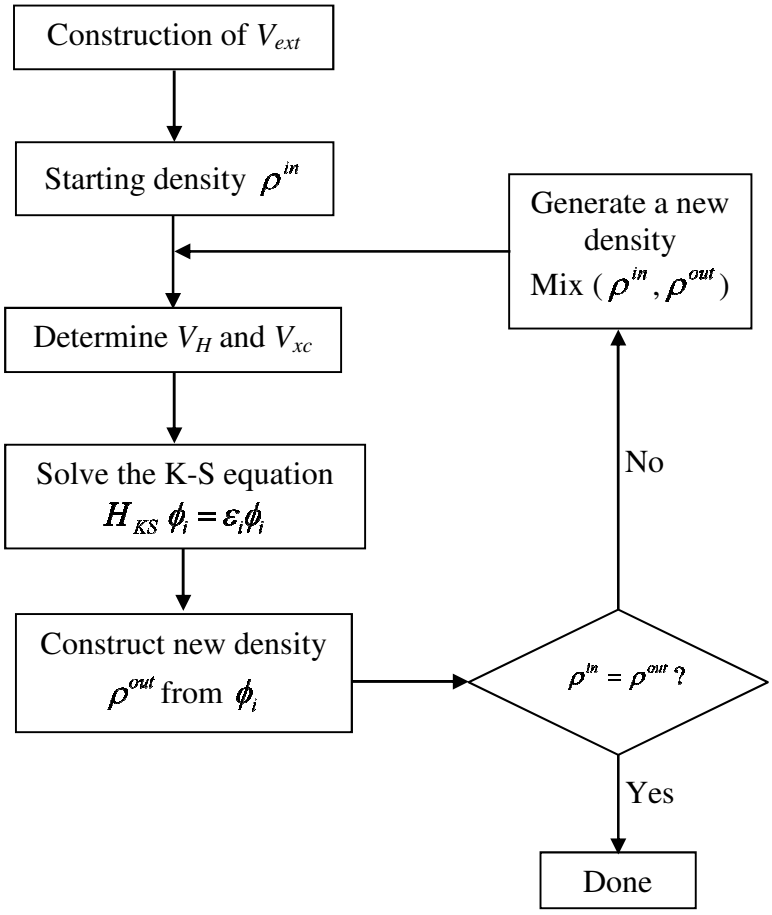

Fig.2.2: Schematic representation of the self-consistent cycle within the framework of the DFT. Electronic density ρ is the fundamental quantity governing the iterative procedure.

[2] The external potential $\hat{V}_{ext}$ does not depend on the density ρ, and as such, can be calculated a single time and reused throughout the self-consistent procedure.

In practice the self-consistency cycle is stopped when some convergence criterion is reached. The two most common criteria are based on the difference of total energies or densities from iteration i and i – 1, i.e., the cycle is stopped when $E_i - E_{i-1} < \eta_E$ or $\rho_i - \rho_{i-1} < \eta_\rho$, where E_i and ρ_i are the total energy and density at iteration i, and η_E and η_ρ are user defined tolerances. If, on the contrary, the criteria have not been fulfilled, one restarts the self-consistency cycle with a new density, which is usually selected by mixing output density with the input density to yield a refined input for the next iteration, and to accelerate the convergence. The simplest mixing scheme is straight mixing [67]:

$$\rho_{i+1}^{in} = (1-\alpha)\rho_i^{in} + \alpha\rho_i^{out} \tag{2.50}$$

where α is the mixing parameter and i the number of iteration. The accuracy of calculation is particularly important that the convergence criterion is low. When convergence is reached, the energy of the ground state of the considered system is known.

2.4.3. DFT implementations

The quest to solve the Kohn-Sham equation (2.39) efficiently has lead to a wide spectrum of very successful and efficient electronic structure methods. Guiding principles to develop electronic structure methods are by obtained by having a closer look at the mathematical nature of the Schrödinger-like Kohn-Sham equation with the kinetic energy operator and the $1/r$ singularity at the nucleus with the simultaneous necessity to calculate the exchange-correlation potential $\hat{V}_{xc}$ and the Hartree potential $\hat{V}_H$. The art of theoretical matter physics is to find a basis set that is a simultaneously efficient and unbiased.

In atomic calculations, for a given electronic configuration, the Kohn-Sham equation has spherical symmetry and is separable into a radial equation and an angular part (whose solutions are the spherical harmonics). Treating isolated clusters or molecules, methods based on localized orbitals are frequently selected going hand in hand with the chemical intuition of system in question. Considering methods applicable to periodic solids, frequently algorithms are chosen where the Bloch boundary condition can be included in the basis set. As it takes advantage of the periodicity of the crystal, a plane-wave expansion of the Kohn-Sham wave-functions is very useful.

A brief summary of the many possibilities to solve the Schrödinger's equation is given in Figure 3.3. In this thesis calculations have been concerned with two particular approaches namely, plane-wave Pseudo-Potential (PP-PW) and the Linearized Augmented Plane-Wave (LAPW).

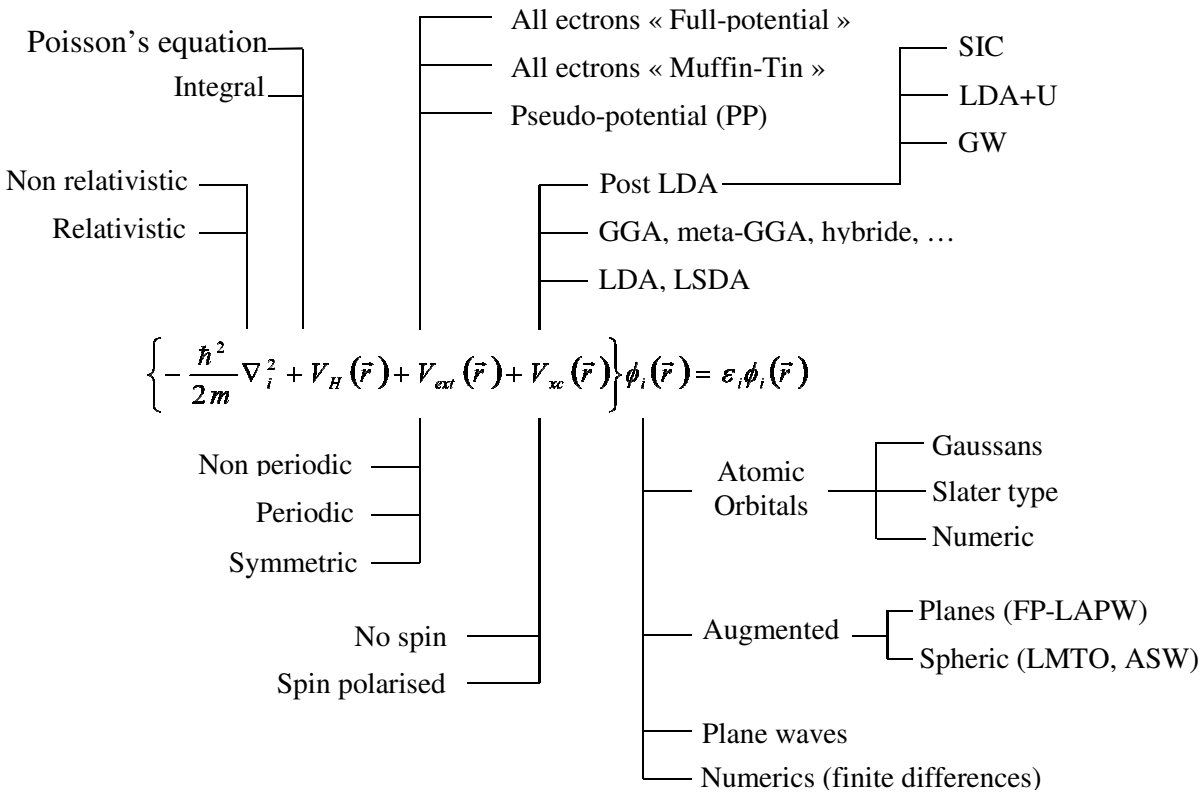

Fig. 2.3: Schematic representation of various DFT-based methods of calculation.

References

[1] R. O. Jones, O. Gunnarsson, *The density functional formalism, its applications and prospects*, Rev. Mod. Phys., Vol. 61, No. 3, 1989.

[2] P. J. H. Denteneer, *The pseudopotential-density-functional method applied to semi-conducting crystals*, Tech. Univ. Eindhoven, Holland, 1987.

[3] S. Cottenier, *Density Functional Theory and the Family of* (*L*) *APW-methods*: *a step-by-step introduction*, Ghent University, Belgium, 2013.

[4] S. Kurth, M. A. L. Marques, and E K U Gross, *Density-Functional Theory*, Freie Univ. Berlin, Germany, 2005.

[5] P. Samal, *Studies in Excited-State Density-Functional Theory*, Indian Inst. of Tech. Kanpur, India, 2006.

[6] L. Vitos, *Computational Quantum Mechanics for Materials Engineers*: *The EMTO Method and Applications*, Springer, London, 2007.

[7] E. Schrödinger, *Quantisierung als Eigenwertproblem* (Dritte Mitteilung), Ann. Phys. (Leipzig) 385, 437-490, (1926); E. Schrödinger, *Quantisierung als Eigenwertproblem* (Vierte Mitteilung), Ann. Phys. (Leipzig) 386, 109-139 (1926).

[8] H. Mathieu, *Physique des semiconducteurs et des composants électroniques*, 5^{e} édition, Dunod, Paris, 2004.

[9] C. Ngo et H. Ngo, *Les semiconducteurs*, Dunod, Paris, 2003.

[10] P. A. M. Dirac, *Quantum mechanics of many-electron systems*, Proc. Roy. Soc (London) 123, 714-733 (1929).

[11] M. Born, R. Oppenheimer, *Quantum theory of the molecules*. Ann. d. Physik 84, 457-484 (1927)

[12] M. Born, K. Huang, *Dynamic Theory of Crystal Lattices*, Oxford University Press, Oxford, 1954.

[13] F. L. Pilar, *Elementary Quantum Chemistry*, McGraw-Hill: New York, 1990.

[14] A. Szabo, N. S. Ostlund, *Modern Quantum Chemistry*, McGraw-Hill: New York, 1989.

[15] I. N. Levine, *Quantum Chemistry*, Prentice-Hall: Englewood Cliffs, NJ, 1991.

[16] C. Cohen-Tannoudji, B. Diu, and F. Laloë, *Mécanique Quantique I*, Collection Enseignement des Sciences, Hermann, Paris, 1977.

[17] D. R. Hartree, *The wave mechanics of an atom with a non-Coulomb central field. Part I. Theory and methods*, Proc. Cambridge. Philos. Soc. 24, 89-110 (1928).

[18] E. Kaxiras, *Atomic and Electronic Structure of Solids*, Cambridge University Press, New York, 2003.

[19] J. D. Patterson, B.C. Bailey, *Solid-State Physics*, Springer, Berlin, 2007.

[20] V.A. Fock, *Näherungsmethode zur Lösung des quantenmechanischen Mehrkörperproblems*, Z. Phys. 61, 126-148 (1930).

[21] J.C. Slater, *A Simplification of the Hartree-Fock Method*, Phys. Rev. 81, 385-390 (1951).

[22] T. Koopmans, *Uber die Zuordnung von Wellenfunktionen und Eigenwerten zu den einzelnen Elektronen eines Atoms*, Physica 1, 104-113 (1934).

[23] R. O. Jones, O. Gunnarsson, *The density functional formalism, its applications and prospects*, Rev. Mod. Phys., Vol. 61, No. 3, July 1989.

[24] W. Koch and M.C. Holthausen. *A Chemists's Guide to Density Functional Theory*. Wiley-VCH, 2001.

[25] L. H. Thomas, *The Calculation of Atomic Fields*, Proc. Camp. Philos. Soc. 23, 542-548 (1927).

[26] E. Fermi, *Eine statistische Methode zur Bestimmung einiger Eigenschaften des Atoms und ihre Anwendung auf die Theorie des periodischen Systems der Elemente*, Z. Phys. 48, 73-79 (1928).

[27] P. A. M. Dirac, *Note on Exchange Phenomena in the Thomas Atom*, Proc. Camb. Philos. Soc., 26, 376-385 (1930).

[28] P. Hohenberg and W. Kohn, *Inhomogeneous Electron Gas*, Phys. Rev. 136, B864-B871 (1964).

[29] W. Kohn and L. J. Sham, *Self-Consistent Equations Including Exchange and Correlation Effects*, Phys. Rev. 140, A1133-A1138 (1965).

[30] C. Fiolhais F. Nogueira M. Marques, *A Primer in Density Functional Theory*, Springer-Verlag, Berlin, Germany, 2003.

[31] E. Wigner, *On the Interaction of Electrons in Metals*, Phys. Rev. 46, 1002-2011 (1934).

[32] S. H. Vosko, L. Wilk, and M. Nusair, *Accurate spin-dependent electron liquid correlation energies for local spin density calculations: a critical analysis*. *Can. J. Phys.* 58, 1200-1211 (1980).

[33] D. M. Ceperley and B. J. Alder, *Ground State of the Electron Gas by a Stochastic Method*. Phys. Rev. Lett. 45, 566-569 (1980).

[34] J. P. Perdew and Y. Wang, *Accurate and simple analytic representation of the electron-gas correlation energy*, Phys. Rev. B 45, 13244-13249 (1992).

[35] J. P. Perdew and A. Zunger, *Self-interaction correction to densityfunctional approximations for many-electron systems*, *Phys. Rev.* B 23, 5048-5079 (1981).

[36] B. Y. Tong, *Kohn-Sham Self-Consistent Calculation of the Structure of Metallic Sodium*, Phys. Rev. B 6, 1189-1194 (1972).

[37] O. Gunnarsson, B. I. Lundqvist, and J. W. Wilkins, *Contribution to the cohesive energy of simple metals: Spin-dependent effect*, Phys. Rev. B 10, 1319-1327 (1974).

[38] U. von Barth and L. Hedin, *A Local Exchange-Correlation Potential for the Spin Polarized Case: I*, J. Phys. C 5, 1629-1642 (1972).

[39] O. Gunnarsson and B. I. Lundqvist, *Exchange and Correlation in Atoms, Molecules and Solids by the Spin-Density Formalism*, Phys. Rev. B 13, 4274-4298 (1976).

[40] J. P. Perdew and Y. Wang, *Accurate and simple density functional for the electronic exchange energy: Generalized gradient approximation*, Phys. Rev. B 33, 8800-8802 (1986.

[41] J. P. Perdew, in *Electronic Structure of Solids* 91, Ed. P. Ziesche and H. Eschrig (Akademie Verlay, Berlin, 1991) p.11.

[42] D. C. Langreth, M. J. Mehl, *Beyond the local-density approximation in calculations of ground-state electronic properties*, Phys. Rev. B 28, 1809-1834 (1983).

[43] A. D. Becke, *Density-functional exchange-energy approximation with correct asymptotic behavior*, Phys. Rev. A 38, 3098-4100 (1988).

[44] C. Lee, W. Yang, R. G. Parr, *Development of the Colle-Salvetti correlation-energy formula into a functional of the electron density*, Phys. Rev. B 37, 785-789 (1988).

[45] J. P. Perdew, K. Burke, M. Ernzerhof, *Generalized Gradient Approximation Made Simple*. Phys. Rev. Lett. 77, 3865-3868 (1996).

[46] W. Kohn, *Electronic structure of matter-wave functions and density functionals*, Rev. Mod. Phys. 71, 1253-1266 (1999).

[47] R. Armiento and A. E. Mattsson, *Functional designed to include surface effects in self-consistent density functional theory*, Phys. Rev. B 72, 085108:1-5 (2005).

[48] Z. Wu and R. E. Cohen, *More accurate generalized gradient approximation for solids*, Phys. Rev. B 73, 235116:1-6 (2006).

[49] J. P. Perdew,A. Ruzsinszky, G. I. Csonka, O. A. Vydrov, G. E. Scuseria, L. A. Constantin, X. Zhou, and K. Burke, *Restoring the Density-Gradient Expansion for Exchange in Solids and Surfaces*, Phys. Rev. Lett. 100, 136406:1-4 (2008).

[50] Yan Zhao and Donald G. Truhlar, *Construction of a generalized gradient approximation by restoring the density-gradient expansion and enforcing a tight Lieb–Oxford bound,* J. Chem. Phys. 128, 184109:1-8 (2008).

[51] P. Haas, F. Tran, P. Blaha, and K. Schwarz, *Construction of an optimal GGA functional for molecules and solids*, Phys. Rev. B 83, 205117:1-6 (2011).

[52] L. He, F. Liu, G. Hautier, M. J. T. Oliveira, M. A. L. Marques, F. D. Vila, J. J. Rehr, G.-M. Rignanese, and Aihui Zhou, *Accuracy of generalized gradient approximation functionals for density-functional perturbation theory calculations*, Phys. Rev. B 89, 064305:1-15 (2014).

[53] A. D. Becke, *A new mixing of Hartree-Fock and local density-functional theories*, J. Chem. Phys. 98, 1372-1377 (1993); *Density-functional thermochemistry. III. The role of exact exchange*, J. Chem. Phys. 98, 5648-5652 (1993).

[54] Y. Zhao, N. E. Schultz, and D. G. Truhlar, *Design of Density Functionals by Combining the Method of Constraint Satisfaction with Parametrization for Thermochemistry, Thermochemical Kinetics, and Non covalent Interactions*, J. Chem. Theory Comput. 2, 364-382 (2006).

[55] Y. Zhao and D. G. Truhlar, *The M06 suite of density functionals for main group thermochemistry, thermochemical kinetics, noncovalent interactions, excited states, and transition elements: two new functionals and systematic testing of four M06-class functionals and 12 other functionals*, Theor. Chem. Acc. 120, 215-241 (2008).

[56] Y. Zhao and D. G. Truhlar, *Density Functionals with Broad Applicability in Chemistry*, Acc. Chem. Res. 41, 157-167 (2008).

[57] A. D. Becke, *Density-functional thermochemistry. IV. A new dynamical correlation functional and implications for exact-exchange mixing*, J. Chem. Phys. 104, 1040-1046 (1996).

[58] J. Tao, J. P. Perdew, V. N. Staroverov, and G. E. Scuseria, *Climbing the Density Functional Ladder: Non-empirical Meta–Generalized Gradient Approximation Designed for Molecules and Solids*, Phys. Rev. Lett. 91, 146401:1-4 (2003).

[59] Y. Zhao and D. G. Truhlar, *A new local density functional for main-group thermochemistry, transition metal bonding, thermochemical kinetics, and noncovalent interactions*, J. Chem. Phys. 125, 194101:1-18 (2006).

[60] M. Gruning, O. Gritsenko, and E. J. Baerends, Improved Description of Chemical Barriers with Generalized Gradient Approximations (GGAs) and Meta-GGAs, J. Phys. Chem. A 108, 4459-4469 (2004).

[61] A. D. Corso, A. Pasquarello, A. Baldereschi, and R. Car, *Generalized gradient approximations to density-functional theory*: *A comparative study for atoms and solids*. Phys. Rev. B 53, 1180-1185 (1996).

[62] D. J. Singh, L. Nordström, *Planewaves, Pseudopotentials, and the LAPW Method*, 2nd Ed, Springer Science + Business Media, Inc., USA, 2006.

[63] M. Sprik, J. Hutter, and M. Parrinello, *Ab initio molecular dynamics simulation of liquid water: Comparison of three gradient-corrected density functionals*, J. Chem. Phys. 105, 1142-1152 (1996).

[64] M. C. Payne, M. P. Teter and D. C. Allan, T. A. Arias and J. D. Joannopoulos, *Iterative minimisation techniques for iterative ab initio total-energy calculations*: *molecular dynamics and conjugate gradients*, Rev. Mod. Phys. 64, 1045-1097 (1992).

[65] R. M. Martin, *Electronic Structure - Basic Theory and Practical Methods*, Cambridge University Press, 2004.

[66] D. G. Anderson, *Iterative Procedures for Nonlinear Integral Equations*, J. Assoc. Comput. Mach. 12, 547-560 (1965).

[67] P. H. Dederichs and R. Zeller, *Self-consistency iterations in electronic-structure calculations*, Phys. Rev. B 28, 5462-5472 (1983).

CHAPTER 3

Pseudopotential Plane-Wave method

Chapter 3

Pseudopotential Plane-Wave method

Contents

3.1. Introduction

In the previous chapter it was demonstrated the that many-body problem of strongly interacting electrons and nuclei has been mapped within the framework of the Born-Oppenheimer approximation and density functional theory onto a problem of single-particles moving in an effective external potential for a set of fixed nuclei. However, there still remains the formidable task of handling an infinite number of non interacting electrons moving in the static potential of an infinite number of nuclei or ions. Two difficulties must be overcome: a wave function must be calculated for each of the infinite number of electrons in the system, and, since each electronic wave function extends over the entire solid, the basis set required to expand each wave function is infinite [1]. Our aim now is to develop a practical numerical scheme to solve the resulting single-particle Kohn-Sham equations for extended systems like crystalline solids or liquids.

Many of the *ab initio* [2] methods that physicists and chemists use have existed for more than a few decades, where most of them were capable only of modeling systems of a few atoms, and hence applicability to real-world systems at that point was extremely limited. All of the *ab initio* methods have been continuously refined over recent years and all have benefited from the availability of increasingly powerful computers. Most methods can now model to study extended systems like solids. Among the most common and widely used methods, the two methods which will be used in this work: Pseudo-Potential Plane-Wave and Full-Potential Linearized Augmented Planewave Methods.

Because of its periodicity, the most straightforward choice for a crystal would be to expand the KS wave-function into plane-waves, because Plane-waves are orthogonal, they are diagonal in momentum space and the implementation of plane-wave based methods is rather straightforward due to their simplicity. However, plane-wave basis sets do not converge at the presence of the singularity of the crystal potential at the nucleus, where electron wave-functions are varying very quickly near it. In this case, the large basis set would be needed to represent the wave-functions accurately, which makes the set-up and diagonalization of the Hamiltonian matrix in terms of plane-waves impracticable if not impossible. Thus, plane-wave basis-sets can only be used in the context of a pseudopotential approximation to the true potential where the (-1/r) potential has been replaced by an appropriate smooth potential [3]. It is the Pseudo-Potential Plane-Waves method (PP-PW). This approach is one of the most widely used methods for calculating ground state properties of extended systems within the framework of density functional theory. The simplicity of plane waves leads to very efficient

numerical schemes for solving the Kohn-Sham equations, and the employment of pseudopotentials guarantees that the wave functions can be expanded in a relatively small set of plane waves.

Pseudopotentials are therefore needed when using plane wave basis sets in order to limit the number of plane waves. The bare coulomb attraction between electrons and nuclei is replaced by pseudopotentials for two main goals. First, only valence electrons are thus included in most calculations, as they are the ones involved in the chemistry of the system while the charge density of core electrons is very steep and would require a much too large number of plane waves to describe. The second role of pseudopotentials is to replace the valence orbitals by smooth functions in the core region, while keeping a very good approximation of them outside the core region [4].

3.2. Why Plane-Waves

3.2.1. Effect of translational symmetry of crystals

One of the fundamental characteristics of crystals is the symmetry of translation due to their periodicity, where the ions are arranged in a regular manner. This property can now be exploited to reduce the computational cost for solving the Kohn-Sham equations. The translational symmetry of the atomic arrangements imposes on the effective potential of Kohn and Sham (as well as the electron density) to possess the invariance by translation, i.e.:

$$V_{eff}^{KS}(\vec{r}) = V_{eff}^{KS}(\vec{r} + \vec{R}) \tag{3.1}$$

where $\vec{R}$ is a Bravais lattice vectors corresponding to an entire linear combination of the three unit vectors $\vec{a}_1$, $\vec{a}_2$ and $\vec{a}_3$ of the lattice in space:

$$\vec{R} = l_1\vec{a}_1 + l_2\vec{a}_2 + l_3\vec{a}_3 \tag{3.2}$$

where l_1, l_2 and l_3 can be any integer number.

Independent electrons, each of which obeys a single-electron Schrödinger equation (Kohn-Sham equation) with a periodic potential, are known as *Bloch electrons*. The stationary states of Bloch electrons have the following very important property as a general consequence of the periodicity of the potential (V_{eff}^{KS}) [5].

Thus, both problems due to infinite number of electrons in the system, and, the infinite number required in the basis set can be surmounted by performing calculations on periodic systems and applying Bloch's theorem to the electronic wave functions [1].

2.2.2. Bloch's theorem

The Bloch's theorem [6] makes it possible to exploit the symmetry properties of the system. Since there is invariance by translation of a vector of the direct lattice, this imposes that the Hamiltonian of Kohn and Sham $\hat{H}^{KS}$ commutes with the translation operator $\hat{T}$. This makes it possible to write the mono-electronic wave function of Kohn and Sham $\phi_i(\vec{r})$ as a Bloch function, as stated in the theorem.

Theorem: *The eigenstates* $\phi_{\vec{k}}^{n}(\vec{r})$ *of the single-electron Hamiltonian* $H=-\hbar^2/2m+V(\vec{r})$, *where* $V(\vec{r}+\vec{R})=V(\vec{r})$ *for all* $\vec{R}$ *in a Bravais lattice, can be chosen to have the form of a plane wave times a function with the periodicity of the Bravais lattice*:

$$\phi_{\vec{k}}^{n}(\vec{r})=e^{i\vec{k}.\vec{r}}u_{\vec{k}}^{n}(\vec{r}) \tag{3.3}$$

where

$$u_{\vec{k}}^{n}(\vec{r}+\vec{R})=u_{\vec{k}}^{n}(\vec{r}) \tag{3.4}$$

for all $\vec{R}$ in the Bravais lattice. Eqns. (2.3) and (2.4) imply that:

$$\phi_{\vec{k}}^{n}(\vec{r}+\vec{R})=e^{i\vec{k}.\vec{R}}\phi_{\vec{k}}^{n}(\vec{r}) \tag{3.5}$$

for every $\vec{R}$ in the Bravais lattice [5].

Physically we can say that the Bloch function (Eqn. 2.3) is the wave function of a free electron $e^{i\vec{k}.\vec{r}}$ (plane wave function) modulated by the periodic potential of the ion lattice through the function $u_{\vec{k}}^{n}(\vec{r})$ [5,7].

The vector $\vec{k}$ represents the wave vector in the first Brillouin zone of the reciprocal lattice crystal and *n* corresponds to the band index. The reason for taking into account only the vectors $\vec{k}$ belonging to the first Brillouin zone is that any vector $\vec{k}'$ of the reciprocal space which does not belong to the first Brillouin zone can be written as $\vec{k}'=\vec{k}+\vec{K}$, where $\vec{K}$ is a reciprocal lattice vector satisfies the relation $\vec{K}.\vec{R}=2\pi m$, with m is an integer. Since $e^{i\vec{K}.\vec{R}}=1$ for any reciprocal lattice vector, if the Bloch form (2.5) holds for $\vec{k}'$, it will also hold for $\vec{k}$ [5].

The index *n* appears in Bloch's theorem because for given $\vec{k}$ there are many solutions to the Schrödinger equation, where *n* indicates the number of the Brillouin zone where $\vec{k}'$ was

in. For n = 1, $\vec{k}$ and $\vec{k}'$ are identical. For $\vec{k}'$ in the second Brillouin zone, we reuse the same set of $\vec{k}$, but n is increased to 2, etc. For each $\vec{k}$, an infinite number of n is possible [8].

Since the unknown functions $u_{\vec{k}}^{n}(\vec{r})$ are periodic they can be expanded in a set of plane waves using the Fourier series:

$$u_{\vec{k}}^{n}(\vec{r}) = \sum_{\vec{G}} c_{\vec{k},\vec{G}}^{n} e^{i\vec{G}.\vec{r}} \tag{3.6}$$

where $\vec{G}$is the reciprocal lattice vectors. The expansion of each electronic wave function $\phi_{\vec{k}}^{n}(\vec{r})$ in the same basis is then[1]:

$$\phi_{\vec{k}}^{n}(\vec{r}) = \sum_{\vec{G}} c_{\vec{k}+\vec{G}}^{n} e^{i(\vec{k}+\vec{G}).\vec{r}} \tag{3.7}$$

and what have to be searched are the coefficients $c_{\vec{k}+\vec{G}}^{n}$.

The plane wave basis set for $\phi_{\vec{k}}^{n}(\vec{r})$ is therefore $\{\varphi_{\vec{k}+\vec{G}}(\vec{r}) = e^{i(\vec{k}+\vec{G}).\vec{r}}\}$. This basis set is $\vec{k}$ -dependent: all eigenstates $\phi_{\vec{k}}^{n}(\vec{r})$ that have the same $\vec{k}$ but a different n will be expressed in the basis set with this particular value of $\vec{k}$. For eigenstates with another $\vec{k}$, a new basis set using that other $\vec{k}$ has to be used [8].

3.2.3. Plane-wave representation of Kohn-Sham equations

In a plane wave representation of the wave functions the Kohn-Sham equations assume a particularly simple form. Substitution of Eqn (7) into Kohn-Sham equation and integration over r we get the matrix eigenvalue equation:

$$\sum_{\vec{G}'}\left[\frac{\hbar^2}{2m}\left|\vec{k}+\vec{G}\right|^2\delta_{\vec{G}\vec{G}'} + V_{ext}\left(\vec{G}-\vec{G}'\right) + V_H\left(\vec{G}-\vec{G}'\right) + V_{xc}\left(\vec{G}-\vec{G}'\right)\right]c_{\vec{k}+\vec{G}'}^{n} = \varepsilon_{\vec{k}}^{n} c_{\vec{k}+\vec{G}}^{n} \tag{3.8}$$

In this form, the kinetic energy is diagonal, and the various potentials are described in terms of their Fourier transforms. This makes it possible to calculate them as desired in the real space or the reciprocal space, according to the ease of the respective calculations; a simple Fourier transform then makes it possible to return to the other space. Solution of Eqn. (3.8)

[1] For non-periodic systems such as those containing a defect, a surface or isolated molecules, the calculations using plane-wave basis sets can only be performed on these systems if a periodic supercell is used. Periodic boundary conditions are applied to the supercell so that the supercell is reproduced throughout space. It is essential to make the supercells large enough to prevent the defects, surfaces or molecules in neighboring cells from interacting appreciably with each other.

proceeds by diagonalization of a Hamiltonian matrix whose matrix elements $H_{\vec{k}+\vec{G},\vec{k}+\vec{G}'}$ are given by the terms in the brackets above.

The electron density in Fourier representation is given by:

$$\rho(\vec{r}) = \sum_{\vec{G},\vec{G}'}\sum_{n,\vec{k}} c^n_{\vec{k}+\vec{G}} (c^n_{\vec{k}+\vec{G}'})^* e^{i(\vec{G}-\vec{G}')\cdot\vec{r}} \tag{3.9}$$

3.2.4. Truncation of the plane-wave basis set

In principle, an infinite plane-wave basis set is required at each *k*-point to expand the electronic wave functions. However, the coefficients $c^n_{\vec{k}+\vec{G}}$ for the plane waves with small kinetic energy are typically more important than those with large kinetic energy. Thus, in practice, the plane-wave basis set can be truncated to include only plane waves that have kinetic energies less than some particular cut-off energy:

$$E_{cut} = \frac{\hbar^2}{2m_e}\left|\vec{k}+\vec{G}_{\max}\right|^2 \tag{3.10}$$

This amounts to selecting a sphere of radius $G_{\max}$ centered at the origin of the reciprocal space by imposing the condition $\left|\vec{k}+\vec{G}\right| \le G_{\max}$. The number of plane waves used is:

$$N_{pw} \approx N_k \times \frac{1}{2\pi^2}\Omega E_{cut}^{3/2} \tag{3.11}$$

where N_k is the number of vectors $\vec{k}$, in which the first Brillouin zone is sampled, and Ω is the volume of the unit cell.

The truncation of the plane-wave basis set at finite cut-off energy will lead to an error in the computed total energy. However, it is possible to reduce the magnitude of the error by increasing the value of the cutoff energy but in principle it is possible to make this error arbitrarily small by increasing the size of the basis set by allowing a larger energy cut-off. This is one of the more advantages of plane wave bases. One of the disadvantages of these latter is the need to employ a large number of plane waves to describe the localized states which have strong oscillations of their wave functions. One way to get around this difficulty is to use the *pseudopotential approximation*.

3.2.5. *k*-Point Sampling

By the use of Bloch's theorem, the problem of calculating an infinite number of electronic wave functions has now transformed to one of calculating a finite number of

electronic wave functions at an infinite number of *k*-points within the first Brillouin zone of the periodic cell. Electronic states are allowed only at a set of *k*-points determined by the Born-von Karman boundary conditions that apply to the bulk solid, in which the $\vec{k}$ vectors occupy the reciprocal space in a discrete manner but almost continuous (quasi-continuous). The number of allowed wave vectors $\vec{k}$ in the first Brillouin zone is equal to the number of sites in the crystal [5]. Thus, the density of allowed *k*-points is proportional to the volume of the solid.

In theory, the Schrödinger equation must be solved for each wave vector $\vec{k}$ of the first Brillouin zone, but in practice things are not so simple because of infinite number of points, *k*. Due to the symmetry of the system, we can reduce the calculation to the first Brillouin zone. Furthermore, the electronic wave functions at *k*-points which are close together will be very similar. Hence it is possible to represent the wave functions of a region of *k*-space by the wave function at a single *k*-point, and we assume a continuous evolution of the bands between two points *k*. In this case the electronic states at only a finite number of *k*-points are required to calculate the electronic potential and hence determine the tota1 energy of the solid [1]. In particular, it is advisable to group the equivalent *k*-points by symmetry in the summation; such methods significantly reduce the number of *k*-points to be considered, called *special points*, while making very good accuracy. To construct such *k*-point meshes, different methods have been developed for obtaining very accurate approximations to the electronic potential and the contribution to the total energy from a filled electronic band by calculating the electronic states at special sets of *k*-points in the first Brillouin zone, like the methods of Chadi and Cohen [9]; Joannopoulos and Cohen [10]; Evarestov and Smirnov [11], or that of Monkhorst and Pack [12]. For our calculations, we have used the Monkhorst and Pack method.

3.3. Pseudopotentials

Although Bloch's theorem states that the electronic wave functions can be expanded using a discrete set of plane waves, a plane-wave basis set is usually very poorly suited to expanding electronic wave functions because a very large number of plane waves are needed to expand the tightly bound core orbitals and to follow the rapid oscillations of the wave functions of the valence electrons in the core region. An extremely large plane-wave basis set would be required to perform an all-electron calculation, and a vast amount of computational time would be required to calculate the electronic wave functions. The pseudopotential

approximation allows the electronic wave functions to be expanded using a much smaller number of plane-wave basis states [1].

3.3.1. Frozen-Core Approximation

It is well known that most physical and chemical properties of solids are dependent on the valence electrons, because binding properties are almost completely due to them, especially in metals and semiconductors. While, the core electrons are strongly bound and do not play a significant role in the chemical binding of atoms, thus forming with the nucleus an (almost) inert core [13]. We can therefore consider that the configuration of the core electrons within the solid is equivalent to that of the isolated atoms, i.e., it does not change when the atoms are placed in a different chemical environment.

These considerations make it possible to separate the valence electrons from the core electrons and to group the latter with the nuclei to form rigid ions: this is the of the *frozen core approximation* [14]. Within this approximation, the problem of treating the core electrons is now solved at the atomic level and the study of the electronic configuration is restricted to the investigation of the behaviour of the valence electrons within the ionic potential.

However, this is not very useful since the valence wave functions still have to maintain their nodal structure in order to be orthogonal to the core states. Much more practical is to replace immediately the ionic core potential by a pseudopotential which will lead to nodeless valence wave functions, as we will show in the following.

2.3.2. The Pseudo-potential Concept

The pseudopotential method is based on the frozen core approximation, which suggests that core electrons can be ignored, thereby reducing the atom to an ionic core that interacts with the valence electrons. The main idea is to replace the strong ionic potential by a weaker pseudopotential that acts on a set of pseudo wave functions ϕ_v^{ps} rather than the true valence wave functions ϕ_v, which is Called "all-electron" valence wave functions. This pseudo-potential must lead to the same eigen-energy in the Schrödinger equation. The use a pseudopotential, that approximates the potential felt by the valence electrons, was first proposed by Fermi in 1934 [15], then Hellmann in 1935 [16], in order to simplify calculations of the electronic structure by eliminating core states which exhibit strong oscillations.

The pseudopotential is constructed, ideally, so that its scattering properties or phase shifts for the pseudo wave functions are identical to the scattering properties of the ion and the core electrons for the valence wave functions, but in such a way that the pseudo wave functions have no radial nodes in the core region (defined by cut-off radius r_c). Outside the core region, the pseudopotential must reduce to the ionic potential, in order for the wave functions and the pseudo wave functions to be identical:

$$V^{ps}(\vec{r}) = V(\vec{r}) \text{ and } \phi_v^{ps}(\vec{r}) = \phi_v(\vec{r}), \text{ for } r > r_c \tag{3.12}$$

with the following boundary conditions:

$$\phi_v^{ps}(\vec{r}) = \phi_v(\vec{r}) \text{ and } \frac{d\phi_v^{ps}(\vec{r})}{dt} = \frac{d\phi_v(\vec{r})}{dt}, \text{ for } r = r_c \tag{3.13}$$

The larger the radius, the smoother the wave function and the potential. Figure 3.1 illustrates the "pseudization" of the valence wave function and the potential. A valid pseudo-potential should be:

(1) *Additive*: i. e., the total pseudopotential must be the sum of the pseudoptentials when several atoms are present.

(2) *Transferable*: i. e., the same pseudopotential must be used in different chemical environments.

(3) *Soft*: A pseudopotential is called *soft* when few plane waves are needed.

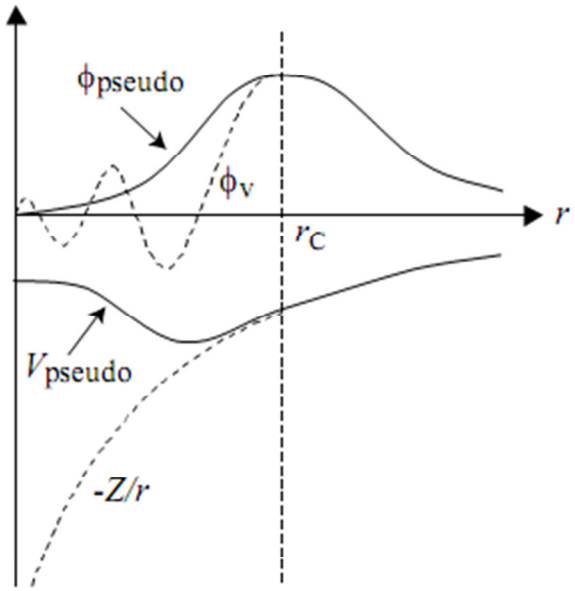

Fig. 3.1: Schematic illustration of all-electron (solid lines) and Pseudo-electron (dashed lines) potentials and their corresponding wave functions. The radius at which all-electron and pseudoelectron values match is designated r_c. The nodes and the oscillations due to the orthonormalization conditions are suppressed, which makes it possible to describe the wave pseudo-functions with a reduced number of plane waves.

3.3.3. The Phillips-Kleinman Formulation

In spite of the simplification pseudo-potentials introduce in calculations, they remained forgotten until the late 50's. It was only in 1959, with Antonick [17] and Phillips and Kleinman [18], that pseudo-potentials began to be extensively used [13], basing on the orthogonalized-plane-wave {OPW} method of Herring (1940) [19,20].

The Phillips-Kleinman Construction of a pseudopotential can be demonstrated in terms of the exact core and valence states $|\phi_c\rangle$ and $|\phi_v\rangle$, respectively, which satisfy:

$$\hat{H}|\phi_n\rangle = \varepsilon_n|\phi_n\rangle, \quad n = c, v \tag{3.14}$$

The valence states are smoothed in the core region by subtracting out the core orthogonality wiggles, leading to pseudostates $|\phi_v^{ps}\rangle$ given by:

$$|\phi_v^{ps}\rangle = |\phi_v\rangle + \sum_c |\phi_c\rangle\langle\phi_c|\phi_v^{ps}\rangle \tag{3.15}$$

Applying the Kohn-Sham hamiltonian to this equation, we obtain:

$$\left\{\hat{H} + \sum_c (\varepsilon_v - \varepsilon_c)|\phi_c\rangle\langle\phi_c|\right\}|\phi_v^{ps}\rangle = \varepsilon_v|\phi_v^{ps}\rangle \tag{3.16}$$

Thus the valence pseudo-states $|\phi_v^{ps}\rangle$ satisfy a Schrödinger equation with an energy-dependent pseudo-Hamiltonian:

$$\hat{H}^{ps} = \hat{H} + \sum_c (\varepsilon_v - \varepsilon_c)|\phi_c\rangle\langle\phi_c| \tag{3.17}$$

but have the same eigenvalues ε_v as the original valence states $|\phi_v\rangle$.

The modified potential for these states is called the "pseudopotential", given by [21]:

$$V^{ps} = V + \sum_c (\varepsilon_v - \varepsilon_c)|\phi_c\rangle\langle\phi_c| \tag{3.18}$$

where the new term $\sum_c (\varepsilon_v - \varepsilon_c)|\phi_c\rangle\langle\phi_c|$ has been introduced to account for the effects of the core states on the valence states. This term is strictly positive and therefore, because $\varepsilon_v > \varepsilon_c$ (valence states have by definition higher energy than core states). Thus, this term is repulsive, making the pseudo-potential V^{ps} much weaker than the true potential V and tends to push the corresponding states $|\phi_v^{ps}\rangle$ outside the core. In this sense, the pseudopotential represents the effective potential that valence electrons feel, if the only effect of core electrons were to repel

them from the core region. Therefore the pseudo-wave functions experience an attractive Coulomb potential which is shielded near the position of the nucleus by the core electrons. All this implies that the pseudo wave-functions will be smooth and will not oscillate in the core region, as desired [22,23,13].

A more useful feature is that the pseudopotential often is rapidly convergent in a PW basis set, and this feature can be utilized for describing most semiconductors as well as metals with no *d* or *f* bands (or 2*p* bands) in the valence region [21]. The disadvantage of this approach is that it requires experimental values to adjust the form factors that describe the potential that will be introduced later in the Schrodinger equation. The improvement made to overcome this difficulty is the *ab-initio* approach [2] that requires only free parameters (such as network parameters and atomic number) to generate the pseudopotential.

3.3.4. Norm Conserving Pseudopotentials

A valid pseudopotential should be *soft*, *transferable* and the pseudo-charge density should accurately reproduce the valence charge density as much as possible. These conflicting goals can be solved by using the concept of norm conservation, which was first used by Topp and Hopfield in 1974 [24] in the context of empirical pseudopotentials and was incorporated into ionic potentials by Starkloff and Joannopoulos in 1977 [25]. This was made the central feature by Hamann, Schlüter and Chiang in 1979 (HSC) [26], then it was refined by Bachelet, Hamann and Schlüter (BHS)[2] [27], Kerker [28] and Hamann [29]. Several modifications have been developed that improve the resulting pseudopotentials, both in terms of transferability and in terms of hardness [30-34].

With the norm conserving pseudopotentials, the conditions proposed by Hamann, Schlüter and Chiang (HSC) [26] are the following:

1. The pseudo-wave function and the all electron wave function correspond to the same eigenvalue:

$$\varepsilon_l^{ps} = \varepsilon_{n,l} \tag{3.19}$$

2. The radial pseudo-wave function should not have nodes, and is identical to the all electron wave function outside a suitably chosen cutoff radius r_c:

[2] With BHC formulation which is rather widely used, the pseudopotentials for all the elements in the periodic table were tabulated accurately from atomic *ab-initio* calculations.

$$R_l^{ps}(\vec{r}) = R_{n,l}(\vec{r}) \text{ for } r > r_c \tag{3.20}$$

3. Inside r_c, the pseudo-wave-functions differ from the true wave-functions, but the norm is constrained to be the same. That is: Inside r_c, the pseudo-wave-functions differ from the true wave-functions, but the norm is constrained to be the same. That is:

$$\int_0^{r_c} \left|R_l^{ps}(\vec{r})\right|^2 r^2 dr = \int_0^{r_c} \left|R_{n,l}(\vec{r})\right|^2 r^2 dr \tag{3.21}$$

4. The logarithm derivatives of the all electron wave function and pseudo-wave function agree for $r > r_c$.

   where $R_l(r)$ is the radial part of the wave-function with angular momentum l. The index n in the true wave-functions denotes the valence level [35,36,28,13].

To obtain the norm conserving pseudo-potential the procedure is:

(i) The free atom Kohn-Sham radial equations are solved taking into account all the electrons, in some given reference configuration:

$$\left\{\frac{\hbar^2}{2m_e}\left[-\frac{d^2}{dr^2}+\frac{l(l+1)}{r^2}\right]+V^{KS}(\vec{r})\right\} rR_{n,l}(\vec{r}) = \varepsilon_{n,l} rR_{n,l}(\vec{r}) \tag{3.22}$$

(ii) Using norm-conservation condition, the pseudo wave-functions are determined. Their shape in the core region needs to be previously defined, and it is here that many modern potentials differ from one another

(iii) Once the pseudo-wave functions are determined, the pseudopotential screened by the valence electrons and acting on the pseudo-wave functions is determined by the inversion of the radial Kohn-Sham equation for the pseudo wave-function [13]:

$$V_{l,scr}^{ps}(\vec{r}) = \varepsilon_l^{ps} - \frac{\hbar^2}{2m_e}\frac{l(l+1)}{r^2} + \frac{\hbar^2}{2m_e}\frac{1}{rR_l^{ps}(\vec{r})}\frac{d^2}{dr^2}\left[rR_l^{ps}(\vec{r})\right] \tag{3.23}$$

(iv) Finally, the ionic pseudopotential corresponding to the orbital moment l is obtained by subtracting the contributions due to the valence electrons in the screened pseudopotential (see Figure 3.2):

$$V_l^{ps}(\vec{r}) = V_{l,scr}^{ps}(\vec{r}) - V_H\left[\rho^{ps}(\vec{r})\right] - V_{xc}\left[\rho^{ps}(\vec{r})\right] \tag{3.24}$$

where $\rho^{ps}(\vec{r})$ denotes an electron pseudo-density constructed from the pseudo-wave functions.

In the above equations the wave-functions refer to the atomic reference state, thus a spherical symmetry is imposed. The wave-function and eigenvalue are different for different

angular momenta, *l*, and this means that the pseudo-potential should also be *l*-dependent. These kinds of pseudo-potentials are called "semi-local" since a different $V^{PS}(r)$ is generated for each l values. The most general form for a pseudopotential is:

$$V^{ps}(\vec{r}) = \sum_{l} \sum_{m=-l}^{l} \left| Y_{l,m} \right\rangle V_l^{ps} \left\langle Y_{l,m} \right| \tag{3.25}$$

where $\left| Y_{l,m} \right\rangle$ are the spherical harmonics and V_l^{ps} is the pseudopotential for angular momentum l [35,1,13,37]. pseudo-potentials of this kind are usually called "semi-local" because they act on the various angular components of the wave function as a consequence of exchange with the core. If all the angular components of the pseudopotential are taken to be the same, then the pseudopotential is said to be local [35] (a local pseudopotential is a function only of the distance from the nucleus).

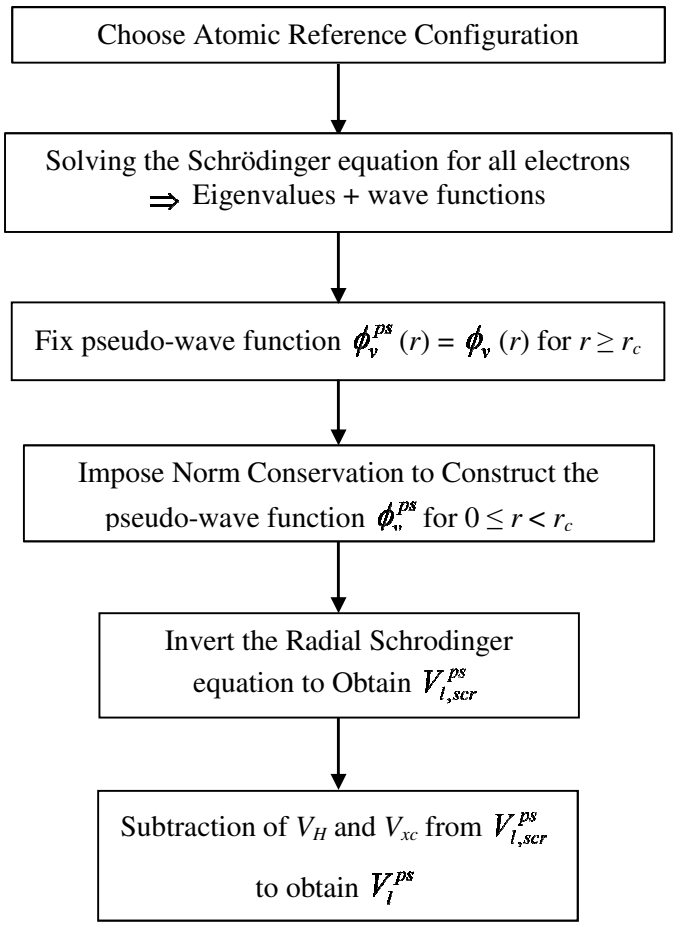

Fig. 3.2: Bachelet, Hamann, Schluter (BHS) procedure for constructing norm-conserving pseudopotentials.

For practical reasons, the pseudopotential of the above form (Eqn. 3.25) is decomposed according to BHS [27] into two parts: a long-range local part V_{loc}^{ps} (l-independent), and a short-range non-local part V_{nloc}^{ps} (l-dependent). The first has a purely radial dependence, and the second, although possessing a radial dependence, contains an average of all the angular contributions:

$$V^{ps}(\vec{r}) = V_{loc}^{ps}(\vec{r}) + V_{nloc}^{ps}(\vec{r}) \tag{3.26}$$

where

$$V_{nloc}^{ps}(\vec{r}) = \sum_{l,m} \left| Y_{l,m} \right\rangle \Delta V_l^{ps}(\vec{r}) \left\langle Y_{l,m} \right| \tag{3.27}$$

with

$$\Delta V_l^{ps}(\vec{r}) = V_l^{ps}(\vec{r}) - V_{loc}^{ps}(\vec{r}) \tag{3.28}$$

The ΔV_l^{ps} can be seen as a "correction" to the local part of the pseudopotential in the core region. Far from this region, the V_l^{ps} are reduced to the Coulomb potentials in (-1/r), and lose their angular dependence, and thus become local. That is, the non-local part of the pseudopotential will disappear.

The main problem with the semi-local form seen above is that the calculations to be handled become quickly too heavy from the computer point of view. Kleinman and Bylander [38] suggested that the non-local part of (Eqn. 3.26) are written as a separable potential, thus transforming the semi-local potential into a truly non-local pseudo-potential, replacing the form of $V_{nloc}^{ps}(\vec{r})$ with an equivalent form:

$$V_{nloc}^{KB}(\vec{r}) = \sum_{lm} \frac{\left| \Delta V_l^{ps} \phi_{lm}^{ps} \right\rangle \left\langle \phi_{lm}^{ps} \Delta V_l^{ps} \right|}{\left\langle \phi_{lm}^{ps} \left| \Delta V_l^{ps} \right| \phi_{lm}^{ps} \right\rangle} \tag{3.29}$$

Kleinman-Bylander separation represents a substantial improvement over the semi-local from a computa-tional point of view. However, this separation of pseudopotentials has some disadvantages leading sometimes to nonphysical results, such as (ghost) states in some cases [39,40].

Reformulation of energy and effective potential

The total energy of the system can be reformulated to account for the use of pseudopotentials:

$$E_{tot}^{KS} = \sum_i \left\langle \phi_i^{ps} \left| -\frac{\hbar^2}{2m}\nabla^2 + V_{nloc}^{ps} \right| \phi_i^{ps} \right\rangle + E_H + E_{ext} + E_{xc} \tag{3.30}$$

where the term E_{ext} of nucleus-electron interactions, now represents the local part:

$$E_{ext} = \int V_{loc}^{ps}(\vec{r})\rho(\vec{r})dr \tag{3.31}$$

At the level of the Kohn and Sham equations, the change results in a reformulation of the effective potential and the addition of the non-local potential:

$$\underbrace{\left[-\frac{\hbar^2}{2m}\nabla^2 + V_{nloc}^{ps} + \underbrace{V_H(\vec{r}) + V_{loc}^{ps}(\vec{r}) + V_{xc}(\vec{r})}_{V_{eff}^{ps}(\vec{r})} \right]}_{H_{NC}^{KS}} \left| \phi_i^{ps} \right\rangle = \varepsilon_i \left| \phi_i^{ps} \right\rangle \tag{3.32}$$

3.3.5. Ultrasoft Pseudopotentials

The development of the norm-conserving pseudopotentials has paved the way to accurate calculations of solid-state properties. However, the utility of this approach to systems containing highly localized valence orbitals (e.g., for first-row and transition-metal atoms) has been limited, because of the difficulty of representing the pseudo-wave-functions in a plane-wave basis, where a large number of plane waves is required, which often makes calculations for such elements prohibitively expensive. A number of attempts have been made to reduce the cut-off energy [28,30,32], but without allowing simulation of extended systems.

To circumvent this problem Vanderbilt [41] and co-workers [42,43] has introduced a new type of pseudopotentials, the so-called ultrasoft pseudopotentials, in which the norm-conserving requirement was removed so that the pseudo-wave-function can be constructed in such a way as to optimize smoothness. Therefore, large values of r_c can be used in this scheme and consequently the plane-wave cut-off needed in calculations can be greatly reduced. In this approach, the pseudo-wave functions are required to be equal to the all-electron wave-functions outside r_c, as with norm-conserving pseudopotentials, but inside r_c they are allowed to be as soft as possible (Figure 3.3).

Nevertheless, the following complications have to be taken into account:

1. As pseudo-wavefunctions are not normalized, this introduces a non-diagonal overlap in the secular equation.

2. The pseudo-wave functions do not make it possible to recover the entire charge of the system. Thus, an augmentation term has to be added in the core region.
3. The resulting pseudopotentials can become less transferable.

However, Vanderbilt pseudopotentials were proposed for use in large scale calculations, for which the cost of generating pseudopotentials is negligible compared with the cost of the calculations [37].

In Vanderbilt's ultrasoft pseudopotential approach the non-local pseudopotential is given in the following form:

$$V_{nloc}^{ps} = \sum_{nm,I} D_{nm}^{0} \left|\beta_n^I\right\rangle\left\langle\beta_m^I\right| \tag{3.33}$$

where D_{nm}^{0} are coefficients which characterize this non-local part of the pseudopotential, and the functions $\beta_n^I(\vec{r}) = \beta_n^I\left(\vec{r} - \vec{R}_I\right)$ are represented in an angular expansion, *i.e.* spherical harmonics multiplied by radial functions, which vanish outside r_c.

The pseudo-charge density ρ is given by the square of the pseudo-wave functions plus the augmentation inside the spheres:

$$\rho(\vec{r}) = \sum_i \left\{ \left|\phi_i^{ps}(\vec{r})\right|^2 + \sum_{nm,I} Q_{nm}^I(\vec{r}) \left\langle\phi_i^{ps}\middle|\beta_n^I\right\rangle\left\langle\beta_m^I\middle|\phi_i^{ps}\right\rangle \right\} \tag{2.34}$$

where the $Q_{nm}^I(\vec{r}) = Q_{nm}^I\left(\vec{r} - \vec{R}_I\right)$ indicates the local functions determined during the generation of the pseudo-potential.

Applying the variational principle to the Kohn-Sham and the pseudo-charge density equations, the secular equation is:

$$\underbrace{\left[-\frac{\hbar^2}{2m}\nabla^2 + V_{eff}^{ps}(\vec{r}) + \sum_{nm,I} D_{nm}^I \left|\beta_n^I\right\rangle\left\langle\beta_m^I\right| \right]}_{H_V^{KS}} \left|\phi_i^{ps}\right\rangle = \varepsilon_i S \left|\phi_i^{ps}\right\rangle \tag{3.35}$$

with

$$V_{eff}^{ps}(\vec{r}) = V_H(\vec{r}) + V_{ion,loc}^{ps}(\vec{r}) + V_{xc}(\vec{r}) \tag{3.36}$$

and

$$D_{nm}^I = D_{nm}^0 + \int V_{eff}^{ps}(\vec{r}) Q_{nm}^I(\vec{r}) dr \tag{3.37}$$

The D_{nm}^I are the D_{nm}^0 with a screening term:

$$D_{nm}^I = D_{nm}^0 + \int V_{eff}^{ps}(\vec{r}) Q_{nm}^I(\vec{r}) dr \tag{3.38}$$

S is a matrix depends on the positions of the atoms in which the orthonormalization condition of the wave functions is replaced by a generalized condition:

$$\left\langle \phi_i^{ps} \middle| S \middle| \phi_j^{ps} \right\rangle = \delta_{ij} \tag{3.39}$$

and is expressed as follows:

$$S = I + \sum_{nm,I} q_{nm} \left| \beta_n^I \right\rangle \left\langle \beta_m^I \right| \tag{3.40}$$

with

$$q_{nm} = \int Q_{nm}(\vec{r}) dr \tag{3.41}$$

and *I* denotes the identity operator.

For our calculations, we have used this scheme of ultrasoft pseudopotential.

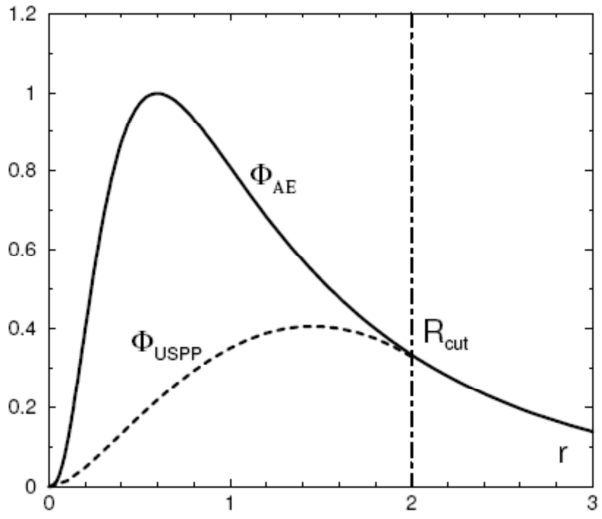

Fig. 3.3: Illustration of a strongly localized valence wave function (solid line) inside the atomic core region and the modified wave function (dashed line) in the Vanderbilt ultrasoft pseudopotential scheme [44].

References

[1] M. C. Payne, M. P. Teter, D. C. Allan, T. A. Arias, and J. D. Joannopoulos, *Iterative minimization techniques for ab initio total-energy calculations: molecular dynamics and conjugate gradients*, Rev. Mod. Phys. 64, 1045-1097 (1992).

[2] C. Pisani, R. Dovesi, *Hartree-Fock Ab Initio Treatment of Crystalline Systems*, Spriger Verlag, 1986.

[3] S. Blügel and G. Bihlmayer, *Full-Potential Linearized Augmented Planewave Method*, edited by Johannes Grotendorst, Stefan Blügel and D. Marx, NIC Series Volume 31, 85-129 (2006).

[4] A. Filippetti, D. Vanderbilt, W. Zhong, Y. Cai and G. B. Bachelet, *Chemical hardness, linear response, and pseudopotential transferability*. Phys. Rev. B 52, 11793-11804 (1995).

[5] N.W. Ashcroft, N.D. Mermin, *Physique du solide*, EDP Sciences, France, 2002.

[6] F. Bloch, *Über die Quantenmechanik der Elektronen in Kristallgittern*, Z. Physic 52, 555-600 (1928).

[7] H.T. Diep, *Physique de la matière condensée*, Dunod, Paris, 2003.

[8] S. Cottenier, *Density Functional Theory and the Family of (L)APW-methods: a step-by-step introduction*, Ghent University, Belgium, 2013.

[9] Chadi, D. J., and M. L. Cohen, *Special Points in the Brillouin Zone*, Phys. Rev. 88, 5747-5753 (1973).

[10] J. D. Joannopoulos and M. L. Cohen, *Electronic charge densities for ZnS in the wurtzite and zincblende structures*, J. Phys. C 6, 1572-1585 (1973).

[11] Evarestov, R. A., and V. P. Smirnov, *Special points of the brillouin zone and their use in the solid state theory*, Phys. Status Solidi 119, 9-40 (1983).

[12] H. J. Monkhorst and J. D. Pack, *Special points for Brillouin-zone integrations*, Phys. Rev. B 13, 5188-5192 (1976).

[13] C. Fiolhais, F. Nogueira and M. Marques, *A Primer in Density Functional Theory*, Springer, Berlin, 2003.

[14] U. von Barth, C. D. Gelatt. *Validity of the frozen-core approximation and pseudo-potential theory for cohesive energy calculations*, Phys. Rev. B 21, 2222-2228 (1980).

[15] E. Fermi, *Sopra lo Spostamento per Pressione delle Righe Elevate delle Serie Spettrali*, Il Nuovo Cimento 11, 157-166 (1934).

[16] H. Hellmann, *A New Approximation Method in the Problem of Many Electrons*, Chem. Phys. 3, 61-61 (1935).

[17] E. Antonick, *Approximate formulation of the orthogonalized plane-wave method*, J. Phys. Chem. Solids 10, 314-320 (1959).

[18] J. C. Phillips and L. Kleinman, *New Method for Calculating Wave Functions in Crystals and Molecules*, Phys. Rev. 116, 287-294 (1959).

[19] W. C. Herring, *A New Method for Calculating Wave Functions in Crystals*, Phys. Rev. 57, 1169-1177 (1940).

[20] W. C. Herring and A. G. Hill, *The theoretical constitution of metallic beryllium*, Phys, Rev. 58, 132-162 (1940).

[21] W.E. Pickett. *Pseudopotential Methods in Condensed Matter Applications*, Comput. Phys. Rep. 9, 115-198 (1989).

[22] E. Kaxiras, *Atomic and Electronic Structure of Solids*, Cambridge University Press, New York, 2003.

[23] P. J. H. Denteneer, *The pseudopotential-density-functional method applied to semi-conducting crystals*, Tech. Univ. Eindhoven, Holland, 1987.

[24] W. C. Topp and J. J. Hopfield, *Chemically Motivated Pseudopotential for Sodium*, Phys. Rev. B 7, 1295-1303 (1973).

[25] T. Starkloff and J.D. Joannopoulos, *Local pseudopotential theory for transition metals*, Phys. Rev. B 16, 5212-5215 (1977).

[26] D. H. Hamalm, M. Schluter, and C. Chiang, *Norm-Conserving Pseudopotentials*, Phys. Rev. Lett. 43, 1494-1497 (1979).

[27] G. B. Bachelet, D.R. Hamann, and M. Schlüter, *Pseudopotentials that work: From H to Pu*, Phys. Rev. B 26, 4199-4228 (1982).

[28] G. P. Kerker, *Non-singular atomic pseudopotentials for solid state applications*, J. Phys. C 13, L189-194 (1980).

[29] D.R. Hamann, *Generalized norm-conserving pseudopotentials*, Phys. Rev. B 40, 2980-2987 (1989).

[30] D. Vanderbilt, *Optimally smooth norm-conserving pseudopotentials*, Phys. Rev. B 32, 8412-8415 (1985).

[31] E. L. Shiriey, D. C. Allan, R. M. Martin and J. D. Joannopoulos, *Extended norm-conserving pseudopotentials*, Phys. Rev. B 40, 3652-3660 (1989).

[32] A. M. Rappe, K. M. Rabe, E. Kaxiras and J. D. Joannopoulos, *Optimized pseudo-potentials*, Phys. Rev. B 41, 1227-1230 (1990).

[33] N. Troullier and J. L. Martins, *Efficient pseudopotentials for plane-wave calculations*, Phys. Rev. B 43, 1993-2006 (1991).

[34] G. Kresse, J. Hafner and R. J. Needs, *Optimized norm-conserving pseudopotentials*, J. Phys. Condens. Matter 4, 7451-7468 (1992).

[35] J. Kahanoff, *Electronic structure calculations and first principles molecular dynamics simulation*, Italy. 16, 1998.

[36] M. Fuchs and M. Scheffler, *Ab initio pseudopotentials for electronic structure calculations of poly-atomic systems using density-functional theory*, Comput. Phys. Comm. 119, 67-98 (1999).

[37] D.J. Singh, L. Nordström, *Planewaves, Pseudopotentials, and the LAPW Method*, 2nd Ed, Springer Science + Business Media, Inc., USA, 2006.

[38] D. Kleinman and D. M. Bylander, *Efficacious Form for Model Pseudopotentials*, Phys. Rev. Lett. 48, 1425-1428 (1982).

[39] X. Gonze, P. Kckell, M. Scheffler, *Ghost states for separable, norm-conserving ab initio pseudopotentials*, Phys. Rev. B 41, 12264-12267 (1990).

[40] X. Gonze, R. Stumpf, M. Scheffler, *Analysis of separable potentials*, Phys. Rev. B 44, 8503-8513 (1991).

[41] D. Vanderbilt, *Soft self-consistent pseudopotentials in a generalized eigenvalue formalism*, Phys. Rev. B 41, 7892-7895 (1990).

[42] K. Laasonen, R. Car, C. Lee and D. Vanderbilt, *Implementation of ultrasoft pseudopotentials in ab initio molecular dynamics*, Phys. Rev. B 43, 6796-6799 (1991).

[43] K. Laasonen, A. Pasquarello, R. Car, C. Lee and D. Vanderbilt, *Car-Parrinello molecular dynamics vrith Vanderbilt ultrasoft pseudopotentials*, Phys. Rev. B 47, 10142-10153 (1993).

[44] B. Meyer, *The Pseudopotential Plane Wave Approach*, edited by Johannes Grotendorst, Stefan Blügel and D. Marx, NIC Series Volume 31, 85-129 (2006).

CHAPTER 4

Full-Potential Linearized Augmented Plane-Wave method

Chapter 4

Full-Potential Linearized Augmented Plane-Wave method

Contents

4.1. Introduction

As a result of the Bloch's theorem, which starts with the periodicity of the crystal lattice, a natural basis set that is certainly unbiased and simple for calculating the single particle wave functions in periodic solids is the plane wave basis set that was introduced in Bloch functions. This basis set is generally coupled with the use of pseudopotential which does not explicitly treats that the valence electrons. However, despite the pseudopotential-plane wave (PP-PW) method is extremely useful because of the simplification brought by it, the use of an all electron method is indispensable if the entry of the core electrons which exhibit strong oscillations is desirable (e. g. to study hyperfine fields or excitation of the core states). This due to the fact that the plan waves are very inefficient basis set for describing the rapid variations of the wave functions near the nucleus. One of the all electron methods, which uses complex but more efficient basis sets, and that does not require the introduction of a pseudopotential, is the Full Potential Linearized Augmented Plane Wave (FP-LAPW) method, which is fundamentally a modification of the original Augmented Plane Wave (APW) method [1]. Thus, before embarking on an exposition of the LAPW method, we review the relevant aspects of the APW method and the motivation for its modification to the LAPW method.

4.2. The APW method

The augmented plane wave (APW) method was developed by Slater [2,3] in 1937 in order to solve the one-electron equations of Kohn and Sham within DFT. It was originally developed to overcome difficulties inherent in the cellular method in the latter it is difficult to satisfy the periodic boundary condition for all points on the boundary of the unit cell [4]. The ideas that lead to the APW basis set are very similar to that introduced in pseudopotential. The APW method is based on the observation of Slater that:

(i) Near an atomic nucleus, the potential and wave functions are similar to those in an atom; they are strongly varying but nearly spherical.

(ii) In the interstitial space between the atoms both the potential and wave functions are smoother.

Accordingly, space is divided into two regions, and different basis expansions are used in the so-called «*muffin-tin*» model of the crystal potential:

(i) Non-overlapping spheres centered on each atom with radius R_α, called a «*muffin-tin*» (MT) *spheres* (S_α), in which, the part of space occupied by the spheres is the

«*muffin-tin*» *region* (Figure 4.1). Inside the spheres, a linear combination of radial functions times spherical harmonics are used to solve the Schrodinger's equation in a spherical potential.

(ii) The remaining space outside the spheres, called the *interstitial region* (*I*), where the plane wave basis set is used to solve the Schrodinger's equation in a constant potential [1,4,5].

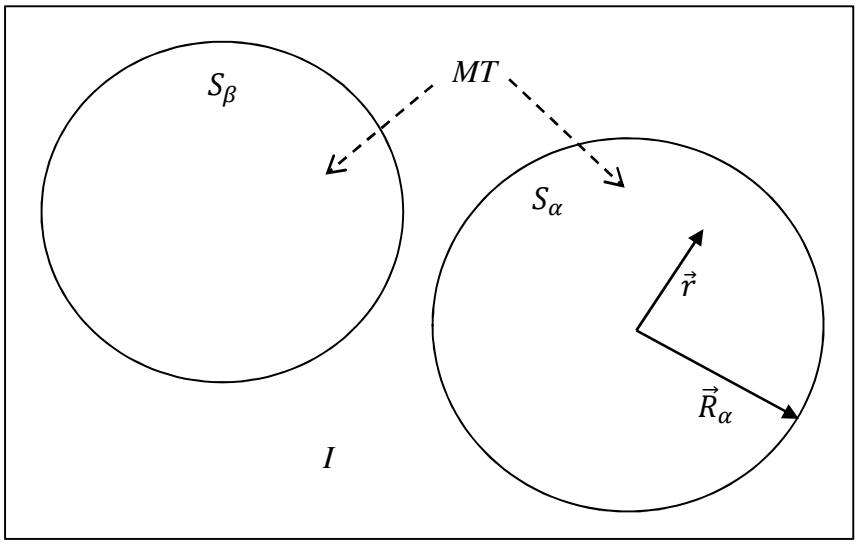

Fig. 4.1: Division of a unit cell in muffin tin regions and the interstitial region, for a case with two atoms.

Thus, the single wave-functions $\phi_{\vec{k}}^{n}(\vec{r})$ are expressed as trial functions:

$$\phi_{\vec{k}}^{n}(\vec{r}) = \sum_{\vec{G}} c_{\vec{G}}^{n,\vec{k}} \varphi_{\vec{G}}^{\vec{k}}(\vec{r}) \tag{4.1}$$

in terms of the APW basis functions. One augmented plane wave (APW) used in the expansion of $\phi_{\vec{k}}^{n}(\vec{r})$ -for the state specified by the wave vector $\vec{k}$- is defined as:

$$\varphi_{\vec{G}}^{\vec{k}}(\vec{r}) = \begin{cases} \Omega^{-1/2} e^{i(\vec{k}+\vec{G})\vec{r}} & , \quad \vec{r} \in I \\ \sum_{\ell m} A_{\ell m}^{\vec{k}+\vec{G}} u_\ell(r) Y_m^\ell(\hat{r}) & , \quad \vec{r} \in S_\alpha \end{cases} \tag{4.2}$$

where Ω is the unit cell volume, $\vec{G}$ is the reciprocal space vector, $A_{\ell m}^{\vec{k}+\vec{G}}$ are expansion coefficients, Y_m^ℓ are the spherical harmonics, and u_ℓ is the regular solution of of the radial Schrödinger equation:

$$\left[-\frac{\hbar^2}{2m_e}\frac{d^2}{dr^2}+\frac{\hbar^2}{2m_e}\frac{\ell(\ell+1)}{r^2}+V(r)-E_\ell\right]ru_\ell(r)=0 \tag{4.3}$$

to the energy parameter E_ℓ. Here, V is the spherical component of the potential in the MT sphere. The position $\vec{r}$ inside the MT spheres is given with respect to the center of each sphere.

Slater motivates these particular choices of functions by noting that plane-waves are the solutions of Schrodinger's equation in a constant potential, while the radial functions are solutions in a spherical potential, provided that E_ℓ is equal to the eigenvalue.

In practical calculations the sum over ℓm is finite. The coefficients $A_{\ell m}^{\vec{k}+\vec{G}}$ are found by expanding each plane-wave into Bessel functions of order ℓ, $j_\ell(|\vec{k}+\vec{G}|r)$ at the MT spheres, $r=r_{\mathrm{MT}}$, requiring the basis functions to be continuous at the sphere boundaries. This yields [6]:

$$A_{\ell m}^{\vec{k}+\vec{G}}=\frac{4\pi i^\ell e^{i(\vec{k}+\vec{G})\vec{r}}}{\Omega^{1/2}u_\ell(\vec{R}_\alpha)}j_\ell(|\vec{k}+\vec{G}|R_\alpha)Y_m^{\ell*}(\vec{k}\hat{+}\vec{G}) \tag{4.4}$$

where the coefficient of each ℓm is matched at the spherical boundary and the origin is taken at the center of the sphere. The variational coefficients $c_{\vec{G}}^{n,\vec{k}}$ uniquely determine the wave-function in the interstitial region. The individual functions, which are labeled by $\vec{G}$ and consist of single plane-waves in the interstitial matched to radial functions in the spheres, are the augmented plane-waves (APWs) [1].

The APW method can be expected to give meaningful results in a wide variety of applications, but it is not the best method to use for all crystals. One of the main advantages of this method has been its applicability to a wide variety of materials, such as the NFE (nearly free electron) crystals and those containing transition elements. Whereas the APW method does not require the difficult separation of the electrons in a crystal containing *d* states into core and itinerant electrons. All that is required in this method is the total electronic charge density based on atomic self-consistent-field calculations which are readily available [4,7].

This formulation of MT approximation is provides a relatively satisfactory description for a faces centered cubic close-packed (*fcc*) structure or a hexagonal close-packed (*hcp)*. It is less good but still reasonable for cubic centered systems (*bcc*) and materials related to this

structure type [1,8]. However, this model becomes increasingly less reliable as the site symmetry and coordination decrease. Furthermore, the APWs are solutions of the Schrodinger's equation inside the spheres, but only at the energy E_ℓ; they lack variational freedom to allow for changes in the wave-function as the band energy deviates from this reference. Accordingly, E_ℓ must be set equal to the band energy. This means that the energy bands (at a fixed k-point) cannot be obtained from a single diagonalization (this is prohibitively expensive for many bands). Rather, it is necessary to solve the secular determinant as a function of energy. Another difficulty with this method is that related to $u_\ell(R_\alpha)$ function, which appears in the denominator of $A_{\ell m}^{\vec{k}+\vec{G}}$ expression (Eqn. 3.4). Indeed, there are in general values of the energy parameter, E_ℓ for which u_ℓ vanishes on the sphere boundary, causing separation of radial functions with respect to plane wave functions. This is the so called asymptote problem.

A more flexible and accurate band structure method in which the basis functions and their derivatives are made continuous by matching to a radial function at fixed E_ℓ plus its derivative with respect to E_ℓ, is the LAPW method.

4.3. The FP-LAPW method

4.3.1. The LAPW Basis functions

To avoid the problems connected with the APW method resulting from the energy dependence of the Hamiltonian, in 1975, linearized methods were invented by Andersen [9] and Koelling and Arbman [10] as a modification of this method, which is not practical for more than simple solids. Based on an idea proposed by Marcus [11], the basis functions u_ℓ in the muffin-tins were supplemented by their energy derivatives $\dot{u}_\ell$, but both, u_ℓ and $\dot{u}_\ell$, are now evaluated at a fixed energy E_ℓ. Effectively, a development of $u_\ell(r)$ to the first order around at some energy E_ℓ brought sufficiency the flexibility to the base in order to obtain all the eigenvalues in a single diagonalization. This gave birth to the Linearized APW (LAPW).

If the radial functions $u_\ell(r)$ was calculated at the fixed energy $E_\ell$which differs slightly from the band energy, ϵ, we could make a Taylor expansion to find it at energies not far away from it:

$$u_\ell(r,\ \epsilon) = u_\ell(r,\ E_\ell) + (\epsilon - E_\ell)\dot{u}_\ell(r,\ \epsilon) + O(\epsilon - E_\ell)^2 \tag{4.5}$$

where $\dot{u}_\ell(r,\ \epsilon) = \frac{\partial u_\ell(r,\epsilon=E_\ell)}{\partial \epsilon}$ and $O(\epsilon - E_\ell)^2$ denotes errors that are quadratic in this energy difference. The radial functions $u_\ell(r)$ are defined exactly as in the APW method (Eqn. 2), with a fixed E_ℓ . The energy derivative, $\dot{u}_\ell(r)$ satisfies:

$$\left[-\frac{\hbar^2}{2m_e}\frac{d^2}{dr^2} + \frac{\hbar^2}{2m_e}\frac{\ell(\ell+1)}{r^2} + V(r) - E_\ell\right] r\dot{u}_\ell(r) = r u_\ell(r) \tag{4.6}$$

These functions are matched to the values and derivatives of the plane-waves on the sphere boundaries. Plane-waves, augmented in this way, are the LAPW basis functions or LAPWs. Substituting the first two terms of the expansion in the APW wave-functions (Eqn. 2) for a fixed E_ℓ gives the definition of the LAPW wave-functions:

$$\varphi_{\vec{G}}^{\vec{k}}(\vec{r}) = \begin{cases} \Omega^{-1/2} e^{i(\vec{k}+\vec{G})\vec{r}} & , \quad \vec{r} \in I \\ \sum_{\ell m}\left[A_{\ell m}^{\vec{k}+\vec{G}} u_\ell(r) + B_{\ell m}^{\vec{k}+\vec{G}} \dot{u}_\ell(r)\right] Y_m^\ell(\hat{r}) & , \quad \vec{r} \in S_\alpha \end{cases} \tag{4.7}$$

where the $B_{\ell m}^{\vec{k}+\vec{G}}$ are coefficients for the energy derivative, analogous to the $A_{\ell m}^{\vec{k}+\vec{G}}$. These coefficients ($A_{\ell m}^{\vec{k}+\vec{G}}$ and $B_{\ell m}^{\vec{k}+\vec{G}}$) are determined by matching the value and derivative of the basis functions at the sphere boundary (i.e. they are chosen to make the basis functions continuous and differentiable at the sphere boundaries). The linear combination of the augmenting functions $u_\ell(r)Y_m^\ell(r)$ and $\dot{u}_\ell(r)Y_m^\ell(r)$, constitute the so called "linearization" of the radial function. $u_\ell(r)$ and $\dot{u}_\ell(r)$ are obtained by numerical integration of the radial Schrödinger equation on a radial mesh inside the sphere.

The LAPWs are just plane-waves in the interstitial region, as in the APW method. Inside the spheres, the wave-function and the band energy are obtained at the cost of very small errors of order $(\epsilon - E_\ell)^2$ and $(\epsilon - E_\ell)^4$, respectively. Despite that, this is an enormous simplification over the standard APW method, because the LAPWs form a good basis set over a relatively large energy region, so that all valence bands (at a given *k*-point) may typically be treated with a single set of E_ℓ and therefore with a single diagonalization.

The asymptote problem found in the APW method is now overcome by the presence of the non-zero $\dot{u}_\ell(R_\alpha)$ value. This, ensure that the plane wave and radial functions do not decouple. Moreover, the LAPWs have more flexibility than APWs inside the spheres. This flexibility is due to the presence of two radial functions ($u_\ell Y_m^\ell$ and $\dot{u}_\ell Y_m^\ell$) instead of one. There is however, a price to be paid for the additional flexibility of the LAPWs: the basis functions must have continuous derivatives and consequently higher plane-wave cut-offs are required to achieve a given level of convergence.

In this method, no muffin-tin or other approximations are made to the charge density or potential. Consequently, such a procedure is often called "Full-Potential LAPW" (FP-LAPW) [12,13]. Because of the greater flexibility of this method, there is no difficulty in treating the non-spherical potentials inside the spheres.

Thus, the efficiency of the LAPW method, which is derived from its use of carefully chosen representations of the wave functions in different regions, made it as the method of choice for accurate electronic structure calculations for materials containing transition metal and rare-earth atoms. Effectively, with this method, rapid variations of the wave functions inside the spheres pose no particular problems, and accordingly the method is well suited to all-electron calculations as well as *d*- and *f*-electron materials [1]. Furthermore, the widespread availability of high quality, user-friendly LAPW codes, like WIEN2k [14], has made it a very popular method for first principles studies of materials. However, it is not without certain shortcomings. Other modifications of the LAPW augmentation have been studied proposed by Takeda and Kubler [15], Smrcka [16], Petru and Smrcka [17] and Shaughnessy *et al.* [18], in order to improve the accuracy of calculations for valence states in systems without the semi-core problem mentioned in the following.

The convergence of a plane-wave basis set is controlled by the cut-off parameter G_{max}. It is not incorrect to use the same criteria for APW and LAPW basis sets, but it is more accurate in the context of these formalisms to consider the product $R_{mt}.G_{max}$, which determines the matrix-size of the system (usually, it assumes values in between 6 and 9), where, the R_{mt} is the smallest muffin-tin radius in the unit cell and G_{max} is the magnitude of the largest reciprocal lattice vector (plane wave cut-off). Compared to a plane wave basis set, the LAPW basis set can be much smaller.

4.3.2. Semi-core states problem

The LAPW is among the most accurate generally applicable techniques. It has been used extensively in electronic structure and total energy calculations in solids. Its role is to obtain accurate energy bands near the linearization energies, E_ℓ. In most materials, simply choose the energies E_ℓ near centers of the bands of interest to be assured of reasonable results. However, this is not always possible, and there are important classes of materials for which there is no single choice of the E_ℓ, and therefore the energy region of interest may be divided into a few (very rarely more than 2) windows and separate solutions carried out for each. A common example arises in the early transition metals [19,20], as well as in 4*f* and 5*f* materials

[21,22]. The reason for this is related to the presence of high lying and extended core states (*e.g.* the 5*p* state in the 4*f* elements) which called also semi-core states (intermediate between valence and core states) in many elements, particularly, the alkali metals, the rare earths, the early transition metals and the actinides. This major problem due to the fact that LAPW method requires non-overlapping spheres, and therefore, the augmenting functions, $u_\ell Y_m^\ell$ and $\dot{u}_\ell Y_m^\ell$, are orthogonal to any core state that is strictly confined within the MT sphere. However, for these elements there are extended core states that are not close enough to zero on the sphere boundary to have the $u_\ell Y_m^\ell$ and $\dot{u}_\ell Y_m^\ell$ orthogonal to them. On the other hand, the valence states may have significant contributions from the same ℓ (Azimuthal quantum number), and therefore there is a risk of confusing the semi-core states with the valence states (*e.g.*, the core states 3*p* extended outside the sphere MT and 4*p* states in the valence region in the copper atoms). This problem is encountered in particular when short bond distances do not allow sufficiently enlarge the sphere MT. There are two common approaches for treating these situations: (i) the use of multiple energy windows and (ii) Relaxation of the linearization using local orbitals.

4.3.2.1. Multiple energy windows

The first method consists to divide the energy spectrum into windows (sometimes called panels) and use a separate set of E_ℓ, in each window. In the two window treatment [23], a division is made into semi-core and valence energy regions (Figure 4.2). Separate calculations are then performed for the two windows where a set of E_ℓ is selected for each window to treat the corresponding states and the relevant bands are used to construct semi-core and valence charge densities. This amounts to two independent LAPW calculations, but always with the same potential.

Although this approach does solve many of the problems associated with the linearization and permits full relaxation of semi-core states, it is not fully satisfactory. First of all, there is a substantial overhead because separate calculations are being done for each window. Other problem with the treatment of semi-core states using multiple windows is that the semi-core states often satisfy the condition of orthogonality poorly even when the largest sphere radii consistent with the crystal structure are chosen. The result is the sufficient overlap between the LAPWs and core state, and the so-called "ghost" band will occurs above the true core state [24, 25].

The ideal solution in such cases is to use the local orbital extension. However, this is not available in some codes. If this is the case, the best solution seems to be to set the sphere radius as large as possible.

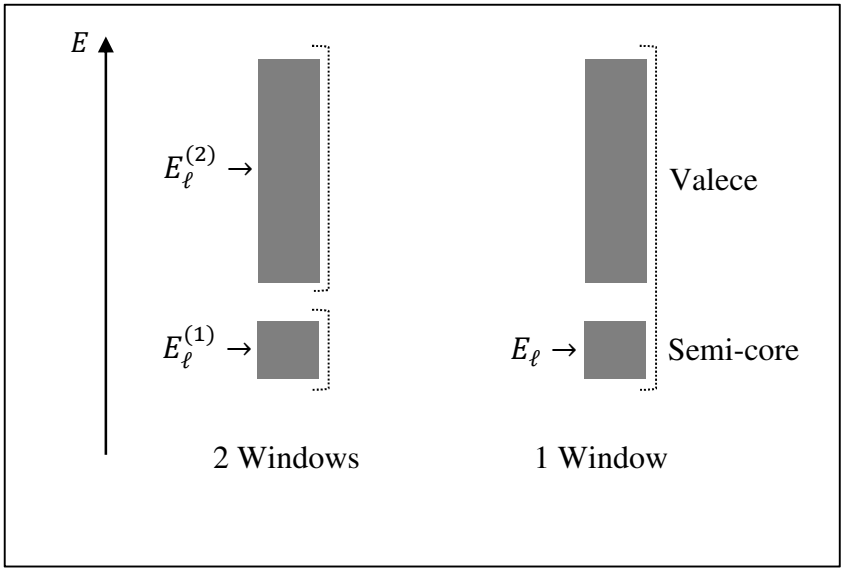

Fig. 4.2: Example of windows with a semi-core state. The E_ℓ corresponding to the semi-core angular momentum is set low in the single window case [1].

4.3.2.2. Local orbitals

4.3.2.2.1. LAPW+LO method

In order to avoid the problem of non-orthogonality that can occurs in calculations in which the semi-core states are either frozen or treated in separate energy windows, Singh, in 1991 [26] has modified this approach, where he saw that is necessary to extend the LAPW basis set with so called local orbitals (LO's). It is the so called LAPW+LO method. With such an extension, higher level semi-core states can be treated, together with the valence states, in one LAPW calculation instead of two (valence and semi-core states) energy windows. The extra basis functions (LOs) are entirely localized inside the muffin-tin spheres, i.e. their value and derivative falls to zero at the muffin-tin radius. Thus, no additional boundary conditions have to be satisfied. This can be achieved for certain ℓ values (*e.g.* those corresponding to semi-core state) via a linear combination including three radial functions, the standard LAPW

functions u_ℓ and $\dot{u}_\ell$, with as linearization energy $E_{1,\ell}$ a value suitable for the highest valence state, plus a further radial function $u_\ell^{(2)}$. This new radial function is constructed in the same way as u_ℓ, but with a different energy parameter $E_{2,\ell}$, which is suitable for the lowest valence state, that is much more free atom-like. Local orbitals are not connected to plane waves in the interstitial region; they have hence no $\vec{k}$- or $\vec{G}$-dependence. A local orbital then is defined for a particular ℓ and m, and for a particular atom as:

$$\varphi_{\ell m}^{LO}(\vec{r}) = \begin{cases} 0 & \vec{r} \in I \\ \left[A_{\ell m}^{LO} u_\ell\left(r, E_{1,\ell}\right) + B_{\ell m}^{LO} \dot{u}_\ell\left(r, E_{1,\ell}\right) + C_{\ell m}^{LO} u_\ell^{(2)}\left(r, E_{2,\ell}\right)\right] Y_m^\ell(\hat{r}), & \vec{r} \in S_\alpha \end{cases} \quad (4.8)$$

where the three coefficients $A_{\ell m}^{LO}$, $B_{\ell m}^{LO}$ and $C_{\ell m}^{LO}$ are determined by requiring that the LO is normalized, and has zero value and zero slope at the muffin tin boundary. The LO is then added to usual LAPW basis set in equation (4.7). In practice the number of local orbitals needed is much smaller than the number of plane-waves which equal a few hundred functions (*e.g.* for *s* and *p* semi-core states, four local orbitals per atom would be used). Thus the convergence of the local orbital extension is practically the same as that of the standard LAPW method. The slightly increased computational time is a small price to be paid for the much better accuracy that local orbitals offer, and therefore they are always used[1] [5].

3.3.2.2.2. APW+lo method

Despite the problem of the energy dependence of the basis set, which encountered in the APW method, was removed in the LAPW method, the drawback of the latter is the slower convergence of the results (e.g. eigenvalues) with respect to the number of basis functions that are used in the calculation. The condition of continuous first derivative at the muffin-tin boundary made the LAPW basis functions "stiffer" as compared to the APW's. An alternative approach of the LAPW method, which combines the advantages of the APW and LAPW methods, and which is shown to be highly effective in reducing the basis set sizes, has been proposed by Sjöstedt *et al* [6], namely APW+lo method. The new basis set APW+lo was defined by the combination of two types of wave functions: (i) the standard APW's (Eqn. 4.2), but at a fixed energies E_ℓ to avoid the non-linear eigenvalue problem. However, it does not give a good description of the eigen-functions. This basis set is therefore augmented,

[1] Local orbitals can also be used beyond the Treatment of semi-core states to improve the base with respect to the conduction bands. This improvement of the LAPW method is at the origin of the success of the linearization method based on the LAPW method Insofar as it allows extending this original method to a much broader category of compounds.

within the muffin-tin spheres, with a few of the second type functions: (ii) the *local orbitals*, but another type as the one used in the LAPW+LO method (they are abbreviated as "lo" instead of as "LO"). They are defined as:

$$\varphi_{\ell m}^{lo}(\vec{r}) = \begin{cases} 0 & , \quad \vec{r} \in I \\ \left[A_{\ell m}^{lo} u_\ell\left(r, E_{1,\ell}\right) + B_{\ell m}^{lo} \dot{u}_\ell\left(r, E_{1,\ell}\right)\right] Y_m^\ell(\hat{r}) & , \quad \vec{r} \in S_\alpha \end{cases} \tag{4.9}$$

The local orbitals are evaluated at the same fixed energy as the corresponding APWs. The two coefficients $A_{\ell m}^{lo}$ and $B_{\ell m}^{lo}$ are determined by normalization, and by requiring that the local orbital has zero value at the muffin tin boundary (not zero slope). It was demonstrated that this new scheme can reach the same accuracy as LAPW but converges faster with respect to the number of basis functions. The smaller basis set and faster matrix set up of APW+lo offers a shorter run-time and uses less memory than LAPW. Then it is favorable for selected atoms and ℓ, to use local orbitals to go back to the APW method, especially for *d*- and *f*-states, and structures with atoms that have a muffin-tin sphere much smaller than others spheres in the unit cell (like O or N) [27].

As the two basis sets, APW+lo and LAPW consist of the same functions u_ℓ and $\dot{u}_\ell$ and could easily be mixed in the same code, it is advantageous to treat those states which are difficult to converge with APW+lo, and keep using LAPW for all other states, *e.g.* calculations for a molecular reaction on a metal surface could be performed with an APW+lo basis set for the adsorbate and a well-tested LAPW treatment for the substrate [6].

4.3.3. The Concept of FP-LAPW method

The full-potential LAPW method (FP-LAPW) [12,13] combines the choice of the LAPW basis set with the treatment of the full-potential and charge density without any shape approximations in the interstitial region and inside the muffin-tins. This generalization is achieved by relaxing the constant interstitial potential $V_I^0$and the spherical muffin-tin approximation $V_{MT}^0(\vec{r})$ due to the inclusion of a warped interstitial and the non-spherical terms inside the muffin-tin spheres. They are developed into harmonics of the lattice within each atomic sphere, and into Fourier series in the interstitial regions:

$$V(\vec{r}) = \begin{cases} \sum_{\vec{G}} V_I^{\vec{G}} e^{\vec{G}\vec{r}} & , \quad \vec{r} \in I \\ \sum_{\ell m} V_{MT}^{\ell m}(\vec{r}) Y_m^\ell(\hat{r}) & , \quad \vec{r} \in S_\alpha \end{cases} \tag{4.10}$$

This method became possible with the development of a technique for obtaining the Coulomb potential for a general periodic charge density without shape-approximations and with the inclusion of the Hamiltonian matrix elements due to the warped interstitial and non-

spherical terms of the potential. The charge density ρ, is represented analogously to Eqn. 4.10, just exchanging V by ρ:

$$\rho(\vec{r}) = \begin{cases} \sum_{\vec{G}} \rho_I^{\vec{G}} e^{\vec{G}\vec{r}} & , \quad \vec{r} \in I \\ \sum_{\ell m} \rho_{MT}^{\ell m}(\vec{r}) Y_m^{\ell}(\hat{r}) & , \quad \vec{r} \in S_\alpha \end{cases} \tag{4.11}$$

References

[1] D. J. Singh, L. Nordström, *Planewaves, Pseudopotentials, and the LAPW Method*, 2nd Ed, Springer Science + Business Media, Inc., USA, 2006.

[2] J. C. Slater, *Wave Functions in a Periodic Potential*, Phys. Rev. 51, 846-851 (1937).

[3] J. C. Slater, *Energy Band Calculations by the Augmented Plane Wave Method*, Advances in Quantum Chemistry 1, 35-58 (1964).

[4] T. L. Loucks, *The Augmented Plane Wave Method*, W. A. Benjamin, Inc., New York, 1967.

[5] S. Cottenier, *Density Functional Theory and the Family of (L)APW-methods: a step-by-step introduction*, Ghent University, Belgium, 2013.

[6] E. Sjöstedt, L. Nordström, D.J. Singh, *An alternative way of linearizing the augmented plane-wave method*, Solid State Communications 114, 15-20 (2000).

[7] D. Liberman, J. T. Waber, D. T. *Cromer, Self-Consistent-Field Dirac-Slater Wave Functions for Atoms and Ions*, Phys. Rev. 137, A27-A34 (1965).

[8] N. Elyashar, D. D. Koelling, *Effect of non-muffin-tin terms on the electronic structure of transition metals Niobium*, Phys. Rev. B 13, 5362-5372 (1976).

[9] O. K. Andersen, *Linear methods in band theory*, Phys. Rev. B 12, 3060-3083 (1975).

[10] D. D. Koelling and G. O. Arbman, *Use of energy derivative of the radial solution in an augmented plane wave method: application to copper*, J. Phys. F (Metal Phys.) 5, 2041-2054 (1975).

[11] P. M. Marcus, *Variational Methods in the Computation of Energy Bands*, Int. J. Quantum Chem. Suppl. 1, 567-588 (1967).

[12] D. R. Hamann, *Semiconductor Charge Densities with Hard-Core and Soft-Core Pseudopotentials*, Phys. Rev. Lett. 42, 662-665 (1979).

[13] E. Wimmer, H. Krakauer, M. Weinert, and A. J. Freeman, *Full-potential self consistent Linearized-augmented-plane-wave method for calculating the electronic structure of molecules and surfaces: O2 molecule*, Phys. Rev. B 24, 864-875 (1981).

[14] P. Blaha, K. Schwarz, G.K.H. Madsen, D. Kvasnicka, and J. Luitz, *WIEN2K, An Augmented Plane Wave + Local Orbitals Program for Calculating Crystal Properties*, K. Schwarz Techn, Universitat Wien, Austria, 2001, ISBN 3-9501031-1-2.

[15] T. Takeda and J. Kübler, *Linear augmented plane wave method for selfconsistent calculations,* J. Phys. F*:* Metal Phys. 9, 661-672 (1979).

[16] L. Smrcka, *Linearized augmented plane wave method utilizing the quadratic energy expansion of radial wave functions*, Czech J. Phys. B 34, 694-704 (1984).

[17] J. Petru and L. Smrcka, *Quadratic augmented plane wave method for self-consistent band structure calculations*, Czech J. Phys. B 35, 62-71 (1985).

[18] D. J. Shaughnessy, G. R. Evans and M. I. Darby, *An improved LAPW method for the calculation of self-consistent electronic band structures*, J. Phys. F 17, 1671-1679 (1987).

[19] P. Blaha, D. J. Singh, P. I. Sorantin and K. Schwarz, *Electric-field-gradient calculations for systems with large extended-core-state contributions*, Phys. Rev. B 46, 1321-1325 (1992).

[20] D. J. Singh, K. Schwarz and P. Blaha, *Electric-field gradients in YBa2Cu3O7: Discrepancy between experimental and local-density-approximation charge distributions*, Phys. Rev. B 46, 5849-5852 (1992).

[21] D. J. Singh, *Adequacy of the local-spin-density approximation for Gd*, Phys. Rev. B 44, 7451-7454 (1991).

[22] S. Goedecker and K. Maschke, *Alternative approach to separable first-principles pseudopotentials*, Phys. Rev. B 42, 8858-8863 (1990).

[23] J. Yu, A. J. Freeman, R. Podloucky, P. Herzig, and P. Weinberger, *Origin of electric-field gradients in high-temperature superconductors: $YBa_2Cu_3O_7$*, Phys. Rev. B 43, 532-541 (1991).

[24] L. F Mattheiss and D. R. Hamann, *Linear augmented-plane-wave calculation of the structural properties of bulk Cr, Mo, and W*, Phys. Rev B 33, 823-840 (1986).

[25] D. Singh and H. Krakauer, *H-point phonon in molybdenum: Superlinearized augmented-plane-wave calculations*, Phys. Rev. B 43, 1441-1445 (1991).

[26] D. Singh, *Ground-state properties of lanthanum: Treatment of extended-core states*, Phys. Rev. B 43, 6388-6392 (1991).

[27] G. K. H. Madsen, P. Blaha, K. Schwarz, E. Söstedt, and L. Nordström, *Efficient linearization of the augmented plane-wave method*, Phys. Rev. B 64, 195134-9 (2001).

PART II

Results and discussions

CHAPTER 5

Structural, elastic, electronic and optical properties of the quaternary diamond-like semiconductors Cu_2MgSiS_4 and Cu_2MgGeS_4

Chapter 5

Structural, elastic, electronic and optical properties of the quaternary diamond-like semiconductors Cu_2MgSiS_4 and Cu_2MgGeS_4

Contents

5.1. Computational details

In order to benefit of the advantages of available computational methods, two complementary first-principles approaches in the framework of density functional theory (DFT) were used to perform a complete investigation of the structural, elastic, electronic and optical properties of the quaternary diamond-like semiconductor compounds Cu_2MgSiS_4 and Cu_2MgGeS_4.

We have employed the first-principles pseudopotential plane-wave (PP-PW) method as implemented in the Cambridge Serial Total Energy Package (CASTEP) code [1] to determine the structural parameters and elastic moduli of the considered compounds. A new version of the generalized gradient approximation (GGA), namely the GGA-PBEsol [2], which has been developed specifically to improve the description of the exchange-correlation in solids, was used. Interactions of the valence electrons with the nucleus and frozen core electrons were modelled using Vanderbilt ultrasoft pseudopotentials [3]. The Cu: $3d^{10}4s^1$, Mg: $2p^6 3s^2$, Si: $3s^2 3p^2$, Ge: $4s^2 4p^2$ and S: $3s^2 3p^4$ orbitals were treated as valence electron states. A Plane-wave basis set cut-off of 450 eV and a Monkhorst–Pack mesh [4] of 9×10×11 for the *k*-points were chosen, after a convergence test, to ensure sufficiently accurate calculations. The optimized structural parameters were achieved via the Broyden-Fletcher-Goldfarb-Shanno (BFGS) minimization algorithm [5]. The fully optimized geometry was performed with the following convergence criteria: (i) total energy difference between two consecutive iterations were smaller than 5.0×10^{-6} eV/atom, (ii) maximum force on any atom was smaller than 0.01 eV/Å^{-1}, (iii) stress was smaller than 0.02 GPa and (iv) atomic displacement was smaller than 5.0×10^{-4} Å.

The single-crystal elastic constants C_{ij}s were determined via a linear fitting of the stress-strain curves obtained from first-principles calculations [1]. The elastic constants were performed with the following convergence criteria: 1.0×10^{-6} eV/atom for total energy, 0.002 eV/Å for Hellman-Feynman force and 1.0×10^{-4}Å for maximal ionic displacement. The polycrystalline aggregate elastic moduli, namely the bulk modulus *B* and shear modulus *G*, were evaluated via the Voigt-Reuss-Hill approximations [6-8].

The electronic band structure and associated density of states and the optical properties of the title crystals were studied using the full-potential linearized augmented plane-wave (FP-LAPW) approach as implemented in the WIEN2K package [9] with the newly developed Tran-Blaha modified Becke-Johnson potential [10], denoted TB-mBJ, for the exchange-correlation potential. The TB-mBJ exchange potential was developed from a

semi-classical exchange potential proposed by Becke and Johnson [11] to reproduce the shape of the exact-exchange optimized-effective potential of atoms. The TB-mBJ functional, resulting from the combination of the mBJ exchange with the LDA or GGA correlation, describes better the exchange-correlation potential than the standard LDA and GGA, known by their serious underestimation of the band gaps [12-14]. The FP-LAPW method with the TB-mBJ potential has proven to be a promising tool for an accurate determination of the electronic structure for a large family of semiconductors and isolators [15]. In the FP-LAPW method, the unit-cell of the crystal is partitioned into non-overlapping muffin-tin spheres, which surround each atom, separated by an interstitial region. The muffin-tin sphere radii are as large as possible without overlapping spheres. The wave functions are expanded in spherical harmonics with an $l_{\max}$ cut-off inside the muffin-tin spheres and Fourier series in the interstitial region with a plane wave cut-off defined by the $K_{max}R_{MT}$ parameter, where R_{MT} is the smallest muffin-tin sphere and $K_{\max}$ is the largest reciprocal lattice vector used in the plane wave expansion. The MT sphere radii are chosen to be 2.34 Bohr for Cu, 2.36 Bohr for Mg, 1.91 Bohr for S and 1.92 Bohr for Si and Ge. The basis set cut-off parameters $K_{max}R_{MT}$ and l_{max} were 8 and 10, respectively. The k integrations over the Brillouin zone (BZ) were performed up to 8×10×10 Monkorst-Pack mesh [4]. The self-consistent procedure was continued until the difference between the total energies in two successive iterations was less than10^{-5} Ry. A dense mesh of uniformly distributed k-points in the Brillouin zone is required to calculate the dielectric function, optical constants and density of states. Hence, for these properties, the Brillouin zone integration was performed using a 30x30x30 Monkhorst-Pack mesh. Details about the calculations of the optical properties can be found elsewhere [16]. The theoretical expression of the dielectric function yields an unbroadened spectrum that will have more structures than the experimental one. To facilitate a comparison with the expected experimental findings, the calculated dielectric function has been broadened with a broaden parameter equal to 0.1.

5.2. Results and discussion

5.2.1. Structural properties

5.2.1.1. Structural description

The quaternary diamond-like semiconductor compounds Cu_2MgSiS_4 and Cu_2MgGeS_4 have an orthorhombic structure and belong to the $Pmn2_1$ space group (no. 31), with three inequivalent S atoms. One conventional cell of the Cu_2MgSiS_4 crystal is depicted in Fig. 5.1 as a prototype. The conventional cell of Cu_2MgXS_4 (X = Si, Ge) contains 16 atoms, 4Cu, 2Mg, 2X and 8S. The atomic positions are Cu: $4b\ (x_{Cu}, y_{Cu}, z_{Cu})$, Mg: $2a\ (0, y_{Mg}, z_{Mg})$, X: $2a\ (0, y_X, z_X)$, S1: $4b\ (x_{S1}, y_{S1}, z_{S1})$, S2: $2a\ (0, y_{S2}, z_{S2})$ and S3: $2a\ (0, y_{S3}, z_{S3})$. This means that the unit cell of Cu_2MgXS_4 contains two unit formulas (Z = 2). The atoms are indexed in order to distinguish between the inequivalent crystallographic positions of the same chemical element. So, the crystalline structures of the title compounds are characterized by 17 parameters not fixed by the group symmetry, 14 atomic coordinates and three lattice parameters. All the atoms have normal tetrahedral coordinates, where every atom has four nearest neighbor atoms located approximately at the corners of a surrounding tetrahedron. Every silicon (Si) or germanium (Ge) atom is surrounded by four sulfur (S) atoms, forming SiS_4 or GeS_4 units (Fig. 5.2); every sulfur atom has four nearest neighbor atoms: two copper (Cu) atoms, one magnesium (Mg) atom and one X atom (either Si or Ge atom).

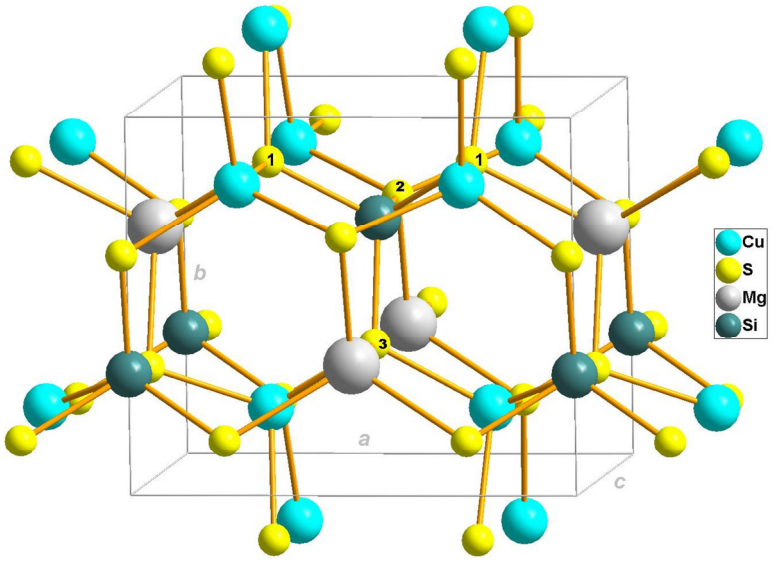

Fig. 5.1: Conventional cell structure of the orthorhombic Cu_2MgSiS_4 compound as a prototype.

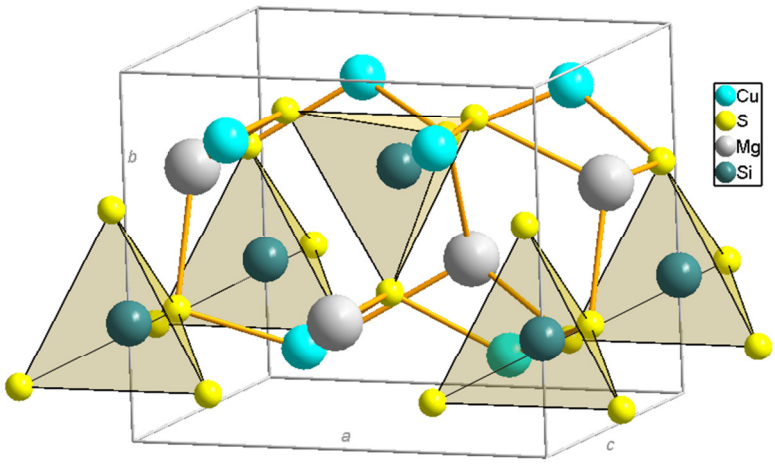

Fig.5.2: Illustration of the tetrahedral centered by Si atom, surrounded by four atoms of S in the Cu_2MgSiS_4 compound.

5.2.1.2. Equilibrium structural properties

The calculated equilibrium lattice parameters, atomic coordinates and interatomic bond-lengths for the title compounds are summarized in Tables 5.1, 5.3 and 5.4, respectively, compared with the available experimental data. Our results are in good agreement with the existing experimental data.

Table 5.1: Calculated lattice parameters (a_0, b_0 and c_0, in Å), unit-cell volume (V_0, in Å^3), cohesive energy (E_{coh}, in eV/atom) and formation enthalpy (E_{form}, in eV/atom) for the orthorhombic quaternary diamond-like Cu_2MgSiS_4 and Cu_2MgGeS_4 compared with the available experimental data

Property	**Cu_2MgSiS_4**		**Cu_2MgGeS_4**	
	Present	Expt. [17]	Present	Expt. [17]
a_0	7.5396	7.563	7.6142	7.638
b_0	6.3544	6.448	6.4580	6.515
c_0	6.1417	6.179	6.2044	6.225
V_0	294.25	301.3	305.09	309.8
E_{coh}	-4.93		-4.71	
E_{form}	-1.20		-1.08	

The relative deviations of the computed lattice parameters a_0, b_0 and c_0 from the measured ones are -0.30% (-0.31%), -1.46% (-0.87%) and -0.60% (-0.34%), respectively, in Cu_2MgSiS_4 (Cu_2MgGeS_4), which make a firm basis for reliability of the subsequent analysis of the elastic, electronic and optical properties of these materials. In order to compare the structures of our studied compounds with other Cu_2-II-IV-S_4 (II = Zn, Cd and Hg; IV = Si, Ge and Sn) quaternary diamond-like semiconductors, we have listed in Table 5.2 the lattice constants and the unit cell volume of each compound.

Table 5.2: Experimental Lattice constants (*a*, *b*, and *c* in Å) and the unit cell volume (in $Å^3$) of some Cu_2-II-IV-S_4 (II = Mg, Zn, Cd and Hg; IV = Si, Ge and Sn) quaternary diamond-like compounds

Compound	Cu_2MgSiS_4	Cu_2ZnSiS_4	Cu_2CdSiS_4	Cu_2HgSiS_4
Structure	$Pmn2_1$ [17]		$Pmn2_1$ [18,19]	
a	7.563	7.435	7.614	7.592
b	6.448	6.396	6.489	6.484
c	6.179	6.135	6.254	6.269
V	301.3	291.8	309	308.6
Compound	Cu_2MgSiS_4	Cu_2ZnGeS_4	Cu_2CdGeS_4	Cu_2HgGeS_4
Structure	$Pmn2_1$ [17]		$Pmn2_1$ [18]	
a	7.638	7.504	7.692	7.679
b	6.515	6.474	6.555	6.522
c	6.225	6.185	6.299	6.325
V	305.1	300.6	317.6	316.8
Compound	Cu_2MgSnS_4	Cu_2ZnSnS_4	Cu_2CdSnS_4	Cu_2HgSnS_4
Structure	-		$I\bar{4}2m$ [19]	
a	-	5.427	5.586	5.566
b	-	-	-	-
c	-	10.848	10.834	10.88
V	-	319.6	338	337.2

The volume calculated of the unit cell is slightly lower than that of experimental data of about 2.36% and 1.52%, respectively for Cu_2MgSiS_4 and Cu_2MgGeS_4. This is due to the fact that our values are calculated at 0 K, while the experimental values are taken at ambient temperature (the volume increases when the temperature increases). We note that the conventional cell volume of Cu_2MgGeS_4 is larger by approximately 3.60% than that of Cu_2MgSiS_4, which can be attributed to the fact that the Ge atom radius is larger than that of Si atom. Same trend was observed in other Cu_2-II-IV-S_4 (II = Zn, Cd and Hg; IV = Si, Ge and Sn) quaternary diamond-like compounds (see Table 5.2) [17-19], i.e., the unit-cell volume of quaternary diamond-like compounds Cu_2-II-IV-S_4 increases when moving down in the column IV of the periodic table, as shown in Fig. 5.3.

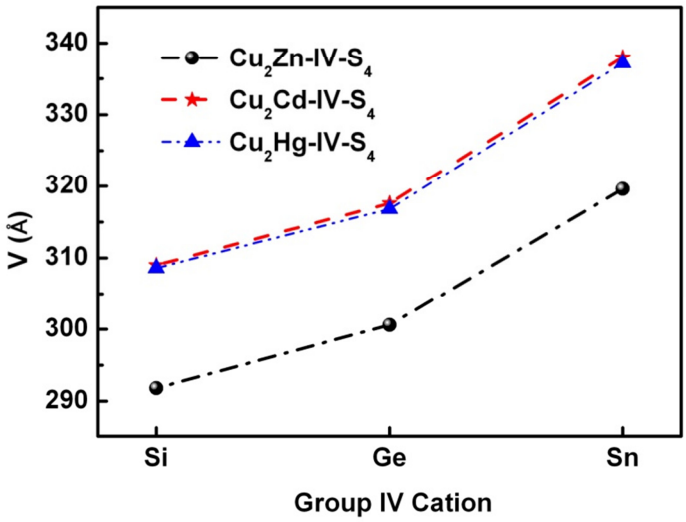

Fig. 5.3: Variation of the unit-cell volume for some Cu_2-II-IV-S_4 quanternary diamond-like compounds with respect to the chemical nature of the IV cation at ambient temperature.

Calculated values for the atomic positions (Table 5.3) deviate by 0.04% to 7.3% from the experimental values, with the exception of the z coordinate of Ge in Cu_2MgGeS_4 unit cell, which deviate by 75% from its experimental value. With respect to the bond lengths between atoms, the difference between our results and those of experience does not exceed 2.5% (Table 5.4). We note that our calculation of (Si,Ge)-S and Mg-S bond lengths are slightly

larger than those of the experimental data, while the calculation of Cu-S bond lengths are slightly lower than those of the experimental data.

Table 5.3: Calculated atomic coordinates for the Cu_2MgSiS_4 and Cu_2MgGeS_4 crystals compared with the available experimental findings

Atom	W.S.	Present work			Expt. [17]		
		x/a	*y/b*	*z/c*	*x/a*	*y/b*	*z/c*
Cu_2MgSiS_4							
Cu	4*b*	0.25207	0.17783	0.49330	0.25258	0.17753	0.4935
Mg	2*a*	0	0.65648	0.50303	0	0.6544	0.5008
Si	2*a*	0	0.32009	0.00099	0	0.3227	0.0010
S(1)	4*b*	0.22842	0.15832	0.12669	0.2286	0.1643	0.1210
S(2)	2*a*	0	0.29907	0.65118	0	0.3083	0.6574
S(3)	2*a*	0	0.64466	0.09991	0	0.6368	0.1078
Cu_2MgGeS_4							
Cu	4*b*	0.25114	0.17519	0.49536	0.25186	0.17587	0.49469
Mg	2*a*	0	0.66115	0.50297	0	0.6609	0.4996
Ge	2*a*	0	0.32311	0.00142	0	0.3246	0.0008
S(1)	4*b*	0.23565	0.15304	0.13195	0.2345	0.1606	0.1266
S(2)	2*a*	0	0.30386	0.63741	0	0.3117	0.6455
S(3)	2*a*	0	0.65844	0.10365	0	0.6487	0.1116

W.S.: Wyckoff site

The thermodynamic and chemical stabilities of the Cu_2MgSiS_4 and Cu_2MgGeS_4 compounds can be judged from their cohesive energies E_{coh} and formation enthalpies E_{form}. The first represents the energy that is required for the crystal to decompose into free atoms, while the second is the difference between the total energies of pure constituent elements in their stable crystal structures and the total energy of the compound. They are calculated for the studied compounds by using the following expression, respectively:

$$E_{coh} = \frac{1}{8}[E(\mathrm{Cu_2MgXS_4}) - 2E_a(\mathrm{Cu}) - E_a(\mathrm{Mg}) - E_a(\mathrm{X}) - 4E_a(\mathrm{S})] \quad (5.1)$$

$$E_{form} = \frac{1}{8}[E(\mathrm{Cu_2MgXS_4}) - 2E_s(\mathrm{Cu}) - E_s(\mathrm{Mg}) - E_s(\mathrm{X}) - 4E_s(\mathrm{S})] \quad (5.2)$$

where $E(\mathrm{Cu_2MgXS_4})$ represents the total energy of Cu_2MgXS_4 molecule; $E_a(\mathrm{X})$ refers to the total energy of an isolated X atom and $E_s(\mathrm{S})$ is the total energy per atom of pure element X, in

solid phase. The energy of the free atom was calculated using a cubic box with a large lattice constant. As can be seen from Table 5.1, both considered compounds have negative cohesive energies and formation enthalpies, indicating that they are energetically stable.

Table 5.4: Calculated bond lengths (*d*, in Å) and bond stiffness (*k*, in GPa) for some bonds in the Cu_2MgSiS_4 and Cu_2MgGeS_4 compounds. The bond stiffness *k* is given by the inverse of the first pressure derivative ($1/|\alpha|$), where α is the first pressure derivative of the bond-length

Bond	**Cu_2MgSiS_4**			**Cu_2MgGeS_4**		
	Bond lengths		*k*	Bond lengths		*k*
	Present	Expt. [17]	Present	Present	Expt. [17]	Present
(Si/Ge)-S1	2.1491	2.143	390.6	2.2542	2.228	341.3
(Si/Ge)-S2	2.1526	2.120	387.6	2.2619	2.213	325.7
(Si/Ge)-S3	2.1501	2.131	366.3	2.2565	2.221	306.7
Cu-S1	2.2621	2.310	238.1	2.2623	2.297	235.8
Cu-S1	2.2925	2.345	260.4	2.2850	2.343	263.2
Cu-S2	2.2684	2.321	253.2	2.2636	2.316	246.9
Cu-S3	2.2793	2.331	219.8	2.2796	2.330	219.8
Mg-S1	2.4808	2.476	228.3	2.4763	2.468	218.8
Mg-S2	2.4466	2.432	257.7	2.4535	2.450	231.5
Mg-S3	2,4769	2.431	227.3	2.4776	2.417	204.5

5.2.1.3. Equations of states and the pressure effect on the structural parameters

One of the more used methods to test the reliability of the obtained theoretical results consists of comparing between the numerical values of one property that are obtained via different theoretical procedures. For this issue, the bulk modulus *B* was used as a test parameter. For this purpose, the structural parameters of the studied compounds were calculated at fixed applied hydrostatic pressures in the range from 0 to 15 GPa with a step of 3 GPa; such an option is implemented in CASTEP code and permits for finding an optimized structure at any axial or hydrostatic pressure. First, the obtained unit-cell volume (V) versus pressure (P) and the associated total energy (E) versus unit-cell volume (V) were fitted to some different versions of the equation of state (EOS) [20-24]: the Birch-Murnaghan and Murnaghan *P-V* EOSs, given respectively by:

$$P(V)=\frac{3}{2}B_0\left[\left(\frac{V}{V_0}\right)^{-\frac{7}{3}}-\left(\frac{V}{V_0}\right)^{-\frac{5}{3}}\right]\cdot\left\{1+\frac{3}{4}(B'-4)\cdot\left[\left(\frac{V}{V_0}\right)^{-\frac{2}{3}}-1\right]\right\} \tag{5.3}$$

$$P(V)=\frac{B_0}{B'}\left[\left(\frac{V}{V_0}\right)^{-B'}-1\right] \tag{5.4}$$

and the Birch-Murnaghan, Murnaghan and Vinet *E-V* EOSs, given respectively by:

$$E(V)=E_0+\frac{9V_0B_0}{16}\left\{\left[\left(\frac{V}{V_0}\right)^{-2/3}-1\right]^3B'+\left[\left(\frac{V}{V_0}\right)^{-2/3}-1\right]^2\left[6-4\left(\frac{V}{V_0}\right)^{-2/3}\right]\right\} \tag{5.5}$$

$$E(V)=E_0+\frac{B_0V}{B'}\left[(V/V_0)^{-B'}\frac{1}{B'-1}+1\right]-\frac{B_0V_0}{B'-1} \tag{5.6}$$

$$E(V)=E_0+\frac{4V_0B_0}{(B'-1)^2}\left\{1-\left[\frac{3}{2}\left\{1-\left(\frac{V}{V_0}\right)^{1/3}\right\}(B'-1)\right].\exp\left[\frac{3}{2}(B'-1)\left\{1-\left(\frac{V}{V_0}\right)^{1/3}\right\}\right]\right\} \tag{5.7}$$

Fig. 5.4 visualizes the fits of the calculated $P(V)$ and $E(V)$ data to the $P(V)$ and $E(V)$ Birch-Murnaghan *EOS*s [20,22], respectively, as a prototype. One can appreciate the good fits of the calculated data to the mentioned *EOS*s. The obtained values for the bulk modulus B and its pressure derivative B' are reported in Table 5.5.

Table 5.5: Calculated bulk modulus (B_0, in GPa) and its pressure derivative B', for the orthorhombic quaternary diamond-like Cu_2MgSiS_4 and Cu_2MgGeS_4

Method	**Cu_2MgSiS_4**		**Cu_2MgGeS_4**	
	B	*B'*	*B*	*B'*
Birch Murnaghan *P-V* EOS [20]	82.28	4.24	78.27	4.22
Murnaghan *P-V* EOS [21]	82.76	4.00	78.76	3.96
Birch Murnaghan *E-V* EOS [22]	83.59	2.59	79.37	2.61
Murnaghan *P-V* EOS [23]	81.28	4.33	76.78	4.36
Vinet E-V EOS [24]	81.71	4.50	77.26	4.54
From β_Xs	82.03		78.99	
From β_V	82.24		79.11	

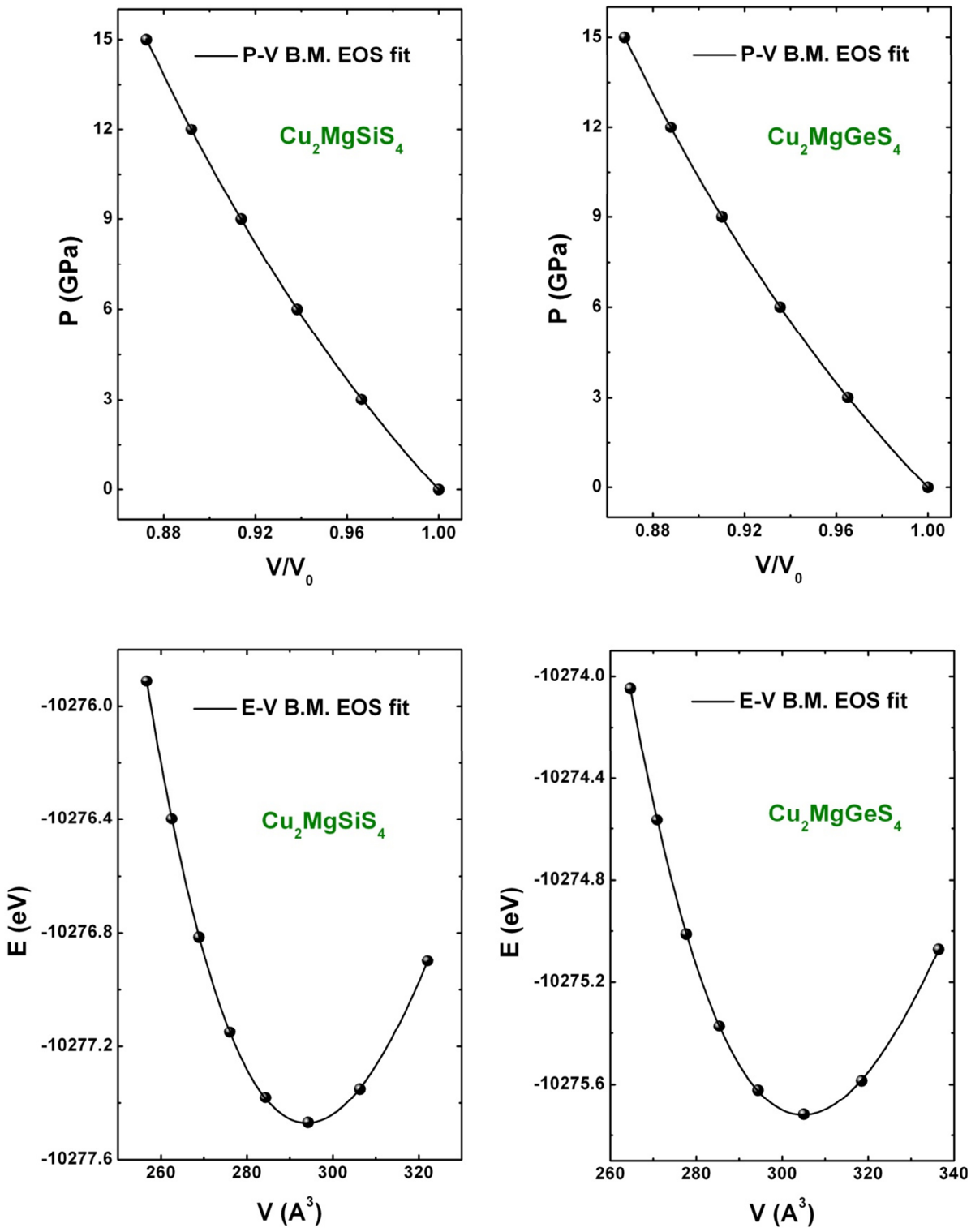

Fig. 5.4: Calculated pressure (P) and total energy (E) versus unit-cell volume V (symbols) and fits to Birch-Murnaghan equation of states (solid lines) for the Cu_2MgSiS_4 and Cu_2MgGeS_4 compounds.

Second, we have estimated the linear compressibilities along the *a*-axis, *b*-axis and *c*-axis, β_a, β_b and β_c, respectively, and the volume compressibility (β_V) for the studied materials by fitting the data of normalized lattice parameters ratio a/a_0, b/b_0 and c/c_0 and the normalized unit-cell volume ratio V/V_0 versus pressure to a third polynomial function given by the following expression (Figs. 5.5 and 5.6):

$$X / X_0 = 1 + \beta_X P + \sum_{n=2}^{3} K_n P^n \tag{5.8}$$

where *X* represents the lattice constants *a*, *b*, *c* and the volume *V* at a pressure *P*, and X_0 is the corresponding values at zero pressure. We can see from the Figs. 5 and 6 that a/a_0, b/b_0 and c/c_0 and V/V_0 decrease with increasing pressure according to the following expressions:

$$a / a_0 = 1 - 0.00360\,P + 6.98\times10^{-5} P^2 - 2.40\times10^{-7} P^3$$

$$b / b_0 = 1 - 0.00505\,P + 1.54\times10^{-4} P^2 - 4.08\times10^{-6} P^3$$

$$c / c_0 = 1 - 0.00354\,P + 9.48\times10^{-5} P^2 - 2.18\times10^{-6} P^3$$

$$V / V_0 = 1 - 0.01216\,P + 3.52\times10^{-4} P^2 - 7.42\times10^{-6} P^3$$

for Cu_2MgSiS_4, and:

$$a / a_0 = 1 - 0.00384\,P + 7.56\times10^{-5} P^2 - 6.29\times10^{-7} P^3$$

$$b / b_0 = 1 - 0.00492\,P + 1.07\times10^{-4} P^2 - 1.29\times10^{-6} P^3$$

$$c / c_0 = 1 - 0.00391\,P + 1.34\times10^{-4} P^2 - 3.89\times10^{-6} P^3$$

$$V / V_0 = 1 - 0.01264\,P + 3.54\times10^{-4} P^2 - 6.65\times10^{-6} P^3$$

for Cu_2MgGeS_4. The obtained linear compressibilities β_a, β_b and β_c, and the volume compressibility β_V were used to estimate the bulk modulus *B* as follows:

$$B = 1 / (\beta_a + \beta_b + \beta_c) \tag{5.9}$$

$$B = 1 / \beta_V \tag{5.10}$$

The obtained results are given in Table 5. One can appreciate the good agreement between the values of the bulk modulus *B* obtained from three different procedures, i.e., the linear compressibilities (β_a, β_b and β_c), the volume compressibility (β_V) and the *EOS*s fits. This constitutes a good proof for the reliability of our calculations.

Third, the obtained bulk modulus values at this step will be compared to the corresponding ones that will be achieved from the elastic constants later.

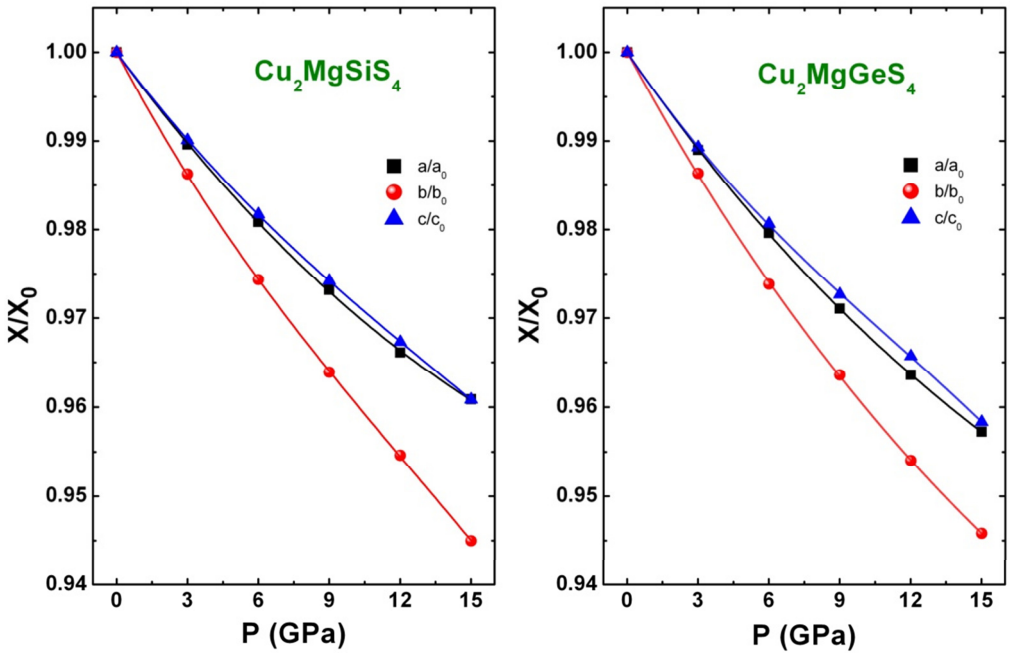

Fig. 5.5: Calculated pressure dependence of the normalized lattice parameters ratio, a/a_0, b/b_0 and c/c_0 (symbols) for the Cu_2MgSiS_4 and Cu_2MgGeS_4 compounds. The solid lines are least squares third-order polynomial fits of the data points.

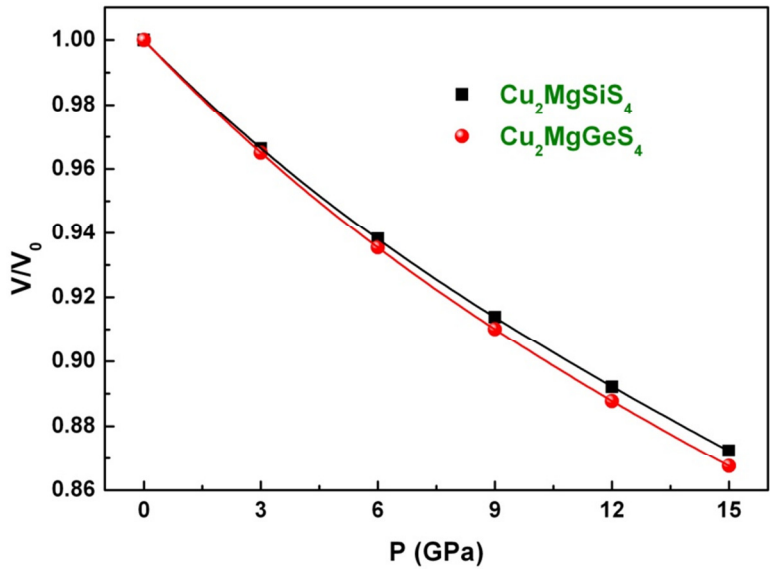

Fig. 5.6: Calculated pressure dependence of the normalized unit-cell volume V/V_0 for the Cu_2MgSiS_4 and Cu_2MgGeS_4 compounds. The solid lines are least squares third-order polynomial fits of the data points.

From Table 5.5, one can see that B_0 (Cu_2MgSiS_4) > B_0 (Cu_2MgGeS_4) of about 5%; knowing that the lattice volume of Cu_2MgGeS_4 is higher than that of Cu_2MgSiS_4, this is in good agreement with the well-known relation between the bulk modulus and the lattice volume $B \propto V^{-1}$. This means that Cu_2MgSiS_4 is slightly harder than Cu_2MgGeS_4. Effectively, one can see from Fig. 5.6 that Cu_2MgGeS_4 is slightly more compressible than Cu_2MgSiS_4. The bulk modulus value for the studied compounds (~ 80 GPa) is smaller than 100 GPa, so these two compounds should be classified as a relatively soft materials. We note that to date, no reported experimental or theoretical data in the scientific literature for the bulk moduli of the Cu_2MgSiS_4 and Cu_2MgGeS_4 compounds to be compared with our obtained results.

From Fig. 5.5, one can observe that the considered materials are less compressible along the [001] and [100] crystallographic directions than along the [010] direction, i.e., the largest compressibility is realized along the *b* crystallographic axis. These materials are slightly less compressible along the [001] direction than along the [100] direction, i.e., the smallest compression is exhibited along the *c*-axis. This result suggests that the chemical bonds along the *b*-axis are less strong than those along the *a*- and *c*-axes.

In order to have an insight on the stiffness of the Cu-S, Mg-S and Si/Ge-S bonds, we have calculated the pressure dependence of their relative length d/d_0 (where d_0 is the equilibrium bond length). The symbols in Fig. 5.7, shows the calculated d/d_0 data while the solid lines represent their fits to a second-order polynomial:

$$d/d_0 = 1 + \alpha P + \beta P^2 \qquad (5.11)$$

Calculated values of the bond stiffness *k*, which given by the inverse of the first pressure derivative ($1/|\alpha|$), where α is the first pressure derivative of the bond-length ($\alpha = dd/dP$) are listed in Table 5.4. From Fig. 5.7 and Table 5.4, it can be seen that Si/Ge-S bonds are the stiffest ones. The difference between the linear compressibilities along different axes could be explained by the orientations of the strongest bonds Si/Ge-S along these axes.

The less compressibility of the considered compounds along the *c*-axis is due to the strongest of the Si/Ge-S2 bond, which is almost oriented along the *c*-axis; there is only about 3.5° between the Si/Ge-S2 bond and the *c*-axis (see Table 6).

Table 5.6: The angles (in deg.) between different strongest bonds Si-S (or Ge-S) and the main crystallographic axes, for Cu_2MgSiS_4 and Cu_2MgGeS_4 compounds

	Cu_2MgSiS_4			**Cu_2MgGeS_4**		
	a-axis	*b*-axis	*c*-axis	*a*-axis	*b*-axis	*c*-axis
Si-S1	36.7	61.4	68.9	37.3	60.8	68.9
Si-S2	90	86.4	3.5	90	86.8	3.4
Si-S3	90	16.5	73.6	90	16.3	73.7

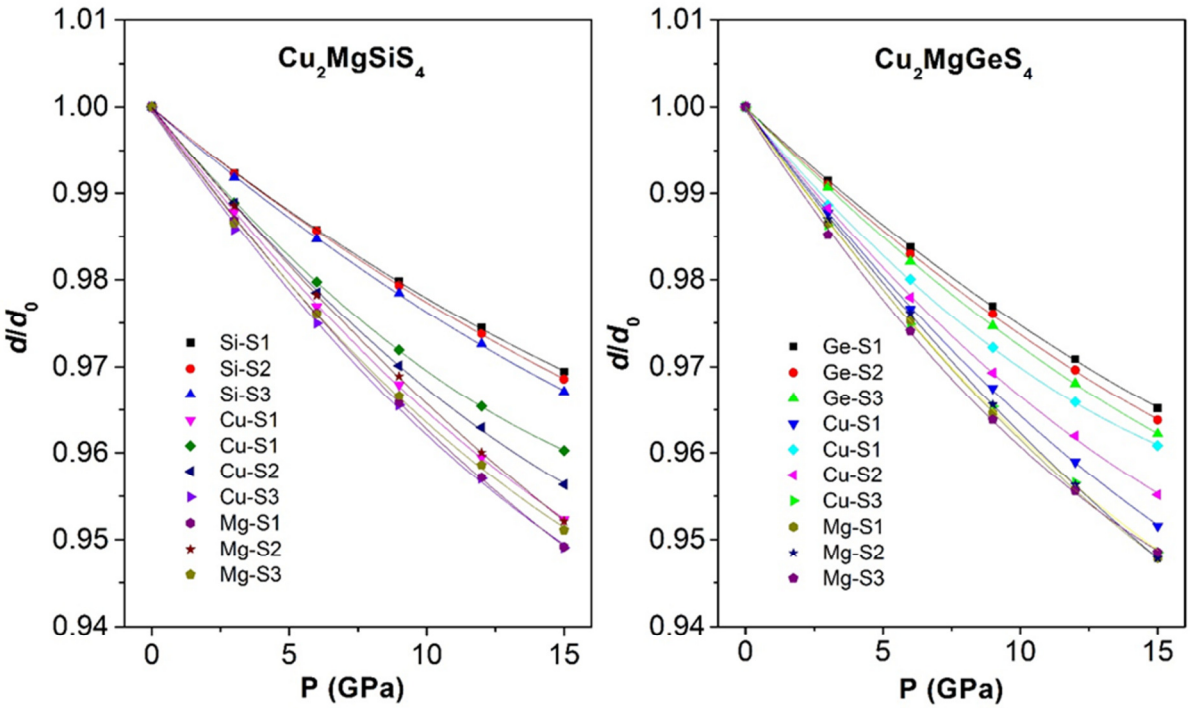

Fig. 5.7: Calculated pressure dependence of the relative bond lengths d/d_0 for the Cu_2MgSiS_4 and Cu_2MgGeS_4 compounds. The solid lines are least squares second-order polynomial fits of the data points.

5.2.2. Elastic properties

The elastic properties of single-crystal and polycrystalline aggregates of the Cu_2MgSiS_4 and Cu_2MgGeS_4 compounds were explored by calculating their independent elastic constants C_{ij}, bulk modulus B, shear modulus G, Young's modulus E, Poisson's coefficient v and related properties. The C_{ij}s were obtained via linear fittings of the stress-strain curves. The main advantage of this method is the great reduction of the independent strain modes number compared to the ab initio total energy versus strain approach. The elastic stiffness tensor is related to the stress tensor and the strain tensor by Hooke's law. Since the stress tensor and the strain tensor are symmetric, the most general elastic stiffness tensor has only 21 non-zero independent components. For our system (orthorhombic crystal), they are reduced to nine independent components, namely C_{11}, C_{22}, C_{33}, C_{44}, C_{66}, C_{12}, C_{13} and C_{23}. The corresponding matrixes of elastic constants C_{ij} are given as follow:

$$(C_{ij}) = \begin{pmatrix} C_{11} & C_{12} & C_{13} & 0 & 0 & 0 \\ C_{12} & C_{22} & C_{23} & 0 & 0 & 0 \\ C_{13} & C_{23} & C_{33} & 0 & 0 & 0 \\ 0 & 0 & 0 & C_{44} & 0 & 0 \\ 0 & 0 & 0 & 0 & C_{55} & 0 \\ 0 & 0 & 0 & 0 & 0 & C_{66} \end{pmatrix} \quad (5.12)$$

To determine the nine independent elastic constants C_{ij} of the elastic tensor for the orthorhombic phase, three strain patterns - one with non-zero ε_{11} and ε_{32} components, second with non-zero ε_{22} and ε_{31} components and the third with non-zero ε_{33} and ε_{12} components were used.

5.2.2.1. Single-crystal elastic constants

The complete set of the calculated independent elastic constants C_{ij}s of the Cu_2MgSiS_4 and Cu_2MgGeS_4 compounds are listed in Table 5.7. No experimental or theoretical values for these quantities are reported in the literature. From the obtained results, we can make the following conclusions:

(i) The C_{11}, C_{22} and C_{33} elastic constants reflect the stiffness-to-uniaxial stress along the crystallographic a, b and c axes, respectively. For both Cu_2MgSiS_4 and Cu_2MgGeS_4, the C_{33} is larger than C_{11} and the latter is larger than C_{22}. This means that these materials are less resistant to applied stress along the [010] crystallographic direction than along the [100] and [001] directions, which is consistent with the results shown in Fig. 5.5. These results can be

again attributed to the more strong bonds Si/Ge-S along the crystallographic *c*-axis. The C_{44}, C_{55} and C_{66}, which represent the shear moduli of the (100), (010) and (001) planes, respectively, are relatively small than the C_{11}, C_{22} and C_{33}, indicating that these materials are more resistance to compression than to shear deformation.

Table 5.7: Calculated independent single-crystal elastic constants (C_{ij}, in GPa), for the Cu_2MgSiS_4 and Cu_2MgGeS_4 compounds

System	C_{11}	C_{22}	C_{33}	C_{44}	C_{55}	C_{66}	C_{12}	C_{13}	C_{23}
Cu_2MgSiS_4	123.27	109.65	148.45	26.17	26.43	27.78	59.20	58.10	48.01
Cu_2MgGeS_4	122.95	111.61	144.36	26.87	24.26	26.85	58.59	53.26	49.21

(ii) To be mechanically stable, orthorhombic crystals should satisfy the following Born-Huang stability criteria [25]:

$$C_{11}>0,\ C_{22}>0,\ C_{33}>0,\ C_{44}>0,\ C_{55}>0,\ C_{66}>0,\ C_{11}+C_{22}-2C_{12}>0,$$

$$C_{11}+C_{33}-2C_{13}>0,\ C_{22}+C_{33}-2C_{23}>0,\ C_{11}+C_{22}+C_{33}+2\left(C_{12}+C_{13}+C_{23}\right)>0 \quad (5.13)$$

Our predicted C_{ij}s satisfy these conditions, implying that the considered systems are mechanically stable.

(iii) The sound wave velocity in a crystal is related to some of its physical properties such as its thermal conductivity, thus it is important to evaluate it. Acoustic wave velocities along different directions in a crystal can be obtained via the resolution of the Christoffel equation [26]:

$$\left(C_{ijkl}\cdot n_j\cdot n_k-\rho v^2\delta_{il}\right)u_l=0 \quad (5.14)$$

where C_{ijkl} is the elastic constant tensor, n is the wave propagation direction, ρ is the density of material, v is the wave velocity and u is the wave polarization. The pure longitudinal and transverse wave velocities for the orthorhombic system along the directions [100], [010] and [001] are given by the following expressions:

$$v_L^{[100]}=\sqrt{C_{11}/\rho};\ v_{T1}^{[100]}=\sqrt{C_{66}/\rho};\ v_{T2}^{[100]}=\sqrt{C_{55}/\rho}$$

$$v_L^{[010]}=\sqrt{C_{22}/\rho};\ v_{T1}^{[010]}=\sqrt{C_{66}/\rho};\ v_{T2}^{[010]}=\sqrt{C_{44}/\rho}$$

$$v_L^{[001]}=\sqrt{C_{33}/\rho};\ v_{T1}^{[001]}=\sqrt{C_{55}/\rho};\ v_{T2}^{[001]}=\sqrt{C_{44}/\rho} \quad (5.15)$$

The calculated sound wave velocities propagating in the [100], [010] and [001] crystallographic directions of the title compounds are listed in Table 5.8. The longitudinal sound wave velocities are larger than the corresponding transverse ones. The elastic wave velocities of Cu_2MgSiS_4 are slightly higher than those of Cu_2MgGeS_4 because Cu_2MgSiS_4 is slightly harder than Cu_2MgGeS_4, as we have already seen previously.

Table 5.8: Calculated elastic wave velocities for some different propagating crystallographic directions (V, in m/s) for the Cu_2MgSiS_4 and Cu_2MgGeS_4 compounds. The subscripts L and T denote the longitudinal and transversal polarization of the sound wave

System	V_L^{100}	V_{T1}^{100}	V_{T2}^{100}	V_L^{010}	V_{T1}^{010}	V_{T2}^{010}	V_L^{001}	V_{T1}^{001}	V_{T2}^{001}
Cu_2MgSiS_4	5957.5	2828.2	2758.6	5618.8	2828.2	2745.0	6537.7	2758.6	2745.0
Cu_2MgGeS_4	5662.7	2646.3	2515.4	5395.2	2646.3	2647.2	6136.0	2515.4	2647.2

5.2.2.2 Polycrystalline elastic properties

In the particular case of randomly oriented polycrystals, the elastic constants C_{ij}s cannot be measured and instead of that the isotropic polycrystalline elastic moduli, such as the bulk modulus B (resistance of a solid against its volume change under hydrostatic pressure) and shear modulus G (resistance to shape change caused by a shearing force), can be measured. Theoretically, these polycrystalline elastic moduli can be derived from the C_{ij}s based on additional hypotheses such as isostress named as Reuss [6] or isostrain named as Voigt [7] states (subscripted, respectively, R and V in the following). The general expressions of the bulk modulus B and shear modulus G in the Voigt and Reuss approaches are as follows:

$$B_V = (1/9)[C_{11} + C_{22} + C_{33} + 2(C_{12} + C_{13} + C_{23})] \quad (5.16)$$

$$G_V = (1/15)[C_{11} + C_{22} + C_{33} + 3(C_{44} + C_{55} + C_{66}) - (C_{12} + C_{13} + C_{23})] \quad (5.17)$$

$$1/B_R = (s_{11} + s_{22} + s_{33}) + 2(s_{12} + s_{23} + s_{13}) \quad (5.18)$$

$$1/G_R = (4/15)(s_{11} + s_{22} + s_{33}) - (4/15)(s_{12} + s_{13} + s_{23}) + (1/5)(s_{44} + s_{55} + s_{66}) \quad (5.19)$$

The s_{ij} are the components of the compliance matrix **S,** which is related to the elastic constant matrix **C** by the following relationship: $\mathbf{S} = \mathbf{C}^{-1}$. Using energy consideration, Hill [8] has

demonstrated that the arithmetic mean of the two above mentioned limits -Voigt and Reuss approximations- are the best effective polycrystalline elastic moduli (Hill's approximation). In the Hill's approximation, the polycrystalline bulk (B_H) and shear (G_H) moduli are given by:

$$B_H = \frac{B_V + B_R}{2} \text{ and } G_H = \frac{G_V + G_R}{2} \tag{5.20}$$

The Young's modulus E and Poisson's ratio v can be computed from the Hill's values of B and G through the following relationships:

$$E = \frac{9BG}{3B+G} \text{ and } \nu = \frac{3B-2G}{2(3B+G)} \tag{5.21}$$

Using the aforementioned relations, the calculated bulk modulus B, shear modulus G, Young's modulus E and Poisson's ratio ν are quoted in Table 5.9.

Table 5.9: Calculated Bulk modulus (B, in GPa), shear modulus (G, in GPa), Young's modulus (E, in GPa), ***B/G*** ratio and Poisson's ratio (v, dimensionless) for the Cu_2MgSiS_4 and Cu_2MgGeS_4 compounds

System	B_V	B_R	B_H	G_V	G_R	G_H	E	B/G	v
Cu_2MgSiS_4	79.11	78.02	78.57	30.48	29.33	29.91	79.62	2.627	0.3331
Cu_2MgGeS_4	77.89	77.33	77.61	30.12	28.89	29.50	78.56	2.630	0.3313

The obtained results allow us to make the following conclusions:

(a) One can appreciate that the estimated bulk modulus value based on the C_{ij}s agrees very well with those obtained via other procedures (see Table 5.5), confirming again the reliability of the present calculations (The B calculated from C_{ij}s deviated from that calculated from different EOSs fits, and from linear and volume compressibilities, by -3.33% to -6.00% for Cu_2MgSiS_4, and by -0.45% to -2.22% for Cu_2MgGeS_4).

(b) The Poisson's ratio v, defined as the ratio of transverse strain (normal to the applied stress) to the longitudinal strain (in the direction of the applied stress), is generally connected with the volume change in a solid during uniaxial deformation and the chemical bonding character [27,28]. If ν is equal to 0.5, no volume change occurs, while if it is lower than 0.5 a large volume change is expected for any elastic deformation. In our case, the value of v is

approximately 0.33 in both Cu_2MgSiS_4 and Cu_2MgGeS_4, suggesting a considerable volume change can be associated with elastic deformation.

(c) To distinguish between brittleness (fragility) and ductility (malleability) behavior of solids, Pugh [29] has proposed a simple empirical relationship between the bulk modulus B and shear modulus G. A B/G value higher than 1.75 is associated with ductility, whereas a lower value than 1.75 is associated with brittleness. According to this criterion, both considered compounds are ductile materials. A ductile material is more resistant to thermal shocks (B/G is about 2.63 for each material).

(d) In Debye model, the Debye temperature θ_D is used to distinguish between high- and low-temperature regions for a solid. Debye temperature θ_D is correlated with many physical properties, such as thermal expansion, melting point and Grüneisen parameter. Debye temperature θ_D can be numerically estimated from the average sound wave velocity V_m as follows [30]:

$$\theta_D = \frac{h}{K_B}\left[\frac{3n}{4\pi}\left(\frac{N_A\rho}{M}\right)\right]^{1/3} V_m \tag{5.22}$$

where, h is Planck constant, k_B is Boltzmann constant, N_A is Avogadro number, ρ is the mass density, M is the molecular weight and n is the number of atoms in the molecule. In polycrystalline materials, the average wave velocity V_m can be evaluated as follows:

$$V_m = \left[\frac{1}{3}\left(\frac{2}{V_t^3}+\frac{1}{V_l^3}\right)\right]^{-1/3} \tag{5.23}$$

Here, V_l and V_t are the average longitudinal and transverse elastic wave velocities, which are defined by Navier's equations [31]:

$$V_l = \left(\frac{3B+4G}{3\rho}\right)^{1/2} \text{ and } V_t = \left(\frac{G}{\rho}\right)^{1/2} \tag{5.24}$$

The calculated sound wave velocities (V_l, V_t and V_m) and Debye temperature (θ_D) for the Cu_2MgSiS_4 and Cu_2MgGeS_4 polycrystalline aggregates are listed in Table 5.10. One can see from this table that the values of V_l, V_t, V_m and θ_D of Cu_2MgSiS_4 are slightly larger than those of Cu_2MgGeS_4 of about 5.8%, 0.63%, 5.4% and 6.7%, respectively.

Table 5.10: Calculated molecular weight (M, in g), density (ρ, in g/cm^3), transverse, longitudinal and average sound velocities (V_t, V_l and V_m, in m/s) and Debye temperatures (θ_D, in K) for the Cu_2MgSiS_4 and Cu_2MgGeS_4 compounds

System	M	ρ	V_t	V_l	V_m	θ_D
Cu_2MgSiS_4	307.722	3.4732	2934.45	5557.96	3280.53	370.02
Cu_2MgGeS_4	352.227	3.8343	2773.98	5522.78	3111.05	346.70

5.2.2.3. Elastic anisotropy

The anisotropy of physical properties in crystals reflects the anisotropy in bonding between atoms in different planes. We have already reported above that Cu_2MgSiS_4 and Cu_2MgGeS_4 are anisotropic in compressibility (Fig. 5.5). Quantification of the elastic anisotropy is necessary and significant due to its implication in the apparition of microcracks in solids [32] and its influence on the nanoscale precursor textures in alloys [33]. To quantify the anisotropy of the elastic properties of the Cu_2MgSiS_4 and Cu_2MgGeS_4 compounds, five different criteria were employe:

1. The shear anisotropic factors are among the used criteria to measure the degree of anisotropy in the bonding between atoms in different planes. The shear anisotropic factor for the {100} shear planes between the <011> and <010> directions in orthorhombic crystals is [34]:

$$A_1 = \frac{4C_{44}}{C_{11} + C_{33} - 2C_{13}} \tag{5.25}$$

For the {010} shear planes between <101> and <001> directions it is:

$$A_2 = \frac{4C_{55}}{C_{22} + C_{33} - 2C_{23}} \tag{5.26}$$

For the {001} shear planes between <110> and <010> directions it is:

$$A_3 = \frac{4C_{66}}{C_{11} + C_{22} - 2C_{12}} \tag{5.27}$$

For isotropic materials, A_1, A_2 and A_3 are equal to one, whereas values smaller or greater than unity measure the degree of elastic anisotropy possessed by the crystal. Table 5.11 shows that A_1 and A_2 anisotropy factors are very different from unity, implying that shears of {100} and

{010} planes both are characterized by a noticeable elastic anisotropy. In contract, the anisotropy factor A_3 is close to unity, implying that the resistance to shears of {001} a plane is less anisotropic. We can see also that Cu_2MgSiS_4 is slightly more isotropic than Cu_2MgGeS_4.

2. Another way for measuring the elastic anisotropy possessed by solids has been proposed by Chung and Buessem [35], which is the percentage anisotropy in compressibility (A_B) and shear (A_G) moduli of elastic anisotropy defined as:

$$A_B = (B_V - B_R)/(B_V + B_R) \text{ and } A_G = (G_V - G_R)/(G_V + G_R) \quad (5.28)$$

The subscripts V and R denote the Voigt and Reuss approximations. A value of zero (0%) is associated to a complete elastic isotropy; while a value of 1 (100%) corresponds to the largest possible anisotropy. The results listed in Table 5.11 for A_B and A_G suggest that Cu_2MgSiS_4 and Cu_2MgGeS_4 are anisotropic.

3. A universal anisotropy index A^U has been proposed by Ranganathan and Ostoja-Starzewski [36] to quantify the elastic anisotropy of crystals accounting for both bulk and shear modulus contributions. The A^U index is defined as follows:

$$A^U = 5\frac{G_V}{G_R} + \frac{B_V}{B_R} - 6 \quad (5.29)$$

For isotropic crystals, A^U is equal to zero and deviations of A^U from zero define the extent of elastic anisotropy. The results listed in Table 5.11 for A^U indicate that Cu_2MgSiS_4 and Cu_2MgGeS_4 have a certain degree of elastic anisotropy.

Table 5.11: Calculated shear anisotropic factors (A_1, A_2 and A_3), percentage of elastic anisotropy for bulk modulus and shear modulus (A_B and A_G) and universal anisotropy index (A^U) for the Cu_2MgSiS_4 and Cu_2MgGeS_4 compounds.

System	A_1	A_2	A_3	A_B (%)	A_G (%)	A^U
Cu_2MgSiS_4	0.6732	0.6523	0.9701	0.70	1.92	0.2093
Cu_2MgGeS_4	0.6685	0.6159	0.9149	0.36	2.09	0.2204

4. The elastic anisotropy can be accurately analyzed by examining the ratio of the principle Young's moduli E_{ii} along crystallographic axes along crystallographic axes. The anisotropic

Young's moduli E_{ii} and Poisson's ratio v_{ij} (i, j=x, y, z) can be estimated from the calculated elastic compliances S_{ii} by using the following relations:

$$E_{ii} = \frac{1}{S_{ii}} \quad \text{and} \quad \nu_{ij} = \frac{-S_{ij}}{S_{ii}} \tag{5.30}$$

The values of the principle Young's moduli E_{ii} and Poisson's ratio v_{ij} are reported in Table 5.12. E_{ii} and Poisson's ratio v_{ij} values illustrate also the considerable anisotropic behavior of Cu_2MgSiS_4 and Cu_2MgGeS_4 with respect to external deformation.

Table 5.12: The calculated elastic compliances S_{ij} (in 10^{-4} GPa^{-1}), principle Young's moduli E_{ii} (in GPa) and Poisson's ratios v_{ij} for the Cu_2MgSiS_4 and Cu_2MgGeS_4 compounds

Cu_2MgSiS_4			**Cu_2MgGeS_4**		
S_{ij}	E_{ii}	v_{ij}	S_{ij}	E_{ii}	v_{ij}
S_{11} = 0.0120216	E_{11} = 83.18328	v_{12} = 0.4293	S_{11} = 0.0116200	E_{11} = 86.05831	v_{12} = 0.4263
S_{22} = 0.0128397	E_{22} = 77.88372	v_{13} = 0.2525	S_{22} = 0.0126561	E_{22} = 79.01319	v_{13} = 0.2237
S_{33} = 0.0086139	E_{33} = 116.09117	v_{21} = 0.4020	S_{33} = 0.0087337	E_{33} = 114.49919	v_{21} = 0.3914
S_{44} = 0.0382075		v_{23} = 0.1661	S_{44} = 0.0372144		v_{23} = 0.1965
S_{55} = 0.0378331		v_{31} = 0.3525	S_{55} = 0.0412187		v_{31} = 0.2976
S_{66} = 0.0360030		v_{32} = 0.2475	S_{66} = 0.0372463		v_{32} = 0.2847
S_{12} = -0.0051612			S_{12} = -0.0049536		
S_{13} = -0.0030361			S_{13} = -0.0025989		
S_{23} = -0.0021320			S_{23} = -0.0024863		

5. A practical way to evidence the elastic anisotropy behavior in crystals is to plot three-dimensional (3D) representation of the directional dependence of the Young's modulus E. In a 3D-representation, a perfectly isotropic system would exhibit a spherical shape, and the degree of deviation of the 3D surface from spherical shape reveals the extent of the elastic anisotropy. In an orthorhombic crystal, the 3D closed surface for the Young's modulus E is given by the following expression [37]:

$$\frac{1}{E} = l_1^4 S_{11} + l_2^4 S_{22} + l_3^4 S_{33} + 2l_1^2 l_2^2 S_{12} + 2l_1^2 l_3^2 S_{13} + 2l_2^2 l_3^2 S_{23} + l_2^2 l_3^2 S_{44} + l_1^2 l_3^2 S_{55} + l_1^2 l_2^2 S_{66} \tag{5.31}$$

Here, l_1, l_2 and l_3 are the directional cosines with respect to the x-, y- and z-axes, respectively, and the S_{ij} refer to the compliance constants, which can be obtained through an inversion of the elastic constant tensor.

Application of equation 5.31 for the cases of Cu_2MgSiS_4 and Cu_2MgGeS_4 yields the Young's modulus closed surfaces and their cross-sections shown in Figs. 5.8. The clearly visible deviations of the 3D surface from spherical shape and its cross-section from the circle form evidence the noticeable elastic anisotropy of the examined compounds. From the Figs. 5.8, one can see clearly that Cu_2MgGeS_4 is slightly more anisotropic than Cu_2MgSiS_4.

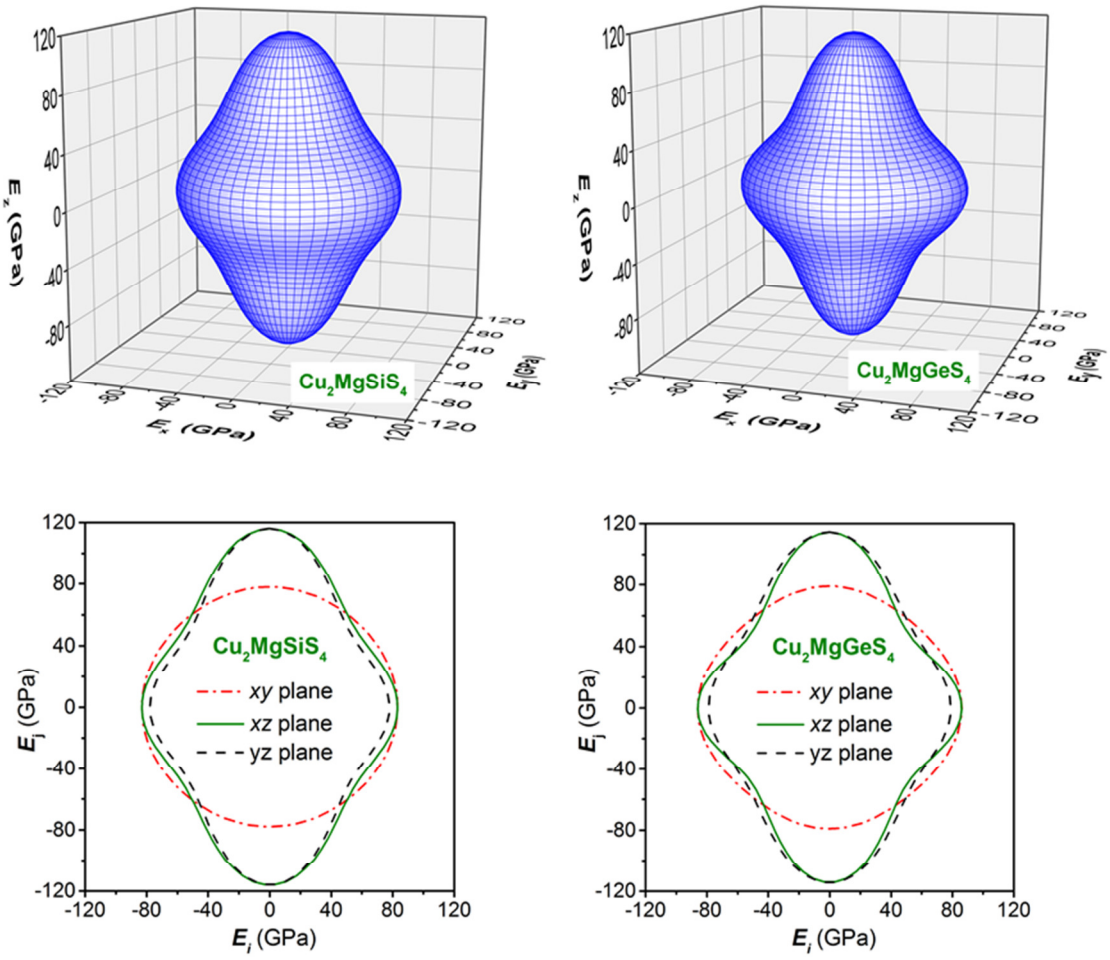

Fig. 5.8: 3D-surface representation of the directional dependence of the Young's modulus (in GPa) and its projection on the *ab* {(001)}, *ac* {(010)} and *bc* {(100)} planes for the the Cu_2MgSiS_4 and Cu_2MgGeS_4 compounds.

5.2.3. Electronic properties

In order to explore the electronic structure and related properties of two compounds Cu_2MgSiS_4 and Cu_2MgGeS_4, we have calculated at zero pressure their electronic band structures, the total and partial electron densities of states (TDOSs and PDOSs), and the effective masses of electrons and holes.

5.2.3.1. Electronic band structure

Figures 5.9 and 5.10 shows the calculated electronic band structures for the Cu_2MgSiS_4 and Cu_2MgGeS_4 compounds at their equilibrium structural parameters, along the lines of high symmetry points in the first Brillouin zone (BZ), associated to the simple orthorhombic lattice: Γ(0 0 0), X(0.5 0 0), Y(0.5 0 0), Z(0 0 0.5), T(0 0.5 0.5), U(0.5 0 0.5) , S(0.5 0.5 0) and R(0.5 0.5 0.5) (Fig. 5.11), using the full potential linearized augmented plane wave (FP-LAPW) method with both the GGA-PBEsol and TB-mBJ approaches for comparison.

As shown in Figures 5.9 and 5.10, there is no sensible difference between features of the band structures predicted by GGA-PBEsol and TB-mBJ functionals but there is a noticeable difference between the band gap values yielded by these two approaches. The TB-mBJ shifts the conduction band upward. The overall energy band profiles of Cu_2MgSiS_4 and Cu_2MgGeS_4 are similar. The valence band maximum (VBMa) and the conduction band minimum (CBMi) for both considered compounds occur at the BZ center (Γ-point). Therefore, the band edge in Cu_2MgSiS_4 and Cu_2MgGeS_4 is of a direct type, (Γ- Γ).

The obtained band gaps using the GGA-PBEsol and TB-mBJ are listed in Table 5.13 along with the existing experimental and theoretical data for comparison. The calculated band gap using the GGA-PBEsol agrees with the previous theoretical gap value [17], but it is underestimated severely compared to the measured one; the measured gap for Cu_2MgSiS_4 (Cu_2MgGeS_4) is 1.71 eV (1.50 eV) higher than the calculated one using the GGA-PBEsol. One can appreciate that the TB-mBJ improves considerably the band gap value compared to that yielded by the GGA-PBEsol. However, the TB-mBJ does not produce exactly the reported experimental values of the band gaps of the title compounds; the band gap is still underestimated. The relative deviation of the calculated band gap using the TB-mBJ regards the measured one is approximately -17% in the case of Cu_2MgSiS_4 and -35% in the case of Cu_2MgSiS_4.

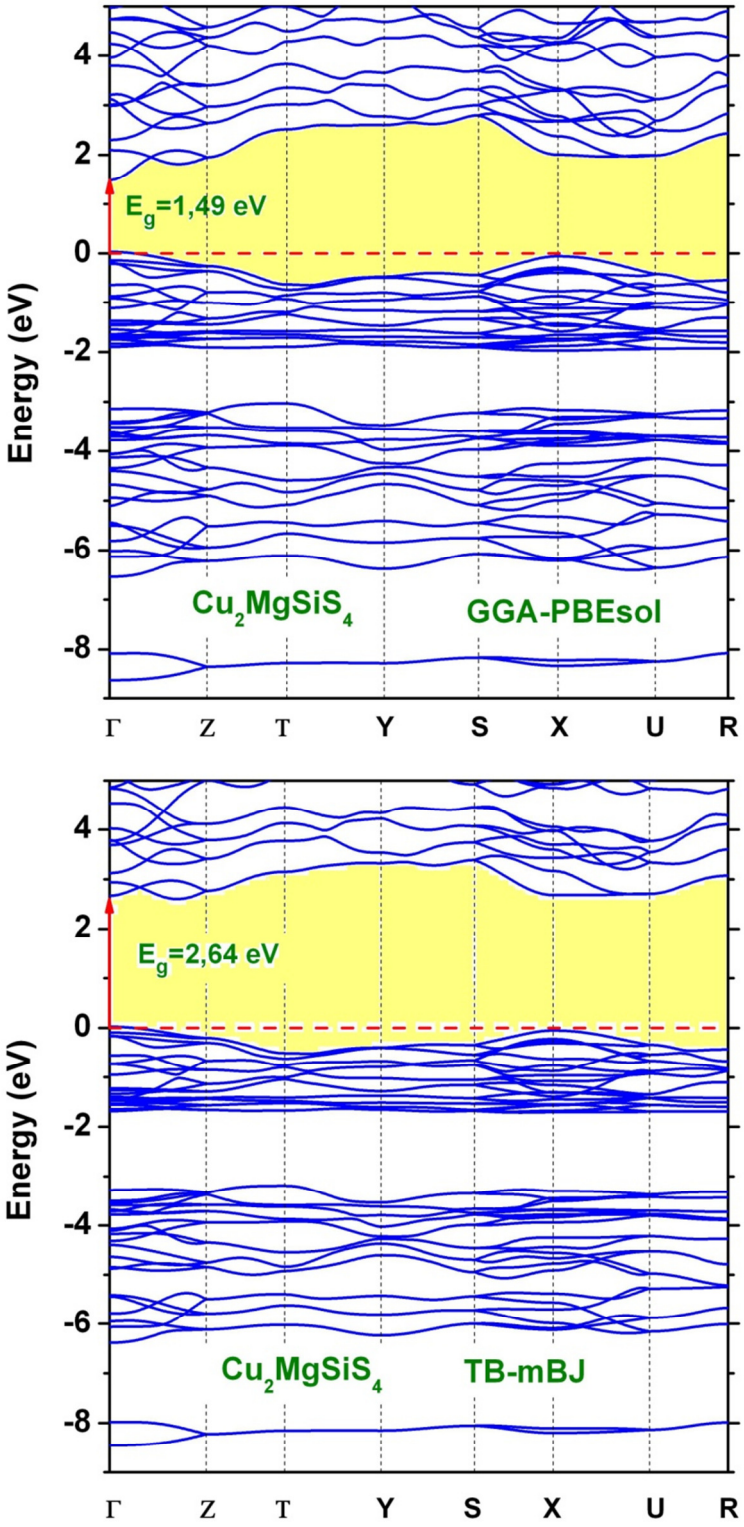

Fig. 5.9: Calculated electronic band structures of the Cu_2MgSiS_4 compound, using the GGA-PBEsol and TB-mBJ approximations. The fundamental band gap is shown by an arrow.

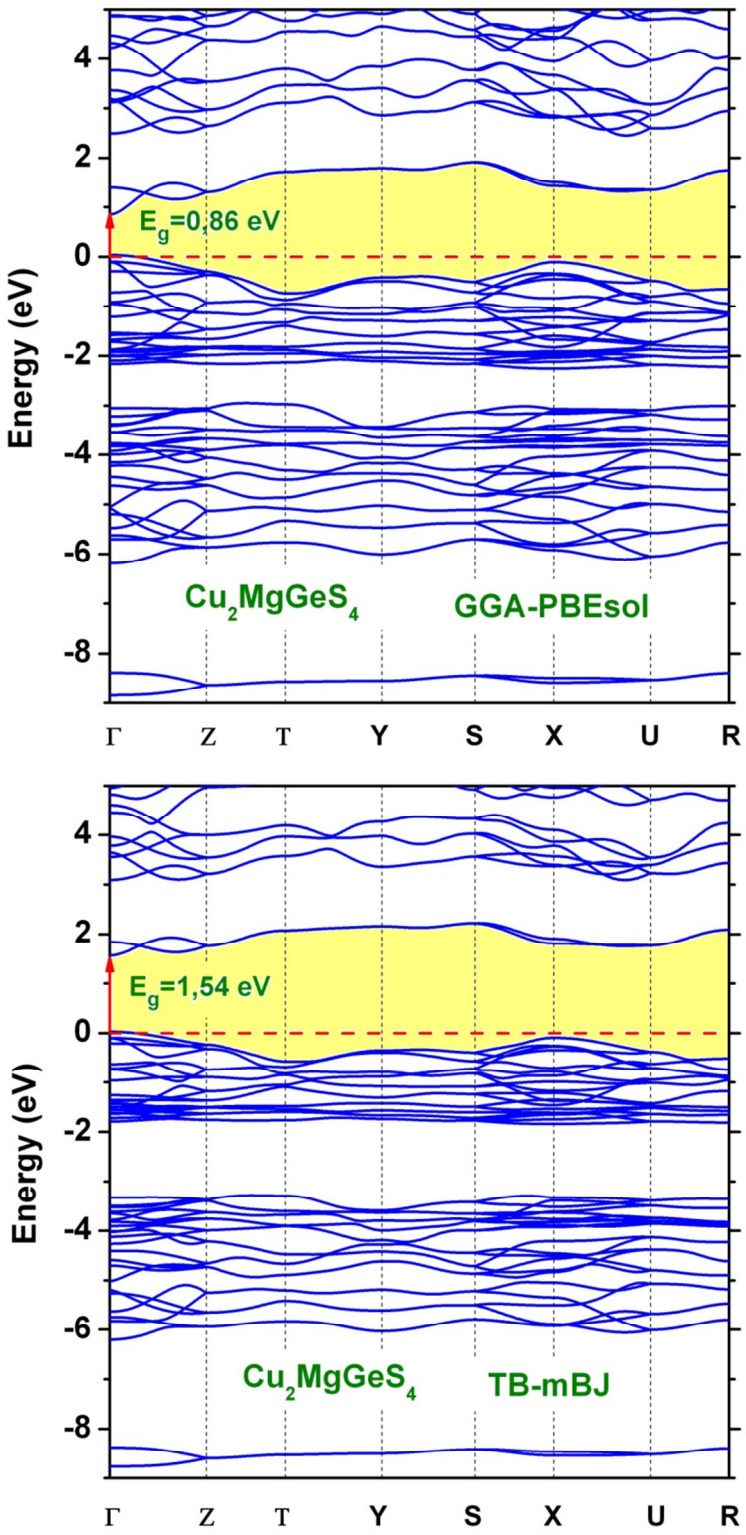

Fig. 5.10: Calculated electronic band structures of the Cu_2MgGeS_4 compound, using the GGA-PBEsol and TB-mBJ approximations. The fundamental band gap is shown by an arrow.

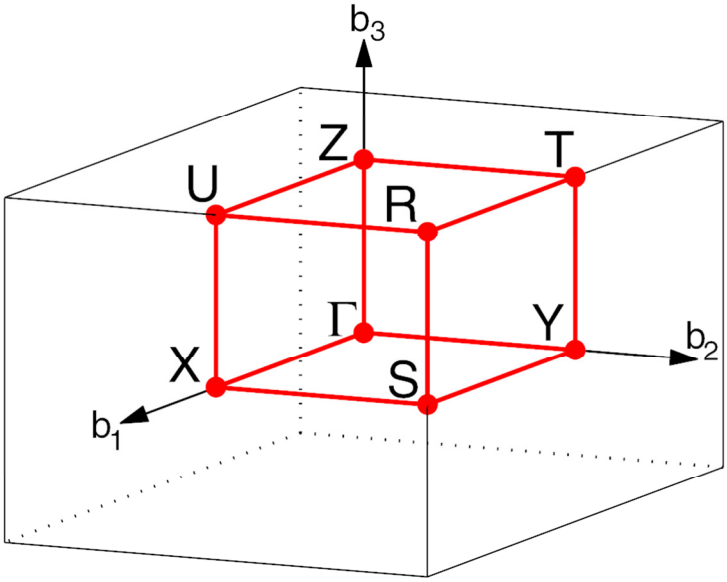

Fig. 5.11: High symmetry points in the first Brillouin zone (BZ) of the simple orthorhombic lattice, in which Cu_2MgSiS_4 and Cu_2MgGeS_4 crystallize. The red line corresponds to the path of the band structure diagram. $\mathbf{b_1}$, $\mathbf{b_2}$ and $\mathbf{b_3}$ are the unit vectors of the reciprocal lattice.

Table 5.13: Calculated energy band gap (in eV) for the Cu_2MgSiS_4 and Cu_2MgGeS_4 compounds compared with the available experimental and theoretical data in the scientific literature

System	This work		Experimental	Other calculations
	TB-mBJ	GGA-PBEsol	[17]	GGA-PP-PW [17]
Cu_2MgSiS_4	2.643	1.491	3.20	2.01
Cu_2MgGeS_4	1.536	0.856	2.36	1.25

As there is only one experimental value and we do not have information about the measurement accuracy, we cannot state with certitude about the capability of the TB-mBJ method to produce acceptable band gap values for the examined systems. Based on the value of the energy band gap, Cu_2MgSiS_4 and Cu_2MgSiS_4 can be classified as wide band gap semiconductors suitable for doping with different impurities to get luminescence in particular spectral region [38]. It is worth to note that the band gap value of Cu_2MgSiS_4 is larger than

that of Cu_2MgGeS_4 by about 60% using the TB-mBJ. This ratio is very close to that between the band gap of the Si (E_g = 1.17 eV) to that of the Ge (E_g = 0.75 eV) semiconductors at zero temperature [39]. This means that the difference between the fundamental band gaps of Cu_2MgSiS_4 and Cu_2MgGeS_4 is due to the nature of the Si and Ge atoms, indicating that the element mutation provides an efficient method for manipulating the positions of the band gap edges.

A comparison between the measured band gaps for the considered compounds and those of other quaternary diamond-like compounds (Table 5.14) reveals that:

(i) The band gap of the Cu_2-II-IV-S_4 diamond-like compounds decreases when moving down in column II of the periodic table in the following consequence: Mg → Zn → Cd [17,40-43] (Fig. 5.12 (a)).

(ii) The band gap decreases when the IV cation is substituted in the following consequence: Si → Ge → Sn (Fig. 5.12 (b)). This trend can be explained by the fact that the increase of cation radius when going from Si to Ge to Sn leads to the increase of the IV-S bond-length, which causes the decrease of the band gap [44]. Effectively, one can see from the Table 5.4 that Ge-S bond-length is higher than that of Si-S bond. The same can be said when moving down in column II of the periodic table. On other hand, the decrease of the electronegativity when moving down in the column causing the decrease of the band gap [44].

Table 5.14: Experimental energy band gap E_g (eV) of some Cu_2-II-IV-S_4 diamond-like semiconductors at ambient temperature

Compound	Cu_2MgSiS_4	Cu_2ZnSiS_4	Cu_2CdSiS_4
E_g (eV)	3.20 [17]	3.04 [40]	2.45 [40]
Compound	Cu_2MgGeS_4	Cu_2ZnGeS_4	Cu_2CdGeS_4
E_g (eV)	2.36 [17]	2.04 [40]	1.95 [41]
Compound	-	Cu_2ZnSnS_4	Cu_2CdSnS_4
	-	1.51 [42]	1.16 [43]

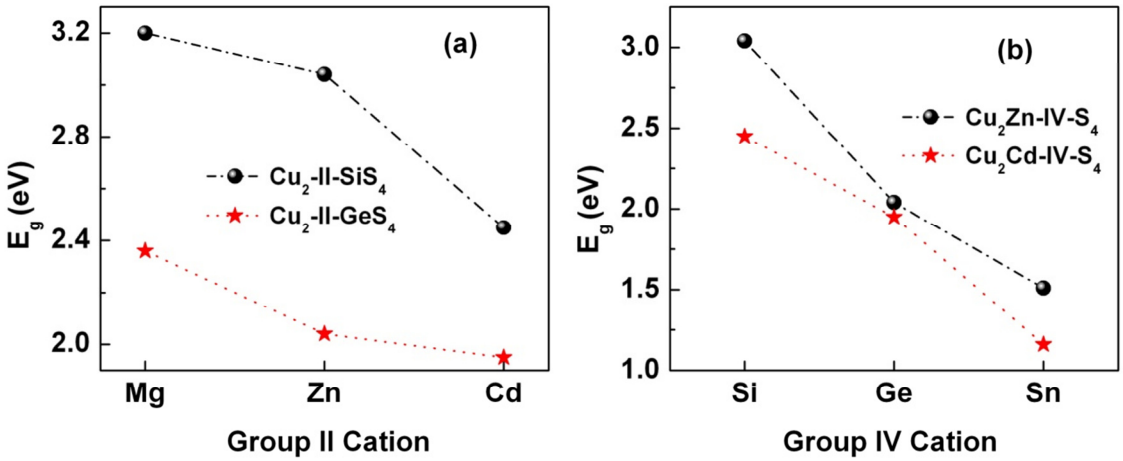

Fig. 5.12: Variation of the band gap E_g in some Cu_2-II-IV-S_4 quaternary diamond-like semiconductors with respect to the chemical nature of the II (a) and IV (b) cations.

5.2.3.2. Study of the effective mass

The effective masses of electrons and holes are fundamental quantities that used in numerous experimental analysis and theoretical models in semiconductor materials, for example the effective charge-carrier mass is one of the main factors that determine the transport properties and electrical conductivity of materials. In the present work, the effective charge-carrier masses are numerically evaluated by fitting the energy band dispersion E-*k* around the extremes to parabolas then the effective mass m^* (in unit of m_0, where m_0 denotes the electron rest mass) is calculated via the following formula:

$$\frac{1}{\mathrm{m}^*} = \frac{m_0}{\hbar^2}\frac{\partial^2 \mathrm{E(k)}}{\partial^2 \mathrm{k}} \tag{5.32}$$

Dense *k*-points through the lines of high symmetry in the Brillouin zone were used to calculate the energy band dispersion and only the nearest ones to the extremes were taken into account to calculate the effective masses. The computed effective charge-carrier masses at the Γ point from the band dispersion around the VBMa and CBMi towards the Z directions in the Brillouin zone are:

$m_e^*(\mathrm{Cu_2MgSiS_4}) = 0.400$, $m_h^*(\mathrm{Cu_2MgSiS_4}) = 2.428$,

$m_e^*(\mathrm{Cu_2MgGeS_4}) = 0.341$ and $m_h^*(\mathrm{Cu_2MgGeS_4}) = 2.283$

The effective electron and hole masses are indicated by the subscripts "e" (m_e^*) and "h" (m_h^*), respectively. From Figures 5.9 and 5.10, one can observe that the electronic states at the conduction-band minimum are more dispersive than the topmost valence-band states; consequently, the conduction-band electrons have lower effective masses than the valence-band holes. Therefore, the mobility of the holes will be substantially lower than that of the electrons.

5.2.3.3. Analysis of the density of states

The nature of the electronic states that composing the calculated energy bands of Cu_2MgSiS_4 and Cu_2MgGeS_4 can be deduced from the associated total density of states (TDOS) and the site and angular momentum decomposed density of states (PDOS) diagrams depicted in Figures 5.13 and 5.14. Overall, the DOS spectra show a rather similar energy distribution of the eigenstates for the title compounds, which can be attributed to the fact that the only different constituting atoms, i.e., the Si and Ge atoms, are isoelectronic. The Cu-3*d* states show two clearly separated structures, whose barycenters are situated approximately at -3.74 eV and -0.9 eV (eV), which are the *d*-e_g and *d*-t_{2g} states, respectively, resulting from the splitting of the Cu-3*d* states in a tetrahedral crystal field. The upper valence bands (UVB), whose width is approximately 1.8 eV (1.9 eV) in Cu_2MgSiS_4 (Cu_2MgGeS_4), is formed prevailingly by the hybridized Cu-3*d*-t_{2g} and S-3*p* states; there is a *p*-*d* hybridization between the Cu cation and S anion.

The group of valence bands in the energy range between -6.5 and -3.1 eV (-6.3 and -3.2 eV) in the Cu_2MgSiS_4 (Cu_2MgGeS_4) DOS diagram is essentially originated from the S-3*p* and *Cu-3*d-e_g states with significant contributions from the Si-3*p* (Ge-3*p*) orbitals and small contributions from the Mg-2*p*3*s* orbitals. There is a hybridization between the S anions and Si (Ge) cations in the deep energy range between ~ -6.5 (-6.4) to -5.2 (-5.0) eV, suggesting a significant covalent character of the Si/Ge-S bonds and explains the fact that Si/Ge-S bond is the strongest one. A handle of valence bands originates from Si-3*s* (Ge-4*s*) and S-3*p* orbitals forms a sharp peak at about -8.3 eV (-8.5eV) in Cu_2MgSiS_4 (Cu_2MgGeS_4). The lowest energetic bands are formed by the S-3s states with the peaks are at about -13.6 eV (-13.54 eV) and -14.9 eV (-14.60 eV) (not shown for the clarity of the figure). The bottom of the conduction band is made mainly by the *s*-*p* hybridization between the group-IV cation (Si and Ge) and the S anion. Finally, due to the difference in the electronegativity between the comprising elements, the ionic character is presented.

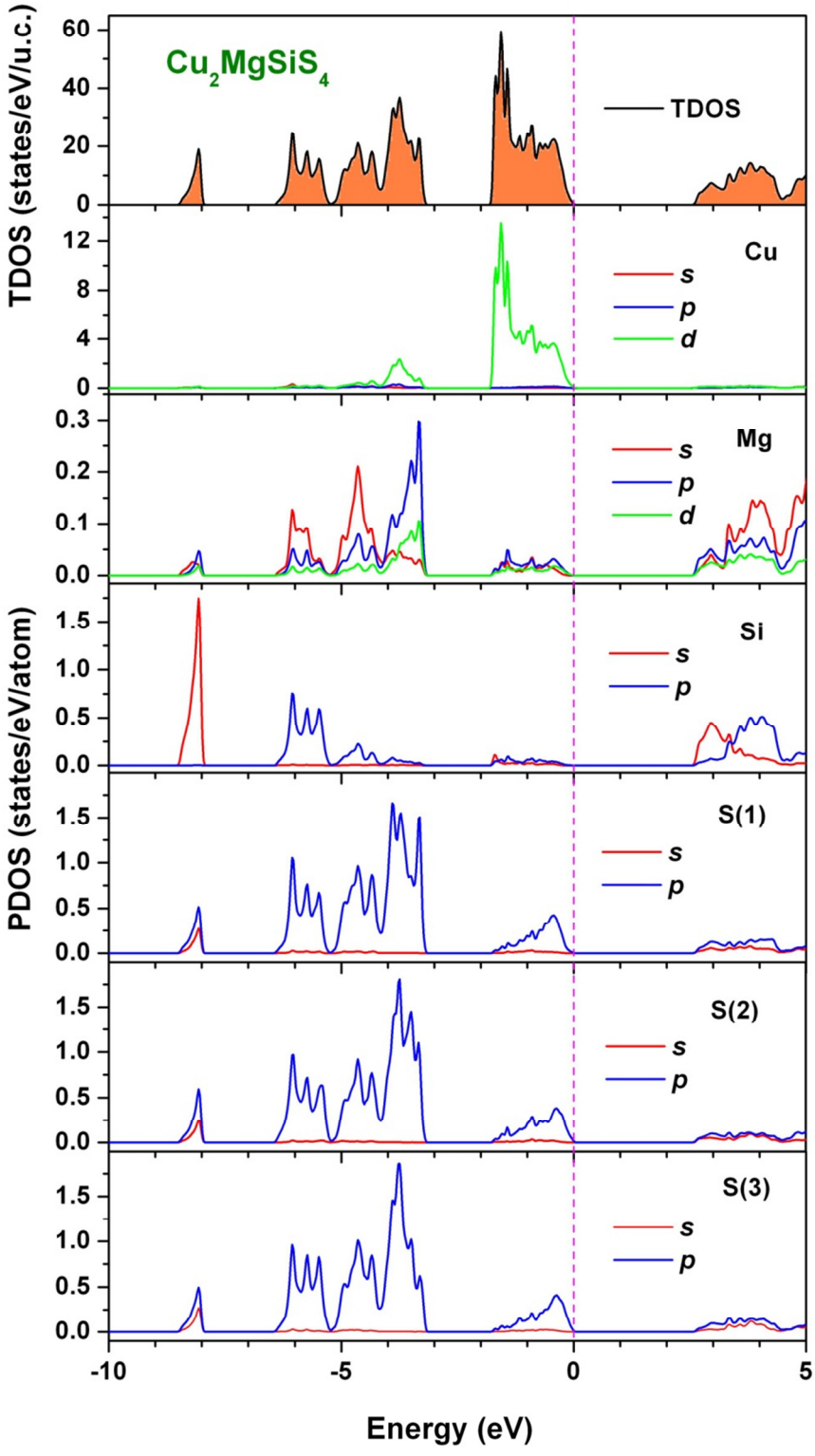

Fig. 5.13: Calculated total density of states (TDOS) and partial density of states (PDOS) of the Cu_2MgSiS_4 compound.

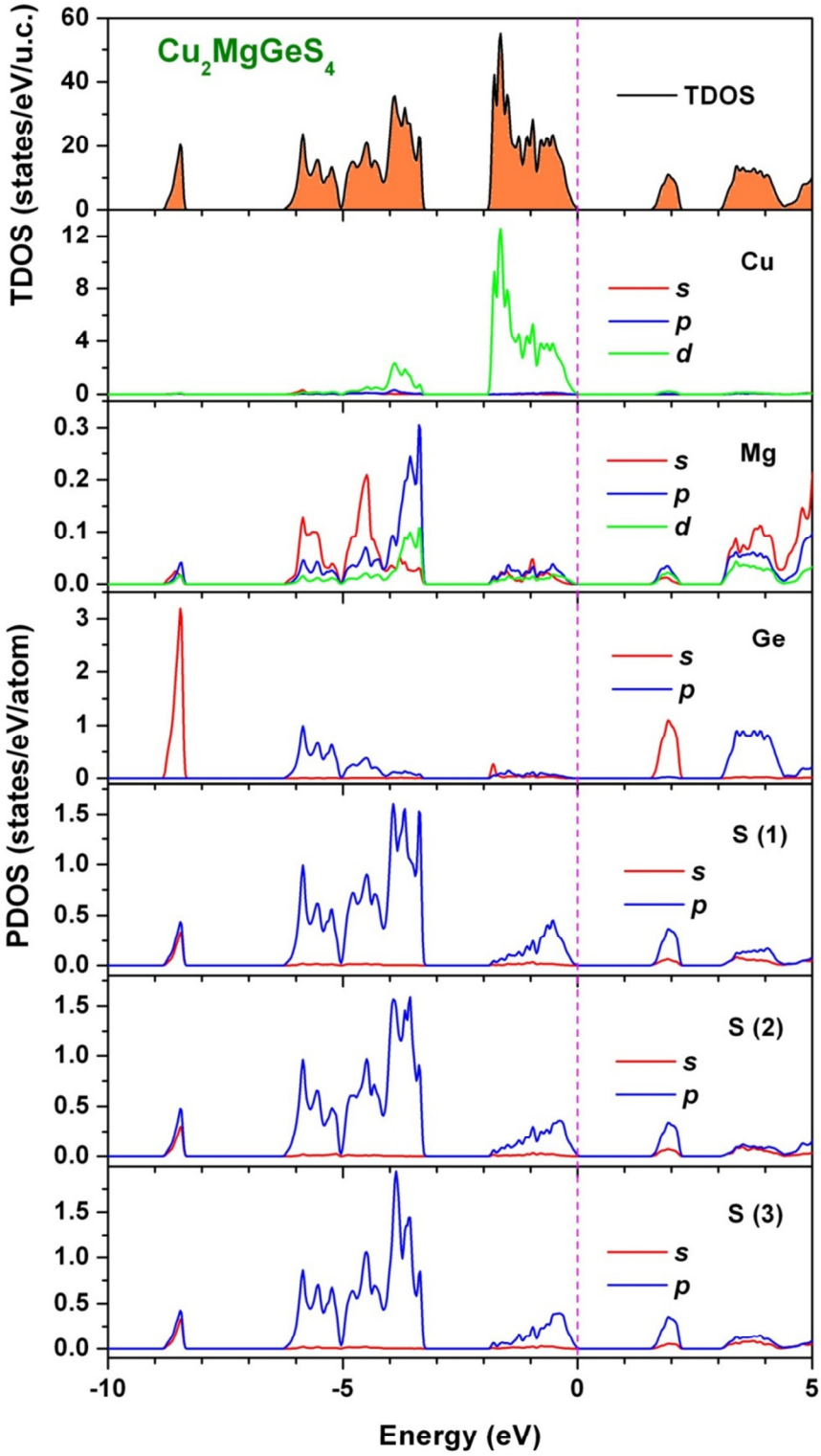

Fig. 5.14: Calculated total density of states (TDOS) and partial density of states (PDOS) of the Cu_2MgGeS_4 compound.

It is worth to note that although there are three inequivalent S atoms, their projected densities of states are similar to each other, indicating their bonding characters are similar. It is clear from Fig. 5.15 the great convergence between the curves of the three atoms. The slight variance between them is due to the fact that S1, S2 and S3 atoms have not identical environment in the crystal.

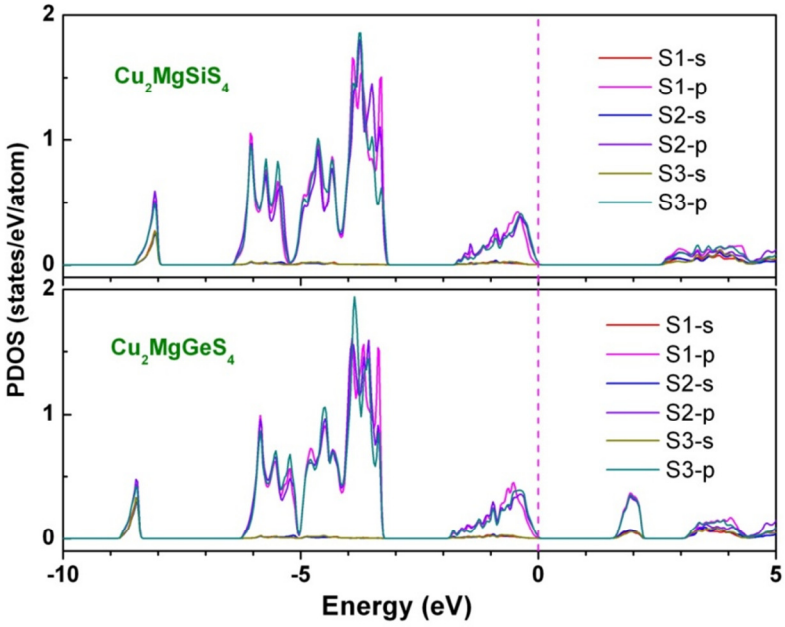

Fig. 5.15: Illustration of the slight variance between the partial densities of states (PDOSs) of S1, S2 and S3 atoms in Cu_2MgSiS_4 and Cu_2MgGeS_4 compounds.

5.2.4. Optical properties

It is of great interest to know the different ways in which light interacts with matter in the physics of the solid state, such as absorption, transmission, reflection, scattering and emission. The optical properties of solids provide an important tool for studying energy band structure, impurity levels, excitons, localized defects, lattice vibrations, and certain magnetic excitations.

5.2.4.1. The dielectric function

The *dielectric constant* is the ratio of the permittivity of a substance to the permittivity of the vacuum. It represents how difficult it is for the field to propagate inside a medium due to the response of the medium to the field. It is the frequency-dependent complex dielectric function $\varepsilon(\omega)$ which is directly related to the energy band structure of solids, where other optical properties are derived from it. It is defined as:

$$\varepsilon(\omega) = \varepsilon_1(\omega) + i\varepsilon_2(\omega) \tag{5.33}$$

The imaginary part of the dielectric function $\varepsilon_2(\omega)$ is calculated from the momentum matrix elements between the occupied and unoccupied states as follows:

$$\varepsilon_2(\omega) = \frac{Ve^2}{2\pi\hbar m^2\omega^2}\int d^3k \sum_{n,n'}|\langle kn|p|kn'\rangle|^2 f_{kn}(1-f_{kn'})\,\delta(E_{kn}-E_{kn'}-\hbar\omega) \tag{5.34}$$

where e is the electronic charge, V is the unit cell volume, p is the momentum operator, $|kn\rangle$ is a crystal wave function, f_{kn} is the Fermi distribution function, and $\hbar\omega$ is the energy of the incident photon. The real part $\varepsilon_1(\omega)$ can be attracted from Kramers-Kroning relationship [45]:

$$\varepsilon_1(\omega) = 1 + \frac{2}{\pi}M\int_0^\infty \frac{\varepsilon_2(\omega\prime)\omega\prime}{\omega\prime^2-\omega^2}d\omega' \tag{5.35}$$

where M is the principal value of the integral. With the knowledge of the complex dielectric function, all other frequency dependent optical constants can be obtained.

Compounds with orthorhombic structures have three nonzero independent components of the dielectric tensor, namely, ε^{xx}, ε^{yy} and ε^{zz}. These components, i.e., ε^{xx}, ε^{yy} and ε^{zz}, correspond to incident light with an electrical field $\vec{E}$ polarized parallel to *x*-, *y*- and *z*-axes, respectively. The calculated components ($\varepsilon_2^{xx}(\omega)$, $\varepsilon_2^{yy}(\omega)$ and $\varepsilon_2^{zz}(\omega)$) of the imaginary part of the dielectric tensor ($\varepsilon_2(\omega)$=Im($\varepsilon(\omega)$)) for the title compounds are shown in Fig. 5.16. There is a considerable anisotropy between the spectra corresponding to the different polarizations for each compound. The components of the absorptive part $\varepsilon_2(\omega)$ exhibit four peaks, labelled E_1, E_2, E_3 and E_4, in Cu_2MgSiS_4 and five peaks, labelled E_1, E_2, E_3, E_4 and E_5,

in Cu_2MgGeS_4. After the absorption edge, the superposed ε^{yy} and ε^{zz} spectra, rise rapidly followed by the ε^{xx} spectrum.

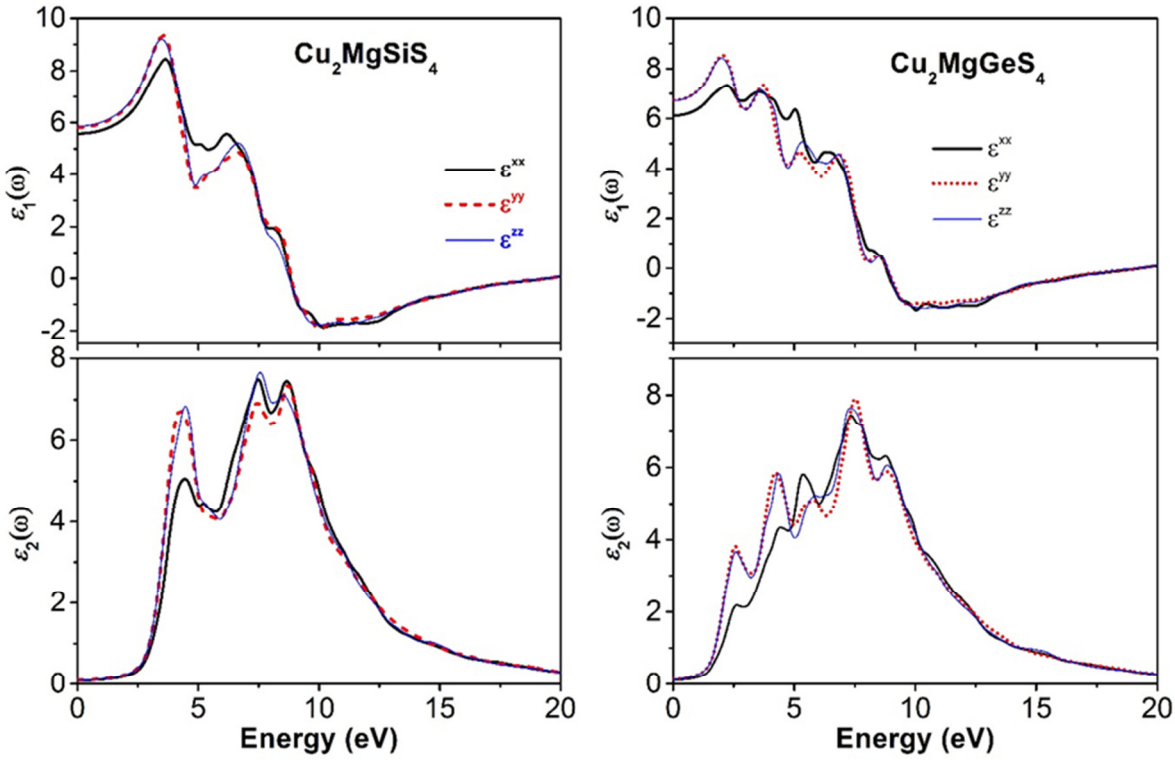

Fig. 5.16: Real and imaginary parts of the dielectric function for incident radiation with electric field polarized parallel to the three different crystal directions, *x*-, *y*- and *z*-axes, for the Cu_2MgSiS_4 and Cu_2MgGeS_4 compounds.

In order to determine the microscopic origin of the observed optical structures, the $\varepsilon_2(\omega)$ spectrum was decomposed to the individual contributions from each direct allowed electronic transition from the occupied state V_i in the valence band to the unoccupied state C_j in the conduction band $(V_i \rightarrow C_j)$ and the transition energy band $E(k)=E_{C_i}(k)-E_{V_j}(k)$ was plotted. Figures 5.17 and 5.18 show the decomposition of each component of the imaginary part of the dielectric function into band-to-band contributions and the structure of the transition energy band for Cu_2MgSiS_4 and Cu_2MgGeS_4. The fundamental absorption edge (threshold energy) E_0 for the direct optical transitions between the highest valence band and

the lowest conduction band, due to the electronic transition $V_1 \rightarrow C_1$, occurs at 2.64 eV in Cu_2MgSiS_4 and at 1.54 eV in Cu_2MgGeS_4. Positions of the center of the main structures (E_i) in the spectra of the components of $\varepsilon_2(\omega)$ and the extended direct inter-band transitions giving the dominant contributions to the optical structures and their regions in the Brillouin zone are given in Tables 5.15-5.20. The counting of the bands is from the top (bottom) for the valence (conduction) bands. The main contributions to the direct optical transitions originate from the upper valence band states to the bottom of the conduction band states. Based on the density of states spectra, we can conclude that the inter-band transitions originate predominantly from the Cu-3*d* valence bands and in a second degree from the S-3*p* valence band states to the Si-3*s* (or Ge-4*s*) and Si-3*p* (or Ge-4*p*) conduction band states.

The components of the dispersive part of the dielectric function ($\varepsilon_1(\omega)=\mathrm{Re}(\varepsilon(\omega))$) were calculated from the imaginary part $\varepsilon_2(\omega)$ via the Kramers-Kronig relation and they are shown in Fig. 5.16 also. The optical dielectric constants which corresponds to the electronic part of the static dielectric constants, a parameter of fundamental importance in many aspect of materials science, is given by the low energy limit of $\varepsilon_1(\omega)$. The calculated static dielectric constants for the considered crystals are listed in Table 5.21. The components of $\varepsilon_1(\omega \rightarrow 0)$ in Cu_2MgSiS_4 are lower than those of Cu_2MgGeS_4. This trend can be explained by the Penn model [46]:

$$\varepsilon_1(0) \approx 1 + \left(\frac{\hbar\omega_p}{E_g}\right)^2 \tag{5.36}$$

Here, $\hbar\omega_p$ is the plasma energy. The $\varepsilon_1(0)$ value is inversely proportional to the band gap E_g.

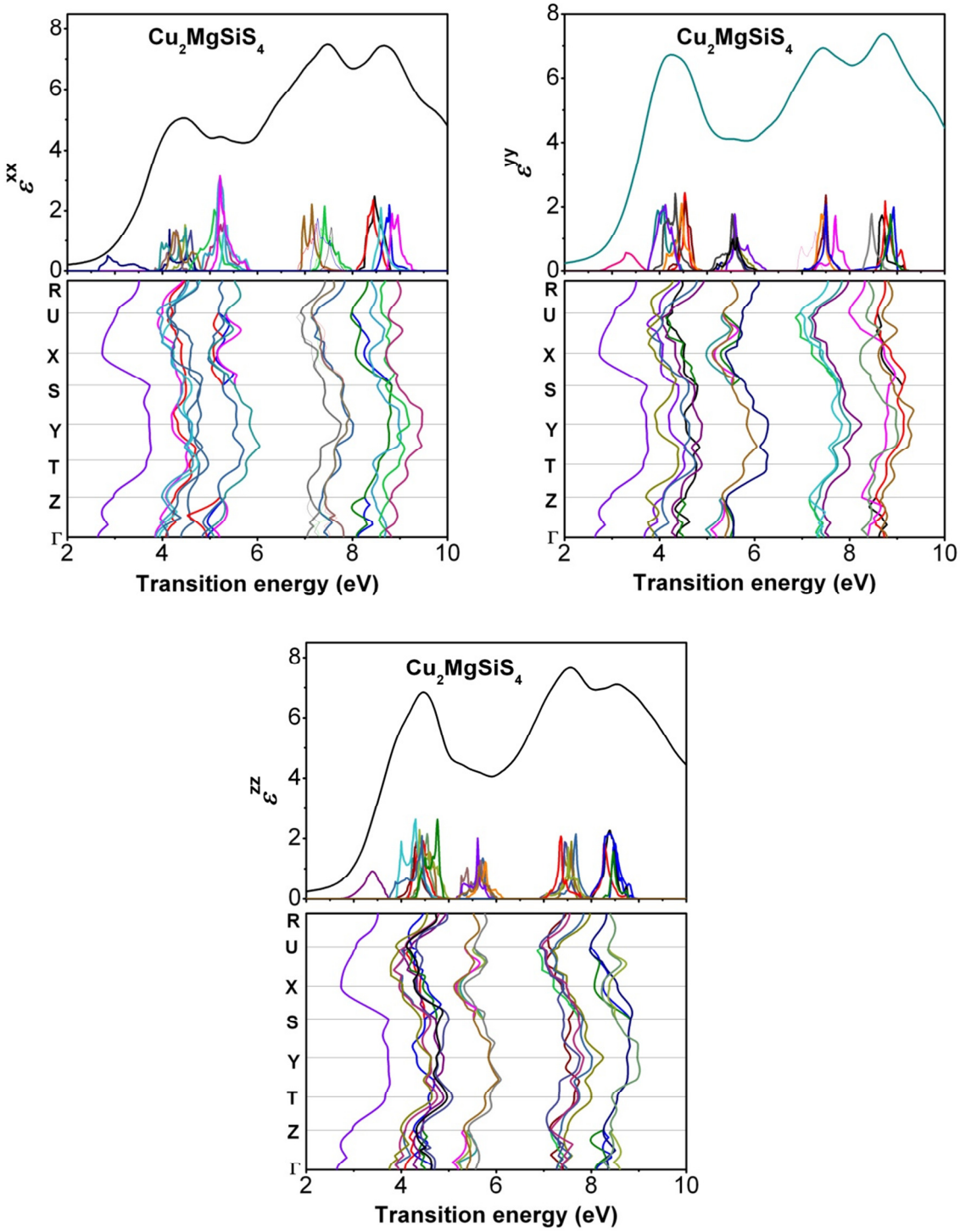

Fig. 5.17: Decomposition of the components of the imaginary part of the dielectric function into band-to-band contributions (top panels) and the transition energy band structure (bottom panels) in the Cu_2MgSiS_4 compound.

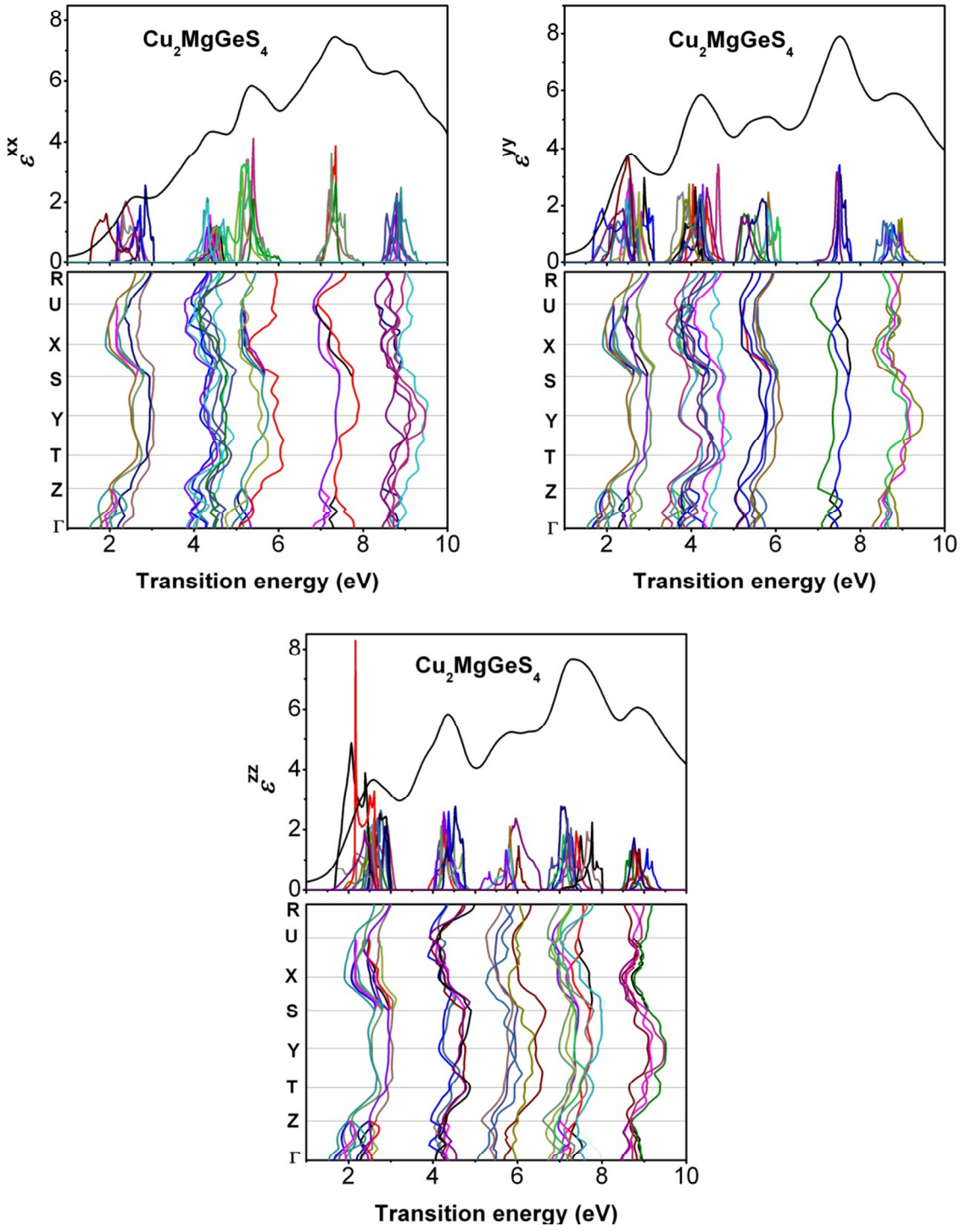

Fig. 5.18: Decomposition of the components of the imaginary part of the dielectric function into band-to-band contributions (top panels) and the transition energy band structure (bottom panels) in the Cu_2MgGeS_4 compound.

Table 5.15: Peaks positions of the $\varepsilon_2^{xx}(\omega)$ spectrum together with the dominant interband transition contributions to every peak and their location in the Brillouin zone of Cu_2MgSiS_4. The energy is in eV

Structure	Peak position	Transitions	Region transitions	Energy
E_1	4.45	V_{10}-C_3	Γ-Z-T-Y-S-X, X-X, X-U	4.60
		V_8-C_3	Z-T-Y-S-X, R-R	4.47
		V_6-C_3	Z-T-Y-S-X, U-R	4.29
		V_3-C_6	Γ-Z-T, X-U-R	4.15
		V_2-C_6	Z-T-Y-S, U-R	4.49
		V_2-C_7	Γ-Z, S-X-U-R	4.23
E_2	5.22	V_2-C_9	Γ-Z, S-X-U	5.09
		V_2-C_{10}	Γ-Z-T, Z-Z, Y-S-X-U-R	5.22, 5.31
		V_2-C_{11}	Γ-Z-T, Z-Z, S-X-U-R	5.32, 5.36
		V_1-C_{10}	Γ-Z-T, Z-Z, S-X-U-R	5.21
		V_1-C_{11}	Γ-Z, S-X-U	5.21
E_3	7.47	V_{26}-C_5	Γ-Z-T, S-X, U-R	7.55
		V_{22}-C_5	Γ-Z-T, S-X, U-R	7.22
		V_{22}-C_7	X-U-R	7.33
		V_{21}-C_6	Γ-Z-T, X-U-R	7.14
		V_{21}-C_7	Γ-Z, S-X-U-R	7.27
		V_{21}-C_8	Γ-Z-T, S-X, U-R	7.42
E_4	8.65	V_{38}-C_1	Z-T, X-U	8.46
		V_{37}-C_1	Z-T, X-U	8.44
		V_{27}-C_{10}	Γ-Z-T, Y-S-X-U	8.77
		V_{27}-C_{11}	Γ-Z, S-X-U, U-U	8.83
		V_{21}-C_{12}	Γ-Z, T-Y-S, X-U	8.60

Table 5.16: Peaks positions of the $\varepsilon_2^{yy}(\omega)$ spectrum together with the dominant interband transition contributions to every peak and their location in the Brillouin zone of Cu_2MgSiS_4. The energy is in eV

Structure	Peak position	Transitions	Region transitions	Energy
E_1	4.25	V_9-C_3	Γ-Z, Z-Z, Y-S-X-U	4.53
		V_6-C_5	Γ-Z-T, S-X, U-R	4.54
		V_5-C_3	Z-Z, S-X-U-R	4.08
		V_5-C_5	Z-Z, S-X, U-R	4.46
		V_4-C_4	Z-T-Y-S-X, U-R	4.12
		V_4-C_5	Z-T, S-X, U-R	4.33
E_2	5.51	V_2-C_{11}	Z-T, Y-S, X-U-R	5.60
		V_2-C_{12}	Γ-Z-T, Y-S-X-U-R	5.55
		V_2-C_{13}	Z-T, S-X-U	5.58
		V_1-C_{11}	Z-T, S-S, U-R, R-R	5.52
		V_1-C_{12}	Z-T, S-S, Y-S-X-U-R	5.54; 5.63
E_3	7.44	V_{28}-C_5	Z-T, S-X, U-R	7.70
		V_{25}-C_3	Z-T, S-X, U-R	7.28
		V_{25}-C_5	Z-T, S-X, U-R	7.50
		V_{24}-C_5	Γ-Z-T, S-X, U-R	7.42
		V_{23}-C_6	Z-T, S-X, U-R	7.50
E_4	8.72	V_{40}-C_1	Γ-Z-T, S-X-U-R	8.68
		V_{39}-C_2	Γ-Z-T, X-U, R-R	8.75
		V_{38}-C_2	S-X	8.92
		V_{25}-C_{11}	Z-T, T-T, S-X-U-R	8.86
		V_{21}-C_{11}	Γ-Z-T-Y, S-X-U-R	8.46

Table 5.17: Peaks positions of the $\varepsilon_2^{zz}(\omega)$ spectrum together with the dominant interband transition contributions to every peak and their location in the Brillouin zone of Cu_2MgSiS_4. The energy is in eV

Structure	Peak position	Transitions	Region transitions	Energy
E_1	4.48	V_8-C_3	Z-T-Y-S-X-U-R	4.42
		V_8-C_4	Γ-Z-T-Y, S-S, X-U, R-R	8.48
		V_6-C_5	Γ-Z-T, S-X, U-R	4.54
		V_5-C_5	Z-Z, S-X, U-R	4.46
		V_4-C_5	Z-T, S-X, U-R	4.33
		V_3-C_5	Z-T, S-X, U-R	4.30
		V_3-C_8	Z-T, S-X, U-R	4.38
		V_2-C_8	Z-T-Y-S-X	4.76
		V_1-C_6	Z-T, Y-S, U-R	4.44
E_2	5.65	V_4-C_{11}	Z-T, S-S, X-U-R	5.71
		V_3-C_{11}	Z-T, S-X-U-R	5.66
		V_3-C_{12}	Z-T, Y-S, X-U-R, R-R	5.77
		V_2-C_{11}	Z-T, Y-S, X-U-R	5.61
		V_1-C_{12}	Z-T, Y-S, U-R	5.63
E_3	7.56	V_{27}-C_4	Z-T-Y, S-X	7.58
		V_{27}-C_5	Z-T, S-X, U-R	7.67
		V_{26}-C_5	Γ-Z-T, S-X, U-R	7.56
		V_{24}-C_5	Z-T, S-X, U-R	7.44
		V_{24}-C_6	Γ-Z-T, S-X, U-R	7.51
		V_{22}-C_6	Γ-Z, T-Y, S-X-U-R	7.36
E_4	8.53	V_{38}-C_1	Γ-Z-T, S-X	8.38
		V_{37}-C_1	Γ-Z-T, S-X, U-R	8.27
		V_{37}-C_2	Γ-Z-T, X-U	8.37
		V_{22}-C_{11}	Γ-Z-T-Y, S-X-U-R	8.50
		V_{21}-C_{11}	Γ-Z-T-Y, S-X-U-R	8.46

Table 5.18: Peaks positions of the $\varepsilon_2^{xx}(\omega)$ spectrum together with the dominant interband transition contributions to every peak and their location in the Brillouin zone of Cu_2MgGeS_4. The energy is in eV

Structure	Peak position	Transitions	Region transitions	Energy
E_1	2.64	V_7-C_1	Z-T, S-X-U-R, U-U	2.71 ; 2.84
		V_5-C_1	Γ-Z-T, S-X-U-R	2.38; 2.72
		V_4-C_1	Z-T, S-X-U-R	2.33; 2.48
		V_4-C_2	Z-T-Y-S-X, U-R	2.68; 2.75
		V_3-C_2	Z-T-Y-S-X, U-R	2.72
		V_1-C_2	Z-T-Y-S-X, U-R	2.57
E_2	4.44	V_{10}-C_3	Γ-Z-T-Y-S-X-U	4.53
		V_8-C_3	Z-T-Y,S-S, S-X	4.38
		V_7-C_4	Z-T-Y, S-S, S-X	4.38
		V_6-C_4	Γ-Z-T-Y-S-X, U-R, R-R	4.23; 4.31
		V_6-C_6	Γ-Z-T, X-U-R	4.56
		V_4-C_6	Z-T-Y-S-X, U-R	4.46
		V_4-C_8	Γ-Z-T-Y-S-X, U-R	4.69
		V_2-C_6	Z-T, Y-S-X, U-R	4.31
E_3	5.36	V_{22}-C_1	Z-T, S-X, U-R	5.32
		V_{22}-C_2	T-Y, S-X, U-R	5.40
		V_{21}-C_1	Z-Z, Z-T, S-X, X-X, U-U	5.14
		V_{21}-C_2	Z-T, S-X, U-R	5.28
		V_3-C_{11}	Γ-Z, S-X-U	5.37; 5.40
		V_1-C_{10}	Γ-Z, S-X-U-R	5.18
E_4	7.33	V_{38}-C_1	T-Y, Y-Y, S-X	7.32; 7.35
		V_{37}-C_2	T-Y, Y-Y, S-X	7.35
		V_{21}-C_7	Γ-Z, X-X, X-U-R	7.20
		V_{21}-C_8	X-U-R	7.25
E_5	8.77	V_{38}-C_4	Γ-Z, T-Y, S-X-U	8.86
		V_{37}-C_4	Γ-Γ, Γ-Z-T-Y-S-X	8.75
		V_{28}-C_{10}	Γ-Z-T, Y-S-X-U	8.80
		V_{27}-C_{10}	Γ-Z-T, Y-S-X-U, X-X	8.79
		V_{27}-C_{11}	Γ-Z, S-X-U	8.90
		V_{21}-C_{13}	Z-T, S-S, S-X-U	8.84; 8.87

Table 5.19: Peaks positions of the $\varepsilon_2^{yy}(\omega)$ spectrum together with the dominant interband transition contributions to every peak and their location in the Brillouin zone of Cu_2MgGeS_4. The energy is in eV

Structure	Peak position	Transitions	Region transitions	Energy
E_1	2.57	V_8-C_1	Z-T, S-X-U-R	2.73; 2.88
		V_7-C_2	Γ-Z-T-Y-S-X, U-R	2.80; 2.99; 3.07
		V_6-C_1	Z-T, S-X-U-R	2.56; 2.82
		V_4-C_1	Z-T, Y-Y, S-X, U-R	2.55
		V_4-C_2	Z-T-Y-S-X, T-T, U-R	2.63; 2.76
		V_3-C_1	Z-T, S-X, U-R	2.45
		V_3-C_2	Z-T-S-X, U-R	2.57
		V_1-C_1	Z-T, S-X, U-R	2.38
		V_1-C_2	Z-T,Y-Y, Y-S-X, U-R	2.50
E_2	4.23	V_{11}-C_3	Z-T, S-X-U-R, U-U	4.64
		V_6-C_4	Z-T-Y-S-X, U-R	4.27
		V_6-C_5	Γ-Z-T, S-X, U-R	4.37
		V_4-C_3	Z-T-Y-S-X-U-R	3.80; 3.92
		V_4-C_5	Z-T, Y-S-X, U-R	4.25
		V_3-C_6	Γ-Z-T-Y-S-X,Y-Y, X-X, U-R	4.06; 4.37
		V_2-C_5	Z-T, Y-S-X, U-R	4.20
		V_1-C_4	Z-T-Y, S-S, R-R	3.95
		V_1-C_6	Z-T, Y-S-X, U-R	4.22
E_3	5.80	V_{28}-C_1	Z-T, S-X, U-R	5.82
		V_{27}-C_1	Z-T, S-X, U-R	5.82
		V_{23}-C_1	Γ-Z-T, X-U, U-U	5.25; 5.35
		V_{23}-C_2	T-T, S-X	5.69
		V_{22}-C_1	Z-T, S-X, U-R	5.32
E_4	7.52	V_{40}-C_1	Γ-Z-T-Y, X-U-R	7.51
		V_{39}-C_2	Γ-Z, T-Y, S-X, U-R	7.54
		V_{38}-C_2	Γ-Z, S-S, S-X	7.44
E_5	8.80	V_{24}-C_{11}	Z-T, S-X-U-R	8.89
		V_{23}-C_{11}	Γ-Z, S-X-U	8.63
		V_{22}-C_{13}	Γ-Γ, Z-T, Y-S, X-U-R	8.91; 8.98
		V_{21}-C_{11}	Γ-Z, S-X-U-R	8.56
		V_{21}-C_{12}	Z-T-Y, S-X-U	8.74

Table 5.20: Peaks positions of the $\varepsilon_2^{zz}(\omega)$ spectrum together with the dominant interband transition contributions to every peak and their location in the Brillouin zone of Cu_2MgGeS_4. The energy is in eV

Structure	Peak position	Transitions	Region transitions	Energy
E_1	2.60	V_7-C_1	Z-T, S-X, U-R	2.84; 2.90
		V_6-C_1	Z-T, S-X-U-R	2.63; 2.76
		V_6-C_2	Z-T, S-X, U-R	2.75
		V_5-C_1	Γ-Z, X-U	2.45
		V_4-C_1	Z-T, Y-S-X, U-R	2.54
		V_4-C_2	Z-T-Y-S-X, U-R	2.64; 2.68
		V_3-C_1	Z-T-Y-S-X, Y-Y, U-R	2.56
		V_3-C_2	Z-T-Y-S-X, U-R	2.61
		V_2-C_1	Z-T, S-X, U-R	2.39
		V_2-C_2	Z-T-Y,S-S, S-X, R-R	2.61
		V_1-C_1	Z-T, Y-S-X, U-R	2.38; 2.48
E_2	4.37	V_8-C_3	Z-T-Y-S, X-X, X-U, R-R	4.34
		V_7-C_4	Γ-Z-T-S-X, U-R	4.31; 4.49
		V_6-C_4	Γ-Z-T-S-X, U-R	4.29
		V_6-C_5	Γ-Z-T, S-X, U-R	4.37
		V_5-C_5	Γ-Z, S-X-U-R	4.26
		V_3-C_7	Γ-Z, S-X-U-R	4.19
		V_2-C_8	Γ-Z-T-Y, S-X, U-R	4.53
E_3	5.86	V_{31}-C_1	Z-Z, X-U-R	5.96
		V_{25}-C_2	T-Y, S-X, U-R	5.82
		V_{24}-C_2	Y-Y, Y-S-X	5.80
E_4	7.32	V_{40}-C_1	Γ-Z-T,T-T, X-U-R	7.50
		V_{39}-C_1	Z-Z, S-X-U	7.39
		V_{38}-C_1	Γ-Z-T, S-X-U-R	7.18; 7.29
		V_{37}-C_2	Γ-Z-T, S-X, U-R	7.03; 7.12
		V_{27}-C_3	Z-T, S-X, U-R	7.27
		V_{25}-C_5	Γ-Z-T, X-X, U-R	7.21
		V_{24}-C_4	Γ-Z, T-T, T-Y-S-X	7.18
E_5	8.84	V_{24}-C_{12}	Γ-Z-T, S-X-U	8.90
		V_{23}-C_{11}	Z-T, S-X-U-R	8.76
		V_{22}-C_{11}	Z-T-Y, S-X-U-R	8.67
		V_{22}-C_{12}	Γ-Z-T-Y-S-X-U	8.76
		V_{21}-C_{13}	Z-T, S-S, X-U	8.88

5.2.4.2. Refractive index and extinction coefficient

One of the most important optical constants of a material is its refractive index, which in general depends on the wavelength of the electromagnetic wave, through a relationship called *dispersion*. In materials where an electromagnetic wave can lose its energy during its propagation, the refractive index becomes complex as follow:

$$\tilde{n} = n + ik \tag{5.37}$$

The real part of $\tilde{n}$, namely n, is the same as the normal refractive index which is defined as the ratio of the velocity of light in free space c to the velocity of light in the medium v; $n = c/v$. The imaginary part of $\tilde{n}$, namely k, is called the *extinction coefficient*, which is directly related to the absorption light of the medium (The extinction coefficient k vanishes for lossless materials). For non-magnetic materials ($\mu = 1$), the complex refractive index can be related to the complex dielectric constant by: $\tilde{n} = \sqrt{\tilde{\varepsilon}}$. Therefore, the refractive index $n(\omega)$ and the extinction coefficient $k(\omega)$, are given as follows:

$$n(\omega) = \sqrt{\frac{|\varepsilon(\omega)| + \varepsilon_1(\omega)}{2}} \tag{5.38}$$

$$k(\omega) = \sqrt{\frac{|\varepsilon(\omega)| - \varepsilon_1(\omega)}{2}} \tag{5.39}$$

Fig. 5.19 displays the frequency dependent refractive index $n(\omega)$ and extinction coefficient $k(\omega)$ for three different polarizations of the incident radiations for Cu_2MgSiS_4 and Cu_2MgGeS_4 in a wider spectral region up to 30 eV. The calculated zero energy ($\lambda = \infty$) $n(0)$ values and the energies for which the dispersion is null ($E(n=1)$) are listed in Table 5.21. The maximum of the $n(\omega)$ is found at ~3.65 eV for the [010] polarization, while the maximum of the $k(\omega)$ appears at high energy (~9.0 eV). The refractive index increases with increasing photon energy in the visible part of the spectrum.

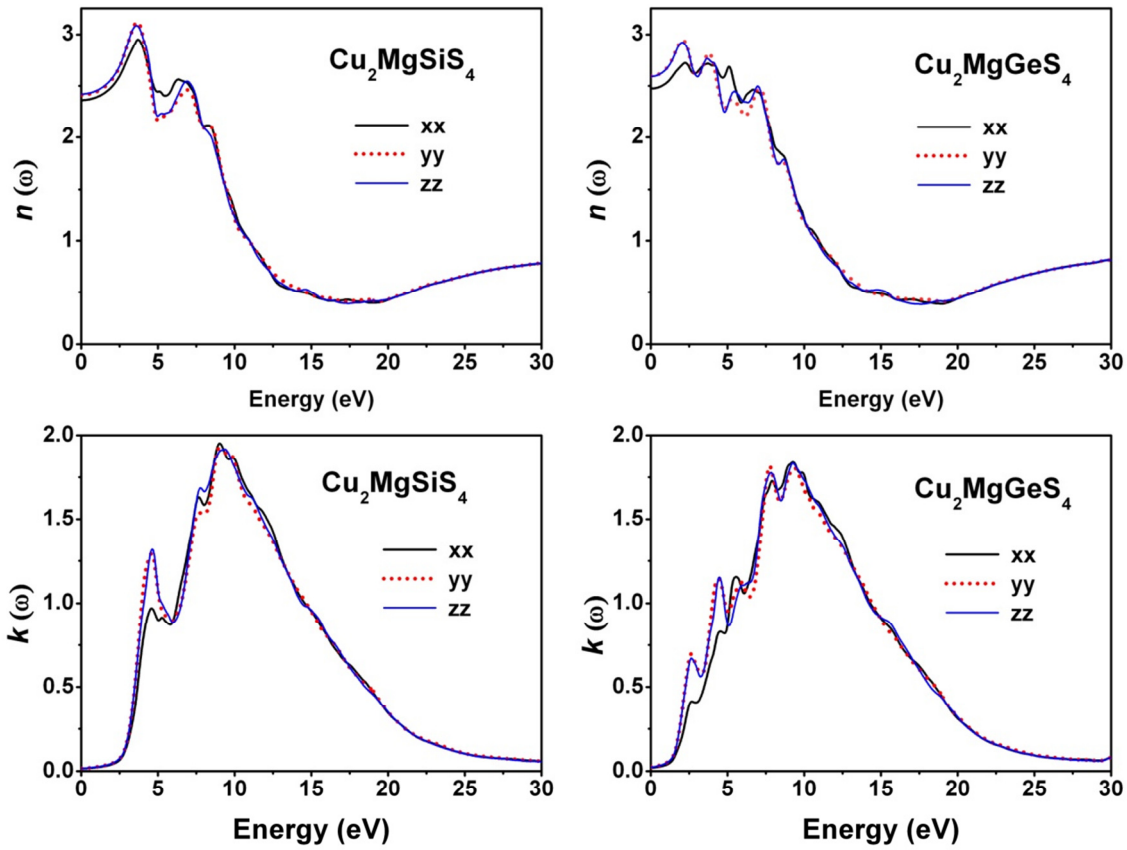

Fig. 5.19: Calculated refractive index $n(\omega)$ and extinction coefficient $k(\omega)$ for the Cu_2MgSiS_4 and Cu_2MgGeS_4 compounds.

Table 5.21: Calculated static dielectric constant $\varepsilon_1(0)$, static refractive index $n(0)$ and energy for which the dispersion is null (E(n=1)) for the Cu_2MgSiS_4 and Cu_2MgGeS_4 compounds for three polarizations. Energy values are in eV

	[100]	[010]	[001]
Cu_2MgSiS_4			
$\varepsilon_1(0)$	5.576	5.816	5.864
n (0)	2.361	2.412	2.422
E (n = 1)	10.98	10.93	10.95
Cu_2MgGeS_4			
$\varepsilon_1(0)$	6.119	6.729	6.716
n (0)	2.474	2.594	2.592
E (n = 1)	10.95	10.90	10.79

5.2.4.3. Absorption coefficient

The absorption of light by an optical medium is quantified by its absorption coefficient α. This is defined as the fraction of the power absorbed in a unit length of the medium. If the wave is propagating in the z direction, the absorption coefficient is given by Beer's law as follow:

$$I(z) = I_0 e^{-\alpha z} \tag{5.40}$$

where $I(z)$ and I_0 are the optical intensities (optical power per unit area) at position z and at z=0, respectively. The absorption coefficient α is directly related to extinction coefficient k. By considering the propagation of plane electromagnetic waves through a medium with a complex refractive index, we can conclude the relationship between α and k, using the relationship between the optical intensity and the electric field, as follow:

$$\alpha(\omega) = \frac{2k\omega}{c} \tag{5.41}$$

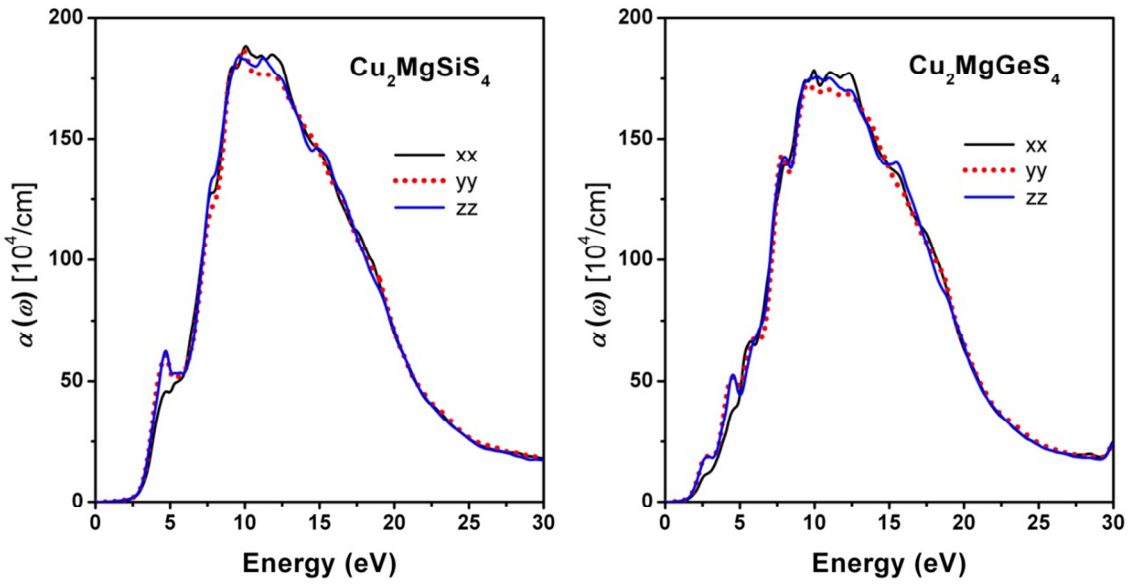

Fig. 5.20: Calculated absorption coefficient $\alpha(\omega)$ for the Cu_2MgSiS_4 and Cu_2MgGeS_4 compounds.

Fig. 5.20 shows the calculated absorption coefficient $\alpha(\omega)$. The absorption coefficient $\alpha(\omega)$ indicates the fraction of energy lost by the incident radiation per length unit when it passes through a material. The absorption coefficient $\alpha(\omega)$ increases rapidly when the photon energy is higher than the absorption edge and reaches its maximal value ($\sim 2\times10^6$ cm^{-1}) at about 10 eV. This is a typical characteristic of semiconductors and insulators. Both Cu_2MgSiS_4 and Cu_2MgGeS_4 exhibit a noticeable absorption in the ultraviolet range. The strong absorption of the UV light makes these quaternary semiconductors very competitive for the UV light detector.

5.2.4.4. Reflectivity and loss function

The reflection at the surfaces is described by the coefficient of reflection or reflectivity *R*. It is defined as the ratio of the reflected power to the power incident on the surface. If we apply appropriate boundary conditions to a solid surface, Maxwell relations lead us to the relationship:

$$R(\omega) = \left|\frac{\tilde{n}-1}{\tilde{n}+1}\right|^2 = \frac{(n-1)^2+k^2}{(n+1)^2+k^2} \tag{5.42}$$

A further property that can be calculated from the complex dielectric constant is the energy loss function $L(\omega)$. It describes the energy lost by an electron passing through a homogeneous dielectric material and is given by:

$$L(\omega) = Im\left(\frac{-1}{\varepsilon(\omega)}\right) = \frac{\varepsilon_2(\omega)}{\varepsilon_1^2(\omega)+\varepsilon_2^2(\omega)} \tag{5.43}$$

Fig. 5.21(a) shows the frequency dependent reflectivity spectra $R(\omega)$ for three different polarizations of the incident radiation for Cu_2MgSiS_4 and Cu_2MgGeS_4. The $R(\omega)$ increases with increasing photon energy in the ultraviolet region and reaches its maximal value of approximately 40-45% at about 15 eV in both title compounds.

The electron energy loss function $L(\omega)$ of Cu_2MgSiS_4 and Cu_2MgGeS_4 is depicted in Fig. 5.21(b). The location of its primary peak is generally associated to the plasma frequency ω_p, which occurs when $\varepsilon_2 < 1$ and $\varepsilon_1 = 0$ [47]. A sharp maximum of the $L(\omega)$ spectrum at approximately 20 eV is associated with the plasma oscillations. The peak of $L(\omega)$ corresponds to the trailing edges in the reflection spectrum.

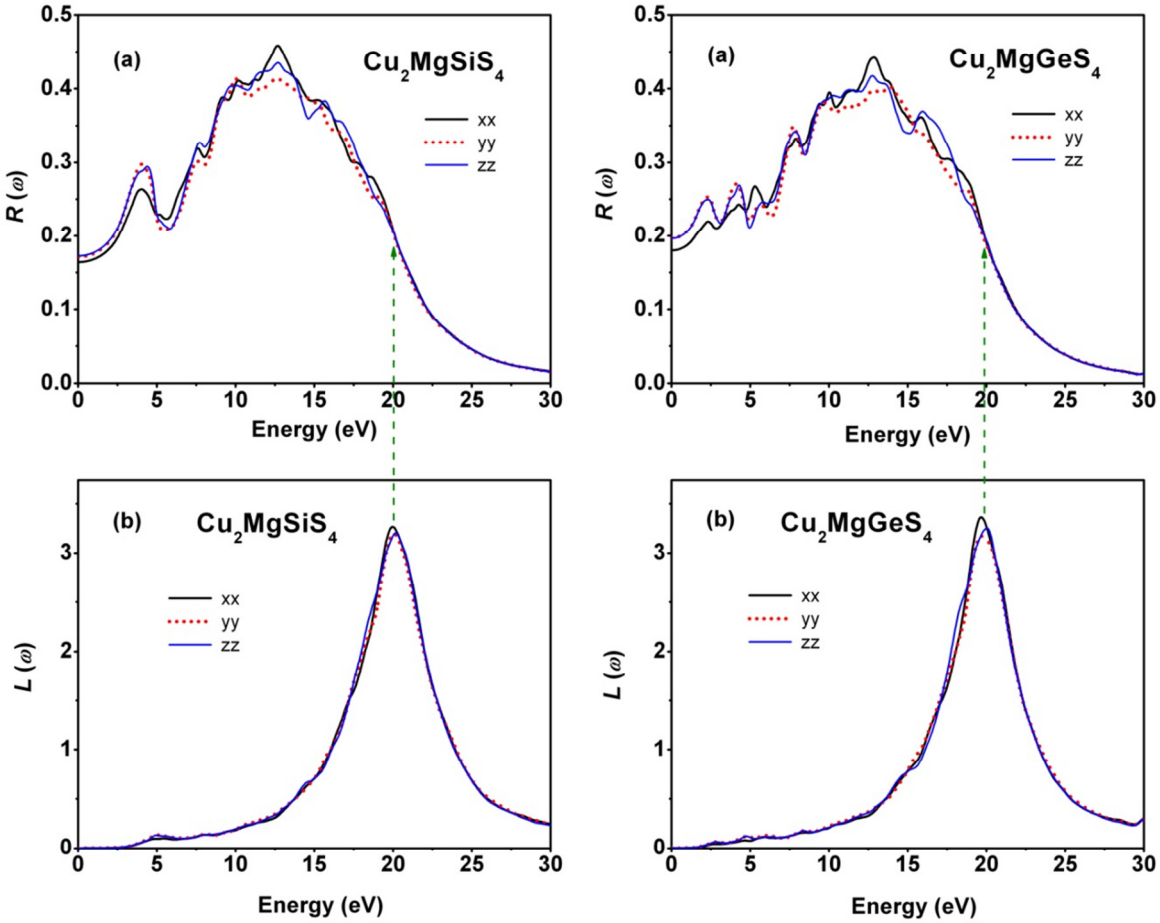

Fig. 5.21: Calculated reflectivity $R(\omega)$ and energy-loss function $L(\omega)$ for the Cu_2MgSiS_4 and Cu_2MgGeS_4 compounds.

5.2.4.5. Optical conductivity

The optical conductivity is a material property, which links the current density to the alternating electric field. The frequency-dependent complex conductivity $\sigma(\omega)$ is also such as dielectric constant directly related to the energy band structure of solids. The optical conductivity is related to the dielectric constant by the following relationship:

$$\sigma(\omega) = \sigma_1(\omega) + i\sigma_2(\omega) = -i\frac{\omega}{4\pi}[\varepsilon(\omega) - 1] \tag{5.44}$$

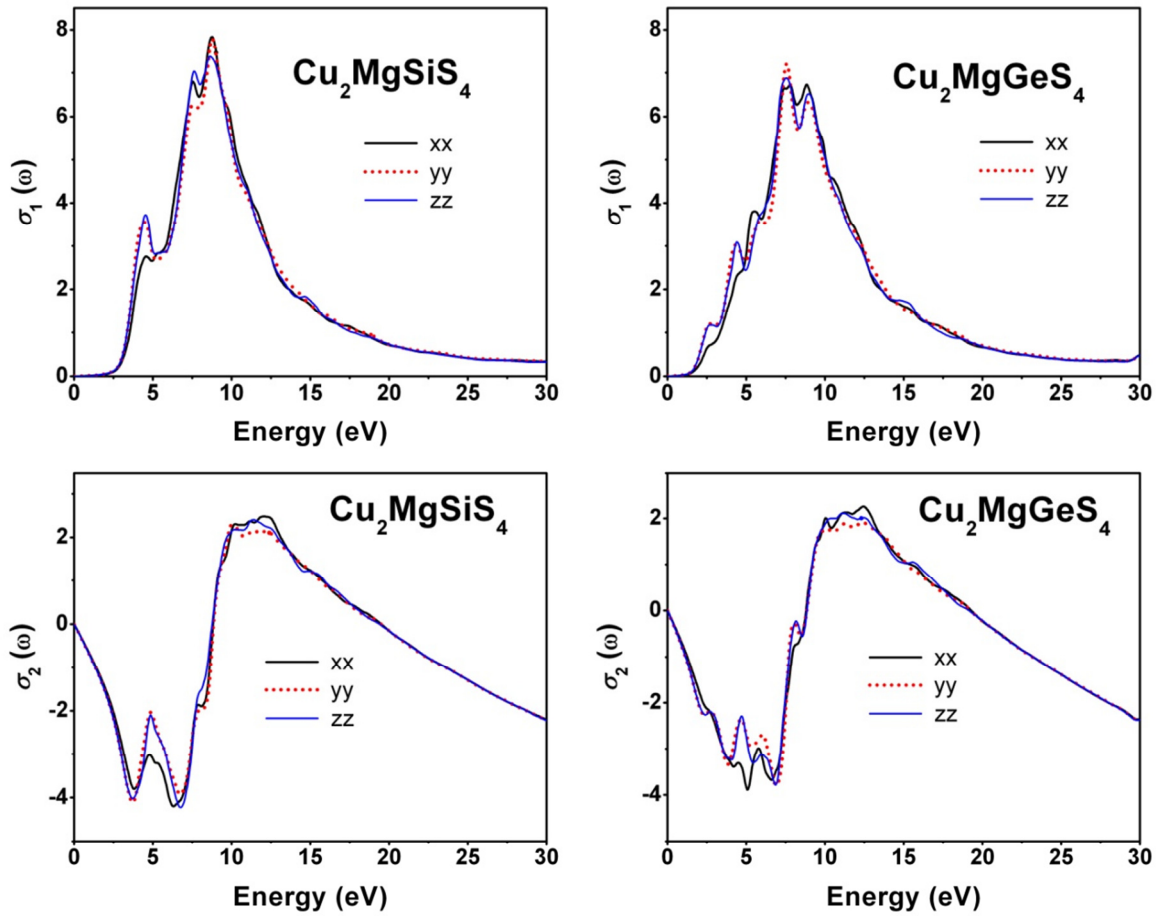

Fig. 5.22: Calculated complex optical conductivity $\sigma(\omega)$ for the Cu_2MgSiS_4 and Cu_2MgGeS_4 compounds.

The optical conductivity function $\sigma(\omega)$ spectra are depicted in Fig. 5.22. The real part ($\sigma_1(\omega)$) of the conductivity function is negligible for photon energy in the band gap, and increases rapidly to reach a maximum in the UV region, confirming that these compounds have semiconductor properties.

We do not find optical data in the literature for Cu_2MgSiS_4 and Cu_2MgGeS_4, and we hope our calculations will lead to further experimental efforts on these materials. By combining the measured data with the calculation results, a near total understanding of the electronic and optical properties of the title materials is possible.

References

[1] S. J. Clark, M. D. Segall, C. J. Pickard, et al, *First principles methods using CASTEP*, Zeitschrift fuer Kristallographie 220, 567-570 (2005).

[2] J. P. Perdew, A. Ruzsinszky, G. I. Csonka, O. A. Vydrov, G.E. Scuseria, L.A. Constantin, X. Zhou, K. Burke, *Restoring the Density-Gradient Expansion for Exchange in Solids and Surfaces*, Phys. Rev. Lett. 100, 136406-4 (2008).

[3] D. Vanderbilt, *Soft self-consistent pseudopotentials in a generalized eigenvalue formalism*, Phys. Rev. B 41, 7892-4 (1990).

[4] H. J. Monkhorst, J. D. Park, *Special points for Brillouin-zone integrations*, Phys. Rev. B 13, 5188-5 (1976).

[5] T. H. Fischer, J. Almlof, *General methods for geometry and wave function optimization*, J. Phys. Chem. 96, 9768-9774 (1992).

[6] W. Voigt, *Lehrbuch der Kristallphysik* (*Textbook of crystal physics*), Teubner, Leipzig, 1928.

[7] A. Reuss, Z. Angew, *Calculation of the yield strength of solid solutions based on the plasticity condition of single crystals*, Math. Mech. 9, 49-58 (1929).

[8] R. Hill, *The elastic behavior of a crystalline aggregate*, Proc. Phys. Soc. A 65, 349-354 (1952).

[9] F. Tran, P. Blaha, *Accurate Band Gaps of Semiconductors and Insulators with a Semilocal Exchange-Correlation Potential*, Phys. Rev. Lett. 102, 226401-4 (2009).

[10] P. Blaha, K. Schwarz, G. K. H. Madsen, D. Kvasnicka, J. Luitz, *WIEN2k: An Augmented Plane Wave + Local Orbitals Program for Calculating Crystal Properties*, Karlheinz Schwarz Techn. Universität, Wien, Austria, 2013 ISBN: 3-950131-1-2

[11] A. D. Becke, E. R. Johnson, *A simple effective potential for exchange*, J. Chem. Phys. 124, 221101-4 (2006).

[12] C. S. Wang, W. T. Pickett, *Density-Functional Theory of Excitation Spectra of Semiconductors: Application to Si*, Phys. Rev. Lett. 51, 597-4 (1983).

[13] W. G. Aulbur, L. Jönsson, J. W. Wilkins, *Quasi particle calculations in solids*, Solid State Phys. 54, 1-218 (2000).

[14] S. Z. Karazhanov, P. Ravindran, H. Fjellvag, B. G. Svensson, *Electronic structure and optical properties of $ZnSiO_3$ and Zn_2SiO_4*, J. Appl. Phys. 106, 123701-7 (2009).

[15] D. Koller, F. Tran, P. Blaha, *Merits and limits of the modified Becke-Johnson exchange potential*, Phys. Rev. B 83, 195134-10 (2011).

[16] C. Ambrosch-Draxl, J. O. Sofo, *Linear optical properties of solids within the full potential linearized augmented plane wave method*, Comput. Phys. Commun. 175, 1-14 (2006).

[17] B. W. Liu, M. J. Zhang, Z. Y. Zhao, H. Y. Zeng, F. K. Zheng, G. C. Guo, J. S. Huang, *Synthesis, Structure, and Optical Properties of the Quaternary Diamond-Like Compounds I_2-II-IV-VI_4 (I = Cu; II = Mg; IV = Si, Ge; VI = S, Se)*, J. Solid State Chem. 204, 251-256 (2013).

[18] W. Schäfer, R. Nitsche, *Zur Sytematik tetraedrischer Verbindungen vom Typ Cu_2-II-IV-VI_4 (Stannite und Wurtzstannite)*, Z. Kristallogr. 145, 356-370 (1977).

[19] W. Schäfer, R. Nitsche, *Tetrahedral quaternary chalcogenides of the type Cu_2-II-IV-S_4(Se_4)* Mater. Res. Bull. 9 (1974) 645-654.

[20] F. Birch, *Finite strain isotherm and velocities for single crystal and polycrystalline NaCl at high pressure and* 300 *K*, J. Geophys. Res. B 83, 1257-1268 (1978).

[21] F. D. Murnaghan, *The compressibility of media under extreme pressure*, Proc. Natl. Acad. Sci. U.S.A. 30, 244-247 (1944).

[22] F. Birch, *Finite elastic strain of cubic crystals*, Phys. Rev. 71, 809:1-16 (1947).

[23] C. L. Fu, K. M. Ho, *First-principles calculation of the equilibrium ground-state properties of transition metals: Applications to Nb and Mo*, Phys. Rev. B 28, 54807 (1983).

[24] P. Vinet, J. Ferrante, J. H. Rose, J. R. Smith, *Compressibility of solids*, J. Geophys. Res. 92, 9319-9325 (1987).

[25] M. Born, K. Huang, *Dynamical Theory of Crystal Lattices*, New York: Oxford University Press, 1988.

[26] L. D. Landau, E.M. Lifshitz, *Theory of Elasticity, Course of Theoretical Physics,* Pergamon Press, New York, 1980.

[27] A. Bouhemadou, G. Uğur, Ş. Uğur, S. Al-Essa, M. A. Ghebouli, R. Khenata, S. Bin-Omran, Y. Al-Douri, *Elastic and thermodynamic properties of $ZnSc_2S_4$ and $CdSc_2S_4$ compounds under pressure and temperature effects*, Compt. Mat. Sci. 70, 107-113 (2013).

[28] K. Haddadi, A. Bouhemadou, L. Louail, *Ab initio investigation of the structural, elastic and electronic properties of the anti-perovskite $TlNCa_3$*, Solid State Commun. 150, 932-937 (2010).

[29] S. F. Pugh, *Relations between the elastic moduli and plastic properties of polycrystalline pure metals*, Philos. Mag. 45, 823-843 (1954).

[30] O. L. Anderson, *A simplified method for calculating the Debye temperature from elastic constants*, J. Phys. Chem. Solids 24, 909-917 (1963).

[31] E. Schreiber, O. I. Anderson, N. Soga, *Elastic constants and their measurements*, McGraw-Hill Companies, New York, 1974.

[32] P. Ravindran, L. Fast, P. A. Korzhavyi, B. Johansson, O. Eriksson, *Density functional theory for calculation of elastic properties of orthorhombic crystals: application to $TiSi_2$*, J. Appl. Phys. 84, 4891-14 (1998).

[33] P. Lloveras, T. Castán, M. Porta, A. Planes, A. Saxena, *Influence of elastic anisotropy on nanoscale textures*, Phys. Rev. Lett. 100, 165707-4 (2008).

[34] D. Connétable, O. Thomas, *First-principles study of the structural, electronic, vibrational, and elastic properties of orthorhombic NiSi*, Phys. Rev. B 79, 094101-9 (2009).

[35] H. Chung, W. R. Buessem, in: F. W. Vahldiek, S. A. Mersol (Eds.), *Anisotropy in Single Crystal Refractory Compound*, Plenum, New York, 1968.

[36] S. I. Ranganathan, M. Ostoja-Starzewski, *Universal Elastic Anisotropy Index*, Phys. Rev. Lett. 101, 055504-4 (2008).

[37] J. F. Nye, Properties of crystals, Oxford University Press, 1985

[38] A. Bouhemadou, K. Haddadi, S. Bin-Omran, R. Khenata, Y. Al-Douri, S. Maabed, *Structural, elastic, electronic and optical properties of the quaternary nitridogallate $LiCaGaN_2$: First-principles study*, Mat. Sci. Semicond. Process. 40, 64-76 (2015).

[39] N. W. Ashcroft, N. D. Mermin, *Solid State Physics*, Saunders College Publishing, New York, 1976.

[40] G. G. Yao, H. S. Shen, E. D. Honig, R. Kershaw, K. Dwight, and A. Wold, *Preparation and characterization of the quaternary chalcogenides $Cu_2B^{(II)}C^{(IV)}X_4$ [$B^{(II)}$ = Zn, Cd; $C^{(IV)}$ = Si, Ge; X = S, Se*], Solid State Ion. 24, 249-252 (1987).

[41] V. V. Filonenko, B. D. Nechiporuk, N. E. Novoseletskii, V. A. Yukhimchuk, Y. F. Lavorik, *Preparation and some properties of Cu_2CdGeS_4 crystals*, Inorg. Mater. 27, 981-983 (1991).

[42] J. S. Seol, S. Y. Lee, J. C. Lee, H. D. Nam, K. H. Kim, *Electrical and optical properties of Cu_2ZnSnS_4 thin films prepared by rf magnetron sputtering process*, Sol. Energy Mater. Sol. Cells 75, 155-162 (2003).

[43] S. Wagner, P. M. Bridenbaugh, *Multicomponent tetrahedral compounds for solar cells*, J. Cryst. Growth 39, 151-159 (1977).

[44] A. H. Reshak, K. Nouneh, I. V. Kityk, Jiri Bila, S. Auluck , H. Kamarudin , Z. Sekkat, *Structural, electronic and optical properties in earth-abundant photovoltaic absorber of Cu_2ZnSnS_4 and $Cu_2ZnSnSe_4$ from DFT calculations*, Int. J. Electrochem. Sci. 9 955-974 (2014).

[45] D. B. Melrose and R. J. Stoneham, Generalised Kramers-Kronig formula for spatially dispersive media. J. Phys. A: Math. Gen. **10**, L17-L20 (1977).

[46] D. R. Penn, *Wave-Number-Dependent Dielectric Function of Semiconductors***,** Phys. Rev. 128, 2093-5 (1960).

[47] C. Li, Z. Wang, C. Wang, *First-principles study of the structural, elastic, electronic and optical properties of the monoclinic $BiScO_3$*, Phys. B 406, 2028-2032 (2011).

CHAPTER 6

Structural, elastic and thermodynamic properties of tetragonal and orthorhombic polymorphs of Sr_2GeN_2

Chapter 6

Structural, elastic and thermodynamic properties of tetragonal and orthorhombic polymorphs of Sr_2GeN_2

Contents

6.1. Computational details

All performed ab initio calculations in the present work were carried out using pseudopotential plane-wave (PP-PW) method in the framework of density functional theory as implemented in the CASTEP module [1]. The exchange-correlation effects were treated using the recent developed generalized gradient approximation of Perdew *et al.* [2], the so-called GGA-PBEsol, which is known to yield better results for solids. To take into account the contribution of core electrons, Vanderbilt ultra-soft pseudopotential [3] was employed. The Sr: $4s^2 4p^6 5s^2$, Ge: $4s^2 4p^2$ and N: $2s^2 2p^3$ orbitals were treated as electronic valence states. The Monkhorst-Pack scheme [4] was used for the *k*-points sampling in the Brillouin zone (BZ). A kinetic energy cutoff of 280 eV and *k*-mesh corresponding to a separation of 0.03Å^{-1} (0.04Å^{-1}) in the reciprocal space for the α-Sr_2GeN_2 (β-Sr_2GeN_2) phase were used. These calculation parameters were chosen after careful convergence tests.

The optimized structural parameters were obtained using the Broyden-Fletcher-Goldfarb-Shanno (BFGS) minimization algorithm [5]. The lattice parameters and internal coordinates were relaxed until: (i) total energy variation was smaller than 5.0 ×10^{-6} eV/atom, (ii) the absolute value of force on any atom was less than 0.01 eV/Å, (iii) stress was smaller than 0.02 GPa and (iv) atomic displacement was smaller than 5.0 ×10^{-4} Å.

The elastic properties of single-crystal and polycrystalline aggregates of α-Sr_2GeN_2 and β-Sr_2GeN_2 compounds were explored by calculating their independent elastic constants C_{ij}, bulk modulus *B*, shear modulus *G*, Young's modulus *E*, Poisson's coefficient σ and related properties. The C_{ij} were obtained via linear fittings of the stress-strain curves computed from accurate ab initio calculations [1]. The main advantage of this method is the great reduction of the independent strain modes number compared to the ab initio total energy versus strain approach. The elastic stiffness tensor is related to the stress tensor and the strain tensor by Hooke's law. Since the stress tensor and the strain tensor are symmetric, the most general elastic stiffness tensor has only 21 non-zero independent components. For a tetragonal crystal, they are reduced to six independent components, namely C_{11}, C_{33}, C_{44}, C_{66}, C_{12} and C_{13}, and for an orthorhombic crystal, they are reduced to nine independent components, namely C_{11}, C_{22}, C_{33}, C_{44}, C_{55}, C_{66}, C_{12}, C_{13} and C_{23}. To determine the six independent elastic constants C_{ij} of the tetragonal system, two strain patterns - one with nonzero ε_{11} and ε_{23} components and the second with nonzero ε_{33} and ε_{12} components - were used. To obtain the

nine independent components of the elastic tensor for the orthorhombic phase, three strain patterns - one with nonzero ε_{11} and ε_{23} components, second with nonzero ε_{22} and ε_{31} components and the third with non-zero ε_{33} and ε_{12} components - were used. The elastic constants were performed with the following convergence criteria: 1.0×10^{-6} eV/atom for the total energy, 0.002 eV/Å for the Hellman-Feynman force and 1.0×10^{-4} Å for the maximal ionic displacement. After calculating the single-crystal elastic constants C_{ij}, the polycrystalline elastic moduli and related properties were evaluated using the well-known Voigt-Reuss-Hill approximations [6-8].

Knowledge of the behaviours of solids when they are under severe constraints such as high pressure and high temperature environment are of a great interest and importance for both the fundamental research and technological applications. To address this interest in the present work, pressure and temperature dependences of the unit-cell volume, bulk modulus, volume expansion coefficient, isochoric heat capacity and Debye temperature of both considered phases were explored using the PP-PW method [1] combined with the quasi-harmonic Debye model as implemented in Gibbs program [9]. Theoretical details about the quasi-harmonic Debye model are available in Ref. [9].

6.2. Results and discussions

6.2.1. Structural properties

6.2.1.1. Structural description

The α-Sr_2GeN_2 compound crystallizes in a tetragonal structure ($a = b \neq c$ and $\alpha = \beta = \gamma = 90°$), space group $P4_2/mbc$ (No. 135), with eight unit formulas (i.e., 8 Sr_2GeN_2) per unit-cell (Z=8), while the β-Sr_2GeN_2 polymorph crystallizes in an orthorhombic structure ($a \neq b \neq c$ and $\alpha = \beta = \gamma = 90°$), space group *Cmac* (No. 64), with eight unit formulas per unit-cell (Z=8) also [10,11]. This implies that the unit-cell of both polymorphs contains 40 atoms: 16 Sr, 16 N and 8 Ge. The atomic positions in the α-Sr_2GeN_2 crystal are Sr1 (x_{Sr1}, y_{Sr1}, 0), Sr2 (x_{Sr2}, y_{Sr2}, 0), Ge (x_{Ge}, y_{Ge}, 0), N1 (x_{N1}, y_{N1}, 0) and N2 (x_{N2}, y_{N2}, 0) and in the β-Sr_2GeN_2 crystal, they are Sr1 (0, y_{Sr1}, z_{Sr1}), Sr2 (0, y_{Sr2}, z_{Sr2}), Ge (0, y_{Ge}, z_{Sr2}), N1 (0, y_{N1}, z_{N1}) and N2 (*0*, y_{N2}, z_{N2}). The atoms are indexed in order to distinguish between the inequivalent crystallographic positions of the same chemical element.

A differentiating factor of the crystalline structures of these two polymorphs is the relative orientation of the GeN_2 units in the lattice [10,11]. Fig. 6.1 displays the unit-cells of the tetragonal and orthorhombic polymorphs of Sr_2GeN_2. As one can observe, the GeN_2 units belong to the plane (001) in the α-Sr_2GeN_2 crystal, while in the β-Sr_2GeN_2 crystal, they belong to the plane (100). From Fig. 6.1, one can observe that both α-Sr_2GeN_2 and β-Sr_2GeN_2 crystals are layered materials; the layers are stacked along the *c*-axis in α-Sr_2GeN_2, while in β-Sr_2GeN_2, they are stacked along the *a*-axis. The structural difference between these two compounds is due to the manner that adjacent planes are stacked. The stacking is carried out in alternating manner for both compounds. As shown in Fig. 6.2, for α-Sr_2GeN_2, the adjacent planes A and A', which are stacked along the *c*-axis according to the following sequence: ...AA'AA'AA'…, are related by a 90° rotation, i.e., A' plane is produced by rotating the A plane by an angle of 90°. Whereas, in β-Sr_2GeN_2, the adjacent planes A and A', which are stacked along the *a*-axis according to the following sequence: ...AA'AA'AA'…, are related by a translation of $\frac{1}{2}\vec{b}$, i.e., A' plane is a result of the translation of the A plane by $\frac{1}{2}\vec{b}$.

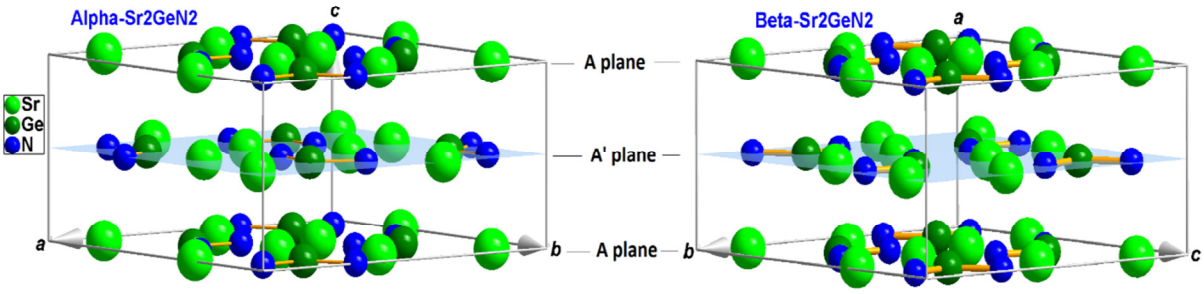

Fig 6.1: Unit-cell structures of the tetragonal and orthorhombic polymorphs of the Sr_2GeN_2 crystal (α-Sr_2GeN_2 and β-Sr_2GeN_2 phases, respectively).

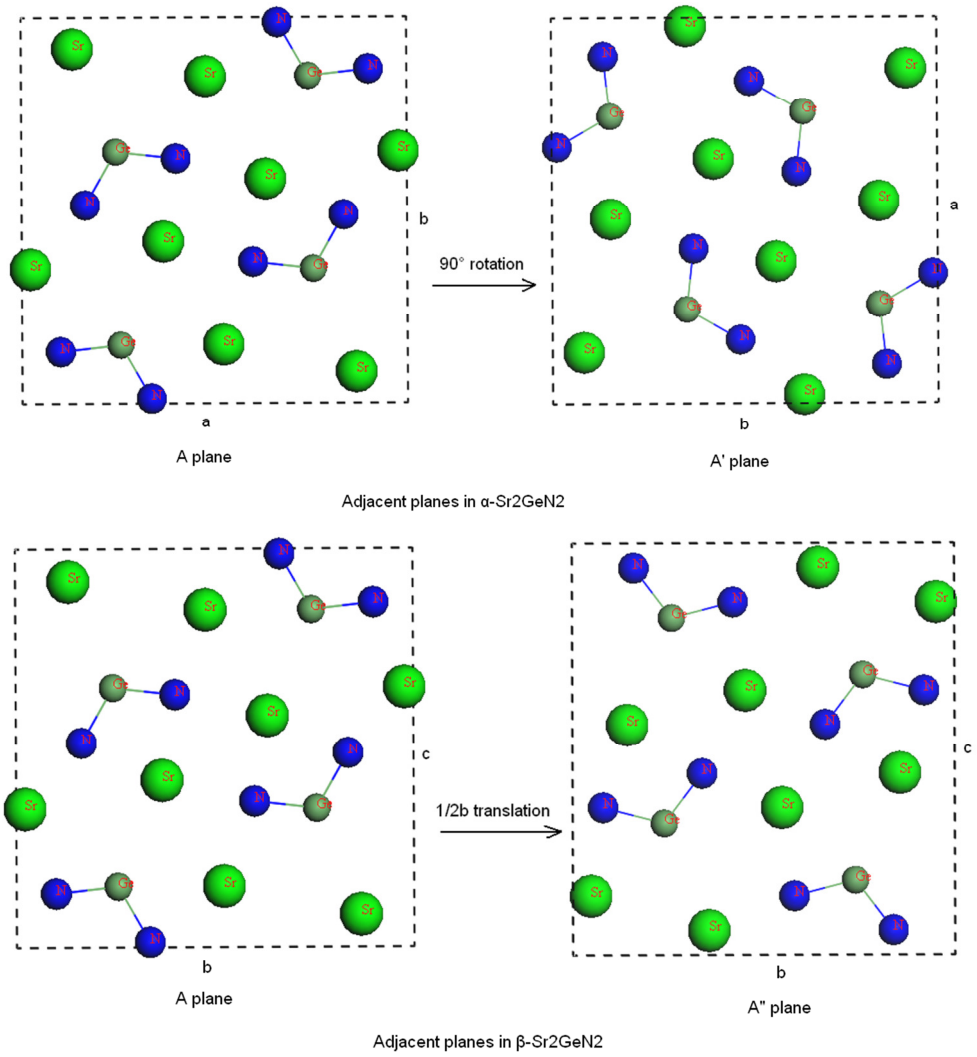

Fig. 6.2: The adjacent planes stacked in both α-Sr_2GeN_2 and β-Sr_2GeN_2 crystals.

6.2.1.2. Equilibrium structural parameters

Knowledge of the equilibrium structural parameters of materials is necessary before investigating their physical and chemical properties using ab initio calculations. Information on the structural parameters of the investigated α and β polymorphs of Sr_2GeN_2, which were used as input data in the present calculations, were taken from Refs. [10] and [11].

The equilibrium structural parameters at zero pressure and zero temperature for α-Sr_2GeN_2 and β-Sr_2GeN_2, calculated with full structural optimization including atomic positions, are listed in Tables 6.1 and 6.2 along with the available experimental values. The obtained equilibrium lattice parameters appear to be in very good agreement with their corresponding experimental data. For α-Sr_2GeN_2, the computed equilibrium lattice parameters a_0 and c_0 are slightly lower than the experimental values and the discrepancies are about -0.25% and -1.59%, respectively. For β-Sr_2GeN_2, the computed equilibrium lattice parameters a_0 and c_0 are slightly lower than the experimental values with relative deviations of about -1.54% and -0.92%, respectively, while the equilibrium lattice parameter b_0 is slightly higher than the experimental value with a relative deviation of about +0.18%. The calculated equilibrium unit-cell volume is slightly lower than the measured one by about -2.08% in α-Sr_2GeN_2 and about -2.26% in β-Sr_2GeN_2. This observed slight relative deviation of the calculated results from the measured ones could be attributed to the fact that our values are calculated at zero temperature while the corresponding experimental ones are measured at ambient temperature; the volume increases with the increasing temperature. This good consistency between our calculated equilibrium lattice parameters and the corresponding measured ones constitutes a proof of reliability of the present calculations and accuracy of the reported results. We note that the two considered polymorphs have practically the same unit-cell volume; the unit-cell volume of β-Sr_2GeN_2 is slightly larger than that of α-Sr_2GeN_2 by about 0.76%.

The optimized atomic positions (Table 6.2) and interatomic bond-lengths (Table 6.1) of α-Sr_2GeN_2 and β-Sr_2GeN_2 are also in good agreement with the corresponding experimental data. Fig. 6.3 shows interatomic bond lengths for each of the bonds belonging to the same planes or those situated between them. From Table 6.1 data, one can observe that both polymorphs have practically the same bond-lengths between the corresponding atoms, where the difference between our results and those of the experiment does not exceed 1.7% (Ge-N1 and Ge-N2 bond lengths of isolated bent anions of GeN_2 for example, are respectively, 1.882 and 1.898 Å for α-Sr_2GeN_2; 1.904 and 1.875 Å for β-Sr_2GeN_2). Both polymorphs have also

practically the same N-Ge-N bond-angles (113.23° for α-Sr_2GeN_2 and 113.49° for β-Sr_2GeN_2). All this indicates that α-Sr_2GeN_2 and β-Sr_2GeN_2 have almost identical local environments. The Sr-N bonds, which are indexed with a star (*) in Table 6.1, ensure the coherence between adjacent planes.

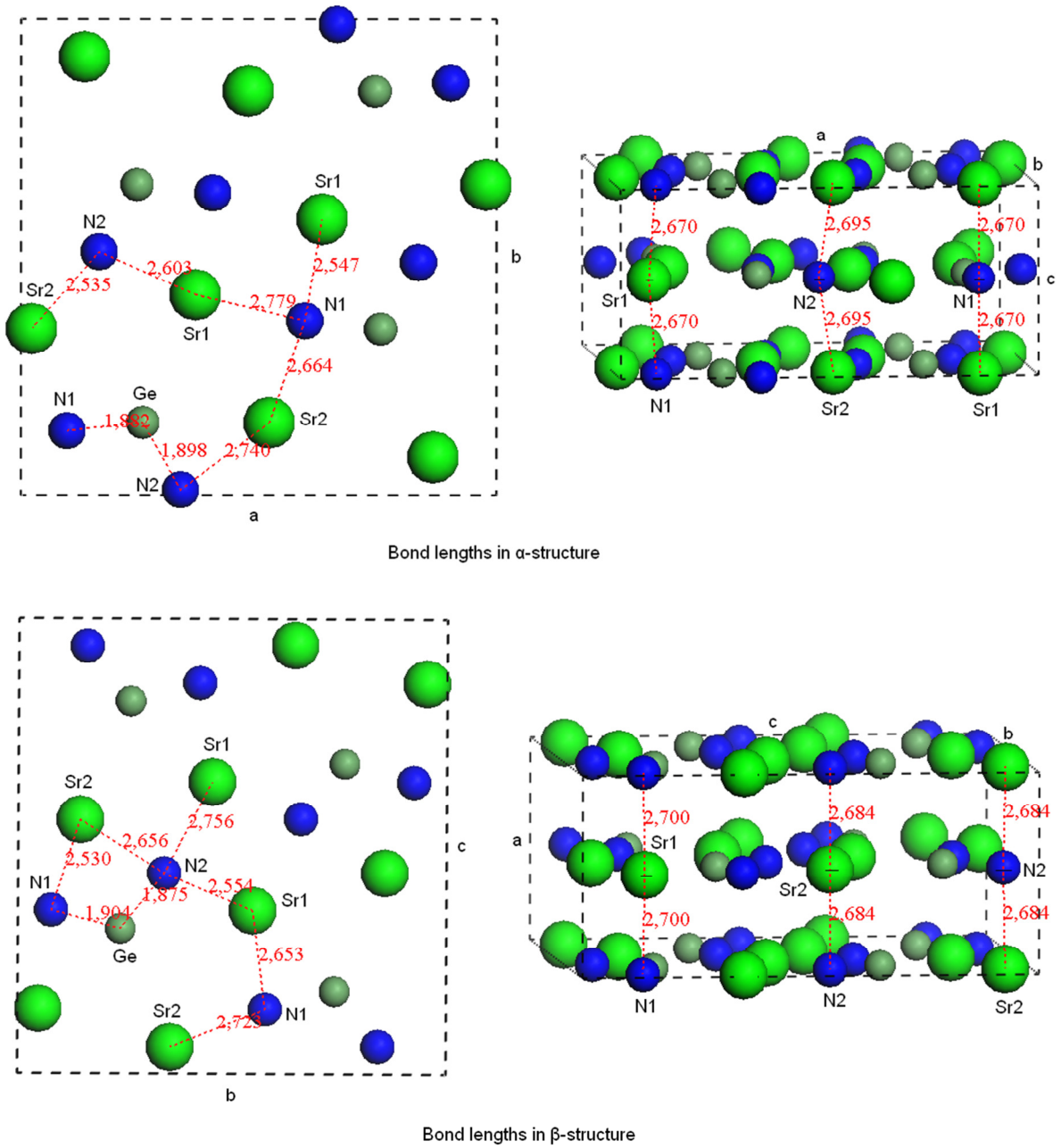

Fig. 6.3: The bond lengths in both α-Sr_2GeN_2 and β-Sr_2GeN_2 structures. The bond lengths presented in the left are those belong to the adjacent planes, while the bond lengths presented in the right are those located between adjacent planes, which ensure the coherence between them.

Table 6.1: Calculated lattice parameters (a_0, b_0 and c_0, in Å), unit-cell volume (V_0, in Å^3), cohesive energy (E_{coh}, in eV/atom), formation enthalpy (E_{form}, in eV/atom), interatomic distances (in Å) and bond-angle (in degree) for the tetragonal and orthorhombic polymorphs of Sr_2GeN_2 together with available experimental data for the sake of comparison

Property	**α-Sr_2GeN_2**		**β-Sr_2GeN_2**	
	Present	Expt. [10]	Present	Expt. [11]
a_0	11.7434	11.773	5.3565	5.441
b_0	11.7434	11.773	11.3982	11.377
c_0	5.3233	5.409	12.1166	12.229
V_0	734.126	749.7	739.776	756.9
E_{coh}	-5.907		-5.898	
E_{form}	-1.500		-1.491	
Ge – N1	1.882	1.851	1.904	1.879
Ge – N2	1.898	1.877	1.875	1.852
Sr1 – N1	2.547	2.562	2.653	2.662
Sr1 – N1*	2.670	2.713	2.700	2.744
Sr1 – N1	2.779	2.807	-	-
Sr1 – N2	2.603	2.628	2.554	2.584
Sr1 – N2	-	-	2.756	2.787
Sr2 – N1	2.664	2.681	2.530	2.561
Sr2 – N1	-	-	2.723	2.737
Sr2 – N2	2.535	2.564	2.656	2.653
Sr2 – N2*	2.695	2.741	2.684	2.728
Sr2 – N2	2.740	2.742	-	-
N1–Ge–N2	113.23	113.51	113.49	113.17

* The bonds that ensure the coherence between adjacent planes.

Table 6.2: Calculated atomic positions for the α-Sr_2GeN_2 and β-Sr_2GeN_2 crystals along with available theoretical and experimental findings for comparison

atom	Present work			Experiments			Other calculations		
	x/a	y/b	z/c	x/a	y/b	z/c	x/a	y/b	z/c
α-Sr_2GeN_2					[10]			[12]	
Sr(1)	0.36669	0.42058	0	0.3671	0.4190	0	0.36642	0.42015	0
Sr(2)	0.02219	0.34864	0	0.0224	0.3482	0	0.02167	0.34869	0
Ge	0.25614	0.15184	0	0.2559	0.1514	0	0.25572	0.15083	0
N(1)	0.09687	0.13442	0	0.0996	0.1340	0	0.09734	0.13392	0
N(2)	0.33567	0.0111	0	0.3353	0.0131	0	0.33538	0.01088	0
β-Sr_2GeN_2					[11]			[12]	
Sr(1)	0	0.04757	0.35851	0	0.0479	0.3576	0	0.04768	0.35739
Sr(2)	0	0.35563	0.44232	0	0.3564	0.4411	0	0.35556	0.44286
Ge	0	0.23881	0.18162	0	0.2398	0.1799	0	0.24001	0.18031
N(1)	0	0.07730	0.14139	0	0.0797	0.1419	0	0.07835	0.14125
N(2)	0	0.34079	0.06024	0	0.3389	0.0597	0	0.34058	0.05971

6.2.1.3. Thermodynamic stability

To ensure the chemical stability of both studied polymorphs, their cohesive and formation energies were calculated. The cohesive energy E_{coh} is the energy that is required for the crystal to decompose into free atoms. Therefore, the cohesive energies of α-Sr_2GeN_2 and β-Sr_2GeN_2 were calculated using the following expression:

$$E_{coh} = \frac{1}{5}\left[E(Sr_2GeN_2) - 2E_a(Sr) - E_a(Ge) - E_a(N_2)\right] \quad (6.1)$$

Here, $E(Sr_2GeN_2)$ represents the total energy of one unit formula of the Sr_2GeN_2 compound, $E_a(X)$ refers to the total energy of an isolated X atom. The $E_a(X)$ energy was calculated using a cubic box with a large lattice constant. The energy of formation (E_{form}) of a compound is calculated by subtracting the total energies of pure constituent elements in their stable crystal structures from the total energy of the compound. Therefore, the E_{form} of α-Sr_2GeN_2 and β-Sr_2GeN_2 were calculated using the following expression:

$$E_{form} = \frac{1}{5}\left[E(Sr_2GeN_2) - 2E_s(Sr) - E_s(Ge) - E(N_2)\right] \quad (6.2)$$

In eqn. (6.1), $E_s(Sr)$ and $E_s(Ge)$ denote the total energies per atom of the pure elements Sr and Ge, respectively, in their solid phase and $E(N_2)$ is the total energy of the N_2 molecule. The obtained cohesive and formation energies for α-Sr_2GeN_2 and β-Sr_2GeN_2 are listed in Table 6.1. Both energies for both considered polymorphs are negative, implying that they are both energetically stable and can be synthesized. Furthermore, one can appreciate that E_{coh} and E_{form} energies for the α-Sr_2GeN_2 crystal are slightly lower than those of the β-Sr_2GeN_2 one, implying that the α-Sr_2GeN_2 structure is more stable than the β-Sr_2GeN_2 one. Additionally, the calculated static total energy versus volume (E-V) curves, presented in Fig. 6.4, show that the unit-cell total energy of α-Sr_2GeN_2 is slightly lower than that of the β-Sr_2GeN_2 one, confirming that α-Sr_2GeN_2 structure is more stable than β-Sr_2GeN_2 one. This result is consistent with the fact that synthesis of the α-Sr_2GeN_2 polymorph was not accompanied with the appearance of the β-Sr_2GeN_2 polymorph, while synthesis of the β-Sr_2GeN_2 compound was accompanied with the production of the α-Sr_2GeN_2 polymorph [10,11].

6.3.1.4. Pressure effect on the structural parameters and equation of states

In order to have insight on the pressure dependence behavior of the structural parameters for the two considered polymorphs, full optimizations of their unit-cell parameters and full relaxations of their atomic positions were performed for fixed pressures in pressure range from 0 to 20 GPa with a step of 5 GPa. Fig. 6.5 displays the pressure dependence of the normalized lattice parameters a/a_0, b/b_0 and c/c_0 and the normalized unit-cell volume V/V_0, where a_0, b_0, c_0 and V_0 are the corresponding values at zero-pressure. From Fig. 5, it can be seen that the α-Sr_2GeN_2 unit-cell is more compressible along the *c*-axis than along the *a*-one, while β-Sr_2GeN_2 unit-cell is less compressible along the *b*-axis than along the *a*- and *c*-ones; *a*- and *c*-axes have practically the same compressibility. Further, a look to the pressure dependence of the unit-cell volume, shown in Fig. 5, shows that α-Sr_2GeN_2 is slightly less compressible than β-Sr_2GeN_2.

The linear compressibility β_X (β_a, β_b and β_c) along the *X*-axis (*a*-, *b*- and *c*-axes, respectively), has been evaluated from the fit of the lattice parameter *X* versus pressure data to a third-order polynomial:

$$X / X_0 = 1 + \beta_X P + \sum_{n=2}^{n=3} K_n P^n \qquad (6.3)$$

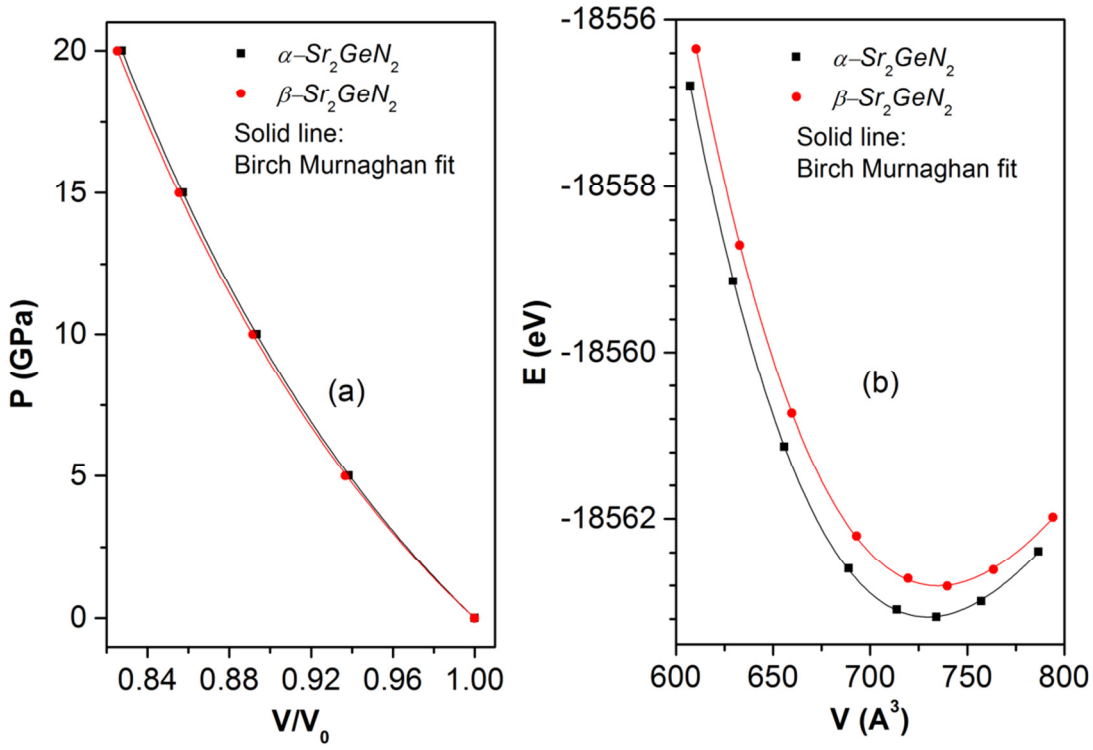

Fig. 6.4: (a) Pressure P versus relative unit-cell volume V/V_0 for α-Sr_2GeN_2 and β-Sr_2GeN_2, **(b)** Total energy E versus relative unit-cell volume V/V_0 for α-Sr_2GeN_2 and β-Sr_2GeN_2.

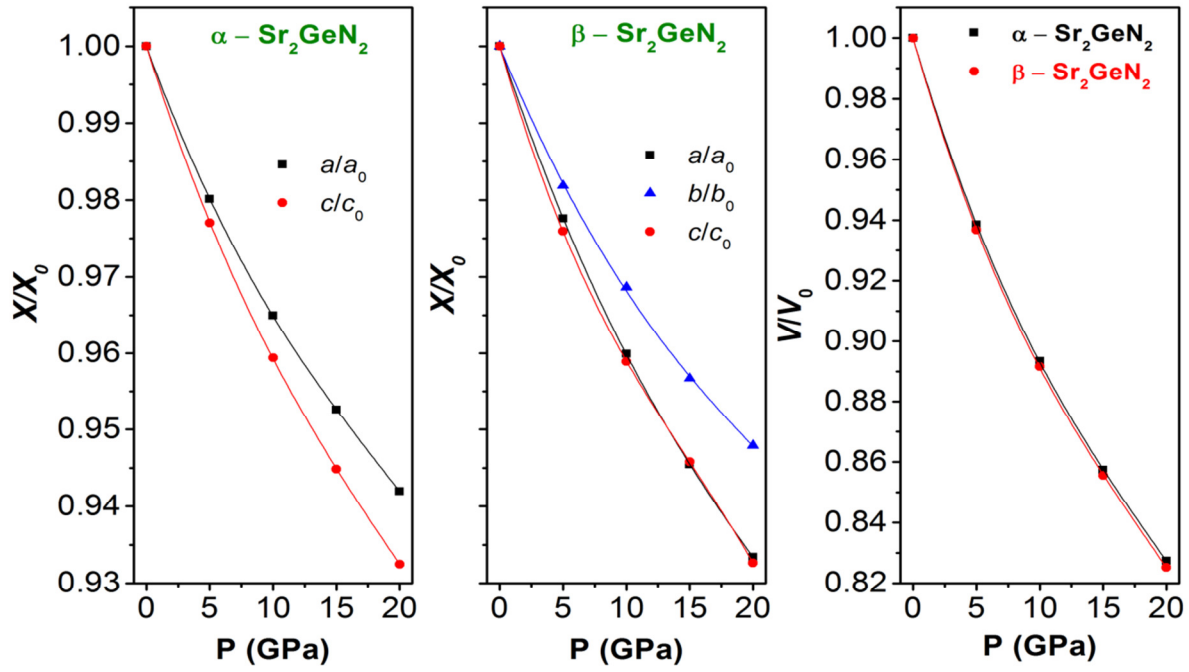

Fig. 6.5: Variation of the normalized lattice parameters ratio; a/a_0, b/b_0 and c/c_0, and the normalized unit-cell volume V/V_0 as a function of hydrostatic pressure P, for the α-Sr_2GeN_2 and β-Sr_2GeN_2 polymorphs. The solid lines are least squares third-order polynomial fits of the data points.

The obtained linear compressibilities are:

$\beta_a = \beta_b = 0.00453\ GPa^{-1}$ and $\beta_c = 0.00518\ GPa^{-1}$ for α-Sr_2GeN_2;

$\beta_a = 0.005 GPa^{-1}$, $\beta_b = 0.00399\ GPa^{-1}$ and $\beta_c = 0.00578\ GPa^{-1}$ for β-Sr_2GeN_2.

The bulk modulus B may be estimated from the linear compressibilities β_a, β_b and β_c via the following relationship:

$$B = 1/(2\beta_a + \beta_c) \tag{6.4}$$

for α-Sr_2GeN_2 (tetragonal structure) and

$$B = 1/(\beta_a + \beta_b + \beta_c) \tag{6.5}$$

for β-Sr_2GeN_2 (orthorhombic structure). Moreover, the volume compressibility has been evaluated from the fit of the volume-pressure (V–P) data to a third-order polynomial expression. The volume compressibility β_V was used to estimate the bulk modulus B as follows:

$$B = 1/\beta_V \tag{6.6}$$

The volume compressibility obtained for two polymorphs are:

β_V (α-Sr_2GeN_2) = 0.01413 GPa^{-1}

β_V (β-Sr_2GeN_2) = 0.01466 GPa^{-1}

From Table 6.1, one can appreciate that the obtained value for the bulk modulus B from the linear compressibilities is in very good agreement with that obtained from the volume compressibility.

One of the more used methods to test the reliability of obtained theoretical results consists of comparing between the numerical values of one property that are calculated using different theoretical procedures. For this issue, the bulk modulus B and its pressure derivative B' were used as test. The bulk modulus values derived from the fitting of the calculated pressure versus unit-cell volume (P-V) data and total energy versus unit-cell volume (E-V) data to the Birch-Murnaghan and Murnaghan P-V EOSs [13,14], and to the Birch-Murnaghan and Vinet E-V EOSs [15,16] are compared to that calculated from the elastic constants, linear compressibility and volume compressibility to testify the reliability and accuracy of the present reported results. Fig. 6.4-panel (a) and Fig. 4-panel (b) present the fits of the P-V and E-V data to the P-V and E-V Birch-Murnaghan EOSs, respectively, as prototype. One can appreciate the good fit of the first-principles calculated data to the mentioned EOSs. The obtained values of B and B' are reported in Table 6.3. The calculated values of the bulk

modulus from the EOS fits are in very good agreement with those calculated from the linear and volume compressibilities for both considered materials. These results are good tests of the accuracy of our simulations. According to our results, the bulk modulus B of α-Sr_2GeN_2 is slightly larger than that of β-Sr_2GeN_2 by about 2.0% to 4.0%, revealing that β-Sr_2GeN_2 is slightly more compressible than α-Sr_2GeN_2. knowing that the lattice volume of β-Sr_2GeN_2 is slightly higher than that of α-Sr_2GeN_2, this is in good agreement with the well-known relation between the bulk modulus and the lattice volume $B \propto V^{-1}$. To date, no reported experimental or theoretical data in the scientific literature for the bulk moduli of the α-Sr_2GeN_2 and β-Sr_2GeN_2 materials to be compared with our obtained results.

Table 6.3: Calculated bulk modulus (B_0, in GPa) and its pressure derivative B', for the tetragonal and orthorhombic polymorphs of Sr_2GeN_2

Method	**α-Sr_2GeN_2**		**β-Sr_2GeN_2**	
	B	*B'*	*B*	*B'*
Birch Murnaghan *P-V* EOS [13]	68.569	4.533	66.614	4.633
Murnaghan *P-V* EOS [14]	69.426	4.161	67.521	4.238
Birch Murnaghan *E-V* EOS [15]	69.00	3.40	67.82	3.35
Vinet E-V EOS [16]	68.808	4.866	66.092	5.048
From β_Xs	70.77		68.21	
From β_V	70.23		67.71	

Fig. 6.6 shows the pressure dependence behavior of the relative bond-length d/d_0 of the Ge-N and Sr-N bonds, where d_0 is the equilibrium bond-length at zero pressure. The obtained numerical data are well fitted with a second-order polynomial expression:

$$d / d_0 = 1 + \alpha P + \beta P^2 . \quad (6.7)$$

From Fig. 6, it can be seen that the Ge-N bond, which belongs to the isolated GeN_2 bent units, is stronger than the Sr-N one.

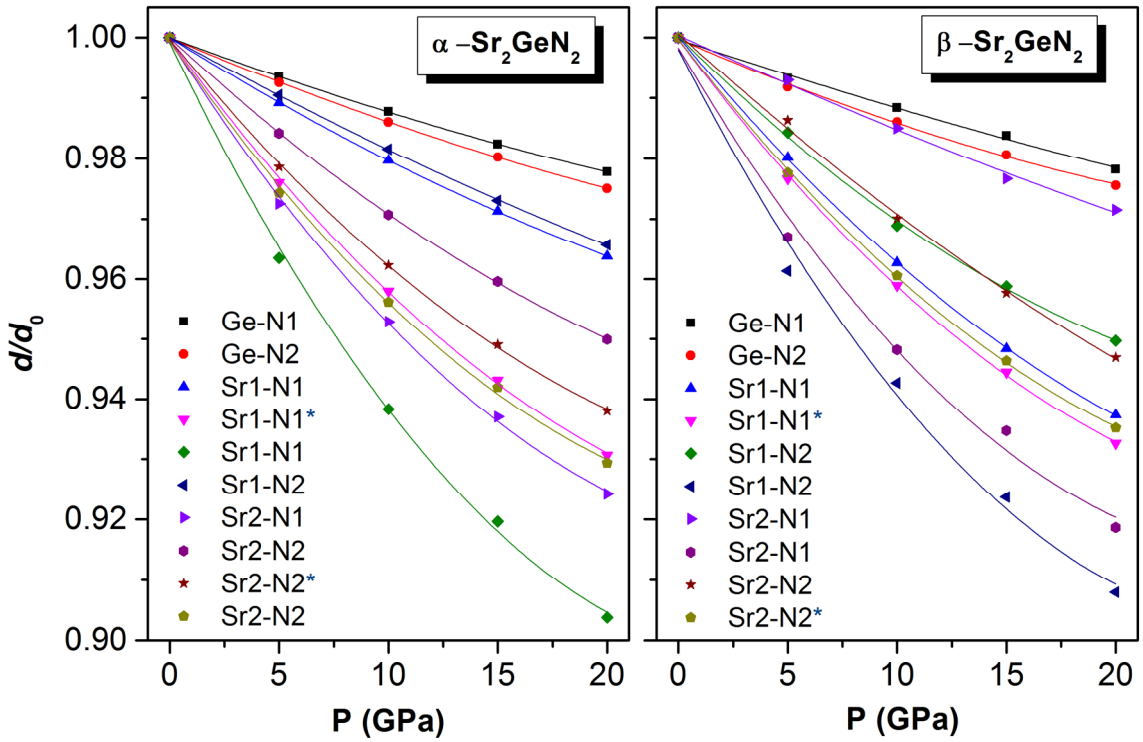

Fig. 6.6: Variation of the relative bond lengths d/d_0 as a function of hydrostatic pressure P for the α-Sr_2GeN_2 and β-Sr_2GeN_2 compounds. The star (*) indicates the bond between the adjacent planes. The solid lines are least squares second-order polynomial fits of the data points.

The so-called bond stiffness coefficient k defined by the following relation:

$$k = 1/|\alpha| \tag{6.8}$$

where α is the first pressure derivative of the bond-length ($d/d_0 = 1 + \alpha P + \beta P^2$), is calculated in order to characterize the stiffness of the existing chemical bonds. The estimated values of the bond stiffness k for the α-Sr_2GeN_2 and β-Sr_2GeN_2 polymorphs are listed in Table 6.4. One can appreciate that the chemical bonding between two atoms belonging to two adjacent planes is weaker than that between two atoms belonging to the same plane. This behavior could explain the more compressibility of the c-axis (a-axis) in the α-polymorph (β-polymorph) seeing that the stacking is along the c-axis (a-axis) in the α-Sr_2GeN_2 (β-Sr_2GeN_2) compound. The less compressibility of β-Sr_2GeN_2 along the b-axis compared to a- and c-axes is due to the fact that, statistically, the strongest bond, namely Ge-N1 ($k = 826GPa$), has greater impact along the b-axis than along the c-one; the angle between the Ge-N1 bond and b-axis is only 14.8° compared to that of 75.2° between the Ge-N1 bond and c-axis.

Table 6.4: Calculated bond stiffness (*k*, in GPa) for some bonds in the α-Sr_2GeN_2 and β-Sr_2GeN_2 compounds. The star (*) indicates the bond between adjacent planes

System	$k_{Ge\text{-}N1}$	$k_{Ge\text{-}N2}$	$k_{Sr1\text{-}N1}$	$k_{Sr1\text{-}N1}$*	$k_{Sr1\text{-}N1}$	$k_{Sr1\text{-}N2}$	$k_{Sr2\text{-}N1}$	$k_{Sr2\text{-}N2}$	$k_{Sr2\text{-}N2}$*	$k_{Sr2\text{-}N2}$
α-Sr_2GeN_2	740.7	653.6	446.4	202.8	134.0	502.5	177.6	300.3	225.7	192.3
	$k_{Ge\text{-}N1}$	$k_{Ge\text{-}N2}$	$k_{Sr1\text{-}N1}$	$k_{Sr1\text{-}N1}$*	$k_{Sr1\text{-}N2}$	$k_{Sr1\text{-}N2}$	$k_{Sr2\text{-}N1}$	$k_{Sr2\text{-}N1}$	$k_{Sr2\text{-}N2}$	$k_{Sr2\text{-}N2}$*
β-Sr_2GeN_2	826.4	632.9	230.9	206.6	279.3	142.0	606.1	162.9	306.7	214.1

Another way to demonstrate that the *b*-axis is less compressed than *a*-axis in the β-Sr_2GeN_2 compound is to use the angle change between axes A and B in its primitive cell. Fig. 6.7 shows that the angle *γ* between **A** and **B** of primitive cell illustrated in Fig. 6.8, decreases when pressure increases, indicating that *b*-axis is less compressible than *a*-axis.

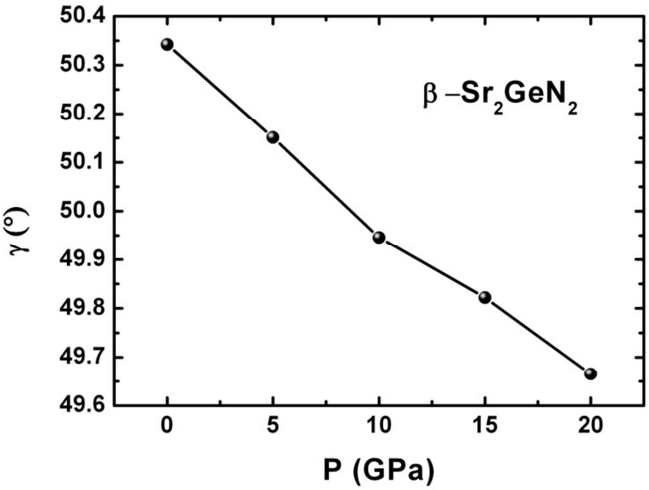

Fig. 6.7: Variation of the angle *γ* situated between two lattice parameters **A** and **B** in primitive cell of β-Sr_2GeN_2.

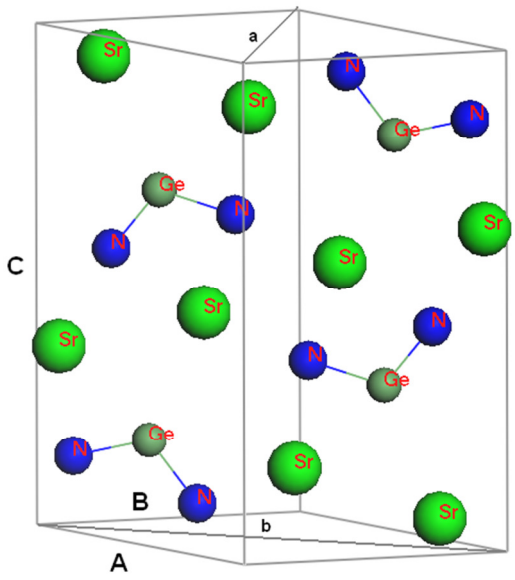

Fig. 6.8: Primitive cell of the orthorhombic Sr_2GeN_2. **A**, **B** and **C** are their lattice parameters, while **a**, **b** and c = **C** are the lattice parameters of the conventional unit cell. The angle γ between A and B decreases when pressure increases, because *a*-axis is more compressible than the *b*-axis.

6.2.2. Elastic properties

6.2.2.1. Single-crystal elastic constants and related properties

The elastic stiffness tensor (C_{ijkl}) (i, j, k, l = 1, 2, 3) is related to the stress tensor σ_{ij} and the strain tensor ε_{kl} by the generalized form of Hooke's law states that:

$$\sigma_{ij} = C_{ijkl}\varepsilon_{kl} \tag{6.9}$$

Due to the symmetry of σ_{ij} ($\sigma_{ij} = \sigma_{ji}$) and ε_{kl} ($\varepsilon_{kl} = \varepsilon_{lk}$) there are only 6 independent stress σ_i, and 6 independent strain components ε_j, according to the scheme,

tensor notation	11	22	33	23, 32	31, 13	12, 21
matrix notation	1	2	3	4	5	6

Therefore, the stiffness constants C_{ijkl} are abbreviated to C_{ij} (i, j = 1, 2, …, 6), and their number is reduced from 81 to 36. This symmetry makes it possible to use the matrix notation [17]:

$$\sigma_i = C_{ij}\varepsilon_j \tag{6.10}$$

The symmetry of the (C_{ij}) matrice further reduces the number of independent elastic constants C_{ij} from 36 to 21. For a tetragonal crystal, they are reduced to 6 components, i.e. C_{11}, C_{33}, C_{44}, C_{66}, C_{12} and C_{13}, and for an orthorhombic crystal, they are reduced to 9 components, i.e. C_{11}, C_{22}, C_{33}, C_{44}, C_{55}, C_{66}, C_{12}, C_{13} and C_{23}. The corresponding matrixes of elastic constants C_{ij} are given as follow:

$$(C_{ij}) = \begin{pmatrix} C_{11} & C_{12} & C_{13} & 0 & 0 & 0 \\ C_{12} & C_{11} & C_{13} & 0 & 0 & 0 \\ C_{13} & C_{13} & C_{33} & 0 & 0 & 0 \\ 0 & 0 & 0 & C_{44} & 0 & 0 \\ 0 & 0 & 0 & 0 & C_{44} & 0 \\ 0 & 0 & 0 & 0 & 0 & C_{66} \end{pmatrix} \tag{6.11}$$

for the tetragonal polymorph, with $4mn$, $\bar{4}2m$, 422 and $4/mmm$ classes, and:

$$(C_{ij}) = \begin{pmatrix} C_{11} & C_{12} & C_{13} & 0 & 0 & 0 \\ C_{12} & C_{22} & C_{23} & 0 & 0 & 0 \\ C_{13} & C_{23} & C_{33} & 0 & 0 & 0 \\ 0 & 0 & 0 & C_{44} & 0 & 0 \\ 0 & 0 & 0 & 0 & C_{55} & 0 \\ 0 & 0 & 0 & 0 & 0 & C_{66} \end{pmatrix} \tag{6.12}$$

for the orthorhombic polymorph [17].

The calculated independent elastic constants C_{ij} and the elastic compliances S_{ij}, which are calculated directly from the C_{ij}, for both studied Sr_2GeN_2 polymorphs are listed in Table 6.5. The obtained data allow us to highlight the following points:

Table 6.5: Calculated independent elastic constants (C_{ij}, in GPa) and elastic compliance (S_{ij}, in GPa^{-1}) for the α-Sr_2GeN_2 and β-Sr_2GeN_2 single-crystals

α-Sr_2GeN_2		**β-Sr_2GeN_2**	
C_{ij}	S_{ij}	C_{ij}	S_{ij}
C_{11} =124.8	S_{11} = 0.0097517	C_{11}=123.2	S_{11} =0.0092388
C_{33} =123.5	S_{33} =0.0090089	C_{22}=134.4	S_{22} =0.0088889
C_{44} =36.7	S_{44} =0.0272196	C_{33}=127.9	S_{33} =0.0088393
C_{66} =40.9	S_{66} =0.0244564	C_{44}=40.0	S_{44} =0.0250226
C_{12} =48.4	S_{12} = –0.0033363	C_{55}=25.2	S_{55} =0.0396926
C_{13} =32.7	S_{13} = –0.0017018	C_{66}=40.6	S_{66} =0.0246356
		C_{12}=41.3	S_{12} = –0.0024495
		C_{13}=28.6	S_{13} = –0.0012805
		C_{23}=40.9	S_{23} = –0.0022928

(i) To be mechanically stable, the C_{ij} of a tetragonal crystal should satisfy the Born–Huang stability criteria [18]:

$$C_{11}> 0,\ C_{33}> 0,\ C_{44}> 0,\ C_{66}> 0,\ C_{11}- C_{12}> 0,$$
$$C_{11}+ C_{33}- 2C_{13}> 0,\ 2(C_{11}+ C_{12}) + C_{33} + 4C_{13}> 0 \quad (6.13)$$

The mechanical stability of an orthorhombic crystal requires the following conditions [18]:

$$C_{11}>0,\ C_{22}>0,\ C_{33}>0,\ C_{44}>0,\ C_{55}>0,\ C_{66}>0,\ C_{11}+ C_{22}-2C_{12}>0,$$
$$C_{11}+ C_{33}-2C_{13}>0,\ C_{22}+ C_{33}-2C_{23}>0,\ C_{11}+ C_{22}+ C_{33}+ 2(C_{12}+ C_{13}+ C_{23})> 0 \quad (6.14)$$

The data listed in Table 6.5 demonstrate that the C_{ij} of both examined polymorphs satisfy the above-mentioned criteria. This implies that the examined polymorphs α-Sr_2GeN_2 and β-Sr_2GeN_2 are mechanically stable.

(ii) C_{11} is slightly higher than C_{33} in the α-Sr_2GeN_2 crystal, which means that the resistance against the applied stress along the [100] crystallographic direction is slightly higher than the resistance to the applied stress along the [001] one. This suggests that the chemical bonding between nearest neighbors along the [100] direction is slightly stronger than those along the [001] one. In the β-Sr_2GeN_2 crystal, C_{22} is slightly higher than C_{11} and C_{33}, implying that the resistance against the external applied stress along the [010] direction is slightly higher than that against the external applied stress along the [100] and [001] directions. This result suggests that the inter-atomic interactions along the [010] crystallographic direction are slightly stronger than those along the [100] and [001] ones. These results are in concordance with those obtained from the pressure dependence behavior of the lattice parameters and chemical bond-lengths, which have been already discussed in Section 5.3.1.4.

(iii) It is important to evaluate the sound velocity in a crystal because they are related to some physical properties of the material such as its thermal conductivity. Single-crystal elastic wave velocities propagating in different crystallographic directions can be predicted from the resolution of the Christoffel equation [19]:

$$\left(C_{ijkl}n_j n_k - \rho V^2 \delta_{il}\right)u_l = 0 \tag{6.15}$$

Here, C_{ijkl} are the components of the elastic constant tensor in the full (4-index) notation, $\vec{n}$ is the wave propagation direction, ρ is the mass density of the propagating medium, V is the sound wave velocity and $\vec{u}$ is the sound wave polarization. The pure longitudinal (L) and transverse (T) wave velocities propagating along the [100], [010] and [001] crystallographic directions in an orthorhombic system are given by the following expressions:

$$\begin{aligned}
&V_L^{[100]} = \sqrt{C_{11}/\rho}\ ;\ V_{T1}^{[100]} = \sqrt{C_{66}/\rho}\ ;\ V_{T2}^{[100]} = \sqrt{C_{55}/\rho} \\
&V_L^{[010]} = \sqrt{C_{22}/\rho}\ ;\ V_{T1}^{[010]} = \sqrt{C_{66}/\rho}\ ;\ V_{T2}^{[010]} = \sqrt{C_{44}/\rho} \\
&V_L^{[001]} = \sqrt{C_{33}/\rho}\ ;\ V_{T1}^{[001]} = \sqrt{C_{55}/\rho}\ ;\ V_{T2}^{[001]} = \sqrt{C_{44}/\rho}
\end{aligned} \tag{6.16}$$

The pure longitudinal (L) and transverse (T) sound wave velocities propagating along the [100] (or [010]), [001] and [110] crystallographic directions of a tetragonal system are given by the following expressions:

$$V_L^{[100]} = \sqrt{C_{11}/\rho}\ ;\ V_{T1}^{[100]} = \sqrt{C_{66}/\rho}\ ;\ V_{T2}^{[100]} = \sqrt{C_{44}/\rho}$$
$$V_L^{[001]} = \sqrt{C_{33}/\rho}\ ;\ V_{T1}^{[001]} = V_{T2}^{[001]} = \sqrt{C_{44}/\rho} \quad (6.17)$$
$$V_L^{[110]} = \sqrt{(C_{11}+C_{12}+2C_{66})/2\rho}\ ;\ V_{T1}^{[110]} = \sqrt{(C_{11}-C_{12})/2\rho}\ ;\ V_{T2}^{[110]} = \sqrt{C_{44}/\rho}$$

The calculated elastic wave velocities along the above-mentioned crystallographic directions for the α-Sr_2GeN_2 and β-Sr_2GeN_2 polymorphs are listed in Table 6.6. One can appreciate that the longitudinal sound wave velocities have almost equal values for both considered compounds (~ 5000 m/s) and they are larger than the transverse ones.

Table 6.6: Elastic wave velocities (in m/s) for some different propagating crystallographic directions for the α-Sr_2GeN_2 and β-Sr_2GeN_2 crystals

α-Sr_2GeN_2	v_L^{100}	v_{T1}^{100}	v_{T2}^{100}	v_L^{001}	v_{T1}^{001}	v_{T2}^{001}	v_L^{110}	v_{T1}^{110}	v_{T2}^{110}
	5000.7	2862.1	2713.0	4971.4	2713.0	2713.0	5054.2	2766.5	2713.0
β-Sr_2GeN_2	v_L^{100}	v_{T1}^{100}	v_{T2}^{100}	v_L^{010}	v_{T1}^{010}	v_{T2}^{010}	v_L^{001}	v_{T1}^{001}	v_{T2}^{001}
	4986.1	2862.6	2255.2	5209.3	2862.6	2840.4	5080.7	2255.2	2840.4

6.2.2.2. Pressure effect on the single crystal properties

Fig. 6.9 shows the variations of the elastic constants C_{ij} versus hydrostatic pressure. One can observe that C_{11}, C_{33} and C_{12}, especially C_{33}, for α-Sr_2GeN_2 are highly sensitive to pressure variations than other constants.The C_{44} remains almost invariable to the pressure variations. For β-Sr_2GeN_2, C_{11}, C_{22}, C_{33} and C_{23}, especially C_{11}, are the highly sensitive to pressure variations than other constants. The C_{44}, C_{55} and C_{66} remain almost invariable to pressure variations. In Fig. 6.10, we have presented the elastic wave velocities under pressure. We can see from this figure, that the longitudinal wave velocities for both α-Sr_2GeN_2 and β-Sr_2GeN_2 are highly sensitive to pressure variations than those of transverse waves, which remain almost invariant to pressure variations.

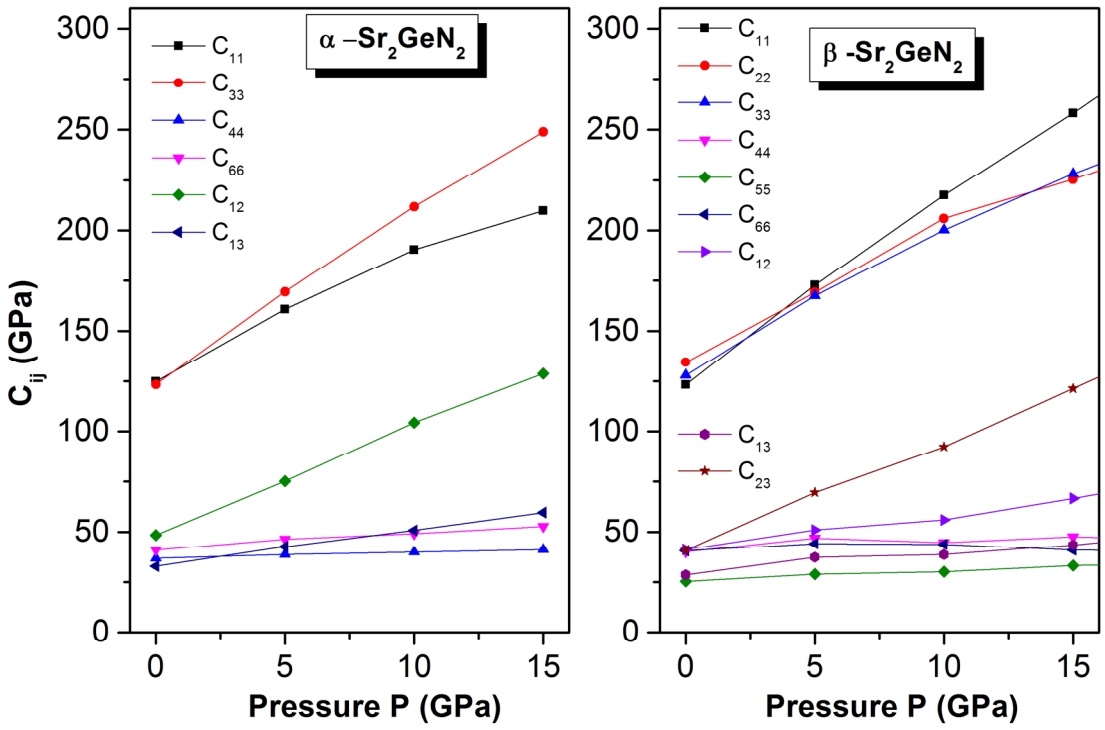

Fig. 6.9: Variation of the elastic constants C_{ij} for the α-Sr_2GeN_2 and β-Sr_2GeN_2 as a function of pressure.

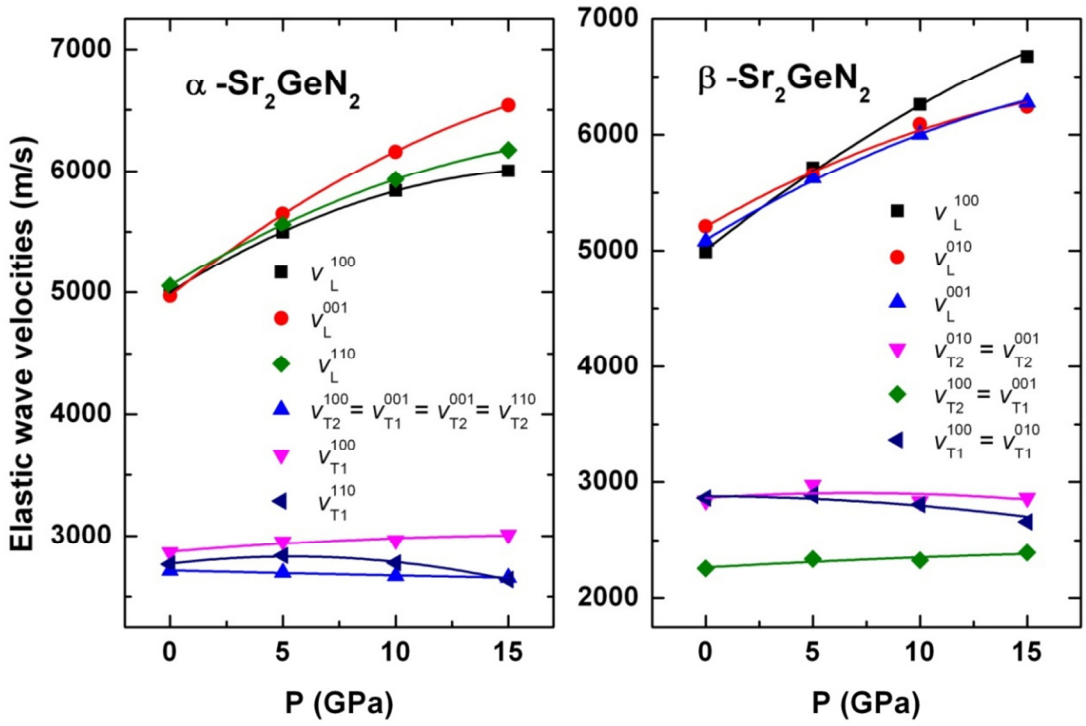

Fig. 6.10. Variation of the elastic wave velocities for the α-Sr_2GeN_2 and β-Sr_2GeN_2 as a function of pressure. The solid lines are least-squares second-order polynomial fits of the data points.

Under pressure, for the tetragonal crystal, the mechanical stability requires that the elastic constants satisfy the following stability criteria [20,21]:

$$C_{11}-P>0,\ C_{33}-P>0,\ C_{44}-P>0 \text{ and } C_{66}-P>0,$$

$$C_{11}-C_{12}-2P>0, C_{11}+C_{33}-2C_{13}-4P>0,\ 2(C_{11}+C_{12})+C_{33}+4C_{13}+3P>0 \quad (6.18)$$

For the orthorhombic crystal, the required criteria are as follows [20,21]:

$$C_{11}-P>0,\ C_{22}-P>0,\ C_{33}-P>0,\ C_{44}-P>0,\ C_{55}-P>0,\ C_{66}-P>0,$$

$$C_{11}+C_{22}-2C_{12}-4P>0,\ C_{11}+C_{33}-2C_{13}-4P>0, C_{22}+C_{33}-2C_{23}-4P>0,$$

$$C_{11}+C_{22}+C_{33}+2(C_{12}+C_{13}+C_{23})+3P>0 \quad (6.19)$$

Both investigated polymorphs satisfy the required criteria for mechanical stability in the considered pressure range.

6.2.2.3. Elastic moduli and related properties for polycrystalline aggregates

Generally, it is difficult to synthetize materials in single-crystal form, and in this case, the elastic constants C_{ij} cannot be measured. In the polycrystalline aggregates form, only the isotropic polycrystalline elastic moduli can be measured. Theoretically, polycrystalline elastic moduli such as the bulk modulus B (which represents the resistance of a solid against volume change under hydrostatic pressure), shear modulus G (which represents the resistance of a solid to shape change caused by a shearing force) and Young's modulus E (which represents the resistance of a solid against uniaxial stress), can be derived from the calculated single-crystal elastic constants C_{ij} using some approximations. In the case of randomly oriented polycrystals, one may evaluate aggregate average elastic properties based on additional hypotheses such as isostress named as Reuss [6] or isostrain named as Voigt [7] states (subscripted, respectively, R and V in the following). The general expressions for the Voigt and Reuss approaches for bulk and shear moduli are expressed as follows [6,7]:

$$B_V = (1/9)\ [C_{11} + C_{22} + C_{33} + 2(C_{12} + C_{13} + C_{23})] \quad (6.20)$$

$$G_V = (1/15)\ [C_{11} + C_{22} + C_{33} + 3(C_{44} + C_{55} + C_{66}) - (C_{12} + C_{13} + C_{23})] \quad (6.21)$$

$$1/B_R = (S_{11} + S_{22} + S_{33}) + 2(S_{12} + S_{23} + S_{13}) \quad (6.22)$$

$$1/G_R = (4/15)\ (S_{11} + S_{22} + S_{33}) - (4/15)\ (S_{12} + S_{13} + S_{23}) + (1/5)\ (S_{44} + S_{55} + S_{66}) \quad (6.23)$$

Here, the S_{ij} are the components of the compliance matrix $\mathbf{S}$ which is related the elastic constant matrix $\mathbf{C}$ by the following relationship: $\mathbf{S}=\mathbf{C}^{-1}$. Hill [8] has demonstrated that the arithmetic mean of the two above-mentioned limits – Voigt and Reuss- are the best effective

polycrystalline elastic moduli (Hill's approximation). In the hill's approximation the polycrystalline bulk (B_H) and shear (G_H) moduli are given by the following expressions:

$$B_H = \frac{B_V + B_R}{2}, \quad G_H = \frac{G_V + G_R}{2} \tag{6.24}$$

The Young's modulus E and Poisson's ratio v, which is defined as the ratio of transverse strain (normal to the applied stress) to the longitudinal strain (in the direction of the applied stress), can be computed from the Hill's values of B and G through the following relations:

$$E = \frac{9B_H G_H}{3B_H + G_H}, \quad \nu_H = \frac{3B_H - 2G_H}{2(3B_H + G_H)} \tag{6.25}$$

Using the above-mentioned relations, the calculated bulk modulus, shear modulus, Young's modulus and Poisson's ratio are summarized in Table 6.7.

Table 6.7: Calculated bulk modulus (B, in GPa), shear modulus (G, in GPa), Yong's modulus (E_H, in GPa), B/G ratio and Poisson's ratio ν_H for the α-Sr_2GeN_2 and β-Sr_2GeN_2 polycrystals. The subscript V, R and H stand to Voigt, Reuss and Hill approximations

System	B_V	B_R	B_H	G_V	G_R	G_H	E_H	B/G	ν_H
α-Sr_2GeN_2	66.75	66.52	66.64	40.15	39.717	39.930	99.850	1.67	0.250
β-Sr_2GeN_2	67.43	67.02	67.224	39.47	37.50	38.480	96.95	1.75	0.260

Furthermore, we have evaluated the effect of the pressure on the isotropic elastic moduli, B, G (μ), E, λ and Poisson's ratio v for α-Sr_2GeN_2 and β-Sr_2GeN_2 as they are depicted in Figs. 6.11 and 6.12. From the obtained results, one can make the following conclusions:

(i) The polycrystalline elastic moduli calculated for both Sr_2GeN_2 polymorphs are almost equal, indicating the resemblance of their mechanical properties. Under pressure, as shown in Fig. 6.11, all these parameters increase with increasing pressure, indicating that their hardness increases with pressure.

(ii) Calculated bulk modulus from the single-crystal elastic constants C_{ij} is in good agreement with that calculated from the EOS fits and from linear and volume comopressibilities, for both considered polymorphs. This serves to give an indication of the reliability and accuracy of our

predicted elastic constants. The calculated bulk modulus value for both compounds is smaller than 100 GPa, so these two compounds can be classified as a relatively soft material.

(iii) The Poison's ration v is often used to reflect the stability of a crystal against shear and provides information about the nature of the bonding forces. The value of v for covalent materials is small (v = 0.1), whereas for ionic materials, a typical value for v is 0.25 [22,23]. The calculated v for both crystals are almost equal: v = 0.25 for α-Sr_2GeN_2 and v = 0.26 for β-Sr_2GeN_2. These values indicate that a considerable ionic contribution in the interatomic bonding should be assumed in these crystals. On the other hand, for covalent and ionic materials, the typical relations between bulk and shear modulus are $G \approx 1.1\ B$ and $G \approx 0.6\ B$, respectively. We found that $G \approx 0.6\ B$ for both crystals, which also suggests the dominance of the ionic nature in the two considered compounds. From the Fig. 6.12 we can see that under pressure, the Poisson's ratio v for both crystals increases with increasing pressure. Under pressure of 15 GPa, they have the same Poisson's ratio (v = 0.32).

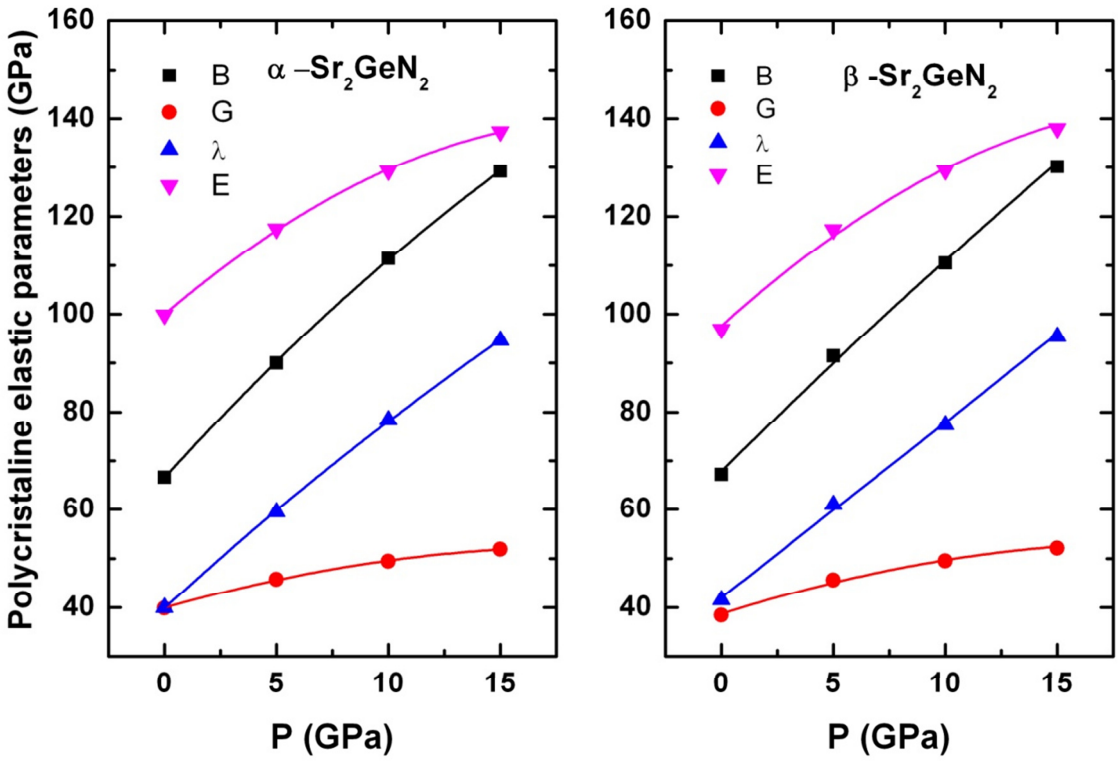

Fig. 6.11: Calculated pressure dependence of the isotropic elastic constants (bulk modulus B, shear modulus G, Young's modulus E and Lamé's coefficient λ) for the α-Sr_2GeN_2 and β-Sr_2GeN_2 compounds. The solid lines are least-squares second-order polynomial fits of the data points.

(iv) To know if a material has a brittle or a ductile behavior, Pugh [24] has proposed a simple empirical relationship between the bulk modulus *B* and shear modulus *G*. The shear modulus *G* represents the resistance to plastic deformation, while *B* represents their resistance to fracture. Therefore, a high *B*/*G* ratio is associated with ductility, whereas a low value corresponds to brittle nature. The critical value that separates ductile and brittle materials is around 1.75 [24]; i.e., if *B*/*G* > 1.75, the material behaves in a ductile manner, otherwise, the material behaves in a brittle manner. For β-Sr_2GeN_2, the *B*/*G* ratio is exactly equal to the critical value (*B*/*G* = 1.75), therefore, its mechanical properties are intermediate between those of a ductile material and a brittle material. For α-Sr_2GeN_2, the *B*/*G* ratio is slightly lower than the critical value 1.75; therefore, this compound is considered somewhat brittle material. As shown in Fig. 6.12, the *B*/*G* ratio, for both crystals increase with increasing pressure away from 1.75, which indicate that both crystals become more ductile with increasing pressure.

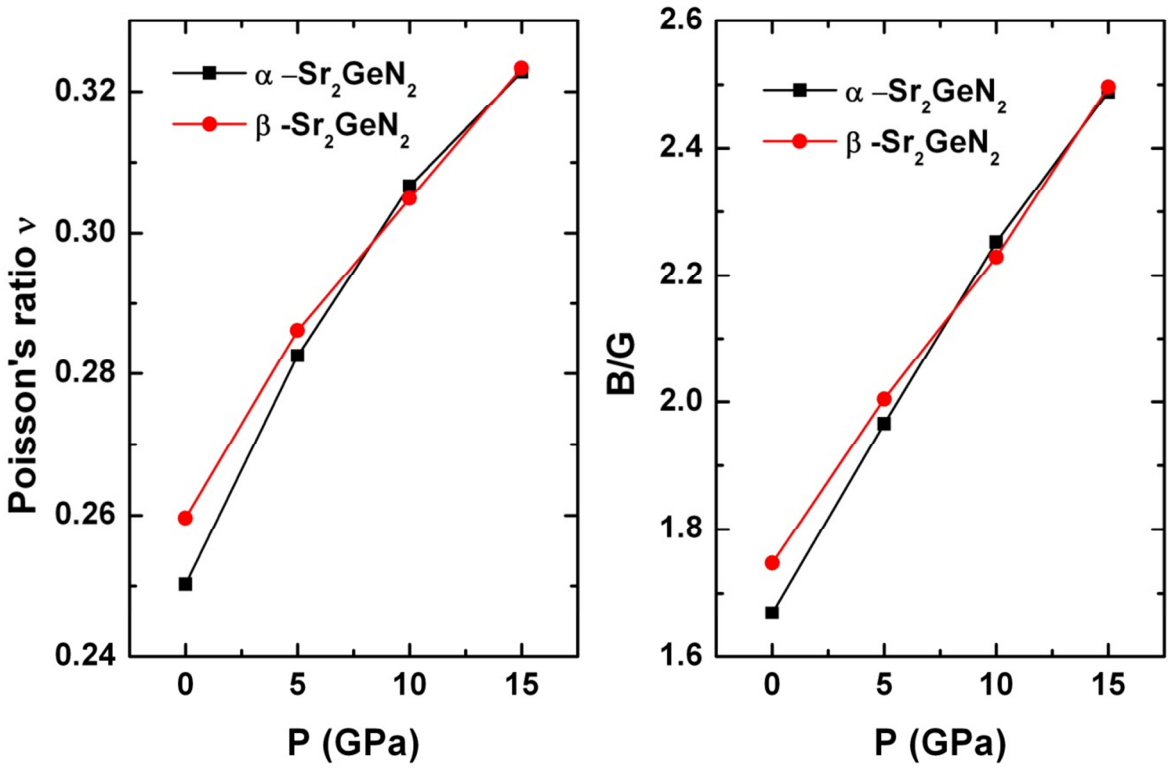

Fig. 6.12: Variation of the Poisson's ratio *ν* and *B*/*G* ratio as a function of pressure for the α-Sr_2GeN_2 and β-Sr_2GeN_2 compounds.

(v) Within the Debye model, the Debye temperature θ_D is one of the fundamental parameters of solids; it is closely correlated with many physical properties, such as heat capacity, melting temperature, thermal expansion, elastic constants and so on. The θ_D is the highest temperature that can be achieved due to a single normal vibration and then it is used to distinguish between high- and low-temperature regions for a solid. The θ_D can be numerically estimated from the average sound-wave velocity V_m through the following relationship [25]:

$$\theta_D = \frac{h}{K_B}\left[\frac{3n}{4\pi}\left(\frac{N_A\rho}{M}\right)\right]^{1/3} V_m \tag{6.26}$$

Her, h is the Planck's constant, k_B is the Boltzmann's constant, N_A is the Avogadro's number, ρ is the mass density, M is the molecular weight and n is the number of atoms in the molecule. The average sound-wave velocity V_m in the polycrystalline materials can be computed using the following expression:

$$V_m = \left[\frac{1}{3}\left(\frac{2}{V_t^3}+\frac{1}{V_l^3}\right)\right]^{-1/3} \tag{6.27}$$

Here, V_l and V_t are the longitudinal and transverse sound-wave velocities in the polycrystalline material, respectively, which can be calculated from the Navier's equation [26]:

$$V_t = \left(\frac{G}{\rho}\right)^{1/2}, \quad V_l = \left(\frac{3B+4G}{3\rho}\right)^{1/2} \tag{6.28}$$

Table 6.8: Molecular weight (M, in g/mol), density (ρ, in g/cm^3), transverse, longitudinal and average sound velocities (V_l, V_t and V_m, respectively, in m/s) and the Debye temperatures (θ_D, in K) for the α-Sr_2GeN_2 and β-Sr_2GeN_2 compounds

Compound	M	ρ	V_t	V_l	V_m	θ_D
α-Sr_2GeN_2	275.844	4.9915	2828.4	4900.7	3140.2	354.4
β-Sr_2GeN_2	275.844	4.9534	2787.3	4891.7	3097.9	348.8

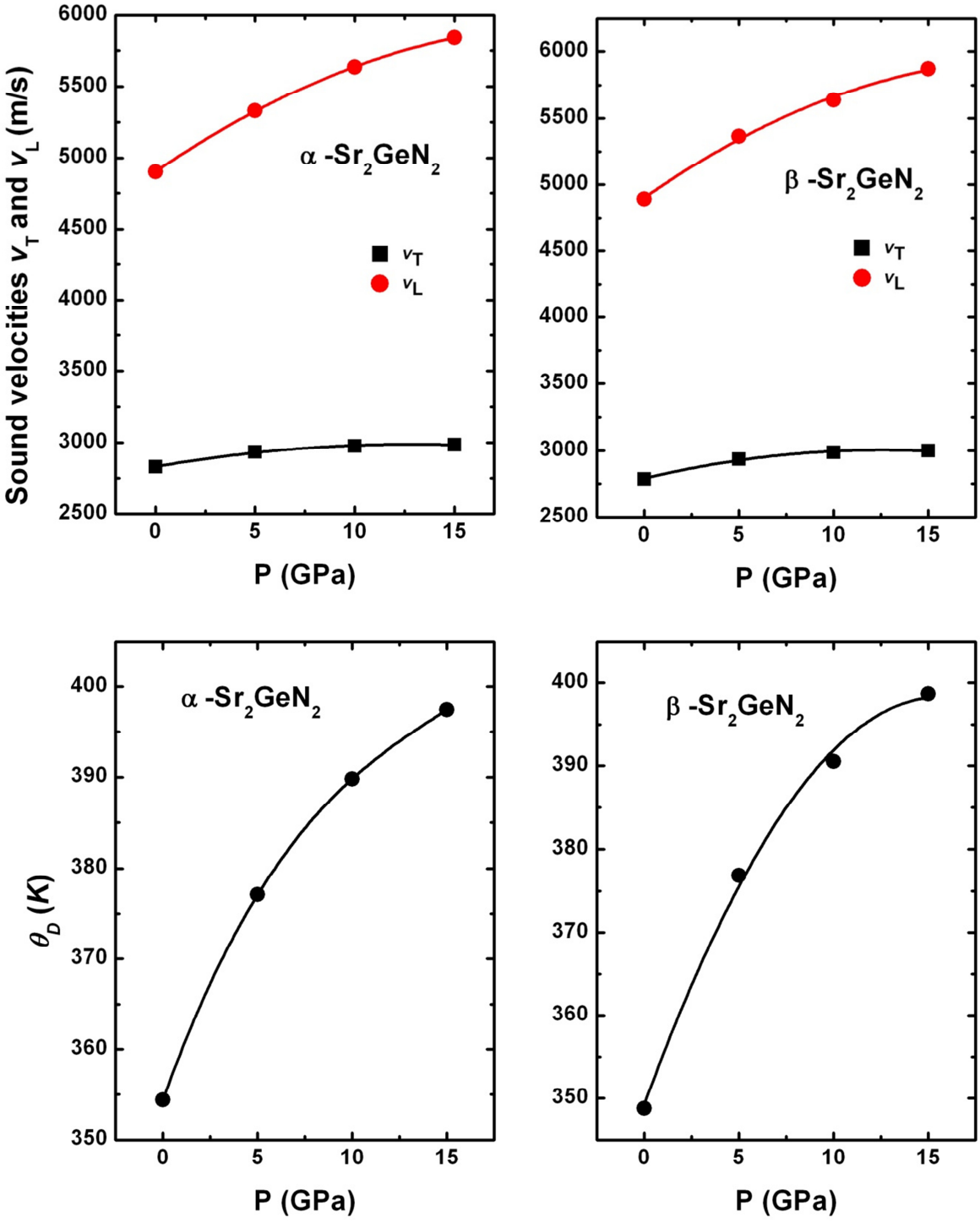

Fig 6.13: Transverse and longitudinal sound velocities (v_t and v_l, respectively) and Debye temperature (θ_D) versus pressure for the α-Sr_2GeN_2 and β-Sr_2GeN_2 compounds. The solid lines are least-squares polynomial fits of the data points.

The calculated sound-wave velocities (V_l, V_t and V_m) and Debye temperature (θ_D) for the polycrystalline α-Sr_2GeN_2 and β-Sr_2GeN_2 compounds are listed in Table 6.8. One can see from this table that the values of ρ, V_t, V_l, V_m and θ_D of α-Sr_2GeN_2 are slightly larger than those of β-Sr_2GeN_2 of about 0.76%, 1.45%, 0.18%, 1.35% and 1.60%, respectively. The variation of V_t, V_l and θ_D as a function of pressure is plotted in Fig. 6.13. We clearly observe a quadratic dependence of these parameters in the considered range of pressure.

6.2.2.4. Elastic anisotropy

Crystal anisotropy reflects the difference between the atomic arrangements along different directions. Many low symmetry crystals exhibit a high degree of elastic anisotropy. Crystal anisotropy has an important implication in engineering science as well as in crystal physics, for example, microcracks can easily induced in materials having significant anisotropy of the thermal expansion coefficient as well as elastic anisotropy [27]. Furthermore, recent research report states that the elastic anisotropy has a significant influence on the nanoscale precursor textures in alloys [28]. Therefore, it is necessary and significant to properly describe the elastic anisotropy of solids in order to understand this property and consequently to find mechanisms that will improve their resistance to microcracks. We have employed different criteria to quantify the anisotropy of the elastic properties for the concerning materials. First, elastic anisotropy behavior of a crystal can be sufficiently and completely described by plotting three-dimensional (3D) representation of directional dependence of its elastic moduli. To visualize the elastic anisotropy extent of the two considered crystals, three-dimensional closed surfaces illustrating the dependence of the Young's modulus E and linear compressibility β on the crystallographic directions are plotted. In tetragonal system with $4mn$, $\bar{4}2m$, 422 and $4/mmm$ classes, and orthorhombic crystals, the 3D closed surfaces for E and β are described by the following relationships [17]:

$$\begin{cases} \dfrac{1}{E} = \left(l_1^4 + l_2^4\right)S_{11} + l_3^4 S_{33} + 2l_1^2 l_2^2 S_{12} + 2\left(l_1^2 l_3^2 + l_2^2 l_3^2\right)S_{13} + \left(l_1^2 l_3^2 + l_2^2 l_3^2\right)S_{44} + l_1^2 l_2^2 S_{66} \\ \beta = \left(S_{11} + S_{12} + S_{13}\right)l_1^2 + \left(S_{12} + S_{11} + S_{13}\right)l_2^2 + \left(2S_{13} + S_{33}\right)l_3^2 \end{cases} \quad (6.29)$$

while for orthorhombic crystals, they are given by:

$$\begin{cases} \dfrac{1}{E} = l_1^4 S_{11} + l_2^4 S_{22} + l_3^4 S_{33} + 2l_1^2 l_2^2 S_{12} + 2l_1^2 l_3^2 S_{13} + 2l_2^2 l_3^2 S_{23} + l_1^2 l_3^2 S_{44} + l_2^2 l_3^2 S_{55} + l_1^2 l_2^2 S_{66} \\ \beta = \left(S_{11} + S_{12} + S_{13}\right)l_1^2 + \left(S_{12} + S_{22} + S_{13}\right)l_2^2 + \left(S_{13} + S_{23} + S_{33}\right)l_3^2 \end{cases} \quad (6.30)$$

Here, l_1, l_2 and l_3 are the directional cosines with respect to the *x*-, *y*- and *z*-axes, respectively, and the S_{ij} stand to the elastic compliance constants that can be obtained through an inversion of the elastic constant tensor. In a 3D-representation, the distance from the origin of the system of coordinates to this surface gives the value of the represented elastic modulus in a given direction. Thus, in a 3D representation, a perfectly isotropic system would exhibit a spherical shape, and the degree of deviation of the 3D surface from spherical shape reveals the extent of the elastic anisotropy.

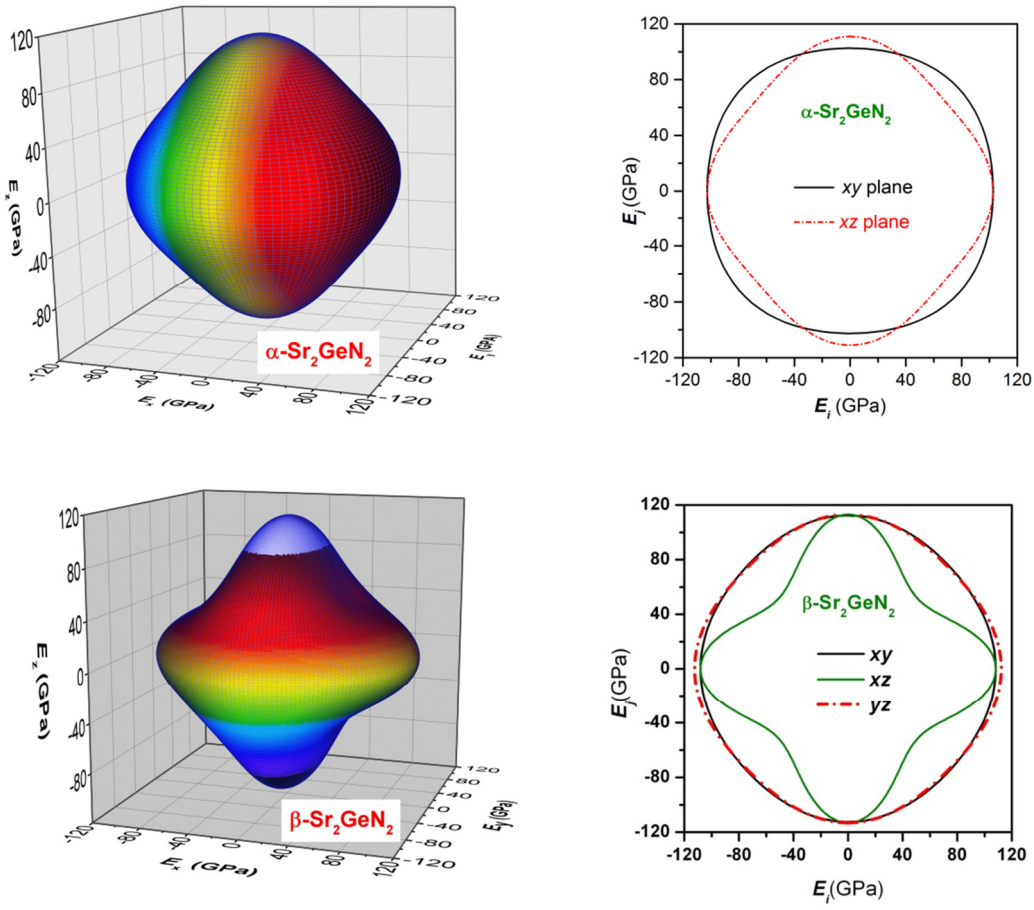

Fig. 6.14: Directional dependence of the Young's modulus and its cross sections in different planes for α-Sr_2GeN_2 and β-Sr_2GeN_2 crystals. The distance between zero and any point on the surface is equal to the Young's modulus in that direction

Fig. 6.14 (Fig. 6.15) illustrates three-dimensional representation of the directional dependence of the Young's modulus *E* (linear compressibility *β*) together with its cross section in the *xy*, *xz* and *yz* crystallographic planes for α-Sr_2GeN_2 and β-Sr_2GeN_2 crystals. From Fig. 6.14 (Fig. 6.15), one can observe the appreciable deviation of the 3-D representation of the Young's modulus (linear compressibility) from the spherical shape in both studied crystals, suggesting that α-Sr_2GeN_2 and β-Sr_2GeN_2 crystals exhibit a pronounced elastic anisotropy. We can see clearly from Figs. 6.15 and 6.15 that β-Sr_2GeN_2 is more anisotropic than α-Sr_2GeN_2.

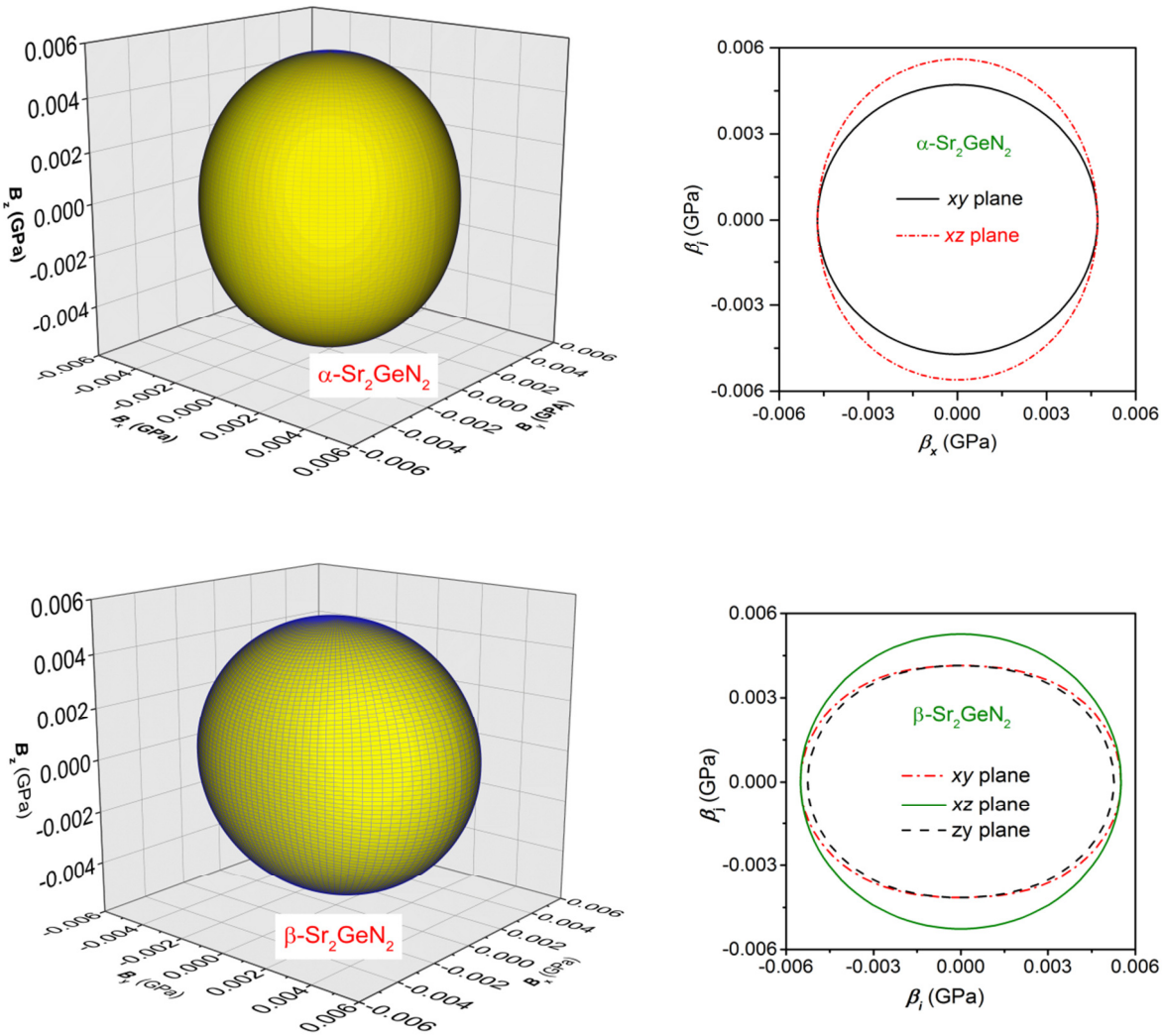

Fig. 6.15: Directional dependence of the linear compressibility and its cross sections in different planes for α-Sr_2GeN_2 and β-Sr_2GeN_2 crystals. The distance between zero and any point on the surface is equal to the linear compressibility β in that direction

Second, the use of the different criteria of the anisotropy factors enables us to analyze the crystal elastic anisotropy for the studied compounds:

(i) Among them, we find the shear anisotropic factors [26], which provide a measure of the degree of anisotropy in the bonding between atoms in different planes. For the tetragonal crystals, the shear anisotropic factors are given by [29]:

$$A_1 = \frac{2C_{66}}{C_{11}-C_{12}} \tag{6.31}$$

for the {1 0 0} or {0 1 0} shear planes, and

$$A_2 = \frac{4C_{44}}{C_{11}+C_{33}-2C_{13}} \tag{6.32}$$

for the {0 0 1} shear planes.

For the orthorhombic crystals, they are given by [30]:

$$A_1 = \frac{4C_{44}}{C_{11}+C_{33}-2C_{13}} \tag{6.33}$$

for the {1 0 0} shear planes.

$$A_2 = \frac{4C_{55}}{C_{22}+C_{33}-2C_{23}} \tag{6.34}$$

for the {0 1 0} shear planes, and

$$A_3 = \frac{4C_{66}}{C_{11}+C_{22}-2C_{12}} \tag{6.35}$$

for the {0 0 1} shear planes. For the orthorhombic crystals, where an isotropic material will have $A_1 = A_2 = A_3 = 1$, while the deviations of A from the unity measure the degree of elastic anisotropy.

The calculated shear anisotropic factors listed in Table 9 indicate that both α-Sr_2GeN_2 and β-Sr_2GeN_2 exhibit some anisotropy. For α-Sr_2GeN_2, the anisotropy factor A_1 is very close to unity, implying that the resistance to shears of {1 0 0} and {0 1 0} planes are almost isotropic. For β-Sr_2GeN_2, the anisotropy factor A_2 is very different from unity, implying that {010} shear planes are characterized by a noticeable elastic anisotropy, compared to {1 0 0} and {0 0 1} shear planes. We can conclude also from Table 6.9 that β-Sr_2GeN_2 has more elastic anisotropy than α-Sr_2GeN_2. Under pressure, as shown in Fig. 6.16, the shear anisotropic factor A_1 of α-Sr_2GeN_2 increases when the pressure increases, while the A_2 decreases. Both factors move away together from 1, indicating that the degree of elastic anisotropy of α-Sr_2GeN_2 increases with increasing pressure. The same behavior is shown for β-Sr_2GeN_2 (i. e. the degree of anisotropy increases when pressure increases) because A_1 and A_3 decrease sharply away from 1, despite the slight increase of A_2.

(ii) Another way for measuring the elastic anisotropy of crystal is given by the percentage of anisotropy in compressibility A_B and shear modulus A_G [31], which are defined as:

$$A_B = (B_V - B_R)/(B_V + B_R) \text{ and } A_G = (G_V - G_R)/(G_V + G_R) \quad (6.36)$$

A value of 0 (0%) corresponds to complete elastic isotropy, while a value of 1 (100%) corresponds the largest possible anisotropy. It can be seen from Table 9 that both compounds are anisotropic in compression and shear. From Fig 6.16, we can see that under pressure, A_B remains almost the invariable, while A_G increases with increasing pressure.

(iii) Finally, The universal anisotropy index A^U [32] was used to measuring the elastic anisotropy of crystals accounting for both bulk and shear modulus contributions. It is defined as:

$$A^U = 5\frac{G_V}{G_R} + \frac{B_V}{B_R} - 6 \quad (6.37)$$

For isotropic crystals A^U = 0; deviations of A^U from zero define the extent of elastic anisotropy. The results listed in Table 6.9 confirm also the elastic anisotropy of the two compounds. We can see from Fig. 6.16 that A^U of both α-Sr_2GeN_2 and β-Sr_2GeN_2, increases with increasing pressure. We show from this figure that the A_B, A_G and A^U of the β-Sr_2GeN_2 are largest than those of α-Sr_2GeN_2. They all demonstrate that the orthorhombic structural of Sr_2GeN_2 is more anisotropic than that of tetragonal structure.

Table 6.9: The shear anisotropic factors (A_1, A_2 and A_3), the percentage of elastic anisotropy in compressibility and shear modulus (A_B and A_G), and the universal anisotropy index (A^U), for the α-Sr_2GeN_2 and β-Sr_2GeN_2 polymorphs

α-Sr_2GeN_2	**A_1**	**A_2**	**A_B (%)**	**A_G (%)**	**A^U**
	1.070	0.804	0.170	0.544	0.058
β-Sr_2GeN_2	**A_1**	**A_2**	**A_3**	**A_B (%)**	**A_G (%)**	**A^U**
	0.824	0.558	0.928	0.303	2.554	0.268

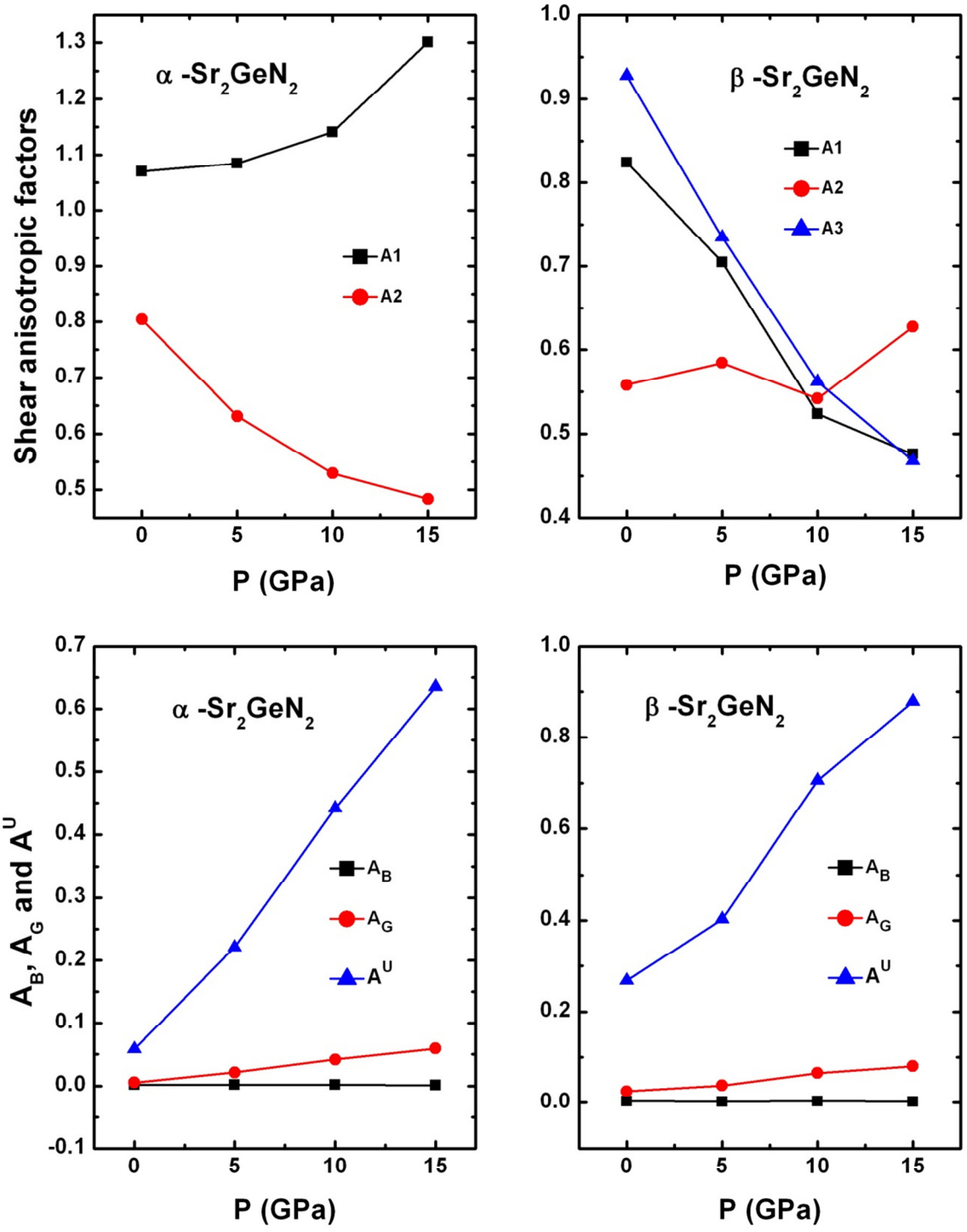

Fig. 6.16: Pressure dependence of shear anisotropic factors(A_1, A_2 and A_3), elastic anisotropy in compressibility and in shear modulus (A_B and A_G), and the universal anisotropy index (A^U), for the α-Sr_2GeN_2 and β-Sr_2GeN_2 polymorphs.

6.2.3. Thermodynamic properties

Investigation of the thermodynamic properties of solids at high pressure and high temperature is an interesting topic in the condensed matter physics. Here, we applied the quasi-harmonic Debye approximation [9] to investigate the thermodynamic properties of the α-Sr_2GeN_2 and β-Sr_2GeN_2 compounds. The thermal properties are determined in the temperature range from 0 to 900 K at some fixed pressures (P = 0, 5, 10, 15 GPa).

6.2.3.1. Normalized volume variation

In Fig. 6.17, we present the normalized volume-temperature diagram of α-Sr_2GeN_2 and β-Sr_2GeN_2 compounds at different pressures. The unit cell volume increases slowly with increasing temperature in the range temperature between 0 and 100 K, then, the rate become more important for the temperature range above 100 K. On the other side, at a given temperature, the normalized volume V/V_0 decreases with increasing pressure. The effect of increasing temperature on the unit cell volume is just the same as decreasing pressure.

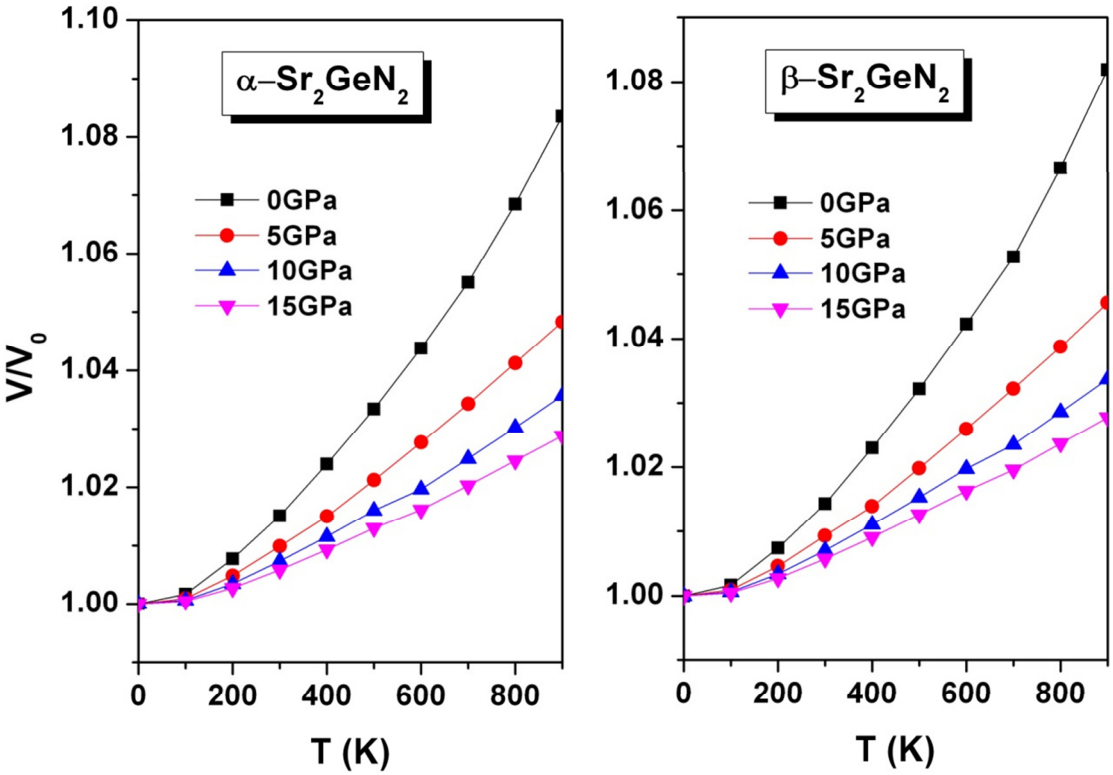

Fig. 6.17: Variation of the normalized volume versus temperature at different pressures for the α-Sr2GeN_2 and β-Sr_2GeN_2. V_0 is the equilibrium volume at T = 0 K.

6.2.3.2. The heat capacity C_V

The heat capacity of a crystal does not only provide essential information on its vibrational properties, but it is also mandatory for many applications. Temperature dependence of the constant volume heat capacity C_V at some fixed pressures is shown in Fig. 6.18. From this figure, one can see the sharp increase of C_V in the temperature range from 0 up to ~200 K and at high temperature, the C_V tends to a constant value (997.7 J.mol^{-1} K^{-1}), the so-called Dulong-Petit limit. At 300 K and zero pressure, C_V = 936.0 J.mol^{-1} K^{-1} for α-Sr2GeN_2 and 935.4 J.mol^{-1} K^{-1} for β-Sr_2GeN_2.

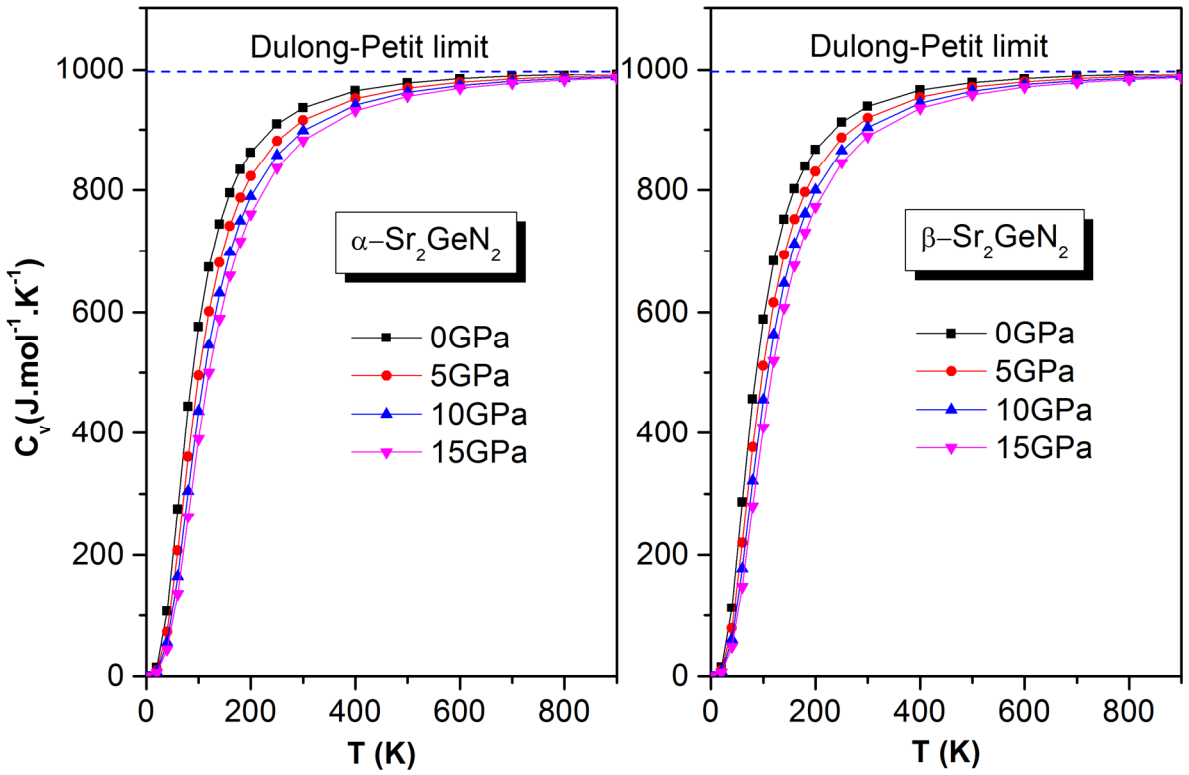

Fig 6.18: The heat capacity versus temperature at different pressures for the α-Sr2GeN_2 and β-Sr_2GeN_2.

6.2.3.3. The thermal expansion coefficient

The thermal expansion coefficient α reflects the temperature dependence of the volume at constant pressure. Fig. 6.19 shows the evolution of the thermal expansion coefficient α with temperatures at some different fixed pressures. From this figure, we can see that the thermal expansion increases sharply with temperature in the temperature range from 0 K up to ~200 K, especially at zero pressure, then for temperature higher than 200 K, the increase becomes slowly and gradually approaches a linear increase. The increase of α is faster at lower pressures than at higher pressures. For a given temperature, α decreases drastically with the increase of pressure. At zero pressure and 300 K, α = 7.91242× 10^{-5} K^{-1} for α-Sr2GeN_2 and 7.42234× 10^{-5} K^{-1} for β-Sr_2GeN_2.

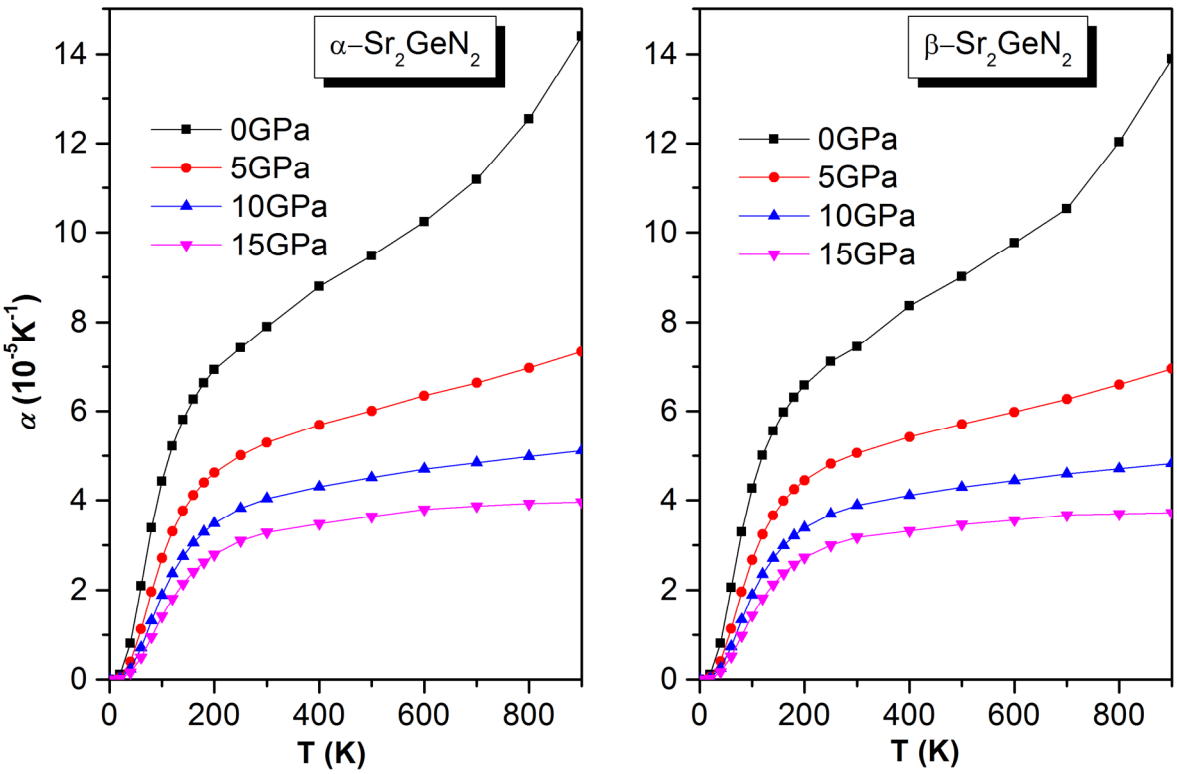

Fig. 6.19: The thermal expansion coefficient versus temperature at different pressures for the α-Sr2GeN_2 and β-Sr_2GeN_2.

6.2.3.4. Debye temperature

Fig. 6.20 shows temperature dependence of the Debye temperature θ_D at some fixed pressures. At fixed pressure, Debye temperature decreases with increasing temperature and at fixed temperature, θ_D increases with increasing pressure, indicating the change of the vibration frequency of particles under pressure and temperature effects. From Fig. 20, one can observe that as the pressure goes higher, the decreasing slope of θ_D with temperature becomes smaller; the high pressure suppresses the temperature effect. At zero pressure and zero temperature, Debye temperatures for α-Sr_2GeN_2 and β-Sr_2GeN_2 are 353.2 K and 353.9 K, respectively. It is worth to note here that the value of θ_D calculated using Debye model is in good agreement with that calculated from the sound velocities (354.43 K and 348.76 K, respectively).

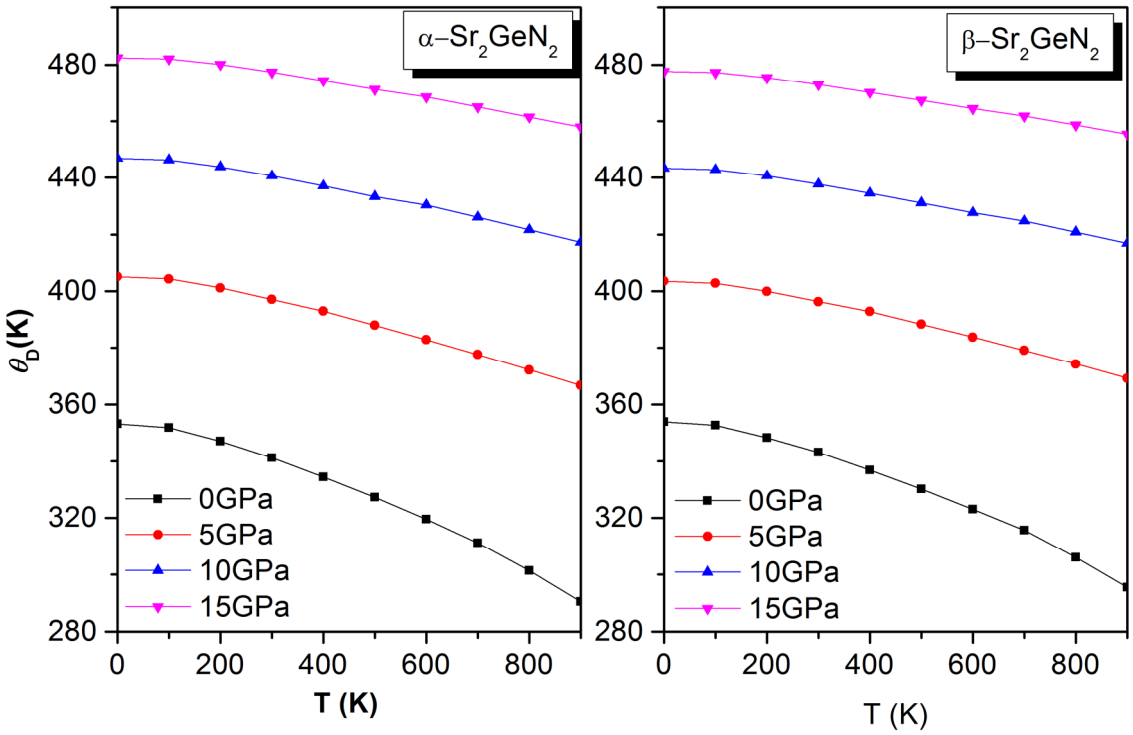

Fig. 6.20: The Debye temperature θ_D versus temperature at different pressures for the α-Sr2GeN_2 and β-Sr_2GeN_2.

6.2.3.5. The bulk modulus

Fig. 6.21 depicts the variation of bulk modulus versus temperature at some given pressures. The bulk modulus *B* decreases with increasing temperature in a quasi-linear manner after 100 K at a given pressure, and increases with pressure at a given temperature. It can be seen from the Diagrams of *B* (T) that the influence of the temperature on the bulk modulus *B* decreases slightly with increasing pressure (The effect of the temperature on *B* is significant at 0 GPa). The calculated values of *B* at 300 K and zero pressure are equal to 59.9 GPa and 58.5 GPa, respectively for α-Sr2GeN_2 and β-Sr_2GeN_2.

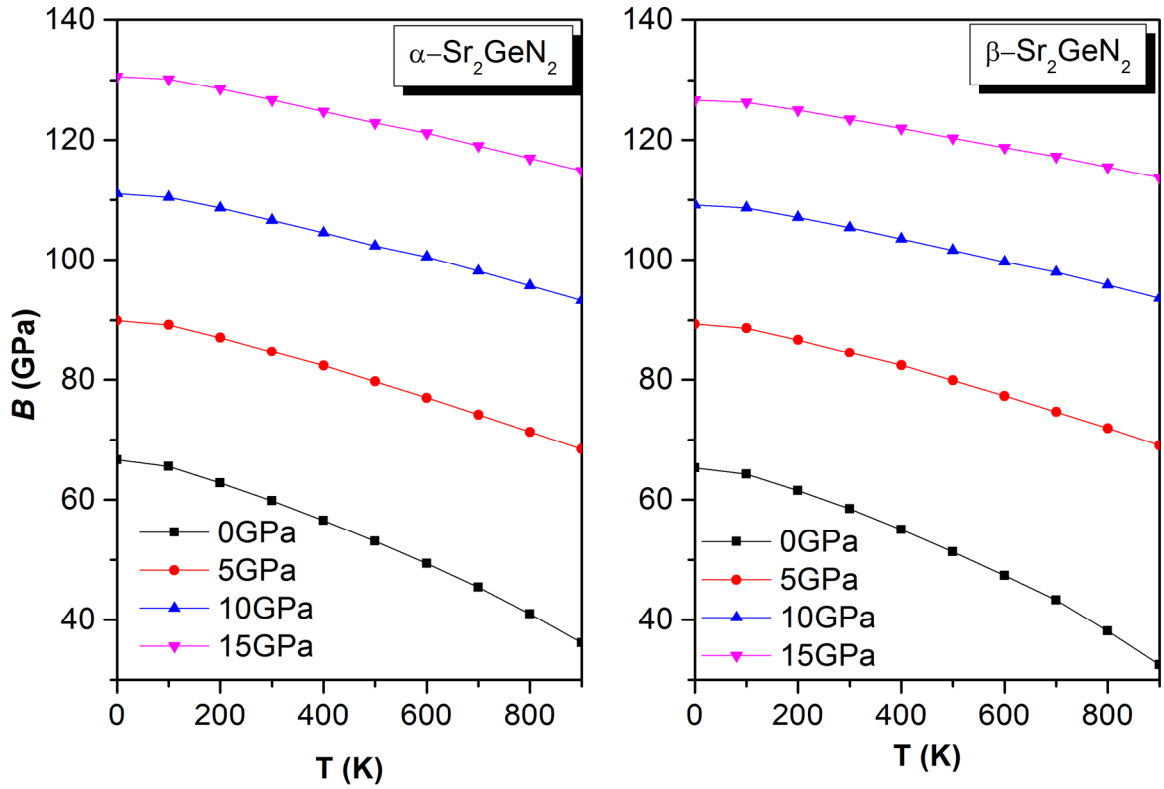

Fig. 6.21: The bulk modulus *B* versus temperature at different pressures for the α-Sr2GeN_2 and β-Sr_2GeN_2.

6.2.3.6. Grüneisen parameter

The Grüneisen parameter, which describes usually anharmonic effects of the vibrating lattice, is an important quantity in geophysics as it often occurs in equations which describe the thermoelastic behavior of materials at high pressures and temperatures [33]. It can be defined as: $\gamma = -\frac{dln\theta_D(V)}{dlnV}$. Fig. 6.22 presents the Gruneisen parameter γ versus temperature at different pressures. We can see from this figure that at a given pressure, the Gruneisen parameter γ increases with increasing temperature, but very slowly at low temperatures (T < 100 K). Moreover, the Grüneisen parameter γ increases more slowly at high pressure than at low pressure.

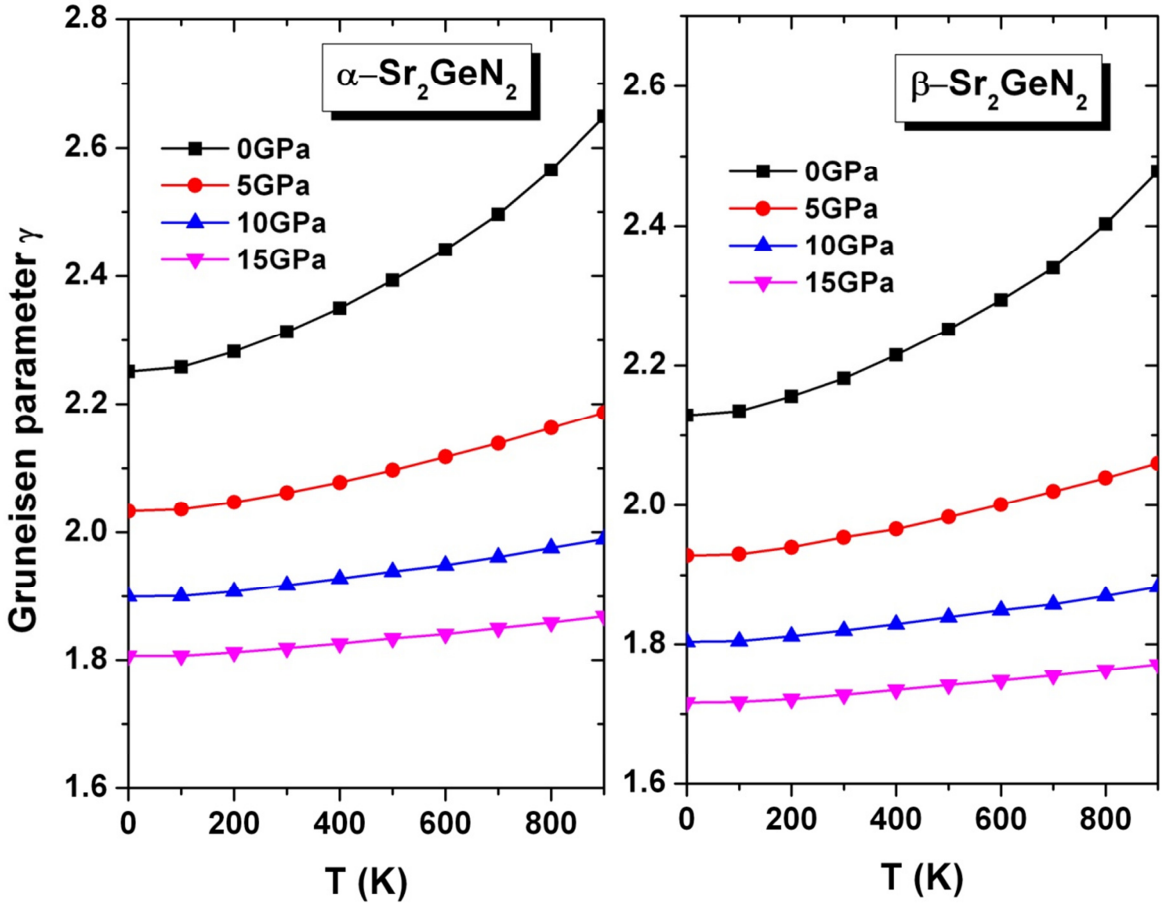

Fig. 6.22: The variation of Grüneisen parameter γ versus temperature at different pressures for the α-Sr2GeN_2 and β-Sr_2GeN_2

References

[1] S. J. Clark, M. D. Segall, C. J. Pickard, et al, *First principles methods using CASTEP*, Zeitschrift fuer Kristallographie 220, 567-570 (2005).

[2] J. P. Perdew, A. Ruzsinszky, G. I. Csonka, O. A. Vydrov, G.E. Scuseria, L. A. Constantin, X. Zhou, K. Burke, *Restoring the Density-Gradient Expansion for Exchange in Solids and Surfaces*, Phys. Rev. Lett. 100, 136406-4 (2008).

[3] D. Vanderbilt, *Soft self-consistent pseudopotentials in a generalized eigenvalue formalism*, Phys. Rev. B 41, 7892-4 (1990).

[4] H. J. Monkhorst, J. D. Park, *Special points for Brillouin-zone integrations*, Phys. Rev. B 13, 5188-5 (1976).

[5] T. H. Fischer, J. Almlof, *General methods for geometry and wave function optimization*, J. Phys. Chem. 96, 9768-9774 (1992).

[6] W. Voigt, *Lehrbuch der Kristallphysik* (*Textbook of crystal physics*), Teubner, Leipzig, 1928.

[7] A. Reuss, Z. Angew, *Calculation of the yield strength of solid solutions based on the plasticity condition of single crystals*, Math. Mech. 9, 49-58 (1929).

[8] R. Hill, *The elastic behavior of a crystalline aggregate*, Proc. Phys. Soc. A 65, 349-354 (1952).

[9] M. A. Blanco, E. Francisco, V. Luaña, *isothermal-isobaric thermodynamics of solids from energy curves using a quasi-harmonic Debye model*, Comput. Phys. Commun. 57, (2004).

[10] S. J. Clarke, G. R. Kowach, F. J. DiSalvo, *Synthesis and Structure of Two New Strontium Germanium Nitrides: $Sr_3Ge_2N_2$ and Sr_2GeN_2*, Inorg. Chem. 35, 7009-7012 (1996).

[11] D. G. Park, Z. Gál, F. J. DiSalvo, *Synthesis and structure of a second polymorph of strontium germanium nitride: β-Sr_2GeN_2*, Bull. Korean Chem. Soc. 26, 786-790 (2005).

[12] Z. A. Alahmed, A. H. Reshak, *DFT calculation of the electronic structure and optical properties of two strontium germanium nitrides: α-Sr_2GeN_2 and β-Sr_2GeN_2*, J. Alloys Compd. 559, 181-187 (2013).

[13] F. Birch, *Finite strain isotherm and velocities for single crystal and polycrystalline NaCl at high pressure and* 300 *K*, J. Geophys. Res. B 83 1257-1268 (1978).

[14] F. D. Murnaghan, *The compressibility of media under extreme pressure*, Proc. Natl. Acad. Sci. U.S.A. 30, 244-247 (1944).

[15] F. Birch, *Finite elastic strain of cubic crystals*, Phys. Rev. 71, 809:1-16 (1947).

[16] P. Vinet, J. Ferrante, J. H. Rose, J. R. Smith, *Compressibility of solids*, J. Geophys. Res. 92, 9319-9325 (1987).

[17] J. F. Nye, Properties of crystals, Oxford University Press, 1985.

[18] M. Born, K. Huang, *Dynamical Theory of Crystal Lattices*, New York: Oxford University Press, 1988.

[19] B. B. Karki, L. Stixrude, S. J. Clark, M. C. Warren, G. J. Ackland, *Structure and elasticity of MgO at high pressure*, J. Crain, Am. Mineral. 82, 51-60 (1997).

[20] G. V. Sin'ko, N. A. Smirnov, *Ab initio calculations of elastic constants and thermodynamic properties of bcc, fcc, and hcp Al crystals under pressure*, J. Phys. Condens. Matter 14, 6989-7005 (2002).

[21] L. P. Feng, Z. T. Liu, Q. J. Liu, *Structural, elastic and mechanical properties of orthorhombic $SrHfO_3$ under pressure from first-principles calculations*, Physica B: Condensed matter 407, 2009-2013 (2012).

[22] A. Bouhemadou, G. Uğur, Ş. Uğur, S. Al-Essa, M.A. Ghebouli, R. Khenata, S. Bin-Omran, Y. Al-Douri, *Elastic and thermodynamic properties of $ZnSc_2S_4$ and $CdSc_2S_4$ compounds under pressure and temperature effects*, Compt. Mat. Sci. 70, 107-113 (2013).

[23] K. Haddadi, A. Bouhemadou, L. Louail, *Ab initio investigation of the structural, elastic and electronic properties of the anti-perovskite $TlNCa_3$*, Solid State Commun. 150, 932-937 (2010).

[24] S.F. Pugh, *Relations between the elastic moduli and plastic properties of polycrystalline pure metals*, Philos. Mag. 45, 823-843 (1954).

[25] O.L. Anderson, *A simplified method for calculating the Debye temperature from elastic constants*, J. Phys. Chem. Solids 24, 909-917 (1963).

[26] E. Schreiber, O.L. Anderson, N. Soga, *Elastic constants and their measurements*, McGraw-Hill Companies, New York, 1974.

[27] P. Ravindran, L. Fast, P.A. Korzhavyi, B. Johansson, O. Eriksson, *Density functional theory for calculation of elastic properties of orthorhombic crystals: application to TiSi2*, J. Appl. Phys. 84, 4891-14 (1998).

[28] P. Lloveras, T. Castán, M. Porta, A. Planes, A. Saxena, *Influence of elastic anisotropy on nanoscale textures*, Phys. Rev. Lett. 100, 165707-4 (2008).

[29] A. Al-Ghaferi, P. Müllner, H. Heinrich, G. Kostorz, J. M. K. Wiezorek, *Elastic constants of equiatomic $L1_0$-ordered FePd single crystals*, Acta Materialia 54, 881-889 (2006).

[30] D. Connétable, O. Thomas, *First-principles study of the structural, electronic, vibrational, and elastic properties of orthorhombic NiSi*, Phys. Rev. B 79, 094101-9 (2009).

[31] H. Chung, W.R. Buessem, in: F.W. Vahldiek, S.A. Mersol (Eds.), *Anisotropy in Single Crystal Refractory Compound*, Plenum, New York, 1968.

[32] S.I. Ranganathan, M. Ostoja-Starzewski, *Universal Elastic Anisotropy Index*, Phys. Rev. Lett. 101, 055504-4 (2008).

[33] L. Vocadlo, J.P. Poirer, and G.D. Price, *Grüneisen parameters and isothermal equations of state*, American Mineralogist, Volume 85, pages xxx–xxx, 2000.

CHAPTER 7

General conclusion

Chapter 7

General conclusion

In the present work, we have reported the results of detailed first-principle calculations of the some physical properties for two groups of compounds: the first group is related to the two novel quaternary diamond-like semiconductors Cu_2MgSiS_4 and Cu_2MgGeS_4, while the second group includes both polymorphs of the ternary nitrides α-Sr_2GeN_2 and β-Sr_2GeN_2. The obtained results for each group are summarized separately as follows:

7.1. Cu_2MgSiS_4 and Cu_2MgGeS_4 diamond like semiconductors

For these two diamond-like semiconductors, we have investigated their structural, elastic, electronic and optical properties, using two *ab initio* density functional theory approaches: (i) the pseudo-potential plane wave (PP-PW) method as implemented in the CASTEP code was employed to calculate the structural and elastic properties. (ii) The electronic and optical properties of the title crystals were studied using the full potential linearized augmented plane wave (FP-LAPW) as implemented in the WIEN2K package. The exchange correlation effects are treated within the new version of the generalized gradient approximation, namely GGA-PBEsol, in addition to the use of TB-mBJ approximation in calculate of the last two properties. The obtained results are summarized as follows:

- ✓ Both Cu_2MgSiS_4 and Cu_2MgGeS_4 have an orthorhombic structure and belong to the $Pmn2_1$ space group (no. 31). All the atoms have normal tetrahedral coordinates.
- ✓ The optimized structural parameters, including lattice parameters, atomic positions and interatomic bond-lengths, reproduce the available experimental data. The structural parameters of Cu_2MgGeS_4 are slightly larger than those of Cu_2MgSiS_4.
- ✓ Both considered compounds have negative cohesive energies and formation enthalpies, indicating that they are energetically stable.

- ✓ The calculated pressure dependence of the lattice parameters shows that both Cu_2MgSiS_4 and Cu_2MgGeS_4 are more compressible along the *b*-axis than along the *a*- and *c*-axes.
- ✓ Pressure dependence of the bond-lengths reveals that the Si/Ge-S bonds are stronger than the other bonds. The different orientations of these bonds along crystallographic axes explain the difference between linear compressibilities.
- ✓ We have evaluated the single-crystal and polycrystalline elastic moduli and related properties. The results indicate that Cu_2MgSiS_4 is slightly harder than Cu_2MgGeS_4.
- ✓ The calculated bulk modulus from the single-elastic constants is in good agreement with those estimated from different EOS fits and from compressibilities. This serves to give an indication of the accuracy of our predicted elastic constants. The two examined chalcogenids are classified as a relatively soft material (B ~ 80 GPa).
- ✓ They are mechanically stable, and behave in a ductile manner (B/G = 2.63 for both compounds).
- ✓ The Poisson's ratio is approximately equal to 0.33 in both Cu_2MgSiS_4 and Cu_2MgGeS_4, suggesting a considerable volume change can be associated with elastic deformation.
- ✓ The different criteria used to quantify the elastic anisotropy indicate that these two compounds exhibit a considerable elastic anisotropy. The Cu_2MgGeS_4 is slightly more anisotropic than the Cu_2MgSiS_4.
- ✓ Analysis of the TB-mBJ potential band structure indicates that Cu_2ZnGeS_4 and Cu_2CdGeS_4 semiconductors have a direct band gap (Γ-Γ) of 2.64 and 1.54 eV, respectively.
- ✓ The introduction of the Mg element instead of the Zn/Cd element in the Cu_2-II-IV-VI_4 diamond-like compounds to the II sites for the first time yields to widen the band gaps of these materials, and thus obtaining new properties.
- ✓ The investigation of TDOS and PDOS has been reported. The top of the valence bands is dominated by the hybridized Cu-3*d* and S-3*p* states, and the bottom of the conduction band is formed by the *s-p* hybridization between the Si/Ge cation and the S anion. The bonding character may be described as a mixture of covalent-ionic.
- ✓ The effective masses of electrons and holes are estimated at the Γ point from the band dispersion around the VBMa and CBMi. The mobility of the holes will be substantially lower than that of the electrons.

- ✓ The frequency dependent polarized macroscopic linear optical spectra, including dielectric function, refractive index, extinction coefficient, absorption coefficient, reflectivity, energy loss function and optical conductivity, were obtained and discussed. Optical spectra of the title materials exhibit a noticeable anisotropy.
- ✓ The microscopic origin of the features in the optical spectra and the contributions of the different regions in the Brillouin zone were identified through decomposing the imaginary dielectric functions into individual inter-band contributions and plotting the transition band structures.
- ✓ Both Cu_2MgSiS_4 and Cu_2MgGeS_4 exhibits noticeable absorption in the ultraviolet range.

7.2. α-Sr_2GeN_2 and β-Sr_2GeN_2 ternary nitrides

We have investigated the structural and elastic properties of the two polymorphs of Sr_2GeN_2, using the *ab initio* pseudopotential plane-wave method (PP-PW) based on DFT, as implemented in the CASTEP code, and with the use of GGAsol approximation to treat the exchange correlation effects. This method was combined with the quasi-harmonic Debye model to calculate the thermodynamic properties for these two compounds. The effect of pressure is taken into account up to 15 GPa. We have reached the following conclusions:

- ✓ The α-Sr_2GeN_2 polymorph in the $P4_2/mbc$ (No. 135) tetragonal space group, while β-Sr_2GeN_2 crystallizes in *Cmac* (No. 64) orthorhombic space group. A differentiating factor of the crystalline structures of these two polymorphs is the relative orientation of the GeN_2 units in the lattice.
- ✓ The optimized structural parameters, including lattice parameters, atomic positions and interatomic bond-lengths, are in good agreement with the experimental data. The two polymorphs have almost identical local environments.
- ✓ The calculated cohesive energy and formation enthalpy demonstrate that both examined polymorphs are energetically stable.
- ✓ The calculated pressure dependence of the lattice parameters shows that α-Sr_2GeN_2 is slightly more compressible along the *c*-axis than along the *a*-axis, whereas β-Sr_2GeN_2 is slightly more compressible along the *c*-axis and *a*-axis than along the *b*-axis. The β -Sr_2GeN_2 is slightly more compressible than α-Sr_2GeN_2.
- ✓ The normalized lattice parameters ratio and the normalized unit-cell volume are well described by a third-order polynomial versus pressure.

- ✓ The differences between linear compressibilities can be explained by the different orientations of the stronger bonds Ge-N along crystallographic axes.
- ✓ Pressure dependence of the bond-lengths reveals that chemical bonding between neighbors inside the stacking planes is stronger than those between adjacent planes.
- ✓ We have evaluated the single-crystal and polycrystalline elastic moduli and related properties at zero pressure and under pressure. The calculated elastic constants C_{ij} satisfy the stability conditions for both α-Sr_2GeN_2 and β-Sr_2GeN_2 at 0 GPa and under the considered pressure range. Their hardness increases with increasing pressure.
- ✓ The calculated bulk modulus from the single-elastic constants is in good agreement with those estimated from different EOS fits and from compressibilities. The two examined polymorphs have relatively a small bulk modulus (B < 100 GPa), so they are classified as a relatively soft material.
- ✓ According to Pugh's criterion, both phases are intermediate between ductile and brittle materials (B/G ~ 1.75 for both compounds).
- ✓ For both crystals The Poisson's ratio is almost equal to 0.25, indicating that a considerable ionic contribution in the interatomic bonding should be assumed in these crystals.
- ✓ The investigated crystals exhibit a strong elastic anisotropy. The orthorhombic polymorph β-Sr_2GeN_2 is more anisotropic than the tetragonal polymorph α-Sr_2GeN_2. Under pressure, the degree of anisotropy increases when the pressure increases.
- ✓ Using the quasi-harmonic Debye model, temperature dependences of the heat capacity, thermal expansion, Debye temperature, bulk modulus and Grüneisen parameter at some fixed pressures are predicted in temperature range from of 0 to 900 K. The effect temperature on these parameters decrease with increasing pressure.
- ✓ The calculated Debye temperature at zero pressure and zero temperature through this model is in good agreement with that calculated from the elastic constants.
- ✓ To the best of our knowledge, there are no previous reports on the elastic and thermodynamic properties, so, we hope future experimental and theoretical investigations of these materials will testify our present reported results.